Behavior of feldspars during the Giant Impact

Anaïs Kobsch

Numéro National de Thèse : 2020LYSEN026

THÈSE de DOCTORAT DE L'UNIVERSITÉ DE LYON

opérée par

l'École Normale Supérieure de Lyon

École Doctorale N°52
Physique et Astrophysique de Lyon (PHAST)

Discipline de doctorat : Sciences de l'univers
Spécialité de doctorat : Physique des Minéraux

Soutenue publiquement le 09/07/2020 par :
Anaïs KOBSCH

Behavior of feldspars during the Giant Impact

L'état physique des feldspaths pendant l'Impact Géant

Devant le jury composé de :

Ispas, Simona	Maître de Conférences	Univ. Montpellier 2	Rapporteure
Morard, Guillaume	Chargé de recherche	Univ. Grenoble Alpes	Rapporteur
Andreani, Muriel	Professeure des Universités	Univ. Claude Bernard Lyon 1	Examinatrice
Meyer, Simon	Directeur Planetarium	Vaulx-en-Velin	Examinateur
Reynard, Bruno	Directeur de recherche	ENS de Lyon	Examinateur
Caracas, Razvan	Directeur de recherche	ENS de Lyon	Directeur de thèse

Avant-propos

La science a besoin de la médiation scientifique et la médiation scientifique de la science. Bien qu'il existe des centres de culture scientifique, technique et industrielle (CCSTI) il reste beaucoup de progrès à faire dans la transmission et vulgarisation de la science.

La recherche est de manière générale assez innaccessible aux curieux, par la difficulté d'accès aux livres et journaux scientifiques, la barrière de la langue et surtout le niveau de compétences nécessaires pour comprendre le sujet abordé. Même s'il existe des journalistes et des revues de vulgarisation, ceci est loin d'être suffisant et représentatif de la recherche scientifique, les sujets de ces journaux étant souvent choisis pour leur attrait et leur potentiel vendeur. Il est nécessaire de développer la médiation scientifique au quotidien. D'une part pour sensibiliser le public à l'importance de la recherche aussi bien fondamentale qu'appliquée et d'autre part pour le simple plaisir d'ouvrir le public à des connaissances que d'aucuns considèrent comme peu accessibles.

Pour toutes ces raisons, ainsi que pour ma propre expérience personnelle et professionnelle, je tiens à ce que cette thèse soit accessible à des non inités, à des étudiants venant d'autres filières mais aussi je l'espère, à n'importe quel curieux de sciences. Cependant je ne souhaite pas non plus maltraîter l'exercice de la thèse, et donc il est important pour moi de garder un corps susceptible d'intéresser les scientifiques rattachés à ce domaine d'étude. C'est pourquoi il y a deux niveaux de lecture dans ce manuscrit, chacun rattaché à une langue. Le français est réservé à la médiation scientifique autour de cette thèse. Pour cela, à chaque début de chapitre se trouve un résumé d'une page maximum, permettant aux curieux de se faire une idée de la recherche effectuée pendant ces trois années. L'anglais quant à lui est consacré à tout le corps de la thèse et traite du sujet de façon attendue pour cet exercice universitaire.

Chaque chapitre est également agrémenté d'un dessin, un *cartoon*, en lien avec le sujet du chapitre en question. Outre l'aspect décoratif, ce choix est pour moi un autre moyen de m'exercer à communiquer la science, car chacun sait qu'une belle image attire l'œil, et qu'un schéma bien conçu remplace quantité de texte.

Enfin, pour que cette thèse puisse servir à des étudiants ou chercheurs voulant reproduire nos résultats, j'ai tenu à donner non seulement mes paramètres expérimentaux mais aussi expliquer en détail le procédé de traîtement des données. C'est pourquoi les scripts principaux utilisés dans cette étude sont expliqués en détails. Leur compréhension approfondie n'est cependant pas indispensable pour l'analyse des résultats.

La thèse est un exercice de recherche, mais aussi de communication. Ma manière de le traîter n'est peut-être pas conventionnelle, mais c'est la façon la plus pertinente pour moi, pour mes convictions et mon parcours professionnel de mener à bien ce travail. Sur ces mots, je vous souhaite une bonne lecture.

Remerciements

Ce manuscrit marque la fin de cette thèse, mais aussi d'un long parcours personnel et universitaire qui s'est réalisé au mieux grâce à de nombreuses personnes qu'il me tient à cœur de remercier ici.

Tout d'abord je tiens à remercier les relecteurs et membres du jury d'avoir accepté d'évaluer mon travail écrit et/ou oral. Merci à Simona Ispas, Guillaume Morard, Simon Meyer, Muriel Andreani et Bruno Reynard.

Ensuite je remercie mon maître de thèse, Razvan Caracas, sans qui cette thèse n'aurait jamais eu lieu. Merci d'avoir répondu aux innombrables questions que je venais te poser à la fin des cours de physique des minéraux, de m'avoir conseillé l'équipe de Bob Downs en Arizona pour mon premier stage de master et de m'avoir proposé ensuite ce stage et cette thèse. Merci également pour le financement ERC que tu as obtenu, car cela m'a permis de réaliser mon stage et ma thèse dans des conditions idéales, sans le stress des recherches de financements et avec la possibilité de partir pour de nombreuses conférences à l'international. Et merci pour ces trois dernières années, pour les « non-group group meetings » au labo ou ailleurs, pour nos discussions à propos de la thèse qui me remontaient toujours le moral et me boostaient dans mon travail, pour la liberté que tu m'as donnée et m'a permis de faire le point sur mon avenir.

I also want to thank every member of the team, whether you were my colleagues and friends for just several months or almost three years. Thank you very much François, Natalia, Zhi, Renata, Tim and Mandy for all the discussions we had together, for the answers to my questions, for the tea breaks in the office and for the travels abroad. Thank you for every moment we spent together, I was extremely happy to be part of this international team with you. Merci également à Lena, pour ces moments complices depuis le début de la préparation de l'exposition Moon Impact et pour l'aide que tu m'as apportée concernant ma candidature à Genève.

Je souhaite remercier également toute l'équipe du PSMN et du CBP d'avoir réglé tous les petits problèmes que j'ai pu rencontrer avec le PSMN ou le serveur de stockage de données pendant ces dernières années, mais aussi pour leur bonne humeur et la convivialité du M7 1H. Merci en particulier à Loïs et Emmanuel pour votre aide constante, pour les discussions diverses et variées et pour votre implication dans le partage des connaissances à tous niveaux avec notamment la Fête de la Science. J'ai été très heureuse de participer à cette dernière édition à vos côtés.

Je remercie de même mes collègues enseignants et anciens professeurs, Vincent, Renaud, Jean-Philippe, Guillemette et Fred, de m'avoir donné la possibilité d'enseigner aux élèves de L2, L3 et M1 dans des matières qui m'ont intéressée. Merci énormément à Renaud d'avoir accepté de transformer les TP Matlab en TP Python, et à Vincent pour

tous les corrigés des TD de géophysique qui m'ont énormément facilité la vie. Merci à Jean-Alexis d'avoir enseigné la partie « spectroscopies vibrationnelles » du cours de Jean-Philippe l'année où j'étais en L3. Ce cours a sans doute marqué une phase décisive dans mes choix de stages et m'a donné envie de l'enseigner à mon tour. Merci à Nadège pour le travail remarquable que tu as réalisé avec ce cours de statistiques. Je suis très heureuse d'avoir pu faire perdurer ton travail pendant deux années supplémentaires. Par extension, merci à tous les enseignants de license et de master du parcours Terre et Planètes de l'ENS/UCBL de m'avoir fait découvrir de nombreuses facettes de la géologie. Merci à Gérard pour l'incroyable formation du diplôme de gemmologie. Et merci aux anciens doctorants pour les TD et surtout les cours d'informatique, alors inédits à l'époque.

Merci également à Marie-Jeanne et Emmanuelle pour votre rapidité d'action et votre professionalisme pour gérer tout l'administratif des missions et des enseignements. Rien ne serait possible sans vous !

Je souhaite aussi remercier l'école doctorale PHAST de nous accompagner tout au long des années de thèses et des périodes difficiles, mais aussi pour ce partenariat avec OTECI. Merci énormément à toi Polita, pour nos entretiens vidéos réguliers et ton soutien constant pendant cette dernière année.

Grâce à toutes ces personnes, de près ou de loin, mon travail et ma vie professionnelle lors de ces trois dernières années se sont bien déroulés. Mais il ne faut pas oublier non plus le rôle des amis, camarades et proches dans le bien-être mental et l'épanouissement personnel. La longueur des remerciements dédiés à chacun ne témoigne en aucun cas du degré de reconnaissance que j'éprouve à leur égard, mais simplement du fait que je parle peu de ma vie personnelle.

Je remercie donc mes amis et camarades de licence, master et doctorat pour tous les bons moments passés en chair et en os, autour d'un thé ou d'une bière, ou par messages WhatsApp interposés. Ces trois années d'études se sont passées dans la bonne ambiance et l'entraide, merci beaucoup à vous.

Je tiens aussi à remercier tous les membres de l'association DéMesures, avec qui j'ai passé des moments exceptionnels depuis 2017. J'ai tant découvert et tant appris au sein de cette association. Merci en particulier à Audrey, Marie, Marylou et Lucile pour tous les moments éprouvants et forts que nous avons passés ensemble avec par exemple Cosmograff et les escape games.

Merci également à mes collocataires, Eden et Damien, pour cette année et demie de cohabitation, jeux-de-rôles, crises de nerfs et j'en passe ! Ce fut une expérience incroyable qui m'a apporté beaucoup plus que si j'étais restée seule dans mon $20\,\mathrm{m}^2$.

Merci aux membres du Thésarium, Momo, Auguste et Nadège, pour ces quelques

mois passés en votre compagnie quand les anciens furent partis. Ils furent courts mais intenses ! Merci à toi Samuel B. pour ces innombrables discussions et le soutien mutuel que l'on s'est apporté pendant ces dernières années. Ton œil expert m'a été d'un grand secours plus d'une fois ! Merci Laurence pour ces pauses thé quand tu étais de passage à l'ENS, bulles impromptues de détente et d'évasion. Et dans la même lignée, merci à Pauline, Auguste et Delphine, pour toutes ces pauses thé/digestion dans les jardins, moments complices capitaux et qui m'ont manqué depuis mon changement de rythme de vie.

Merci à Débora d'être ma meilleure amie depuis toujours et ce malgré nos caractères explosifs et la distance. Merci à toi Delphine, pour ton soutient, ces discussions en tête-à-tête, ces sorties shopping et ton amitié malgré nos sens de l'organisation diamétralement opposés. Merci énormément à toi Nadège, pour ces soirées Disney, ces dégustations de thé et j'en passe ! Entrer dans ton cercle d'amis fut une des meilleures choses qui me soient arrivées de toute ma vie.

Bien évidemment je remercie aussi mes parents de m'avoir toujours soutenue dans mon parcours scolaire et mes choix de vie. Merci pour tout ce que vous avez fait pour moi, votre confiance en moi, votre présence et votre écoute. Vous m'avez permis d'arriver là où j'en suis maintenant. Merci à toi mon petit frère, d'être là et de partager tes découvertes vidéoludiques avec moi. Et merci à toi, mon Chat, qui m'a trouvée, apprivoisée, rassurée et soutenue dans les moments difficiles de ces six derniers mois. Je n'imagine plus ma vie sans toi. Merci pour tout.

Abstract

The impact of a planet in formation with the proto-Earth, also known as the Giant Impact, is now the main hypothesis for the Moon formation. Nevertheless, there are still discrepancies between the impact simulations and the observations of the current Earth-Moon system. To improve their models, geophysicists need a better understanding of geological materials not only at high pressures and high temperatures, typical of impacts, but also at low pressures and high temperatures, typical of the debris disc that follows the impact. Since this latter region cannot be reached by experiments we use here ab-initio molecular dynamics simulations.

We work on feldspars, with formula $(Ca,K,Na)(Al,Si)_4O_8$, as they represent the major mineral component of the crust of terrestrial bodies. Using the VASP® code for numerical experiments and the home-made UMD package for post-processing, we obtain structural, transport and thermodynamic data on a wide range of temperatures (2000–7000 K) and densities (0.5–6 g cm^{-3}).

The three feldspar end-members display a critical density between 0.4 and 0.9 g cm^{-3} and critical temperatures as follows: $5000\,\mathrm{K} < T_K < 5500\,\mathrm{K}$, $6000\,\mathrm{K} < T_{Na} < 6500\,\mathrm{K}$ and $7000\,\mathrm{K} < T_{Ca} < 7500\,\mathrm{K}$. At low densities and below the critical temperatures, we can identify the start of gas bubble nucleation. The vaporization is incongruent, the gas is mostly made of free Na or K and of SiO, SiO_2 or O_2 molecules. There is an O_2 degassing of the fluids above 4000 K at all densities.

Our study at very high temperatures and pressures tells us that impacts in a cold crust would at most melt the crust, whereas impacts in a hot crust or in a magma ocean would completely bring the crust into supercritical state.

Ma thèse en 1 page

L'hypothèse majeure pour la formation de la Lune est celle d'un Impact Géant entre deux planètes en formation, généralement appelées Théïa et Gaïa. L'agglomération du disque de débris résultant aurait ensuite formé la Lune. Cependant aucune des simulations d'impacts ne permet de reproduire totalement les observations du système Terre-Lune actuel. Une solution à ce problème pourrait être d'améliorer notre compréhension des propriétés des différents minéraux, non seulement à hautes pressions et hautes températures (typiques des impacts), mais aussi à basses pressions et hautes températures (typiques de l'état du disque dans l'espace).

Comme les expériences en laboratoire ne permettent pas d'atteindre ces dernières conditions, nous réalisons ici des expériences numériques. Nous travaillons sur les feldspaths, les minéraux les plus abondants dans les croûtes lunaire et terrestre. Il existe une multitude de compositions différentes de feldspaths, ici nous nous limitons aux trois compositions extrêmes idéales : $NaAlSi_3O_8$, $KAlSi_3O_8$ et $CaAl_2Si_2O_8$. Au moyen d'un ensemble de codes informatiques appelé VASP® nous obtenons de nombreuses données sur les trois feldspaths pour des températures allant d'environ 2000 à 20 000 °C et des masses volumiques entre 0.5 et 6 $g\,cm^{-3}$. Les codes du « package » UMD développés pendant ces trois années au sein de l'équipe permettent l'analyse de ces données.

Ces expériences numériques permettent de construire un diagramme de phases indicatif pour chacun des feldspaths étudiés. Nous avons visuellement identifié les conditions de pressions et températures pour lesquelles le liquide se vaporise (des bulles de gaz apparaissent). Ce gaz semble être constitué majoritairement d'atomes libres Na et K, mais aussi de petites molécules comme SiO, SiO_2 ou O_2. Nous avons également estimé la température critique. En dessous de cette température il est possible de voir un changement de phase liquide-gaz, mais au-dessus nous trouvons un fluide unique appelé fluide supercritique. Cette température est estimée entre 5250 °C et 5750 °C pour $KAlSi_3O_8$, entre 6250 °C et 6750 °C pour $NaAlSi_3O_8$ et entre 7250 °C et 7750 °C pour $CaAl_2Si_2O_8$.

Les propriétés des feldspaths à très hautes pressions (jusqu'à 4 000 000 de fois la pression atmosphérique) et températures (jusqu'à 20 000 °C) nous permettent d'estimer l'état physique qu'une croûte planétaire composée de feldspaths pourrait avoir lors d'impacts météoritiques. Lorsque l'impact se produit sur une croûte froide (entre le zéro absolu et les conditions atmosphériques classiques) il pourrait au maximum faire fondre la croûte. Au contraire, lorsque l'impact a lieu sur une croûte chaude voire fondue (2200 °C et plus) il pourrait transformer toute la croûte en fluide supercritique.

Si c'était bien le cas de l'Impact Géant qui a formé la Lune, alors ce fluide supercritique ainsi créé pourrait permettre de résoudre bien des problèmes de composition chimique que les simulations d'Impact Géant présentent.

Contents

CHAPTER 1

INTRODUCTION

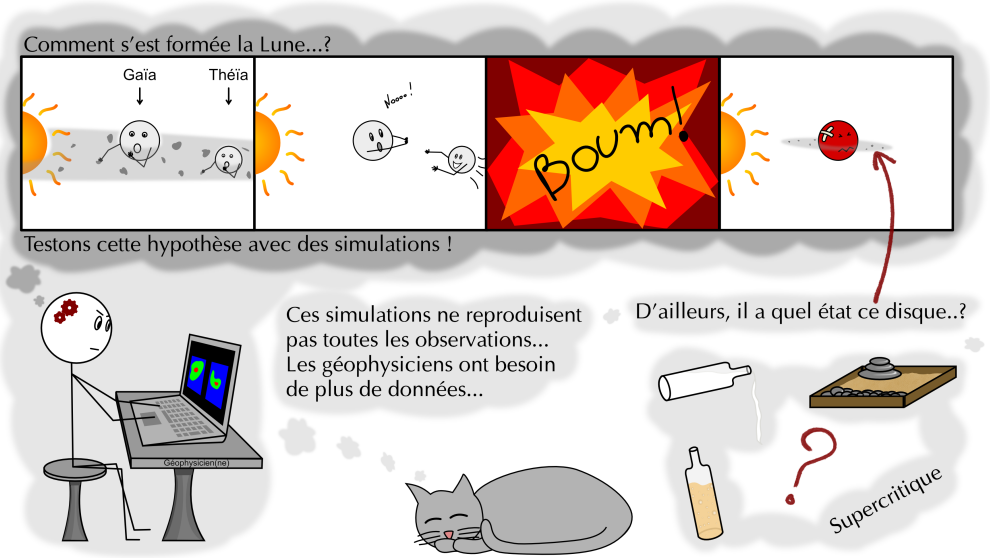

Quel est le but de cette thèse ? Apporter de meilleures données aux géophysiciens qui simulent l'impact géant à l'origine de la Lune et trouver l'état physique du disque de débris ainsi formé (liquide, solide, mélange liquide+gaz, supercritique).

Il faut un début à tout

Depuis 1969 et les premières missions Apollo, les hypothèses et études sur la formation de la Lune se sont multipliées considérablement. Dans les années 70-80 on comptait trois scénarios majeurs pour la formation de la Lune : la fission, l'accrétion binaire et la capture (Wood, 1986). À partir de 1984 c'est l'hypothèse d'un Impact Géant entre deux planètes en formation qui devient le scénario le plus accepté. Selon les modèles d'impacts « canoniques », une planète en formation de la taille de Mars (appelée Théïa) frappe la proto-Terre (appelée Gaïa). Le disque de débris résultant, à partir duquel se forme la Lune, proviendrait en majorité de l'impacteur.

Suite à l'incompatibilité des modèles d'impacts canoniques avec les mesures précises de composition chimique des échantillons lunaires, les modèles d'impacts de haute énergie et/ou haut moment angulaire apparaissent (ex. Canup, 2012; Ćuk and Stewart, 2012; Reufer *et al.*, 2012). Comme ils ne sont toujours pas totalement satisfaisants de nouveaux modèles continuent à être développés (ex. Hosono *et al.*, 2019; Lock *et al.*, 2018).

Nous pensons que la découverte du modèle « parfait » d'Impact Géant passe par une meilleure compréhension des propriétés des minéraux, non seulement à hautes pressions et hautes températurse (typiques des impacts), mais aussi à basses pressions et hautes températures (typiques de l'état du disque dans l'espace). Comme les expériences en laboratoire ne permettent pas d'atteindre ces dernières conditions, nous réalisons ici des expériences numériques. Les deux seules études à basses densités et hautes températures qui ont déjà été réalisées ont étudié des compositions très simples : SiO_2 (Green *et al.*, 2018) et $MgSiO_3$ (Xiao and Stixrude, 2018).

Nous avons donc décidé de travailler sur des minéraux plus complexes : les feldspaths. Ce sont les minéraux les plus abondants dans les croûtes lunaire et terrestre. Il existe une multitude de compositions différentes de feldspaths, ici nous nous limitons aux trois compositions extrêmes idéales : $NaAlSi_3O_8$, $KAlSi_3O_8$ et $CaAl_2Si_2O_8$. Le but de cette thèse est d'améliorer notre compréhension des propriétés diverses des feldspaths, d'étudier la transformation liquide-gaz des différents feldspaths ainsi que l'état physique (solide, liquide, gaz, etc.) dans lequel ils se trouvent lors d'un impact météoritique.

La suite présente donc la méthode employée dans nos expériences numériques au chapitre 2, puis les résultats et implications de nos expériences dans les chapitres 3 à 6. Tout d'abord, il est question de la structure des fluides (chapitre 3), puis de l'évaporation des feldspaths (chapitre 4), suivi de l'étude du déplacement des atomes (chapitre 5) et enfin des propriétés thermodynamiques (comme la pression, la température, etc.) dans le chapitre 6. La conclusion de cette thèse et l'ouverture vers d'autres travaux sont finalement présentées dans le chapitre 7.

Brief outline This chapter presents first a short historic of the Moon formation theories to introduce and justify the work done in this thesis. The goal of this section 1.1 is to give an overview of the Moon formation research. For more information about each theories, pros and cons etc., you can refer to the numerous reviews already written about it (e.g. Barr, 2016; Canup, 2004; Wood, 1986). Section 1.2 presents quickly the pressures and temperatures ranges that can be attained by different experimental techniques, from the in-lab experiments to the numerical experiments. The next part, section 1.3, explains why we choose to work on feldspars. And finally section 1.4 summarizes the goals of this thesis and presents the outline of this manuscript.

1.1 Moon formation

The Moon is Earth's only permanent[1] natural satellite. It has been a source of inspiration and questions for centuries, but it is only in the last one that scientists could really investigate its origin.

1.1.1 The canonical impact and before: brief historical overview

Since 1969 and the first Apollo missions, our understanding of the Moon significantly improved, mostly thanks to the chemical analysis of lunar samples. In the 70'-80's there were essentially three major scenarii for the Moon formation: fission, capture and binary accretion (Wood, 1986). In the fission model, originally suggested by Darwin (1879), a very fast-spinning unstable Earth ejected part of its material into space. The Moon that formed from this material would have the same composition as Earth's mantle. It would be depleted in iron if fission occurred after Earth's core formation. This model was extensively tested and improved (e.g. Binder, 1974; O'Keefe and Sullivan, 1978) but was finally abandoned because of many composition and dynamical problems (Taylor, 1982). The capture model (e.g. Singer, 1972), in which a Moon formed somewhere else in the Solar System and was captured by Earth's attraction field, is quickly dismissed by geochemical analysis of lunar rocks (Taylor, 1982). The binary model suggests that the Moon formed at the same time as Earth from materials which were captured into geocentric orbit (e.g. Ruskol, 1960). But this scenario cannot explain neither the angular momentum of the current Earth-Moon system, nor the density difference between the two bodies (Taylor, 1987).

The Giant Impact theory, in which a roughly Mars-sized object impacted the forming Earth, was first proposed by two independent groups: Hartmann and Davis (1975) and Cameron and Ward (1976). Mainly ignored by the scientific community, the Giant

[1] At the moment I am writing these lines, the asteroid 2020 CD3 is leaving Earth's orbit. It is the second known asteroid, after 2006 RH120, to be temporarily captured by Earth's attraction.

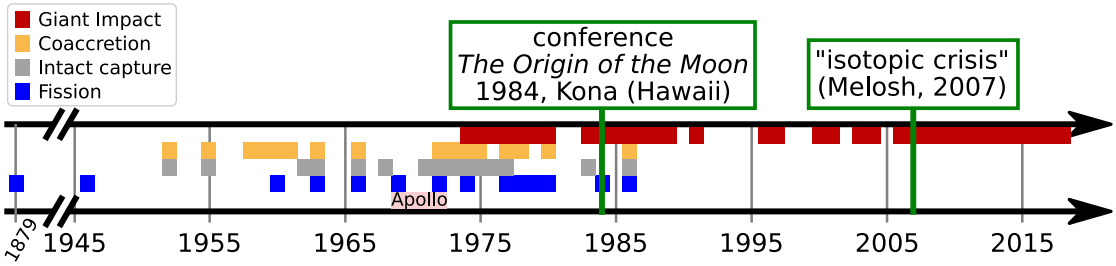

Figure 1.1 – Timeline of the main Moon formation scenarii. Colored squares indicate years for which one or more article is published about the corresponding scenario. The 1984 conference about Moon formation marks the end of studies about fission, capture and coaccretion scenarii. After the "isotopic crisis", highlighted by Melosh (2007), mostly high-energy/high-angular momentum Giant Impact are studied.

Impact theory had to wait until the 1984 conference about the Moon formation in Kona, Hawaii, to become the main theory (Canup, 2004; Stevenson, 1987). This is best seen on the timeline figure 1.1. With the development of supercomputers, the following decades see a great advance on Giant Impact simulations. For example, it was demonstrated that "large impacts are common in late-stage terrestrial accretion", "a single impact is consistent with the Earth-Moon system", and that "impact-generated material accretes into a single moon" (Canup, 2004). At this moment, the successful standard Giant Impact simulations, also called the canonical impact, involve an impactor velocity approximately equal to Earth's escape velocity, a total mass M_T (target + impactor) between 0.97 and 1.02 Earth masses, moderate impact angles and an impactor-to-total mass ratio $\gamma = \frac{M_i}{M_T}$ between 0.1 and 0.11 (Barr, 2016).

1.1.2 The isotopic crisis and after

While the canonical impact seemed to become the most widely accepted theory for the Moon formation, isotopic measurements precision increased and finally led to the conclusion that Earth and Moon are isotopically identical relative to several elements, for example oxygen (Pahlevan and Stevenson, 2007), titanium (Zhang *et al.*, 2012) or silicon (Armytage *et al.*, 2012). In canonical impacts, about 70 % of the Moon's mass is derived from the impactor, then to explain the identical isotopic measurements Pahlevan and Stevenson (2007) considered the hypothesis of a turbulent mixing between the protolunar disk and the terrestrial magma ocean. But then appear the so-called "isotopic crisis" from Melosh (2007): "Without a plausible mechanism to strongly separate angular momentum transport from mass exchange, the Pahlevan and Stevenson (2007) mechanism cannot explain the equilibration of isotopes between the Earth and Moon.". Likewise, another mixing mechanism investigated by Pahlevan *et al.* (2011) can explain the isotopic equilibration of some refractory elements but is thought to generate a silicon isotopic difference (Halliday, 2012). Then, how to reconcile the Giant Impact scenario

Table 1.1 – Approximate comparison of the two main Giant Impact models. ✓ means the constraint is verified by the model, X means the constraint is usually not verified by the model and ∼ indicates the constraint is not entirely verified or requires additional models to be validated.

	Canonical Impact	High E/AM Impact
1. Current Earth and Moon masses (M_E,M_M)	✓	✓
2. Current Earth-Moon angular momentum (L_{EM})	✓	∼
3. Iron depleted Moon ($w_M^{Fe} \simeq 8\,wt\,\%$)	✓	✓
4. Moon (crust) chemistry (volatile depletion...)	X	∼
5. Initial Lunar Magma Ocean (LMO ∼ 200–300 km thick)	✓	✓
6. Physical plausibility	✓	∼

with isotopic measurements? Several alternative models of the Giant Impact then appeared. For example we can cite the impact on fast spinning Earth model proposed by Ćuk and Stewart (2012), the "half-Earth" impacts investigated by Canup (2012), the very energetic hit-and-run models (Reufer *et al.*, 2012), the creation of a planetary structure called synestia in the context of high-energy, high-angular momentum giant impacts (Lock *et al.*, 2018) or more recently an impact on a proto-Earth covered by a magma ocean (Hosono *et al.*, 2019).

1.1.3 Comparison of scenarii

To be valid, a scenario of the Moon formation has to verify five major observations: Earth and Moon current masses, the system's angular momentum, an iron depleted Moon (about 8 wt % of iron), the Moon chemistry and a lunar magma ocean initially 200–300 km thick (Barr, 2016). Wood (1986) examined the fission, capture, coaccretion and Giant Impact scenarii with the knowledge they had at that time and graded the different scenarii (see table 3 in part 4 of the review by Wood (1986)). Later, other reviews exposed the pros and cons of the two main Giant Impact models. I summarized them in table 1.1. The canonical impact usually fails to reproduce the Moon chemistry, while the other constraints are verified. On the contrary, the high-energy, high angular momentum scenarii (e.g. Canup, 2012; Ćuk and Stewart, 2012; Reufer *et al.*, 2012) seem to verify both chemical and physical properties, even though they contain an excess of angular momentum that needs to be removed from the system afterward. However they usually correspond to a very narrow range of impact parameters, which makes them less probable to happen than scenarii with less constraints on the impact parameters.

The recent apparition of new scenarii (Hosono *et al.*, 2019; Lock *et al.*, 2018) shows that the Moon formation is still an on-going research area and new hypotheses are considered to allow more flexibility in the choice of impact parameters.

1.1.4 What can we do now?

Aside from developing new hypotheses, how the existing giant impacts scenarii can be improved to, maybe, match all the criteria?

One solution is improving our knowledge and understanding of material behavior. The giant impacts simulations usually model the mantle and the core using particles of dunite (or forsterite) and iron respectively, whose thermodynamic behavior is ruled by the widely used equations of states: Tillotson (Tillotson, 1962), ANEOS (Thompson and Lauson, 1972) or M-ANEOS (Melosh, 2007). These equations not only lack data at very low pressures, they also model a simple gas instead of a real gas (ANEOS and M-ANEOS model respectively mono and di-atomic gas). It is then of primary importance to improve these equations of states by obtaining more data on many different mineral compositions, from high temperatures and pressures to high temperatures and low pressures.

Another solution is allowing chemical equilibration in the protolunar disk, as suggested initially by Pahlevan and Stevenson (2007). This idea was investigated by several studies for Moon formation times ranging from several years to 10^3–10^5 years (e.g. Charnoz and Michaut, 2015; Ward, 2012). Reviews about the Moon formation tend to show that long term equilibration in the disk between liquid and gas phases may not be the solution, or at least needs further work on the physical mechanisms responsible for mixing (Asphaug, 2014; Barr, 2016). On the contrary, chemical mixing on a much shorter timescale, on the order of days, may be a solution to explain the Moon's chemistry. This idea was already developed by Lock *et al.* (2018) using the synestia concept but maybe it can also work in the case of a protolunar disk with part of its material in the supercritical state, instead of the traditional liquid and gas phases. One of the particularities of the supercritical state is that there is no discontinuities in the material properties between this state and the liquid or gas states. Under these circumstances, chemical and isotopic mixing can occur more rapidly with a supercritical phase than only between liquid and gas phases. To investigate this hypothesis it is mandatory to obtain for many different mineral compositions the thermodynamic conditions of the supercritical state, defined by the critical temperature as indicated in figure 1.2 (see section 6.1.3 for more explanations).

1.2 One step toward the answer: experiments

1.2.1 In-lab experiments

High-pressure experiments were first conducted using a multi-anvil apparatus and then, since the late 1950s, using diamond anvil cell (DAC) devices. These static techniques are still used today for the several advantages they offer. For example, they can be easily

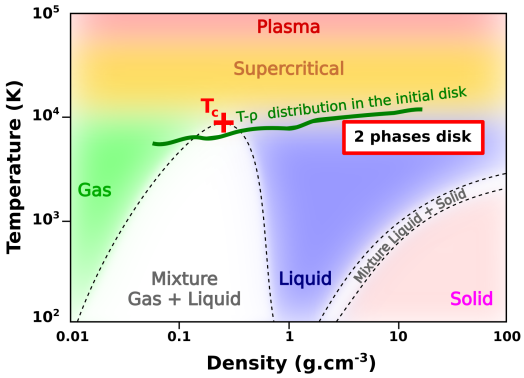

(a) In case of a high critical temperature we have a two-phases disk.

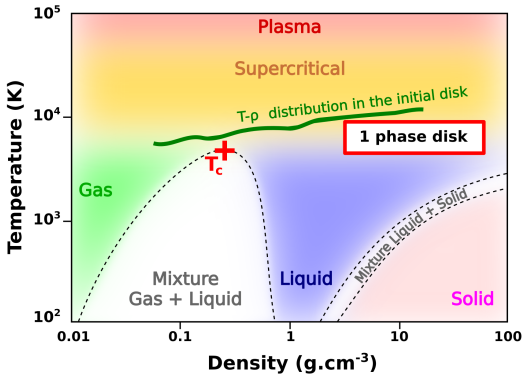

(b) In case of a low critical temperature we have a one-phase disk (gas and supercritical).

Figure 1.2 – Schematic phase diagram showing the physical state of a schematic temperature-density distribution in a protolunar disk depending on the position of the critical point.

coupled with electrical or laser heating and they allow thermodynamic equilibrium. For these reasons many phase diagrams were experimentally found using coupled high-temperature high-pressure static experiments (Saxena and Wang, 2007). Nevertheless they are usually limited to temperatures of some thousands kelvins and pressures of terapascals at room-temperature (Saxena and Wang, 2007; Yagi *et al.*, 2020).

In order to reach higher pressures and temperatures, shock compression experiments were developed. The goal of these experiments is to create a shock wave that propagates through the sample and changes its pressure, temperature, density and energy according to a shock equation of state called Hugoniot (see section 6.1.4 for more information). The shock wave can be created by several techniques: from the in-contact explosive system to flyer-plate device (with for example the widely used gas-gun systems) or more recently using a high energy laser. In each case the sample is never in direct contact with the explosive, laser or flyer-plate. It is in contact with another material that protects it and in which the shock wave appears from the explosive, laser or flyer-plate impact (Forbes, 2012). With these techniques, in particular the laser-driven shock experiments, it is then possible to achieve extreme pressures up to several terapascals and temperatures up to 20 000 K or more (Duffy and Smith, 2019). However the temperature measurements during shock experiments are not entirely reliable and still require improvements.

To date, these experiments improved equations of states of a variety of major geological materials, like $MgSiO_3$ glass, enstatite or olivine (Luo *et al.*, 2004), silica (Kraus *et al.*, 2012), or MgO (Root *et al.*, 2015). Nevertheless, while these techniques are appropriate to sample extreme high pressure, high temperature conditions, they can hardly reach the low pressures and high temperatures typical of the protolunar disk. For this case it is mandatory to use numerical experiments.

1.2.2 Numerical experiments

When an experiment cannot be performed in laboratory, due to problems like mechanical, financial etc., simulations are used instead to get the properties we are looking for. The first step is to model the material investigated, for example, to create an atomic description of a real liquid. Then we carry out computer simulations from this model and compare the results obtained with experimental results on the one hand and theoretical predictions on the other hand. The simulations we talk about here are often called "numerical (or computer) experiments" for two reasons. First, they play the role of a bridge between the in-lab experiments, models and theoretical predictions. And second, they are very similar to in-lab experiments in the way they are conducted and analyzed (Allen and Tildesley, 1989).

From an atomic description of a liquid we can obtain its thermodynamic properties thanks to statistical mechanics: it links the thermodynamic properties of the matter to its microscopic behavior, as the velocities, positions or momenta of atoms (Frenkel and Smit, 2002a). Only very few systems can be solved analytically, like the two-dimensional Ising model. For more complicated systems we need the help of computers to obtain data that can be compared to experimental results.

The first work on computer experiments, in 1953, was the basis of the modern "Monte Carlo" simulations (Allen and Tildesley, 1989). In order to also obtain the dynamic properties of the material, like the transport properties, the molecular dynamics (MD) simulations were developed a few years later, in 1957. In short, the MD solves Newton's equations of motion for a system of interacting atoms or molecules. Since we are interested in both thermodynamic and dynamic properties of minerals, we want to use MD simulations. For more information about MD and the similarities with in-lab experiments regarding the process, see sections 2.1.1 and 2.2.1 respectively.

Today we can distinguish between two main categories of MD simulations: classical molecular dynamics and first principles molecular dynamics (FPMD), also called Ab-Initio Molecular Dynamics. In classical MD, interactions between the different atoms or molecules are represented by interatomic potentials, as the Lennard Jones potential. These potentials are usually fit to a set of experimental data, which means they cannot be used for other systems nor very different thermodynamic conditions (Adjaoud *et al.*, 2008). It also means they may not be accurate for simulations outside the pressure and temperature range already investigated by experiments. Nevertheless, they have the big advantage of being extremely fast. Classical MD simulations can usually model several thousands of atoms for hundreds of picoseconds or even several nanoseconds. On the contrary, FPMD simulations can model no more than about 200 atoms for only tens of picoseconds. Their main advantage is they do not require experimental data. The

density functional theory (DFT) is used to accurately describe the electronic structure and then provide the interatomic forces (see section 2.1.2 for more information). This method is not only easily transferable, but also accurate to predict material behavior for thermodynamic conditions that have not been investigated experimentally before. As previously mentioned, we want to investigate the properties of minerals outside the range of experiments. This is why we decide to use FPMD simulations.

Many simulations on liquid minerals were already carried out using FPMD. We can cite for example the numerous studies on liquid $MgSiO_3$ (e.g. Stixrude and Karki, 2005; Wan *et al.*, 2007), Mg_2SiO_4 (e.g. de Koker *et al.*, 2008; Hernández *et al.*, 2015) and silica (e.g. Karki *et al.*, 2007). Studies on more complicated melts are rarer. We have for example the first fully ab-initio study on calcium aluminosilicate melt (Benoit *et al.*, 2001) or some studies about liquid anorthite (de Koker, 2010; Karki *et al.*, 2011), diopside (Sun *et al.*, 2011) and pyrolite (Caracas *et al.*, 2019; Solomatova and Caracas, 2019). In each of these studies, the thermodynamic range investigated is the high-pressure, high-temperature range, typical of planet interiors and magma oceans. To date there are only two studies in the low-pressure, high-temperature range, and both investigate simple systems: silica (Green *et al.*, 2018) and $MgSiO_3$ (Xiao and Stixrude, 2018). Then there is a real need of computational experiments on a more complex mineral in this thermodynamic region.

1.3 Working material

1.3.1 Earth and Moon

Earth and Moon have complex structure and composition, but both can be approximated as follow: a metallic core, a mantle and a crust. It is thought that Earth's core has 85 wt % of Fe, 5 wt % of Ni and 10 wt % of light elements (McDonough, 2018). The crust is separated into two parts: the thin oceanic crust (between ∼3 and 10 km thick) with an approximate basaltic composition, and the thick continental crust (in average ∼35–40 km thick) with roughly andesitic composition (Perfit, 2018). The mantle extends from the core-mantle boundary, at 2900 km depth, to the base of the crust. Its composition is mostly peridotitic (Stracke, 2018).

Compared to Earth's iron core, the Moon's core is tiny: 350 km radius at best for a mean lunar radius of 1737.1 km. The successful Giant Impact models show that the majority of iron from the impactor, denser than the silicates, is located within the Earth's Roche limit, the distance below which a celestial body would be torn apart due to the competition between its gravitational self-attraction and Earth's tidal forces (Canup and Asphaug, 2001). Then, most of the impactor iron sank into the early Earth.

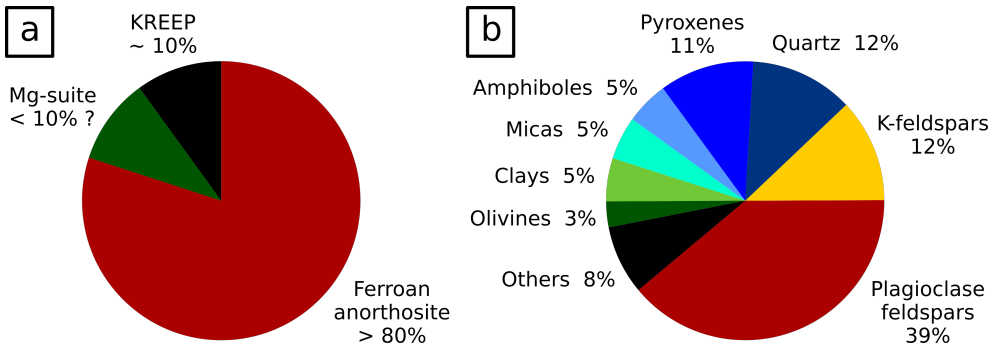

Figure 1.3 – Pie charts of the Earth and Moon crusts compositions. (a) Composition of the Moon highland crust from Taylor and McLennan (2008). (b) Modal composition of the Earth bulk crust from Ronov and Yaroshevsky (1969).

The crust is visually made of two parts: the mare basalts and the highland crust. The highland crust is about 50 km thick and is mostly made of ferroan anorthosites (at least 80 %), followed by the Mg-suite (about 10 %) and in minor proportion other components like KREEP (Taylor and McLennan, 2008). Its formation is explained by the cristallization and flotation of plagioclases (the major components of anorthosites), in the lunar magma ocean (e.g. Smith *et al.*, 1970; Warren, 1985). The mare basalts cover 17 % of the lunar surface but represent in volume less than 1 % of the crust (Anderson, 1989; Taylor and McLennan, 2008). They are ferroan lava flows that are concentrated within great impact basins (Warren, 1985). The bulk Moon shows an enrichment in refractory elements and a depletion in volatile elements compared to Earth.

During meteoritic impacts, the part of the planet that is mostly affected is the crust. The anorthosite Moon crust averages more than 95 % of plagioclase feldspars $(Ca,Na)(Al,Si)_4O_8$, which contain 95–97 % anorthite ($CaAl_2Si_2O_8$) and 3–5 % albite ($NaAlSi_3O_8$) (Taylor and McLennan, 2008). Regarding the total bulk upper lunar crust, it averages about 75 % plagioclase (Warren, 1985). For Earth, the normative mineralogy of the current bulk continental crust shows about 58.9 % of feldspars, with 6.5 % of orthoclase ($KAlSi_3O_8$) and 52.4 % of plagioclase feldspars which are evenly distributed between albite and anorthite (Taylor and McLennan, 1995). As the major mineral of Earth and Moon crusts (see figure 1.3), feldspars are of great interest to study.

1.3.2 Feldspars

Feldspars are aluminosilicates with general formula $(Ca,Na,K)(Al,Si)_4O_8$. They are classified into two principal series of solid solutions: the alkali feldspars (Na-K) and the plagioclase feldspars (Na-Ca). Feldspars have been widely studied for more than a century. The first melting experiments were done in the beginning of the last century on plagioclase feldspars (Bowen, 1913), in which Ca- and Na- end-members melted at about 1823 and 1373 K respectively. Structure, composition, thermodynamic parameters, etc.,

the amount of data about feldspars is substantial in the solid region and close to the melting curve (e.g. Angel, 1994; Nekvasil, 1994; Smith and Brown, 1988). The Hugoniot lines for the three end members and several intermediate compositions were investigated through shock experiments (e.g. Ahrens *et al.*, 1969; Asimow and Ahrens, 2010; McQueen *et al.*, 1967). More recently, MD simulations gave access to a lot of additional information (e.g. thermodynamic properties, structure and dynamics of the melts) over a large range of temperatures (2500–6100 K) and pressures (0–160 GPa), using either classical MD (e.g. Neilson *et al.*, 2016; Spera *et al.*, 2009) or FPMD (e.g. Karki *et al.*, 2011). Some of the results obtained in these studies will be presented and compared to our own results in the analysis chapter of this thesis.

1.4 Goals and outline

In this thesis we want to obtain an indicative phase diagram of the liquid-gas regions of feldspars, with the position of the critical point. Combined with a shock state analysis applied to high velocity impacts, this phase diagram may allow us to infer the physical state of Earth and Moon crusts (or at least their feldspathic part) during meteoritic impacts. With the assumption of similar compositions for the early crusts, we may also infer the physical state of the crusts during the Giant Impact. To help geophysicists improve their impact simulations we also want to make available various data about the structure of the fluids, transport and thermodynamics properties of feldspars over a wide range of densities and temperatures, spanning the liquid and liquid-gas regions.

Chapter 2 presents the methodology used in this work. We give key points about the theory of MD simulations and DFT, along with the several parameters and processes used in the numerical experiments. It also presents the post-processing package (UMD) our group developed during these years and the figure 2.7 that concludes this chapter gives the working axis of this thesis, each one of them defining a separate chapter.

In the first analysis part (chapter 3) we talk about the structure of the fluid. In other words, we look at the organization in space of all the atoms using two tools: the bond distance and the coordination number. We also study more finely this latter property by computing the coordination polyhedra proportions.

The chapter 4 is about the vaporization of the fluid. Unlike the previous chapter, in which we were interested in the short-range structure of the fluids, here we want to look for the chemical species, defined as the largest chains of connected atoms. We expect the liquid to be made of one infinite 3D species (all atoms linked together), while if gas appears it will be made of small finite species not linked to the main species.

The next chapter (n°5) presents the transport properties of the fluids, in other words the translation motion of atoms inside the fluids. This is done through two main tools:

the mean square displacement (MSD) and the self-diffusion coefficient.

In the last analysis part (chapter 6), we investigate the thermodynamic properties of the fluids. We present first some results about equations of states and then the spinodal analysis used to estimate the position of the critical point. This leads to an attempt of phase diagrams which are used to infer on the physical state of feldspars during meteoritic impacts.

Finally this thesis ends with a conclusion chapter (n°7) to summarize the main results and discussions presented here, and talk about future work and applications in this field.

☾

CHAPTER 2

METHODOLOGY

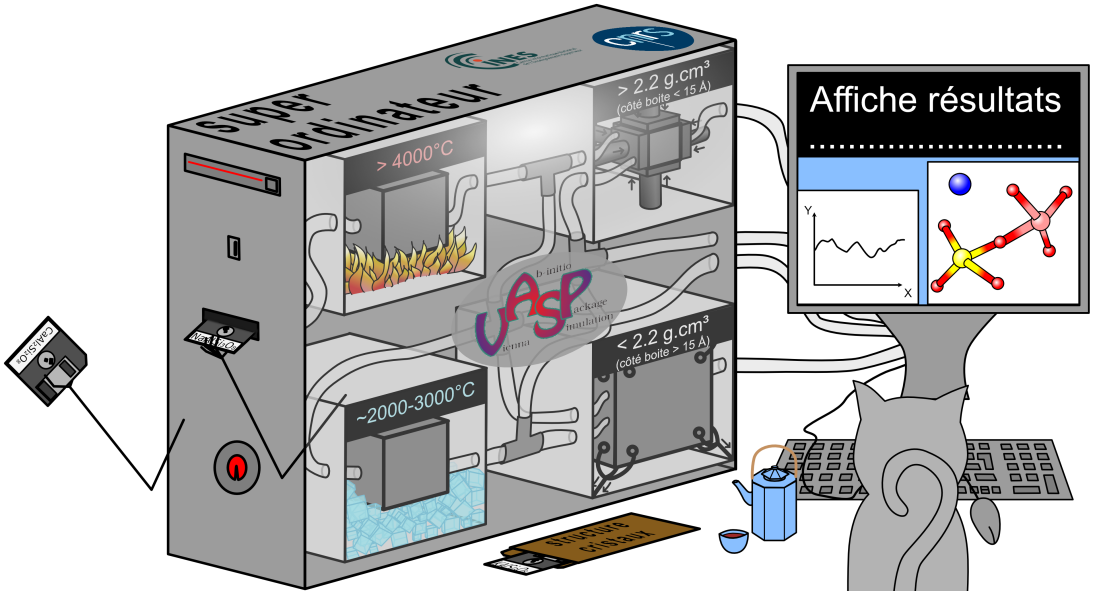

Je réalise ici des expériences numériques : le logiciel VASP® joue à la fois le rôle de four, presse, système de refroidissement ou d'extension et de machine d'analyse. Il mesure et enregistre l'état des feldspaths (position des atomes, pression...) pour toutes les densités et températures voulues.

Méthodologie en bref

Le travail réalisé ici peut être rangé dans la catégorie des expériences numériques, car il suit le même schéma que celui des expériences en laboratoire. Tout d'abord, il faut un échantillon sur lequel travailler. Pour les expériences en laboratoire c'est par exemple un morceau de roche ou de minéral. Ici, nous travaillons à partir de la structure atomique des feldspaths, c'est-à-dire des positions dans l'espace des différents atomes constituant le cristal. Ensuite il nous faut des outils de travail, presque l'équivalent du four qui va chauffer nos échantillons et des machines qui vont analyser la position des atomes, la composition, la température etc. Nous utilisons un ensemble de codes informatique appelé VASP® pour Vienna Ab-initio Simulation Package. Ce groupe de codes simule le mouvement des atomes dans notre cristal en fonction des conditions (pression, température, etc.) imposées à l'échantillon. C'est le mouvement résultant des atomes qui change les propriétés du matériau, par exemple l'état physique (solide, liquide, gazeux, etc.). En voici le principe général.

Chaque atome a une position et une vitesse qui lui sont propres et exerce sur ses voisins une force qui peut être attractive ou répulsive, appelée force électrostatique. En utilisant une théorie fondée sur la mécanique quantique, appelée la théorie de la fonctionnelle densité (DFT), le code va estimer pour chaque atome la force résultante, qui nous donne ensuite l'accélération grâce à la seconde loi de Newton. La sélection d'un pas de temps dt, généralement de l'ordre de $1\,\mathrm{fs} = 10^{-15}\,\mathrm{s}$, nous permet d'obtenir la nouvelle vitesse de chaque atome (au temps $t + dt$), ainsi que sa nouvelle position.

Ceci clôt un cycle de dynamique moléculaire (MD). C'est en répétant des milliers de fois ce cycle, en utilisant à chaque fois les nouvelles positions et vitesses des particules, que l'on reproduit les déplacements naturels des atomes dans la matière. Mais avant de faire les expériences et d'acquérir des données, il faut un protocole. Il consiste ici à chauffer progressivement notre système, c'est-à-dire à accélérer artificiellement les atomes, pour atteindre les différentes températures que l'on souhaite étudier et à augmenter ou diminuer la taille de notre cellule de simulation pour changer la masse volumique, balayant ainsi une large portion du diagramme de phases que l'on souhaite construire.

Enfin, il est nécessaire d'exploiter les données acquises en réalisant des schémas, des tableaux de données, des statistiques etc. À cause du nombre phénoménal de données recueillies il est impossible d'utiliser un logiciel comme Excel®. Il est dans ce cas nécessaire d'écrire ses propres codes d'analyse et de visualisation à l'aide d'un langage informatique adapté. Ici nous avons choisi Python®, un langage très simple, efficace et avec une grande diversité de fonctions adaptées au traitement de données texte, pour nous créer un ensemble de codes de traîtement de données constituant le « package » UMD.

Brief outline As mentioned before, we use here *ab-initio* molecular dynamics simulations to perform our study of the three feldspar end-members. This chapter presents you first a short explanation of the molecular dynamics (MD) process and the concept of density functional theory (DFT) in section 2.1. Then the parameters and initial structure used for the calculation on the three feldspar end-members are presented in section 2.2. Finally the section 2.3 clarifies which energy is used in the following and presents the post-processing package (UMD) our group developed during these years. The figure 2.7 that concludes this chapter gives the working axis of this thesis, each one of them defining a separate chapter.

2.1 The theory

2.1.1 Molecular Dynamics

Atoms are always in motion[1], which is a combination of translations, rotations and vibrations. MD simulations reproduce these movements over a short period of time, from several picoseconds to nanoseconds by following the process summarized on figure 2.1. First, from the atomic positions we compute the forces acting on each atom. This part is done either using interatomic potential (in classical MD), or using DFT (in FPMD, see next section for more information). Then, using Newton's 2nd law of motion and the Verlet algorithm, we obtain the atomic velocities and positions at one timestep dt later[2]. From this point a new MD loop starts until the required number of loops is achieved. At each timestep, all the results needed are written in the output file, including the velocities and positions, so that new MD loop can be started at any timestep.

Each snapshot of the MD simulation is characterized by its configuration, in other words the position and momentum of every particle in the system. In statistical physics, a snapshot is called a microstate of the system. The collection of microstates is called a statistical ensemble. The nature of the constraints imposed on the system defines the type of statistical ensemble. For example, a system with a fixed number of particles N (no creation of loss), a fixed volume V and a constant energy E, is called a microcanonical NVE ensemble. When we force the average temperature T to be constant, we define the canonical NVT ensemble. Likewise if we also force the average pressure to be constant we define the isothermal-isobaric NPT ensemble. There are other statistical ensembles we will not mention here.

Here, in order to obtain pressure-density isotherms for the spinodal analysis pre-

[1] even at 0 K there is a random motion coming from the zero-point energy

[2] This step requires the atomic velocities of the current time t. Since we do not have them for the first loop, the MD code we use (VASP®) automatically choose them at random according to a Maxwell-Boltzmann at the desired temperature.

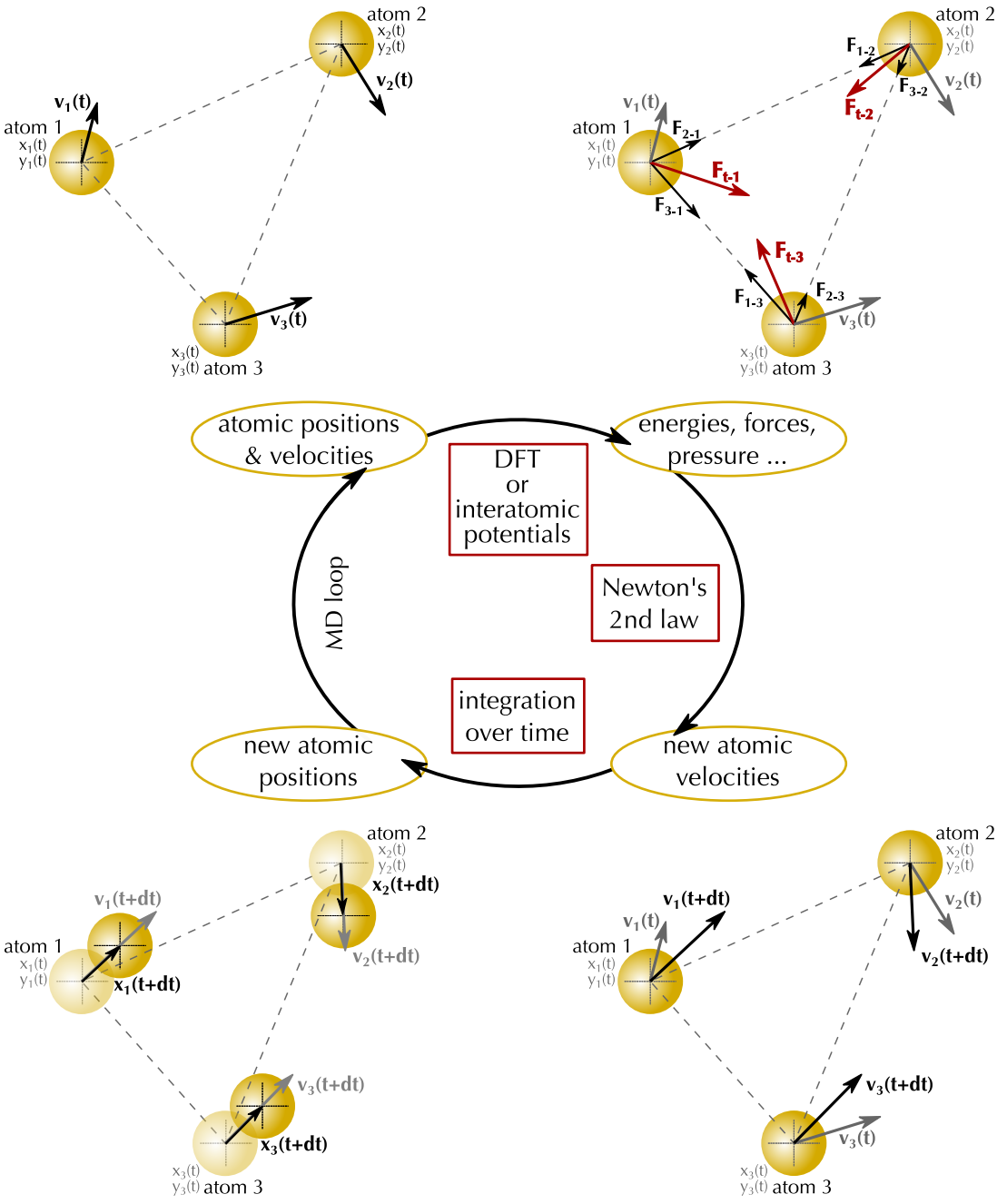

Figure 2.1 – Simplified schematics of the MD process. Starting from the atomic positions and velocities, we compute each inter-atomic forces using interatomic potential or directly the total force on each atom using the DFT. The total forces are used in the integration of Newton's 2nd law of motion to find the new velocities and atomic positions (at one timestep dt later), from which a new MD loop can start.

sented in section 6.1.3, we choose to use the canonical ensemble. N and V are microscopic parameters, then their constant value is directly defined in the input file. To reproduce the behavior of real thermostats we allow the temperature to fluctuate around a fixed average value. The temperature being a macroscopic concept, the kinetic theory is used to have a microscopic and instantaneous description of this value using the following equation:

$$\frac{1}{2}\sum_{i=1}^{N} m_i|\overrightarrow{v_i}|^2 \quad = \quad \frac{3}{2}k_B N_{df} T(t) \tag{2.1}$$

with the number of degrees of freedom $N_{df} = 3N - 3$ (fixed center of mass), m_i and $\overrightarrow{v_i}$ the masses and velocities of individual atoms i and k_B the Boltzmann constant (Frenkel and Smit, 2002b). We usually use the Nosé-Hoover thermostat (Hoover, 1985; Nosé, 1984) to make the temperature fluctuate around the desired average. This is done by adding a force inside the equation of motion in order to adjust the atomic velocities at each MD loop to obtain the desired temperature fluctuations.

In MD simulation, the macroscopic values are obtained with a time average over all the snapshots of the simulation (see section 6.1 for computational details). In statistical physics, the value of a macroscopic property A is obtained by averaging the value A_l over all the microstates l weighted by their probability. In the ergodic hypothesis, performing a time-average of the value $A(t)$ is the same as an ensemble average. In practice no system is fully ergodic, that is why we need a long enough MD simulation in order to visit most of the different type of microstates. Hence, in the following we use the ergodic hypothesis and the thermodynamic parameters are computed using time average over the entire simulations.

2.1.2 Density Functional Theory

This section will not explain the whole theory around DFT, but only gives key points to understand the process for computing the energy of a molecular system since many books already explain it much better (e.g. Fiolhais *et al.*, 2003; Martin, 2004).

The energy of an atomic system is exactly defined by the well-known Schrödinger equation. The time-independent form is

$$\mathcal{H}\psi(\overrightarrow{R}) = E\psi(\overrightarrow{R}) \tag{2.2}$$

with $\mathcal{H}$ the Hamiltonian operator, $\overrightarrow{R}$ the position of all the particles in the system (nuclei + electrons) and ψ the wavefunctions (nuclei + electrons). Unfortunately, it is not possible to analytically solve this equation for molecular systems. The Born-Oppenheimer approximation (Born and Oppenheimer, 1927) simplifies this equation

by decoupling the dynamic of the electrons and the nuclei[3]. Then the total energy of the system is found in two separate steps: considering the nuclei on one side and the electrons on the other side. However, the second part (i.e. the purely electronic Schrödinger equation), still cannot be easily solved. The solution is found using the DFT, thanks to the work of Hohenberg and Kohn (1964), who replaced the electronic wavefunctions by an electronic density. Shortly after, Kohn and Sham (1965) found a practical application of this theory using a functional[4] formulation of the electronic free energy F for a fixed nuclei configuration:

$$F[n(r)] = \begin{array}{l} \overbrace{\phantom{E_{kin\ e-}[n(r)]}}^{\text{homogeneous e- gas}} \\ \left.\begin{array}{l} E_{kin\ e-}[n(r)] \\ + \ e- \bigcap_{e-}[n(r)] \\ + \ ion \bigcap_{e-}[n(r)] \\ - \ TS_{e-}[n(r)] \end{array}\right. \end{array} \begin{array}{l} \overbrace{\phantom{+ E_{kin\ e-\ unknown}}}^{\text{exchange correlation}} \\ \left.\begin{array}{l} + \ E_{kin\ e-\ unknown} \\ + \ e- \bigcap_{e-\ unknown} \\ - \ TS_{unknown} \end{array}\right. \end{array} \tag{2.3}$$

with $n(r)$ being the electronic density in a point r of space. The four energies on the left side are the kinetic energy of non interacting electrons, the interaction energies between point charge particles and the electronic entropy of the homogeneous electron gas. They are all exactly known as a function of the electronic density. But to describe real systems there are remaining unknowns terms, which take into account electron correlation (screening), and are grouped under the term "exchange-correlation free energy". This term is solved numerically using an approximation function. The most common approximations are the Local Density Approximation (LDA) and the Generalized Gradient Approximation (GGA). The LDA considers the exchange-correlation function varies only with the electronic density, which is locally uniform, whereas the GGA also considers the gradient of the electronic density in the exchange-correlation function. For this reason it is thought to be more precise for systems with non-locally uniform electronic density. Now the equation 2.3 gives us a value for the system free energy as a function of the electronic density. As stated by the principle of minimum energy, the system is at the equilibrium when its energy reached a minimum. By changing sequentially the electronic density and computing the related energy, we are able to find the best electronic configuration when the energy is minimized. The electronic density is represented here by a sum of periodic planewaves. Its shape is controlled by the amplitude and wavevector of all the different planewaves, in other words their coefficients. In order to accelerate the calculation, the core electrons are presumed to not participate to the chemical bonds, and then are not represented by planewaves. They are instead approximated by pseudopotentials, which pseudowavefunctions are simpler than the ac-

[3] the electrons instantaneously respond to the dynamic of nuclei
[4] in other words a "function of functions"

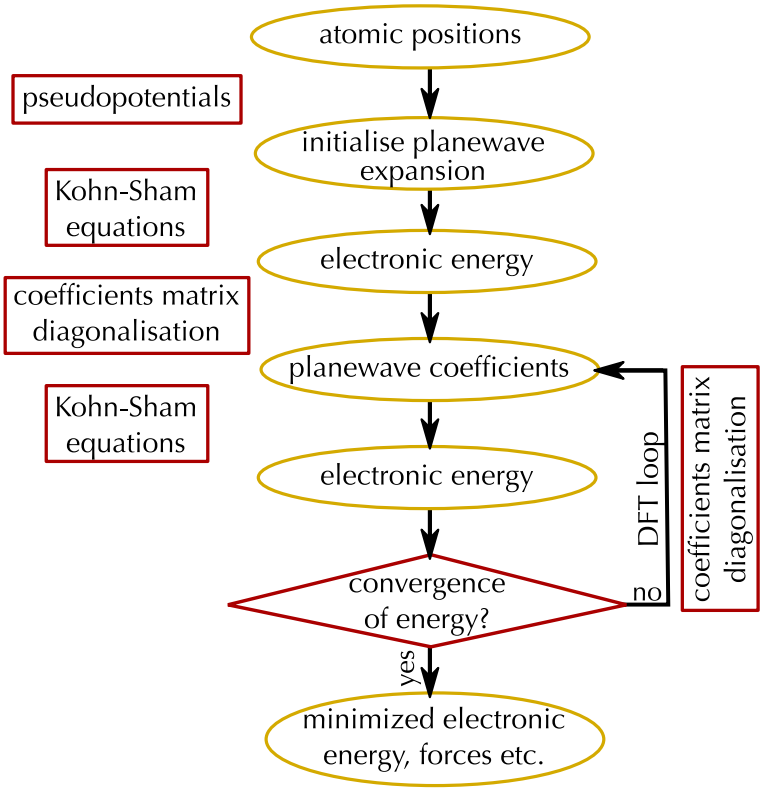

Figure 2.2 – Simplified DFT flowchart. The coefficients mentioned in the coefficient matrix diagonalisation steps are the amplitude and wavevectors of all the planewaves.

tual wavefunctions that would have been used otherwise. Finally, the DFT process can be summarized by the flowchart in figure 2.2.

2.2 The process and parameters

2.2.1 Main study

Parameters

We perform first-principle molecular dynamics simulations as implemented in the Vienna Ab-initio Simulation Package (VASP®) (Kresse and Furthmüller, 1996a,b; Kresse and Hafner, 1993; Kresse and Joubert, 1999). We use the projector augmented-wave (PAW) formulation (Blöchl, 1994) of the density functional theory (DFT) (Hohenberg and Kohn, 1964; Kohn and Sham, 1965; Mermin, 1965) to compute energies and forces, with the Perdew-Burke-Ernzerhof (PBE) parametrization of the generalized gradient approximation (Perdew *et al.*, 1996) for the exchange correlation functional. We employ an energy cutoff of 550 eV for the plane waves and we sample the reciprocal space in the Gamma point. Simulations are performed in the canonical NVT ensemble where the temperature is controlled by the Nosé-Hoover thermostat (Hoover, 1985; Nosé, 1984)

around an average fixed value. At each timestep the energy is converged to 1×10^{-3} eV, which corresponds to at least 7 representative digits in the absolute value of the energy. All the calculations are performed on the supercomputers OCCIGEN and ADA (and then Jean-Zay) from the CINES and IDRIS computing center respectively. You can find a typical VASP® input file (INCAR) for the production run in annex page 144.

Initial structure

We model the feldspar end-members in a cubic cell with periodic boundary conditions and containing 208 atoms (16 formula units). This totals 1024 or 1152 electrons for the Na- and K,Ca-feldspars respectively (see table 2.1 for details).

We use the triclinic P-1 crystal structure of pure anorthite from Angel *et al.* (1990) available on the American Mineralogist Crystal Structure Database (AMCSD database code n°0001286). One conventional cell is made of 8 formula units and totals 104 atoms. To obtain the final cubic cell of 208 atoms (figure 2.3 b) we add a second conventional cell along the shortest axis (figure 2.3 a) and we force this supercell to a cubic shape with 15 Å side in VASP®. The resulting increase or decrease of lengths in the structure is less than 17 %. This cubic supercell has a density of 2.19 g cm^{-3} and 2.06 g cm^{-3} for the Ca,K and Na feldspars respectively.

To switch from the $CaAl_2Si_2O_8$ structure to the (K,Na)$AlSi_3O_8$ structures we replaced the Al atoms which are labeled on the figure 2.3 by Si atoms and all the Ca atoms are replaced by either K or Na. Since we melt the structure and we only work with fully molten and well mixed material in this project, we consider that forcing the initial structure to be cubic has no effect on the results we obtain.

Process

Production simulations are performed in the 2000–7500 K and 1–6 g cm^{-3} range. We use a timestep of 1 fs in all simulations above 4500 K and 1.6 g cm^{-3} and of 2 fs below these conditions. The initial liquid state is obtained by heating the initial supercell described above up to 4000 K for 8 ps and let it equilibrate (thermalize) for 2 ps. The other temperatures of interest are reached with one or more heating/cooling steps of 1000 K during 1 ps. At all temperatures and pressures we thermalize the fluids for at least 1 ps. We record production runs of 15–20 ps length after the total equilibration and we use the final state to compress or expand the cell in order to reach higher or lower densities respectively. This heating and cooling process is summarized on figure 2.4.

For MD users interested in knowing the organization and naming rules I used for my 556 simulations, please refer to the annex A.3.1.

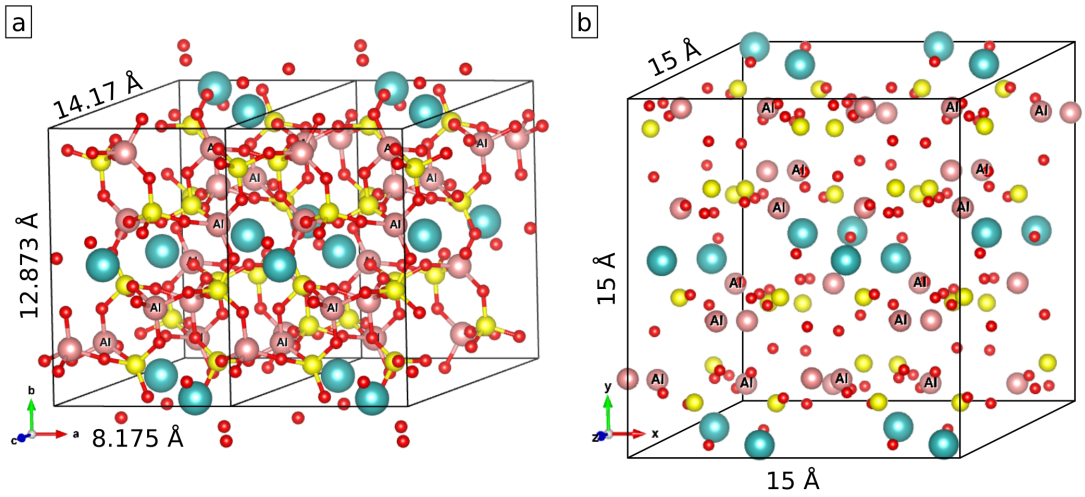

Figure 2.3 – **(a)** Two conventional anorthite cells (along a axis) from Angel *et al.* (1990) (AMCSD database code n°0001286) used to create the initial supercell of 208 atoms **(b)**. To switch from the $CaAl_2Si_2O_8$ structure to the (K,Na)$AlSi_3O_8$ structures we replaced the labeled Al atoms by Si atoms and all the Ca atoms by Na or K. Colors indicate elements: cyan - Ca, pink - Al, yellow - Si, red - O.

Table 2.1 – Characteristics of the PAW-PBE pseudopotentials used in the different studies.

element	# valence electrons	valence configuration	outmost cutoff radius	Type of study
Ca	10	$3s^2 3p^6 4s^2$	2.3	m, h2
Ca	8	$3p^6 4s^2$	3	l
K	9	$3s^2 3p^6 4s^1$	2.3	m, h2
K	7	$3p^6 4s^1$	3.1	l
Na	1	$3s^1$	2.2	m, l
Al	3	$3s^2 3p^1$	1.9	m, l, h2
Si	4	$3s^2 3p^2$	1.9	m, l, h2
O	6	$2s^2 2p^4$	1.52	m, h2
O	6	$2s^2 2p^4$	1.85	l
Na	9	$3s^1$	1.45	h1
Al	3	$3s^2 3p^1$	1.7	h1
Si	4	$3s^2 3p^2$	1.5	h1
O	6	$2s^2 2p^4$	1.1	h1

m - main study of all feldspars
l - low density of all feldspars
h1 - high density $NaAlSi_3O_8$
h2 - high density $CaAl_2Si_2O_8$ and $KAlSi_3O_8$

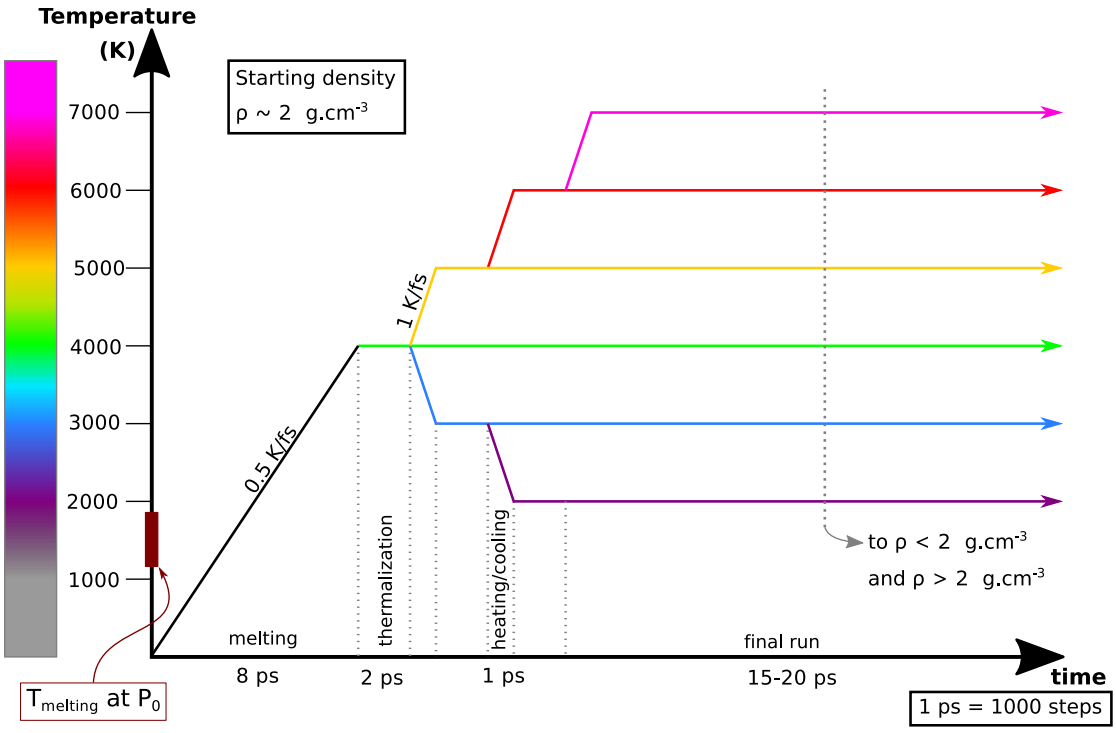

Figure 2.4 – Schematics of the heating and cooling processes. Only the main temperatures are displayed here. Each heating/cooling step or change in density is followed by a thermalization of 1–2 ps.

2.2.2 Special cases

Low density study

In order to find the critical density we have to investigate densities below $1\,\mathrm{g\,cm^{-3}}$. The computation time in FPMD rises with the volume of the simulation cell. Then to increase the speed of calculations and be able to reach low densities, we use pseudopotentials which require a lower plane wave energy cutoff. The value then used in the INCAR is now 370 eV instead of 550 eV. The pseudopotentials used for this low density study, between 0.5 and $2.5\,\mathrm{g\,cm^{-3}}$, are summarized in the table 2.1. They lead to a total number of valence electrons of 1024 or 1120 for the Na- and K,Ca-feldspars respectively. In this region, the production runs last about 4 ps, which is enough to estimate the global pressure and temperature.

The complete temperature-pressure-density range investigated (main study + low density study) is represented on figures 2.5 (a) and (b). Those who are not familiar with the concept of negative pressures are invited to consult the review about cavitation in water from Caupin and Herbert (2006). The process we use here to reach densities lower than $2\,\mathrm{g\,cm^{-1}}$ is simply a stretching of the fluid, which allows us to reach negative pressures.

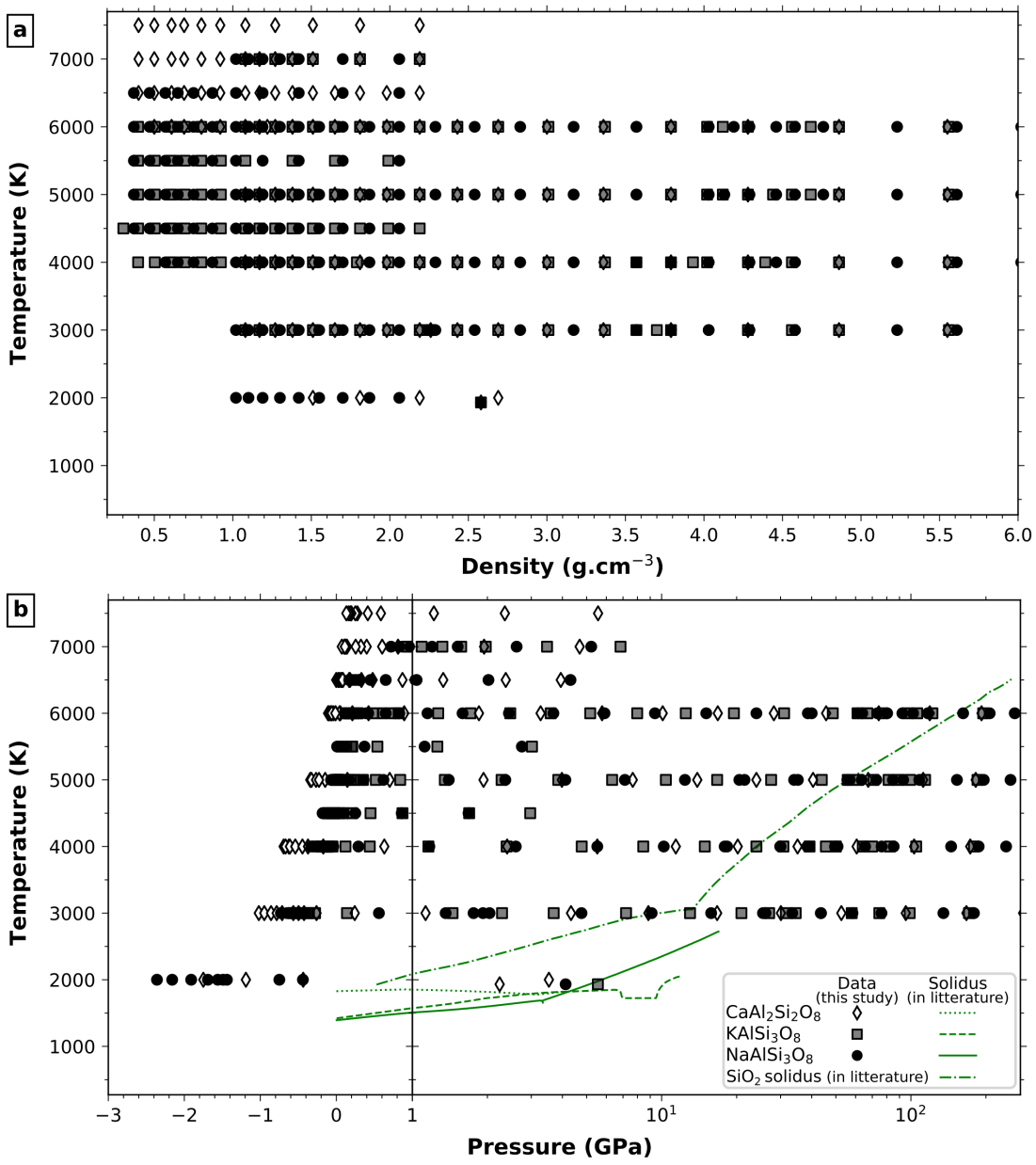

Figure 2.5 – Position of the data points obtained here for the main study and the low density study in the (a) temperature-density and (b) temperature-pressure projections. Green lines are solidus for silica from Tsuchiya and Tsuchiya (2011); Zhang *et al.* (1996) and for feldspars (and jadeite above 2 GPa) from Bell and Roseboom Jr. (1969); Hariya and Kennedy (1968); Lindsley (1966); Litvin and Gasparik (1993); Urakawa *et al.* (1994).

High density study

For the study of the behavior of shocked feldspars, we have to investigate densities above 3.5 g cm^{-3} and temperatures above 10 000 K. The pseudopotentials used for the Ca- and K-feldspars are adapted to a complete study over the range 1–6 g cm^{-3} and up to 20 000 K, which is not the case for the Na pseudopotential. Then for the Na- end-member only, we use hard pseudopotentials in order to reduce the overlap of electronic spheres, in particular for Na-Na pairs. They are summarized in the table 2.1. The energy cutoff for this set of pseudopotentials is 950 eV and the total number of valence electrons rises to 1152. This is due to the various semicore states that are now considered as valence states and computed explicitely in the DFT step. Simulations run for about 5–10 ps for temperatures between 3000 and 6000 K. Above 10 000 K the timestep is set to 0.5 fs and simulations run for about 2000 steps since such high temperatures lead to very short equilibration times.

2.2.3 Tests and convergence

We carried out convergence tests using 416 atoms (instead of 208) for two density-temperature couples (2.1 g cm^{-3} at 5000 K and 1.2 g cm^{-3} at 4000 K). We obtain a pressure difference of less than 0.12 GPa and an internal energy difference of less than 10 meV/atom between the simulations with 416 atoms and those with 208 atoms. A larger number of atoms would be preferable for the chemical analysis presented in chapter 4, but the calculations with 416 atoms take more than four times longer to run than those with 208 atoms. Then, it is not possible to perform them in a reasonable amount of time.

The influence of the initial state on the pressure and energy of the final state is tested and shown on figure 2.6. We used four different initial states of lower of higher temperature or density. For each of them we followed the required process as described in section 2.2.1 to reach the same density-temperature point of 1.55 g cm^{-3} and 5000 K. Then we run each simulation for 17.5 ps and compute the average pressure and internal energy displayed next to the corresponding initial state on figure 2.6. The difference in internal energy is less than 20 meV/atom, and the difference in pressure is less than 0.11 GPa.

2.3 The post-processing

2.3.1 The output file

The output file (OUTCAR) that we obtain from VASP® is a huge source of information. What one can find inside highly depends on the parameters and commands indicated in

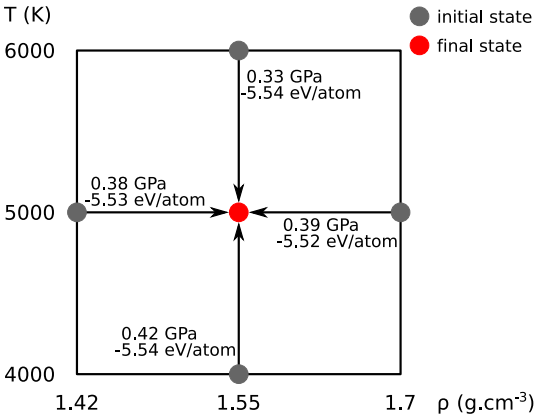

Figure 2.6 – Schematics and numerical results showing the influence of the initial state (grey dot) over the pressure and energy of the final state (red dot). The average pressure and internal energy of each final state obtained from each different initial state is displayed next to the corresponding initial state.

the INCAR file. In this thesis we will work only with the thermodynamic parameters (values of stress tensor, temperature and energies), and the position of atoms of the materials at each timestep. The first and main step of the post-processing is to extract and compute the right values. It is straightforward for the atomic positions and the instantaneous temperature, the latter being computed using the formula 2.1 and directly displayed in the OUTCAR. It is also easy for the instantaneous external pressure of the simulation, obtained with the mean of the stress tensor diagonal coefficients. But it is more complicated for the energy, since VASP® compute and displays several different energies in the OUTCAR which links can be summarized as follow[5]:

$$\underbrace{\underbrace{\underbrace{\mathrm{ETOTAL} = -TS_{e-}}_{\text{energy without entropy}} + \mathrm{PE} + \mathrm{EKIN}_{e-} + \mathrm{EKIN}_{ion}}_{\text{kinetic internal energy}} + \underbrace{\mathrm{EKIN}_{latt}}_{=0 \text{ in NVT}} + \overbrace{\mathrm{ES} + \mathrm{EPS}}^{\text{thermostat}}}_{\text{total internal energy}} \qquad \text{TOTEN} \tag{2.4}$$

with S_{e-} the electronic entropy, PE $=_{ion} \bigcap_{ion} +_{ion} \bigcap_{e-} +_{e-} \bigcap_{e-}$, the potential internal energy (sum of interaction energies between every ions and electrons), EKIN_{latt} the kinetic energy of the lattice, and ES and EPS the kinetic and potential energy of the thermostat respectively. In this equation, VASP® displays in the OUTCAR file the free energy (ETOTAL), the blue terms and the last four terms. TOTEN is the free energy minimized in the DFT loop. ETOTAL being the sum of all the energies involved in the simulation, it is the value to use in order to check energy conservation. It is not the real free energy of the system since we should remove the lattice and thermostat contribution and also the entropic energy of the ions, which is unknown. For equation of state and heat capacity calculation we need the total internal energy, which is the sum

[5] for the values that are directly given by VASP® we kept the same notations here

of the potential and kinetic internal energies, the latter being divided into an electronic and ionic contribution.

2.3.2 The UMD package

All the post processing was undertaken using the UMD package our group developed these last years. Its goal is to give an extensive set of tools for the analysis of any MD simulations, no matter the output file format. This is done through a parser (`VaspParser.py`), which extract all the data of interest from the output file and creates a *.umd.dat* file with a specific keywords-based format. Through these keywords, each of the post-processing scripts can access the required data, even if additional lines of data are added to the *.umd.dat* file after modifying the parser. This allows each user to create its own parser for each different MD simulation package or specific use of the simulations and save post-processing time (no need to read the whole output file each time) or save storage space (for a 15 ps simulation OUTCAR files take around 2 GB each compared to 0.5 GB for UMD files). For more information, the reader can refer to the 1st release of the package (Caracas *et al.*, 2020c) or to the UMD article (Caracas *et al.*, 2020a).

As previously seen (section 1.4), this work is separated into four axis of study representing the different chapters: structure of the fluids, volatilization phenomenon, transport properties and thermodynamics. Then, the methodology specific to each axis of study is detailed in the related chapter. The box diagram figure 2.7 shows the main steps of analysis for each axis of the study and underlines the chronological links between them. Each analysis step (box) is done successively from top to bottom. A step with several incoming line requires the results from each related previous step before it can be started. Each step is completely described and explained in the chapter corresponding to its axis of study. The complete post-processing is performed using Python® scripts from the UMD package or from my personal library. The main ones are explained in the following chapters, along with the options used at the moment of the script execution in a shell[6] environment. These scripts are launched using either:

```
python3 path/to/script/scriptname.py -option1 optionvalue -optionN optionvalue
```

or

```
scriptname.py -option1 optionvalue -optionN optionvalue
```

if the script has been changed to executable (`chmod +x scriptname.py`) and its directory path added to the PATH list in the `.bashrc`[7] file. Each script contains a small documentation summarizing the different options available. You can access it using the option `-h`.

[6] for example the BASH environment available on most UNIX terminals
[7] configuration file usually located in your home directory on your computer

All the scripts mentioned in this thesis are available either in the UMD Git Hub repository (Caracas *et al.*, 2020c) (or in the zenodo version Caracas *et al.* (2020b)) or in my analysis repository (Kobsch, 2020). For user who are interested in data visualization, all the scripts I made and used to create the figures presented here are also available in my personal Git Hub repository with the associated figures.

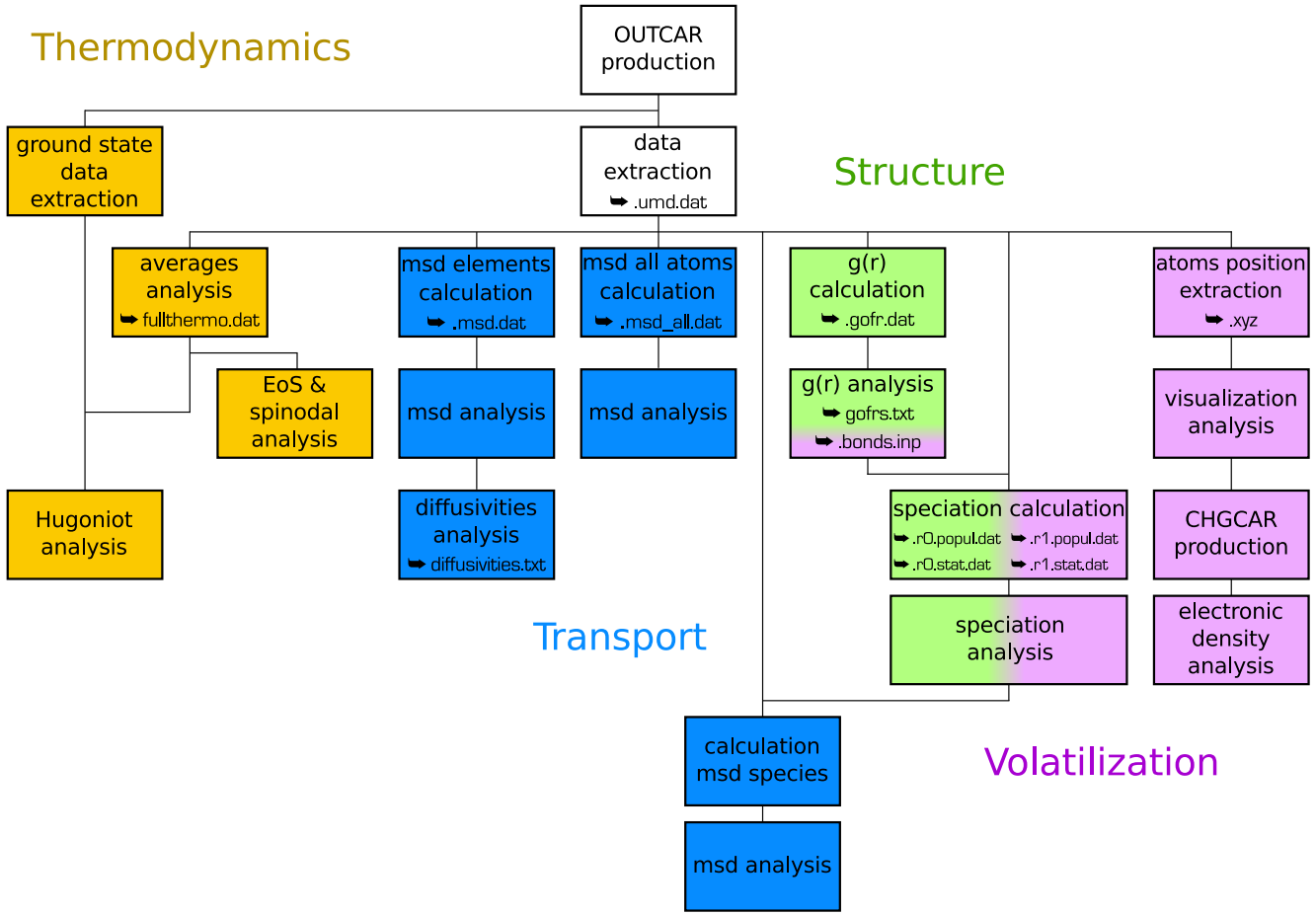

Figure 2.7 – Box diagram of OUTCAR files post processing showing the different axis of study in this thesis: structure of the fluids, volatilization phenomenon, transport properties and thermodynamics. Post-processing order goes from top to bottom. Each action or box is fully explained in the chapter corresponding to its axis of study. The extension of intermediates data files created by the scripts of the UMD package are indicated in the boxes when they are created.
accronyms: g(r) = pair distribution function; EoS = Equation of States; msd = mean square displacement; CHGCAR = charge density output file from VASP®

CHAPTER 3

STRUCTURE OF THE FLUIDS

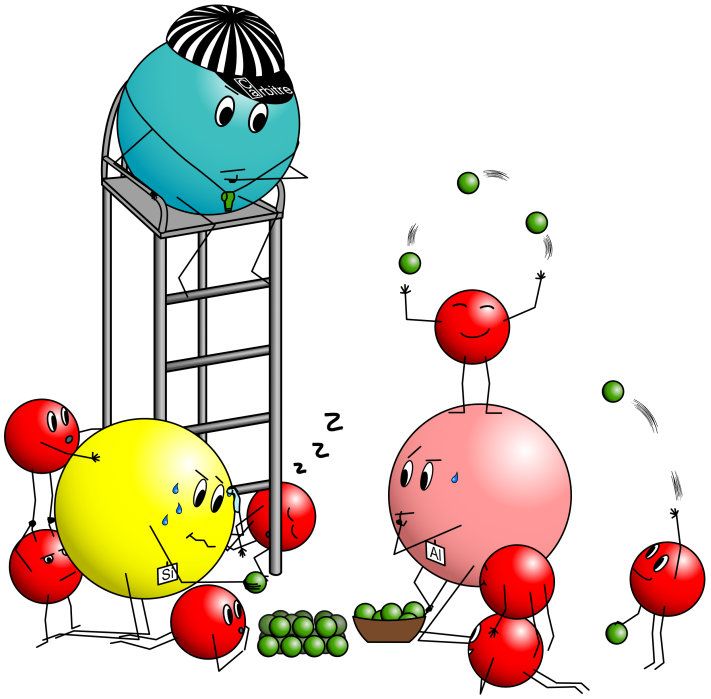

"Comment sont organisés les atomes dans les feldspaths fluides ?"
S'ils le pouvaient c'est sans doute une question que se poseraient les atomes eux-mêmes lors de leurs parties d'empilage de boules...

L'art de placer ses billes (atomes) pour un feldspath fluide

Ce premier chapitre de résultats présente la structure des feldspaths fluides (liquides ou gazeux), autrement dit, l'organisation dans l'espace des atomes constituant les fluides. Pour analyser la structure on utilise ici un outil mathématique appelé « fonction de distribution de paires ». Cela consiste d'abord à compter le nombre d'atomes de chaque type se trouvant dans une coquille sphérique centrée autour d'un atome en particulier. Ensuite ce comptage est répété pour chaque atome de la simulation. Et enfin on moyenne les résultats obtenus pour les différentes combinaisons {type d'atome central-type d'atome autour}. On obtient ainsi une courbe qui nous donne ce qui pourrait s'apparenter à la probabilité de présence des atomes voisins de type B en fonction de la distance à l'atome central de type A (figure 3.1). Notons que les éléments notés A et B peuvent aussi être identiques. La position du premier pic de cette courbe donne la distance séparant le plus souvent les atomes de type A et B. Elle est donc utilisée comme estimation de la distance moyenne de liaison entre les éléments A et B. La position du premier creux définit le rayon de la première sphère de coordinence. Le nombre moyen d'atomes B situés dans cette sphère donne le nombre de coordination de A avec B.

Quand la pression dans le fluide augmente, le nombre de coordination de Al, Si, Ca, K ou Na avec O augmente (figure 3.9). Ce nombre de coordination est, comme sa définition l'indique, une moyenne du nombre d'atomes entourant l'atome central. En réalité il y a en général un mélange de différentes coordination. La figure 3.13 montre par exemple que à 3000 K et 20 GPa, une valeur moyenne de 4.4 pour le nombre de coordination de Si avec O correspond en réalité à environ 42 % de SiO_4 (4 atomes O autour de Si) et SiO_5 (5 atomes O autour de Si) et environ 15 % de SiO_6 (6 atomes O autour de Si). Ces groupements {atome central entouré par X atomes O} sont appelés polyhèdres de coordination. À 3000 K, on voit clairement une dominance par soit la coordination 4, soit 6 à plus haute compression. À 6000 K on se retouve avec un mélange plus homogène de différentes coordinations.

Pour chaque couple de pression-température analysé ici, autrement dit pour chaque simulation, on peut ainsi obtenir quel est le polyhèdre de coordination majeur dans chacun des feldspaths et l'indiquer dans un diagramme température-pression (figure 3.14). On voit ainsi que le nombre de O autour de Al ou Si augmente continuement avec la pression quel que soit la température, passant de 4 à 5, 6, 7 et même 8 au delà de 100 GPa. Au contraire dans les cristaux de feldspaths on retrouve uniquement soit 4 O autour de Al et Si soit 6 à hautes pressions. À très hautes températures et basses pressions on voit qu'il n'y a plus que 3 O ou moins autour de Al ou Si, ce qui est sans doute signe que de petites molécules sont formées. Cette hypothèse est à vérifier dans le chapitre suivant.

Brief outline In this first analysis chapter we talk about the structure of the fluid, in other words we look at the organization in space of all the atoms. First, section 3.1 presents the theory of atomic structure analysis and the corresponding computer codes written to perform these analyses. This section is separated into two parts: subsection 3.1.1 about the classic analysis (bond distance and coordination number), widely used in MD simulations works, and subsection 3.1.2 about a more advanced analysis which requires additional post-processing (coordination polyhedra proportions). Sections 3.2 and 3.3 present the results and discussions relative to the analyses described in subsections 3.1.1 and 3.1.2 respectively.

3.1 Post Processing

3.1.1 Pair distribution function, bond length and coordination number

The theory

The average bond length and coordination of each pair of elements are obtained with the radial pair distribution function $g_{AB}(r)$, schematically drawn in figure 3.1 for a liquid. It is the average number of atom of type B in a spherical shell of radius r and thickness $\mathrm{d}r$ centered around each atom of type A, relative to the number of atoms at the same distance in an ideal gas at the same density. Mathematically $g_{AB}(r)$ is defined as

$$g_{AB}(r) = \frac{n_B(r)}{n_B^{ideal}(r)} \tag{3.1}$$

$$n_B^{ideal}(r) = \frac{4\pi}{3}\rho_B((r+\mathrm{d}r)^3 - r^3) \tag{3.2}$$

$$n_B(r) = \frac{1}{N_A \tau_{run}} \sum_{\tau=1}^{\tau_{run}} \sum_{A=1}^{N_A} \sum_{B=1}^{N_B} \Pi_{(r,r+\mathrm{d}r)}(r_{AB}), \tag{3.3}$$

with $\rho_B = \frac{N_B}{V_{cell}}$ being the atomic density of type B atoms in the simulation cell of volume V_{cell}, N_A and N_B the number of atoms of type A and B in the cell, τ_{run} the total number of time steps and $\Pi_{(r,r+\mathrm{d}r)}(r_{AB})$ the gate function which is equal to 1 if $r \leq r_{AB} < r + \mathrm{d}r$ (r_{AB} being the distance between the center of atoms A and B) and 0 else. Likewise we define the cumulative integral in spherical coordinates of the pair distribution function $Int(g(r))$ as

$$Int(g_{AB}(r)) = 4\pi\rho_B \int_0^r g_{AB}(r')r'^2 \ \mathrm{d}r'. \tag{3.4}$$

Its value at the end of the first coordination sphere, defined by the first minimum of the *g(r)* curve (xmin), gives the coordination number (CN) of A with B. For a CN value of X, it means there is in average X B atoms around one A atom.

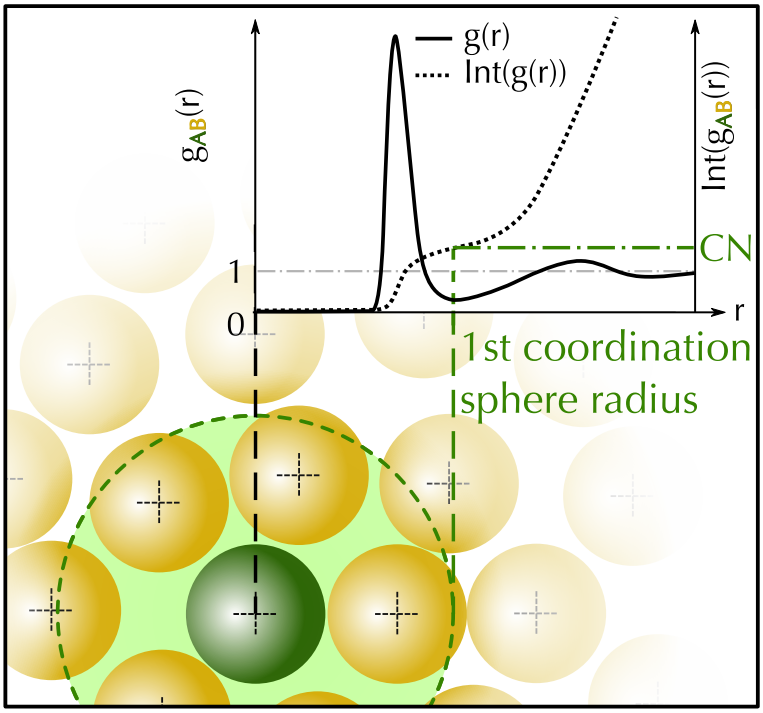

Figure 3.1 – Schematics of the radial pair distribution function $g_{AB}(r)$ for a liquid and its cumulative integral $Int(g_{AB}(r))$, with A as the central atom (green) and B the surrounding atoms (yellow). The first coordination sphere is defined up to the first minimum of the *g(r)* curve. The coordination number (CN) corresponds to the value of the cumulative integral in spherical coordinates (as defined by the equation 3.4) at the first minimum of the pair distribution function.

The first peak of the *g(r)* (xmax) gives the highest probability bond length, and is often taken as an approximation of the average bond length between A and B. But in case of very a skewed distribution, we can question whether it is the best estimation of the average bond length. We can, for example, compute the weighted average of the *g(r)* up to the first minimum, also defined by

$$d1_{AB} = \frac{\int_0^{xmin} g_{AB}(r) r \ \mathrm{d}r}{\int_0^{xmin} g_{AB}(r) \ \mathrm{d}r}. \tag{3.5}$$

Another estimation, which is considered in statistics to be less biased by extreme values, is the median of the distribution up to the first minimum. An example of the differences between these three estimations of the bond length for a very skewed distribution is illustrated in figure 3.2.

Computer implementation details

The pair distribution function and its cumulative integral are both computed using the script `gofrs_umd.py` from the UMD package, with a shell width of 0.05 Å (option `-d`) and a sampling every timestep (option `-s`). This python script creates one *.gofr.dat* file per UMD file given as input. It is an implementation of the equations 3.1, 3.2 and 3.3: it counts the atoms located at a certain distance and averages over all the atoms and timesteps.

As shown in figure 3.1, we are interested in the location of the first peak and of

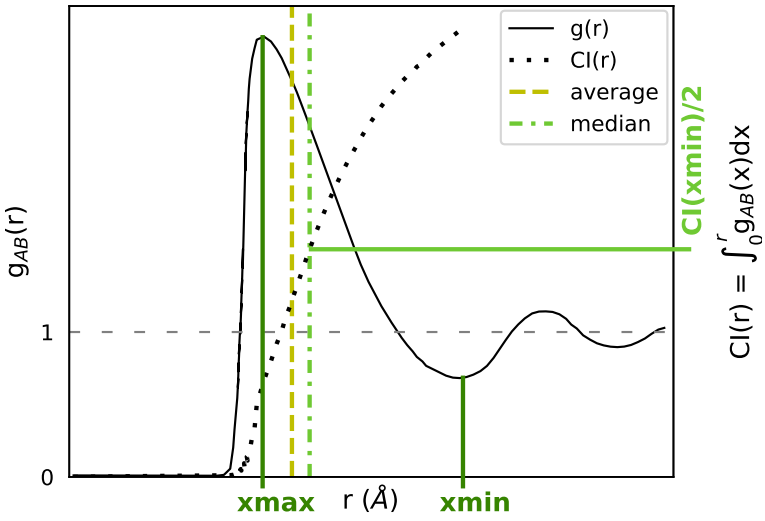

Figure 3.2 – Schematics of the different estimation of bond length on a skewed pair distribution function. The "average" (yellow dashed line) is the weighted average defined by the equation 3.5. CI(r) is the cumulative integral of the distribution *g(r)* as defined in statistics, it is not the same as in figure 3.1 and in equation 3.4. The value *r* for which CI(r) = CI(xmin)/2 gives the "median" (light green dash-dotted line) of the *g(r)* distribution up to the first minimum xmin.

the first minimum of the pair distribution for each file and pair of atoms. For this purpose we developed tools to: 1) semi-automatically find these maxima and minima for all the files we want at once (script `analyze_gofr_semi_automatic.py`), 2) check the values automatically found (`check_gofrs_analysis.py`) and 3) correct the wrong ones if necessary (`analyze_1gofr_update.py`).

`analyze_gofr_semi_automatic.py` is adapted to work for simulations of consecutive pressure or density. For the best experience, we have to first sort all the *.gofr.dat* files in separated folders, one for each different temperature, and make sure their pressure or density change progressively when all the files are alphabetically sorted according to their filename. Then, in the parent folder (the one in which we have all subfolders per temperature), we analyze the pair distribution function of every atomic pair (default behavior of `-a` option) and print the additional *.bonds.inp* files (`-b 1` option). The following paragraph explains the principle of the `analyze_gofr_semi_automatic.py` script, also summarized in the algorithm 1 in annex.

The script searches all the subfolders for *.gofr.dat* files. For each subfolder it alphabetically sorts them in a list of files. Then for each atomic pair AB we enter the interactive part: the pair distribution function is displayed and we can manually click on the first maximum and minimum to register their position along the x axis (xmax and xmin respectively). This action does not require high precision from the user since it is used only to have initial guesses for the third polynomial fit of the first peak and valley which appear on the graph. These fits use only a small portion of the pair distribution function to the left and to the right of the guesses, since a complete decomposition of the pair distribution function into individual peaks is not easily possible. Neither the peaks nor the valleys are third polynomial functions but to date it is the best and simplest way

to fit them. If the fits are good we can click on the "Good" button and the maximum and the minimum of the two fitted curves are stored in memory. If one or both of the fits are not good, then we can click on the "Bad" button and only zeros are stored in memory. Once this interactive step is done for each atomic pair, the script checks the values registered. If they are non-zeros then they are used as initial guesses for the fits of the next file and the script records automatically all the values for the files of this subfolder. If they are zeros then, for the atomic pair in question, the interactive part starts for the next file. This is followed by the automatic part if the values are good, or a new interactive part if not. In the best case scenario, the user only has to perform the manual actions once per temperature and per AB atomic pair (without counting the reverse BA pairs since they have the same pair distribution function), namely $\frac{N_{typat}^2+N_{typat}}{2} * N_T$, with N_{typat} the number of elements and N_T the number of temperatures.

`analyze_gofr_semi_automatic.py` produces one output file per subfolder named *subfoldername_gofrs.txt*. These files contain the following information for each AB atomic pair (including the reverse BA pairs):

xmax the x coordinate of the *g(r)* first peak obtained with the 3rd order polynomial fit if it was good, 0 else

ymax the corresponding y coordinate if the fit was good, 0 else

xmin the x coordinate of the *g(r)* first minimum obtained with the 3rd order polynomial fit if it was good, 0 else

coord the corresponding y coordinate of the *g(r)* spherical integral if the fit was good, 0 else

bond the average bond length computed using the equation 3.5

It also produce one *.bonds.inp* file per *.gofr.dat* with three columns of $2^{N_{typat}}$ lines (N_{typat} being the number of atomic types). The third column gives the xmin value of the corresponding atomic couple, whose elements are written in the two first columns. For users who want to easily compare other estimations of the interatomic bond length (as in figure 3.5), the script `analyze_bond-length-estimators.py` uses the values in the *gofrs.txt* and all the *.gofr.dat* files to create one *_bonds.txt* file with xmax, weighted average, median of the distribution and another calculation for test purposes.

In some cases, the automatic procedure may fail to correctly fit the maximum and minimum of *g(r)*, that is why we developed the `check_gofrs_analysis.py` script, which goal is to plot the *g(r)* functions of all the atomic pairs selected (option `-a`), for every *.gofr.dat* file in the subfolders (or in the selected subfolder with the option `-d`), and to add on these vertical lines to indicate the xmin and xmax values as recorded in the

gofrs.txt file (option `-g`). This way it is easy to identify which pairs of atoms for which files may need to be reanalyzed. To update the data automatically we developed the `analyze_1gofr_update.py` script, which requires the *.gofr.dat* file and a finite list of atomic pairs to work. It uses the same Interac.Analysis procedure as before with three decision buttons ("Fit", "Bad", "Click") instead of two ("Good", "Bad") which give respectively in the output fitted, 0 and clicked values of the parameters for the current atomic pair. This script is also very flexible in its use depending on the options and files used:

`-b` ***.bonds.inp*** If indicated, it updates the values in the *.bonds.inp* file with the selected xmin values.

`-g` ***gofrs.txt*** If the *gofrs.txt* file is indicated, it updates the values in the *gofrs.txt* file with the selected results. This *gofrs.txt* can also be a concatenated version of all the individual *gofrs.txt* files previously created (providing that only the first header is kept), or even a modified version with lines added in the header (provided that the two initial header lines remain unchanged and are located right before the first data line).
If this option is not used, it creates by default a new *gofr_[.gofr.dat filename].txt* file with two result lines for the fitted and clicked values.

`-a O2` If "O2" is indicated in the atomic pair list and `-g` *gofrs.txt* is also indicated, then it adds 5 columns (xmax,ymax,xmin,coord,bond) at the end of the file for O_2, allowing the analysis of the additional small peak that can appear in the $g_{OO}(r)$. All the other lines (files) of the *gofrs.txt* file for these new columns are filled with 0. If the *.bonds.inp* file is also indicated, then the xmin value of O_2 replaces the one of O-O.

Once columns for O_2 are added to the *gofrs.txt* file, it is possible to check the values with the `check_gofrs_analysis.py` by selecting `-a O2`. This creates a plot of the $g_{OO}(r)$ magnified on the O_2 peak, making easier the values check.

3.1.2 Coordination polyhedra analysis

Definitions

The integral over $g_{AB}(r)$ up to its first minimum yields the CN of A with B. As said before, it is the average number of atoms B around each atom A. But at each snapshot there is often a mix of different coordinating polyhedra AB_n (n atoms B located in the first coordination sphere of A), each present in different proportions.

Every individual coordination polyhedra i is characterized by its composition, in terms of atomic indexes (from 0 to 207), and by the time t (or snapshot number) when

it appears (i.e. when the n atoms B are inside the 1st coordination sphere of the selected atom A). We call "polyhedra ID" the atomic composition of the coordination polyhedra. We can define the coordination polyhedra index i as the association {polyhedra ID, appearance time}: $i = [A, B_1, ..., B_n, t]$. Hence, we define the coordination polyhedra species $AB_{n,i}$ as the coordination polyhedra with n atoms B around one atom A and with the index i. The lifetime of this species, represented by $L_{n,i}$, is the difference between its disappearance time (when at least one atom B left the 1st coordination sphere of A) and its appearance time t.

In a given simulation, we compute the total lifetime of a coordination polyhedra AB_n, represented by L_n, as:

$$L_n = \sum_i L_{n,i} \tag{3.6}$$

Then, the proportion of a coordination polyhedra AB_N, represented by R_N is:

$$R_N = \frac{L_N}{\sum_n L_n} \tag{3.7}$$

Computer implementation details

In order to obtain the proportion, lifetime and composition of each coordination polyhedra AB_n, we use the `-r 0` option of the `speciation_umd.py` script from the UMD package. Its process can be summarized by the flowchart in figure 3.3, while the actual computing process is summarized in the algorithm 2 in annex. We sample every timestep (`-s` 1), with all the cations as central atoms (i.e. atoms inside coordination polyhedra, option `-c`) and only O as vertices of coordination polyhedra (`-a`). We use the first minimum of the *g(r)* for each atomic pair (`-i` *.bonds.inp*) as threshold to define if two atoms are bonded or not: if their interatomic distance is smaller than this radius, they are considered bonded. We let the minimum lifetime of the species being equal to the timestep of the simulation (option `-m 1` step).

As seen before, the `analyze_gofr_semi_automatic.py` script automatically creates one *.bonds.inp* file per *.gofr.dat*. Then each *.bonds.inp* file can be individually updated with the `analyze_1gofr_update.py` script. But in some cases, the xmin location is quite uncertain, mainly due to small peaks appearing or disappearing in this region. A complete decomposition of the *g(r)* function into individual peaks would allow a perfect location of the xmin, since it would be defined as the intersection of the two first peaks. But not only the peaks are incorrectly represented by functions like Gaussian or Lorentzian, a decomposition of the *g(r)* signal leads to huge uncertainties on the peak tails, and consequently on the xmin location. That is why we prefer to only slightly smooth the xmin variations in order to reduce the effect of mislocating the xmin on the coordination polyhedra proportions. This is done through the `plot_distances+analysis_xmin.py`

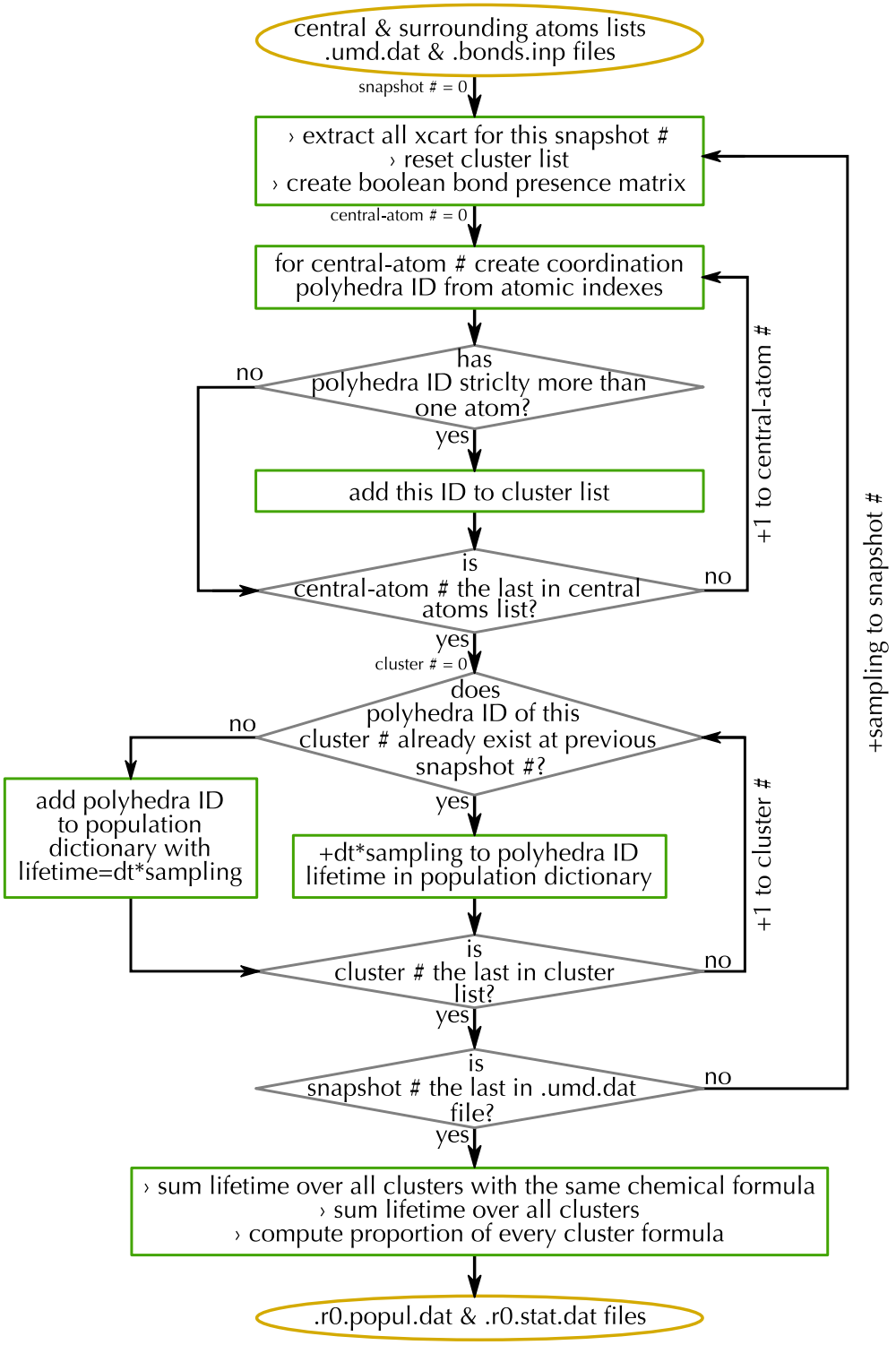

Figure 3.3 – Simplified flowchart of the coordination polyhedra analysis from the `speciation_umd.py` script (option `-r 0`). dt is the timestep used in the simulations, while "sampling" is the sampling frequency value we indicate in the option `-s`. Here we choose 1 to sample every step.
accronyms and definitions: xcart = cartesian coordinates; boolean bond presence matrix = matrix of $N_{\text{central atoms}}+N_{\text{surrounding atoms}}$ atoms side filled with 0 (no bonds) and 1 (bonds between the atoms); coordination polyhedra ID = string of atomic indexes present in the coordination polyhedra;

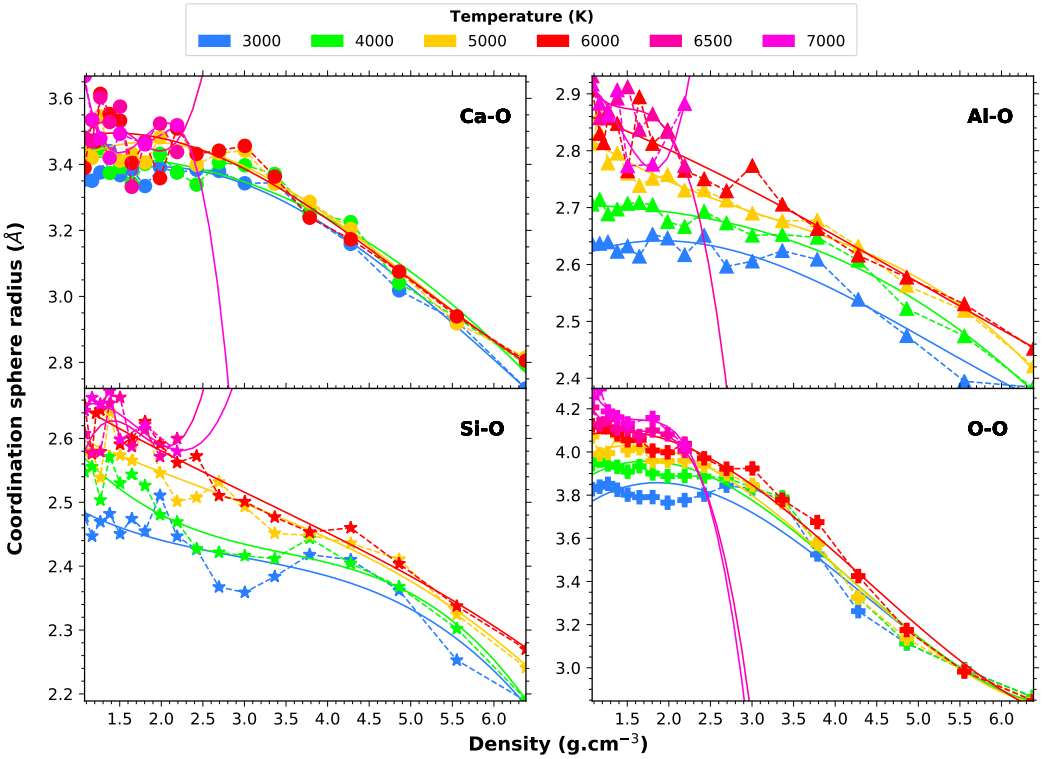

Figure 3.4 – Radius of the 1st coordination sphere as a function of density and temperature for $CaAl_2Si_2O_8$. Colors represent temperatures: blue - 3000 K, green - 4000 K, yellow - 5000 K, red - 6000 K, pink - 6500 K, magenta - 7000 K. We use third-order polynomial fits (solid lines) to smooth the xmin values that appear in the *.bonds.inp* files.

script which uses a third-order polynomial fit when we have at least six data point, and a linear fit else. As shown by figure 3.4, third-order polynomial fitting appears to be a good and simple way to smoothen the data while keeping long range variations.

3.1.3 Future improvements of the UMD package

There are many other structural properties of interest other than the bond distance or the coordination polyhedra proportion. We can cite for example the variation with pressure and temperature of the angular distributions or the number of bridging and non-bridging oxygens. These properties are not computed here because their calculations are not yet implemented in the UMD package. They will be implemented in a future version of the `speciation_umd.py` script.

3.2 Bond distance and coordination number

Bond distance

To date, there is no definitive and clear definition of the bond length. Experimentally it is often measured through X-ray diffraction, but the results vary depending on the

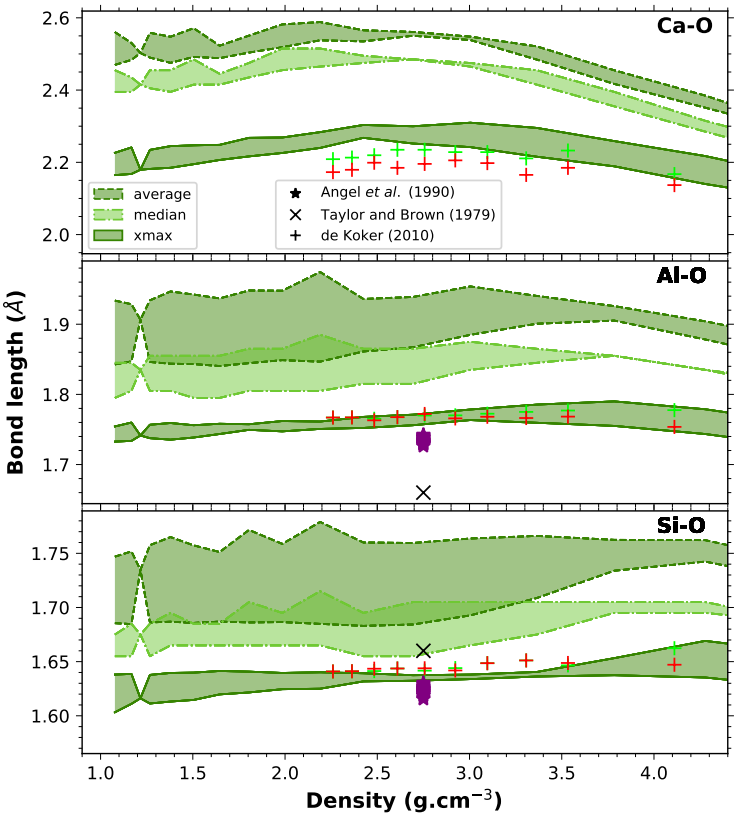

Figure 3.5 – Comparison of the different bond length calculations for the Ca-end-member with experimental results (Angel *et al.*, 1990; Taylor and Brown, 1979) and simulations (de Koker, 2010). The filled regions represent the bond length variation between 3000 and 7000 K. Colors represent temperature: green - 4000 K, red - 6000 K. Results from Angel *et al.* (1990) are obtained from natural crystal after a heat treatment at temperatures between 1600 and 1800 K followed by quenching, while the value of Taylor and Brown (1979) is the average value of all T-O bonds (T being Al or Si) in feldspar glasses at room temperature.

selected crystal structure used in the refinement process. In the figure 3.5 we compare each of the three average bond length calculations defined in section 3.1.1 for the Ca-end-member with experimental results from Angel *et al.* (1990) and Taylor and Brown (1979), and with simulations from de Koker (2010). The maximum of the peak is more in agreement with experimental results, especially with the computational experiments, than the weighted average or the median. The weighted average value appears to be influenced a lot by the xmin location, which varies a lot with temperature as seen in figure 3.4 and on the pair distribution functions displayed on figures 3.6 and A.3. The median seems to be less influenced by the xmin location but still shows larger variation than the xmax.

Figure 3.6 shows the pair distribution functions for each feldspar end-members at 2 g cm^{-1} as a function of temperature. At 2 g cm^{-1} and 2000 K, conditions that are close to a hot magma at ambient pressure, the Si-O and Al-O pair distribution functions are very close to 0 at the first minimum, a feature that is close to what we see in a solid.

The pair distribution function of O-O displays one main peak located around 2.7 Å, which represents the position of oxygens sharing the same edge of polyhedra around the Al or Si cations. The peak is found at all densities and temperatures and its position varies from below 2.2 Å at high densities to about 2.8 Å at low densities. For temperatures above 4000 K, $g_{O-O}(r)$ exhibits a second smaller peak located around 1.4 Å. Its

position varies from approximately 1.5 Å around 3 g cm^{-3} to 1.3 Å at 1.0 g cm^{-3}. It is presented for two representative densities: 2 g cm^{-3} that is in the fully fluid region on figure 3.6 and 1.0 g cm^{-3} that is below the liquid-gas boundary density on figure A.3 (see chapter 4 and 6 for the determination of the physical state of feldspars). We interpret this peak as an indication of molecular O_2 since the average bond distance in gaseous dioxegene is 1.2074 Å (Haynes, 2011). The O_2 peak location can be quite imprecise when the peak is very small, for example at high densities or at 4000–4500 K, which may explain the fluctuations from one density to another.

We use the maximum of the first peak of the pair distribution functions to estimate the average bond lengths. They are represented for each feldspar end-member at each densities (or pressure) and temperatures on figures 3.7 and A.4. The three feldspars display very similar behavior of their bond length variations. At 2 g cm^{-1} and 3000 K, the Si-O, Al-O, Na-O, K-O and Ca-O average bond lengths are 1.64 Å, 1.76 Å, 2.31 Å, 2.79 Å and 2.27 Å respectively. Below about 100 GPa, we notice very little influence of the density and temperature on the average T-O bond distance (T being Al or Si): over 100 GPa pressure range the relative decrease is about 2 %. On the opposite, the relative variation of the M-O bond distance (M being Na, K or Ca) over the same pressure range is on the order of 10 and 20 % for {Na,Ca}-O and K-O respectively. In general the bond lengths in the liquid at 3000 K are comparable to the values recorded in the solids at ambient conditions.

Figures 3.8 and A.5 shows that the interatomic distances of O-O, T-O and M-O pairs are always smaller than the interatomic distances of two cations. This is true for every temperatures and densities studied. Moreover, the decrease of interatomic distances is far greater for cation-cation pairs than for T-O pairs over the same pressure range. Feldspars are tecto-silicates, their crystal structure is built of a polymerized framework of SiO_4 and AlO_4 tetrahedra, in other words of $\cdots$-T-O-T-O-$\cdots$ chains in the three directions of space, with the cations (Na, K, Ca) distributed orderly in the pores of this polymer. In the liquid state, the framework and polymerization are still present. Thus, we consider there is not interatomic bonds between the cations. This will be of importance in the chapter 4 for the search of chemical species in the fluids.

Coordination number

The density of solid feldspars ranges from 2.5 g cm^{-3} to 2.8 g cm^{-3} at ambient pressure and temperature. In the liquid state, the framework and polymerization of SiO_4 and AlO_4 tetrahedra are still present, but the dominant coordination changes as a function of both pressure or density and temperature.

The coordination number of Si and of Al by O is very similar for the three feldspar

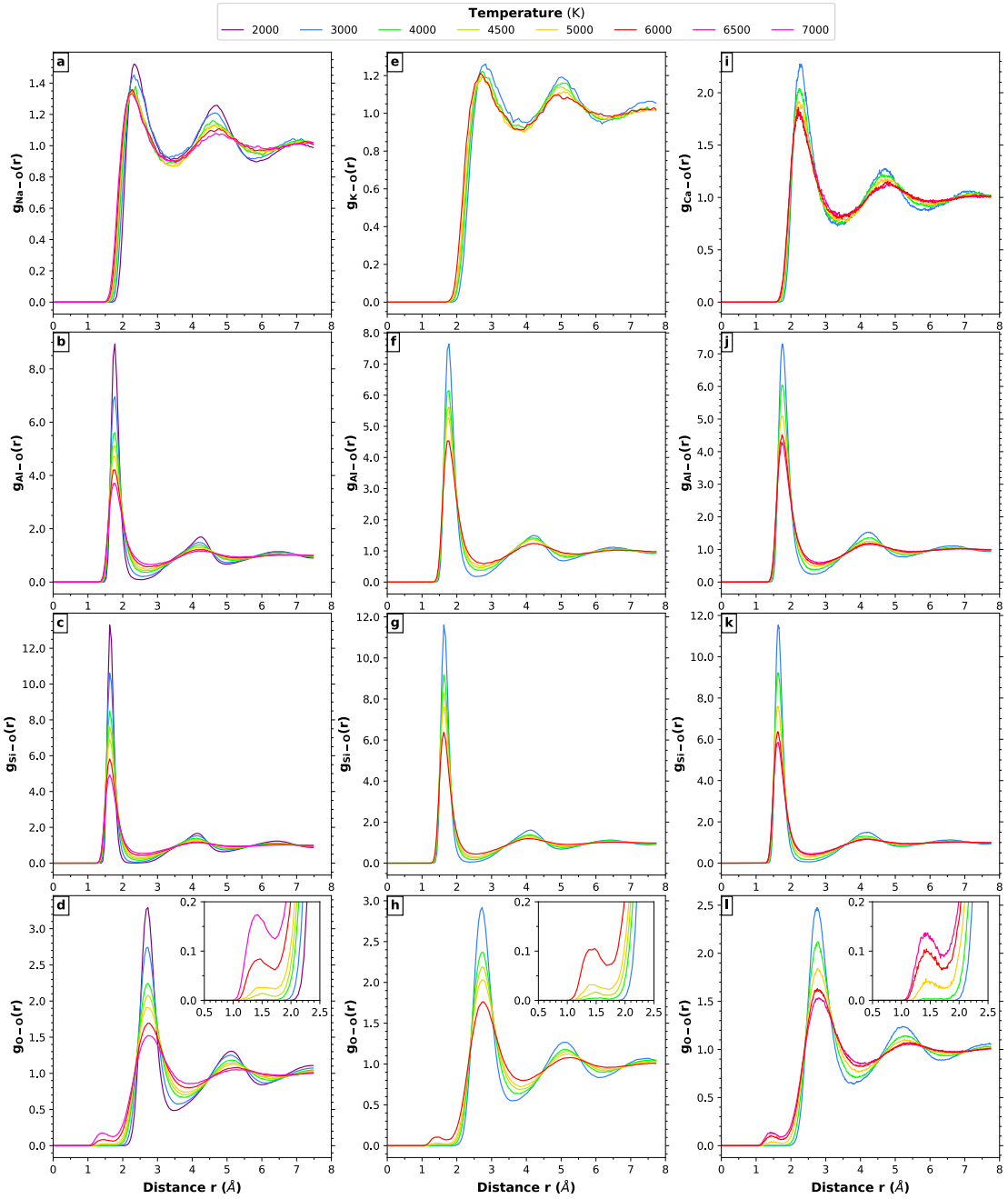

Figure 3.6 – Pair distribution functions of X-O (X being Na, K, Ca, Al, Si and O) in $NaAlSi_3O_8$ (a,b,c,d), $KAlSi_3O_8$ (e,f,g,h) and $CaAl_2Si_2O_8$ (i,j,k,l) at $2\,g\,cm^{-1}$. Colors indicate temperatures. The insert shows a zoom on the region 0.5–2.5 Å. The small peak located around 1.4 Å marks the presence of O_2 molecules. The same figure at $1\,g\,cm^{-1}$ is available in annex, figure A.3.

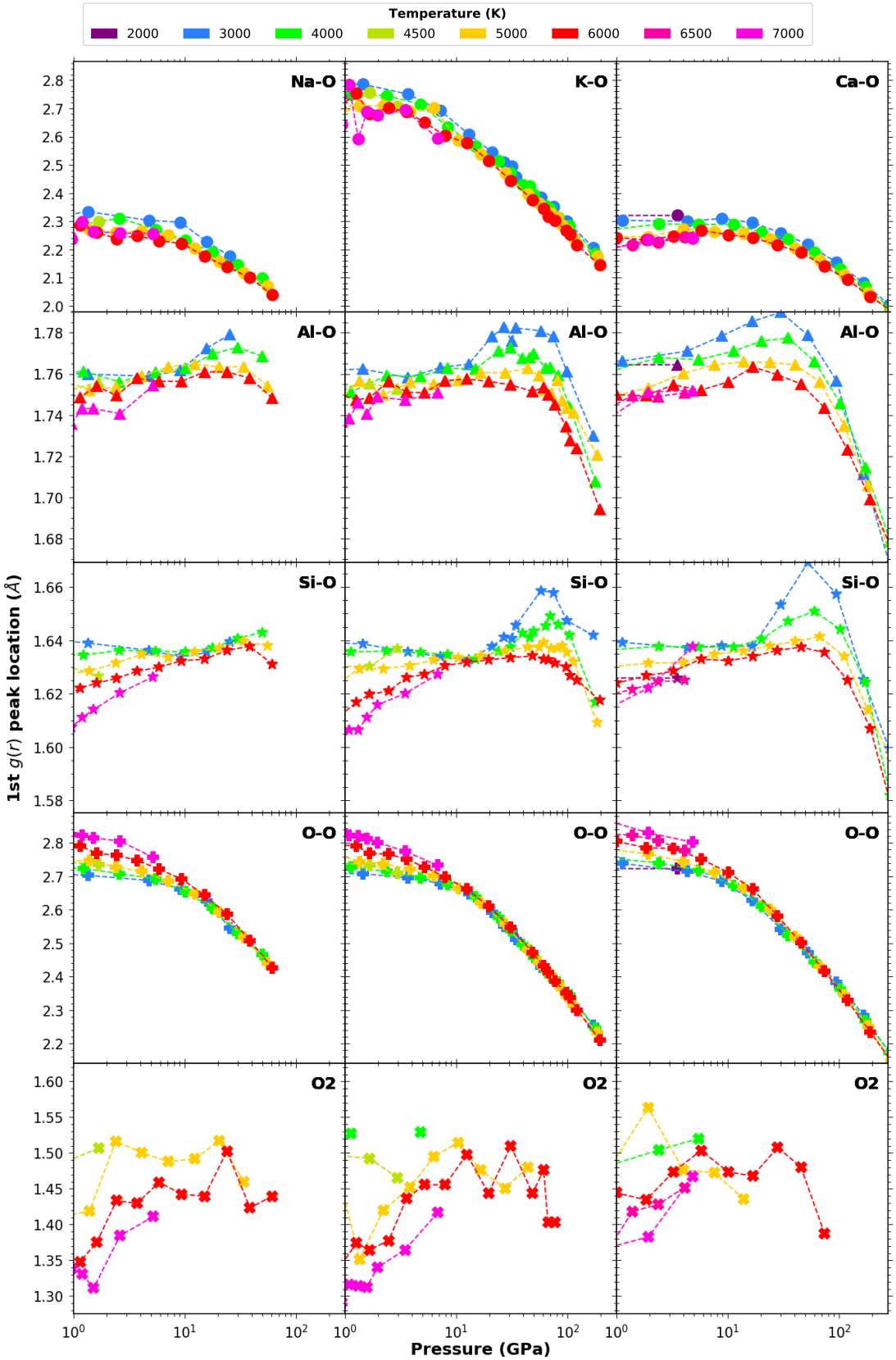

Figure 3.7 – Position of the first *g(r)* peak for each feldspar end-member (columns) as a function of pressure and temperature (colors) for T-O and M-O pairs. O2 corresponds to the small additional peak seen on the $g_{O-O}(r)$. The same figure as a function of density instead of pressure is presented figure A.4.

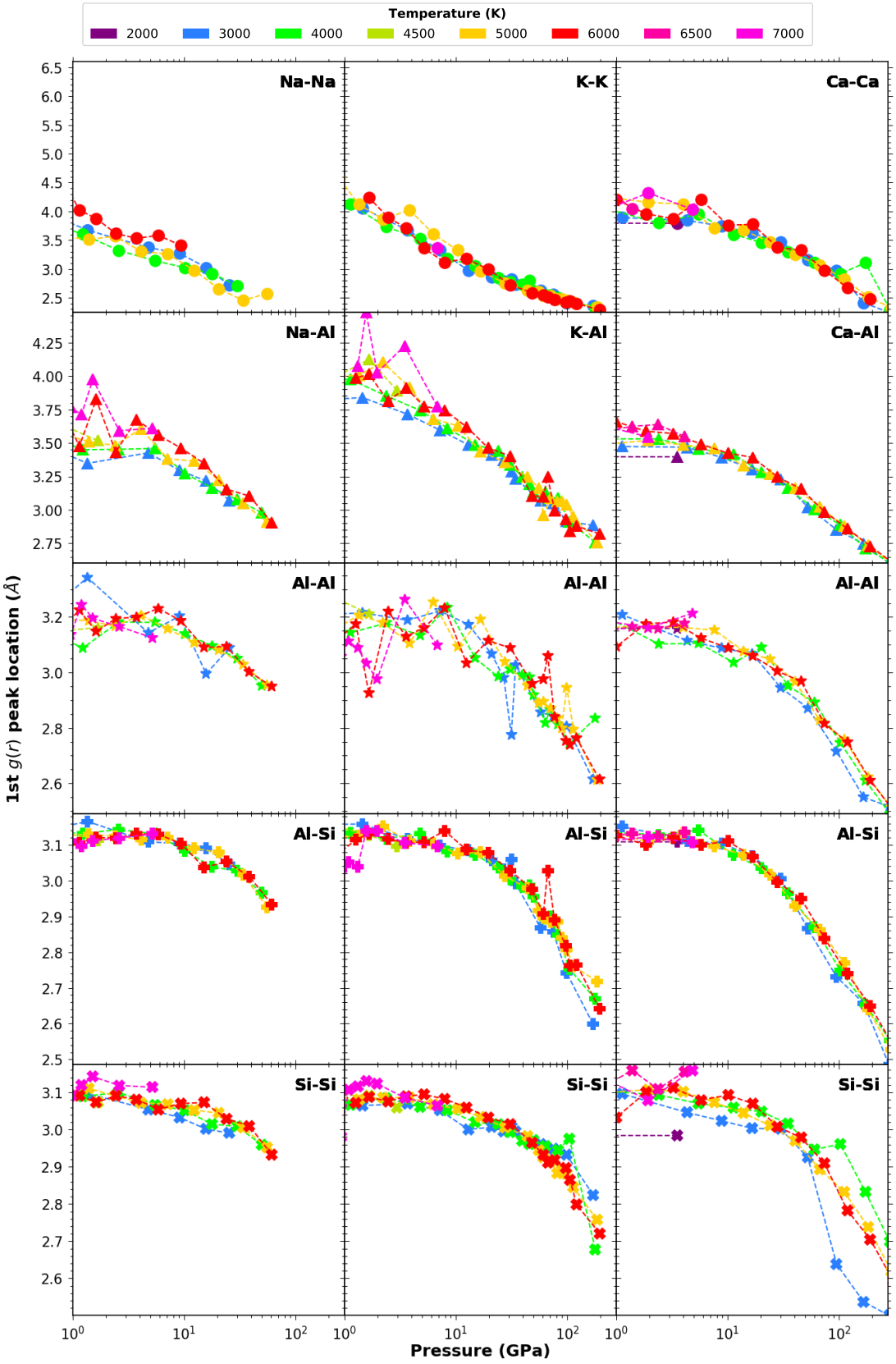

Figure 3.8 – Position of the first *g(r)* peak for each feldspar end-member (columns) as a function of pressure and temperature (colors) for five cation pairs. The same figure as a function of density instead of pressure is presented figure A.5.

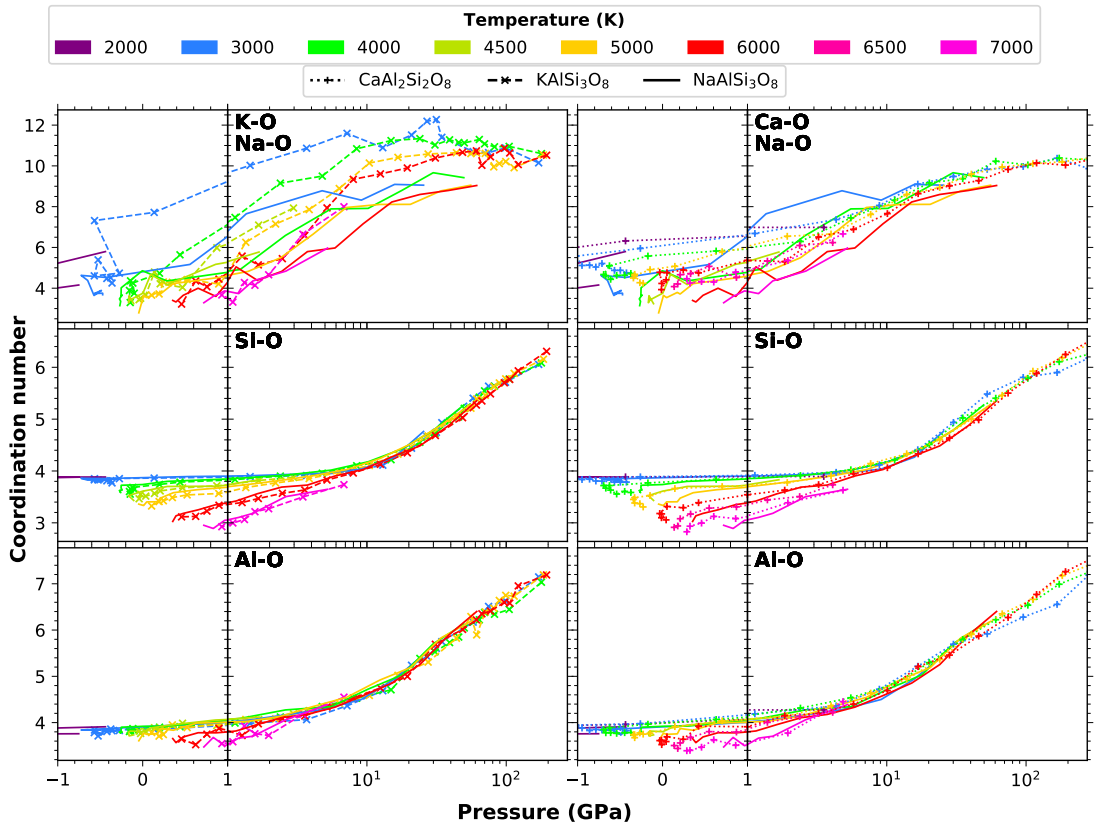

Figure 3.9 – Average coordination number of Ca, K, Na, Al and Si by O as a function of pressure and temperature. Ca- (+ and dotted lines) and K- (x and dashed lines) are both compared with Na-feldspar (solid lines). Colors indicate temperatures. The same figure as a function of density is available in annex, figure A.6.

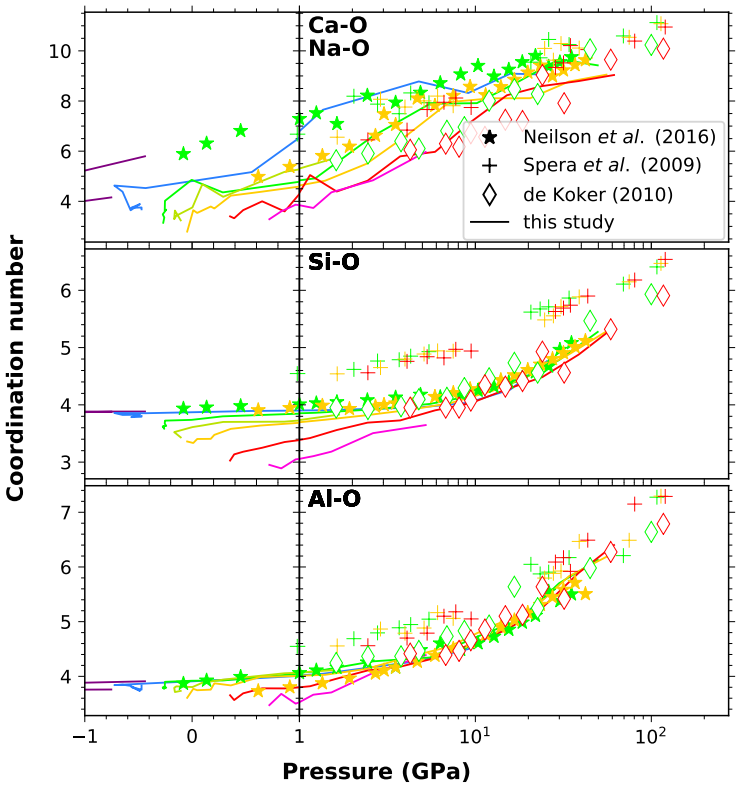

Figure 3.10 – Comparison of the average coordination number obtained in this study for the Na- end-member (solid lines) with the results previously obtained by Spera *et al.* (2009) and de Koker (2010) for the Ca- end-member and by Neilson *et al.* (2016) for the Na- end-member. Colors indicate approximate temperatures: green - 4000 K, yellow - 5000 K, red - 6000 K. For clarity and since the two plagioclase feldspars show identical results, we only plot our results for the Na-end-member.

end-members (figure 3.9). For Si, it increases from about 4 at 7 GPa to more than 6 above 100 GPa. Above 7 GPa it is only weakly dependent on temperature. At lower pressures the dependence is stronger with temperature: at 1 GPa it decreases from about 3.8 at 4000 K to 3 at 7000 K. For Al, the coordination increases monotonously from about 4.2 at 3 GPa to about 7 above 100 GPa. The spread of coordination numbers due to temperature is less than 0.5 units between 3000 K and 6000 K at all pressures.

The coordination number of Al by O is larger than the coordination number of Si by O at all pressures and temperatures. Regarding the interstitial cations environment, the coordination number of Na and Ca by O are very similar, while K displays a larger coordination number by O at all temperatures above 1 GPa.

For clarity and since our results for the two plagioclase feldspar are identical, we compare only our results for the Na-end-member with other computational experiments on plagioclase at similar temperatures (figure 3.10). In general we have a good agreement between the results obtained with FPMD on the Ca- end-member (de Koker, 2010) and also those obtained with classical MD on the Na- and Ca- end-member respectively (Neilson *et al.*, 2016; Spera *et al.*, 2009). Nevertheless, in the anorthite melts we can note larger values obtained by Spera *et al.* (2009) for the coordination of Si and Al with O and lower values obtained by de Koker (2010) for the coordination of Ca with O.

3.3 Coordination polyhedra

3.3.1 Coordination polyhedra SiO_n and AlO_n

Proportion

In terms of actual coordination polyhedra rather than average coordination numbers, the three feldspar systems behave in a similar way to other silicate melts (Karki *et al.*, 2018; Solomatova and Caracas, 2019). The melt is dominated by SiO_4 tetrahedra up to about 25 GPa at 3000 K and 20 GPa at 6000 K. SiO_5 is present in the melt at low pressures at all temperatures. SiO_6 appears around 10 GPa at 3000 K and 5 GPa at 6000 K; it is the dominant species above 70 GPa at 3000 K and above 50 GPa at 6000 K. This behavior is different in liquid $MgSiO_3$, where the coordination state increases more rapidly with pressure: SiO_5 is the dominant species above around 15 GPa and SiO_6 becomes the dominant coordination above 25 GPa Stixrude and Karki (2005). Upon decompression below 2.2 g cm^{-3}, the amount of under-coordinated Si and Al, i.e. SiO_n and AlO_n species with $n < 4$, increases with decreasing density and increasing temperature.

As a general trend, at high temperature the speciation shows a more uniform distribution between various coordination polyhedra. Figures 3.11, 3.12 and 3.13 shows the proportion of the SiO_n and AlO_n species in the Na-, K- and Ca- end-members for two relevant temperatures (3000 K and 6000 K) as a function of pressure. The same figures as a function of density are available in annex figures A.7, A.8 and A.9. For the alkali feldspars, we observe systematically that above 10 GPa the dominant species contains more O atoms for Al than for Si (i.e. when AlO_5 starts to be dominant). This is also true for the anorthite melt at 6000 K, but at 3000 K we have to wait up to 150 GPa (i.e. AlO_7 to be dominant) to see the same behavior.

Figure 3.14 shows the change in the major coordination of Si and Al by O as a function of pressure and temperature and the comparison between the fluids and the solids (crystalline forms). The melts are characterized by a series of structural changes where the dominant coordination goes as $TO_4 \rightarrow TO_5 \rightarrow TO_6 \rightarrow TO_7$ ($\rightarrow TO_8$), T being Si or Al. This transition series follows closely the changes recorded in the solids, but the sequence is generally shifted towards higher pressures. The increasing temperature in the fluid shifts to larger pressure the change in dominant coordination. However the solids, more precisely the crystalline forms, do no show five, seven or eight-fold coordination. On the contrary, glasses show a behavior similar to those of liquids, with the appearance of five-fold coordination (e.g. Li *et al.*, 1995), even though not every study succeed in observing this feature (e.g. Sykes *et al.*, 1993).

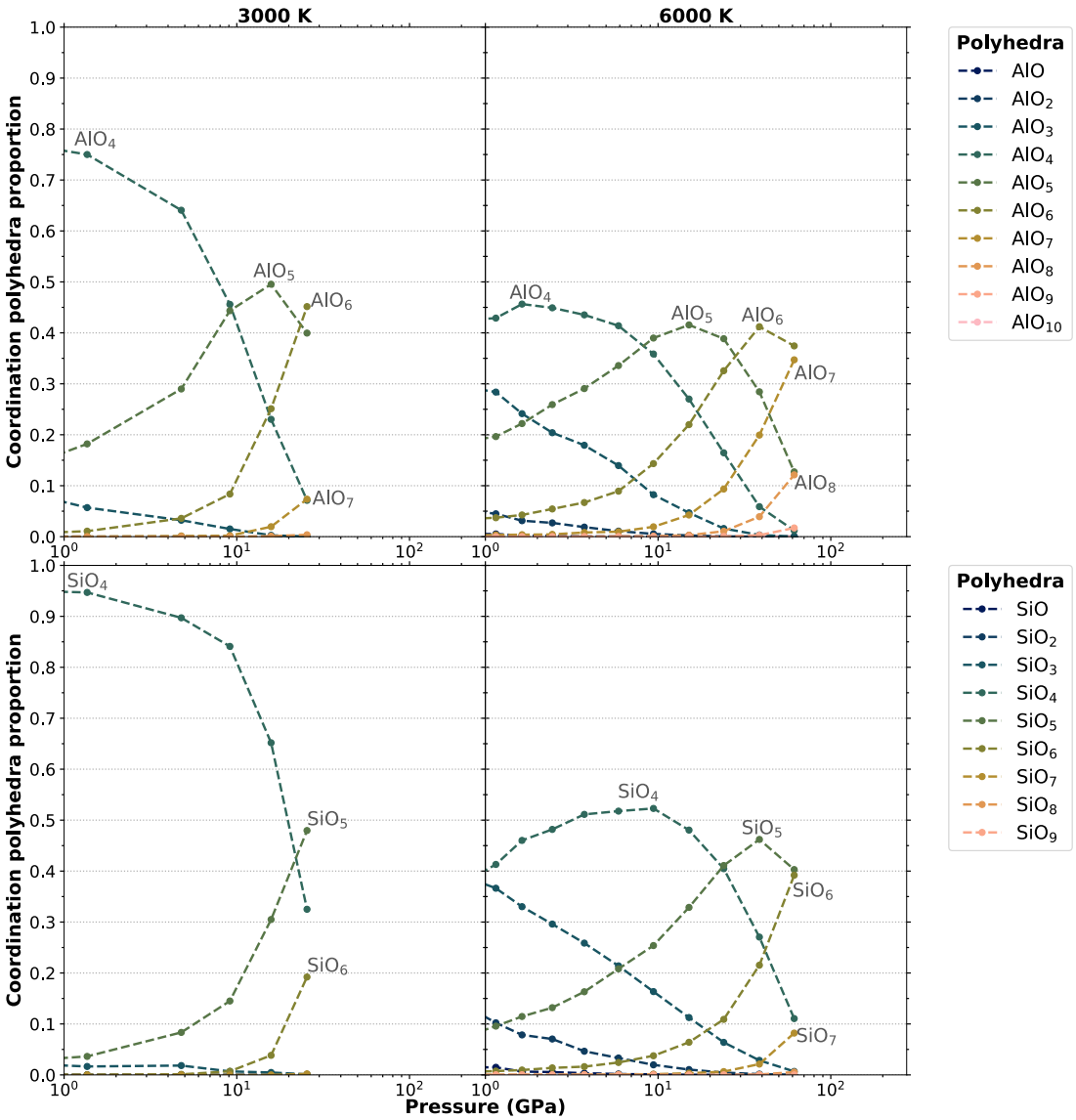

Figure 3.11 – Relative proportion of SiO_n and AlO_n coordination species in $NaAlSi_3O_8$ for 3000 K and 6000 K as a function of pressure. The same figure as a function of density is available in annex, figure A.7.

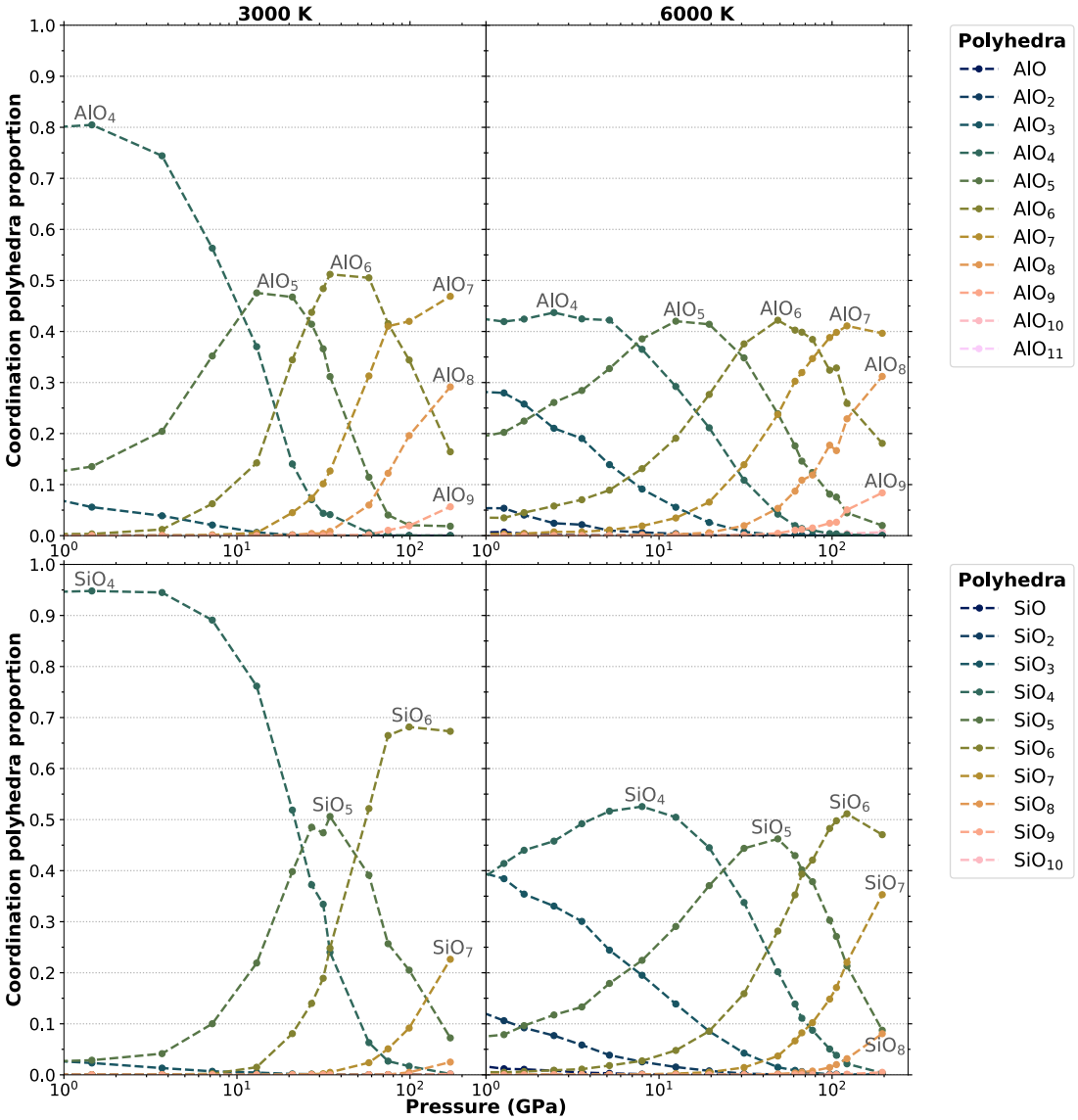

Figure 3.12 – Relative proportion of SiO_n and AlO_n coordination species in $KAlSi_3O_8$ for 3000 K and 6000 K as a function of pressure. The same figure as a function of density is available in annex, figure A.8.

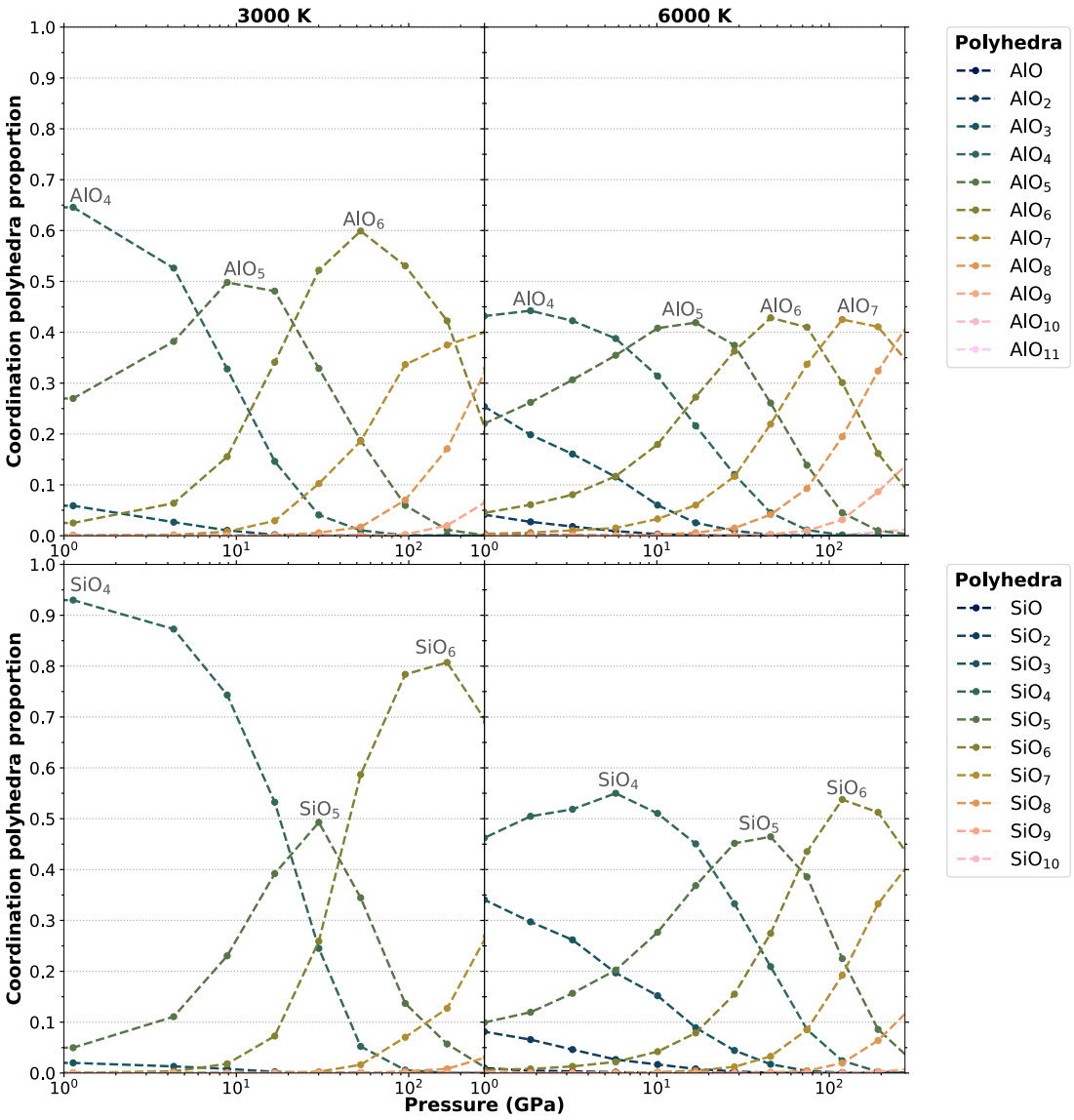

Figure 3.13 – Relative proportion of SiO_n and AlO_n coordination species in $CaAl_2Si_2O_8$ for 3000 K and 6000 K as a function of pressure. The same figure as a function of density is available in annex, figure A.9.

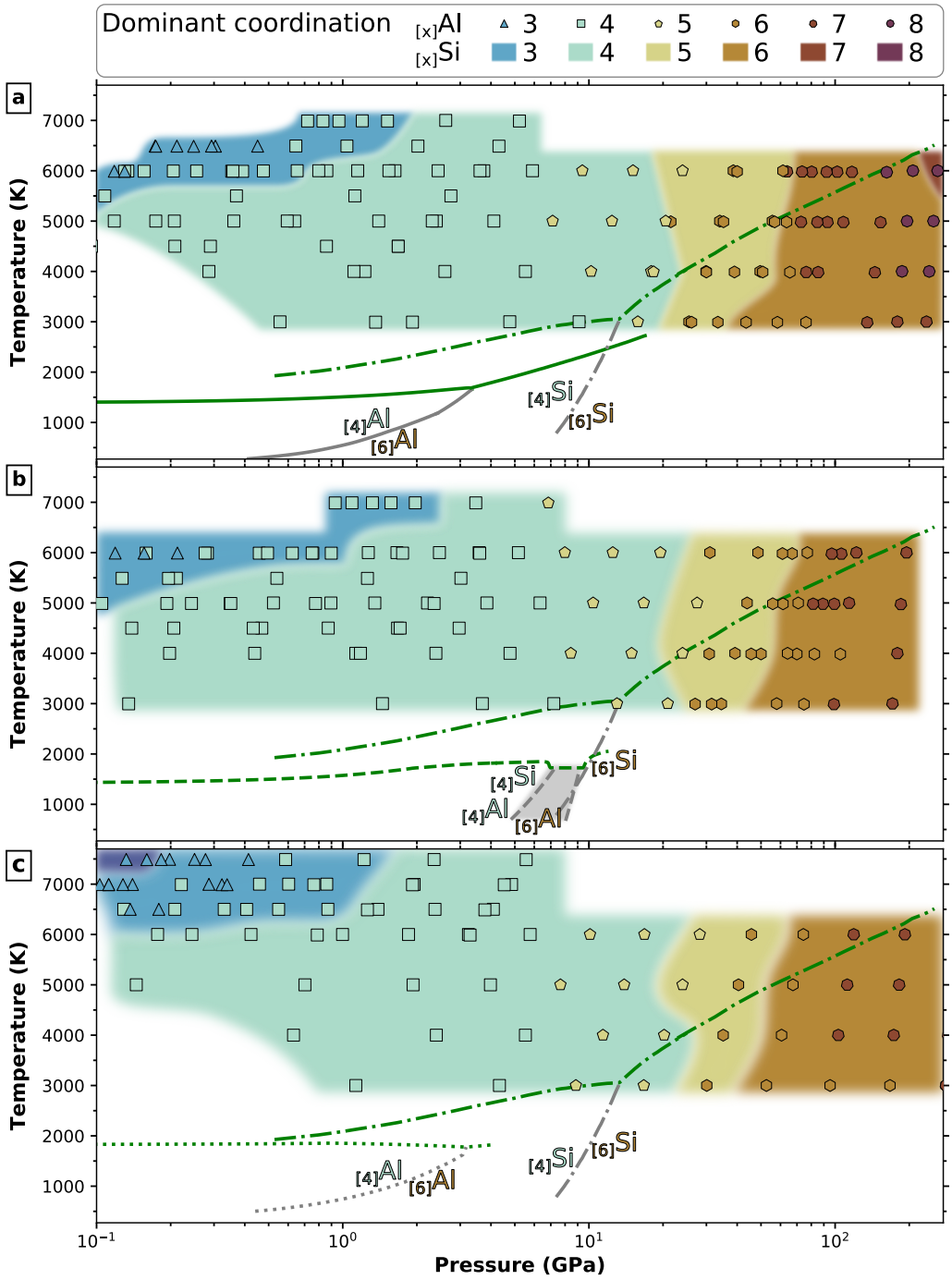

Figure 3.14 – Changes of the major coordination of T by O (T being Al, Si) for (a) Na-, (b) K- and (c) Ca-feldspar compositions in the temperature-pressure projection plane. Background color indicate the number of O atoms in the SiO_x coordination polyhedra that dominates the structure of our computed melt. The shape and color of symbols indicate the number of O atoms in the AlO_x coordination polyhedra that dominates the structure of our computed melt. Dash-dotted lines are solidus (green) and coesite-stishovite phase transition (gray) for silica from Tsuchiya and Tsuchiya (2011); Zhang *et al.* (1996). The other lines are solidus (green) and solid-solid phase transitions (gray) for feldspars (and jadeite above 2 GPa) from Akaogi *et al.* (2004); Bell and Roseboom Jr. (1969); Lindsley (1966); Litvin and Gasparik (1993); Newton and Smith (1967); Urakawa *et al.* (1994). The subsolidus coordination indicated in this diagram (denoted $_{[4]}$T and $_{[6]}$T for coordination number of T by O of 4 and 6 respectively) are for the crystalline phases. They may differ from the glasses coordination. The gray area indicate the region of $K_2Si_4O_9$ wadeite-type mineral, with Si 4 and 6-fold coordinated to O.

Lifetime

As explained in section 3.1.2, we obtain the lifetime of each coordination polyhedra species that is formed in the simulation. One way to represent the individual lifetimes for one simulation is using a bar plot: the height of each individual bar corresponds to the lifetime of each individual cluster. Due to the large number of species among each coordinating polyhedra, we display on figure 3.15 the outline of the initial bar plot at about $2.2\,\mathrm{g\,cm^{-3}}$ for two temperatures of interest, 3000 K and 6000 K.

Figure 3.15 shows that the lifetime distributions are all very skewed: there are more species with short lifetimes than species with very long lifetimes. Then, in order to compare the different densities, temperatures and feldspars together, we use the median of the lifetime distributions as an unbiased estimator or the mean lifetime. The maximum lifetime is also used to have an idea of the lifetimes range for each coordination polyhedra. The figures 3.16 and 3.17 show respectively the median and maximum lifetime of AlO_x and SiO_x coordination polyhedra as a function of density at (a) 3000 K, (b) 6000 K and as a function of temperature at (c) $1.02\,\mathrm{g\,cm^{-3}}$, (d) $2.29\,\mathrm{g\,cm^{-3}}$. Since the three feldspar end-members show very similar evolution of their mean and median lifetime, the same representation for the two other end-member are available in annex, figures A.10, A.11, A.12 and A.13. The lifetime of the coordination polyhedra underlines the long-lasting nature of the 4-fold coordination species SiO_4 and AlO_4 in the three melts. For example, at low densities and 3000 K, the SiO_4 tetrahedra live up to 10 ps, and at 4000 K up to almost 4 ps. The very large maximum lifetimes, about 10 ps, may be underestimated since the length of the simulations is only about 15 ps. Increasing temperature leads to decreasing the maximum lifetime of all coordination polyhedra and extending the tail of lifetimes, as the bonds form and break with higher frequency. The lifetime decreases almost a factor 10 when the temperature rise from 3000 K to 6000 K. The SiO_n species tend to live longer than the AlO_n species at the same density and temperature.

3.3.2 Coordination polyhedra NaO_n, KO_n and CaO_n

Na, K and Ca act as interstitial cations in the large Si-Al-O polymer that constitutes the framework of the melt. For this reason their coordination polyhedra by O show a much larger variability than their equivalent Si and Al (figures 3.18 and A.14). Below about 15 GPa (about $2.5\,\mathrm{g\,cm^{-3}}$), each coordination polyhedra becomes the major coordination species one after another, following the same behavior as AlO_n and SiO_n coordination polyhedra. On the contrary, at higher pressure the behavior is a bit more erratic: some coordination polyhedra never becomes the major species (for example KO_{13} and KO_{14}) and some coordination polyhedra become the most abundant in the whole high pressure

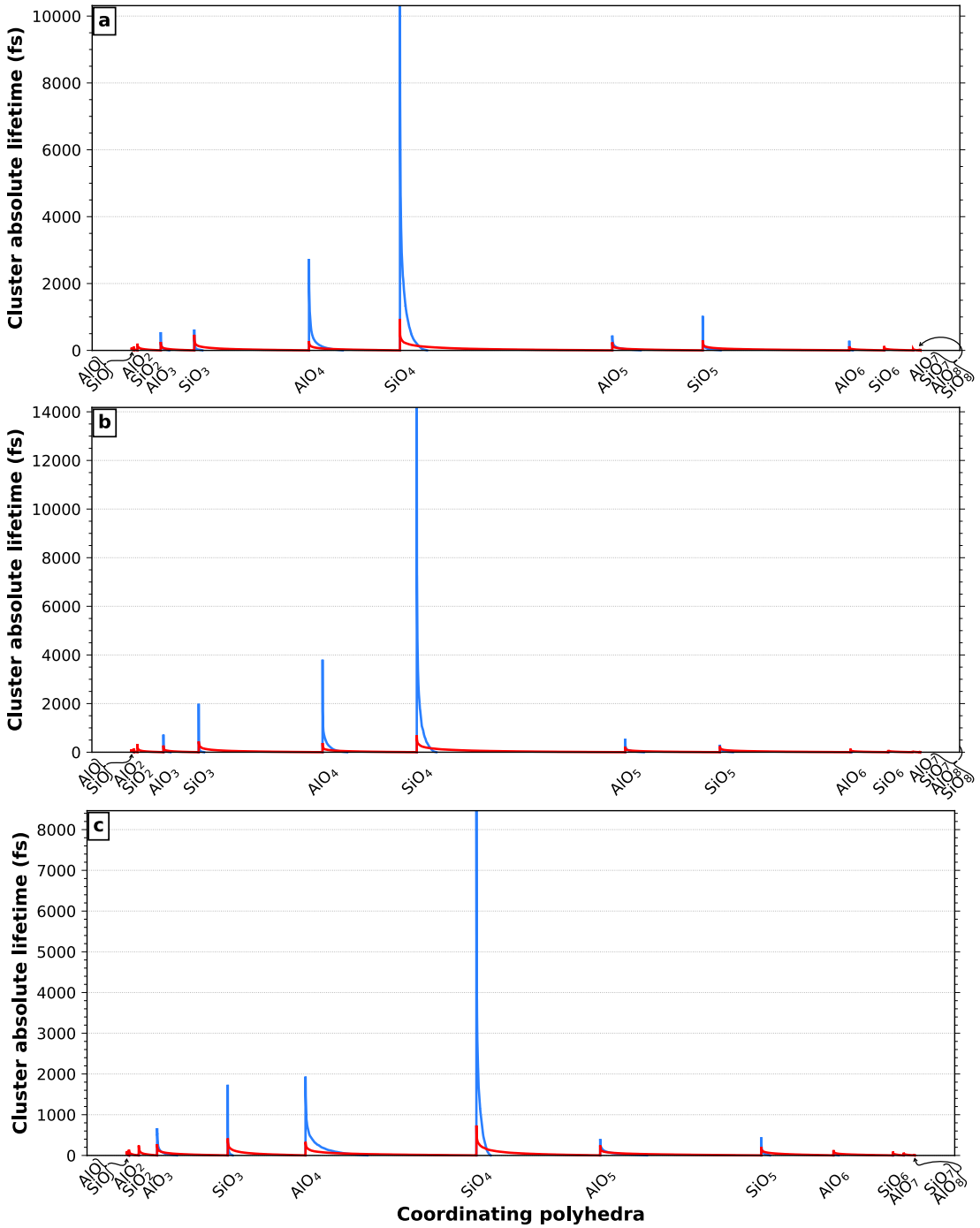

Figure 3.15 – Lifetime of SiO_n and AlO_n coordinating polyhedra at about 2.2 g cm^{-3} below the critical temperature (blue - 3000 K) and around or above the critical temperature (red - 6000 K) for (a) Na- (b) K- and (c) Ca-feldspar fluids. Due to the large number of individual species among each coordinating polyhedra, we display here the outline of the initial bar plot. The height of the each individual bar corresponds to the lifetime of each individual cluster.

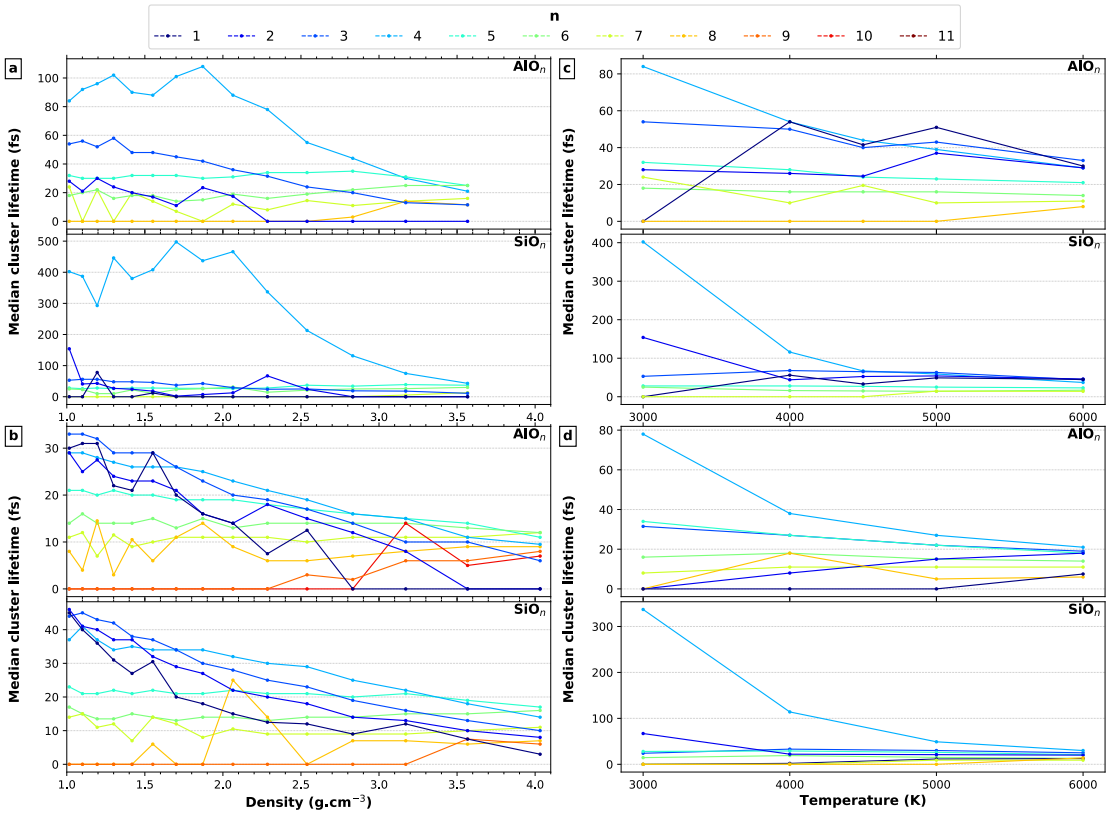

Figure 3.16 – Median lifetime of AlO_n and SiO_n coordination polyhedra for $NaAlSi_3O_8$ as a function of density at (a) 3000 K, (b) 6000 K and as a function of temperature at (c) 1.02 g cm^{-3}, (d) 2.29 g cm^{-3}. Can be compared with the same representations for $CaAl_2Si_2O_8$ (figure A.10) or $KAlSi_3O_8$ (figure A.11).

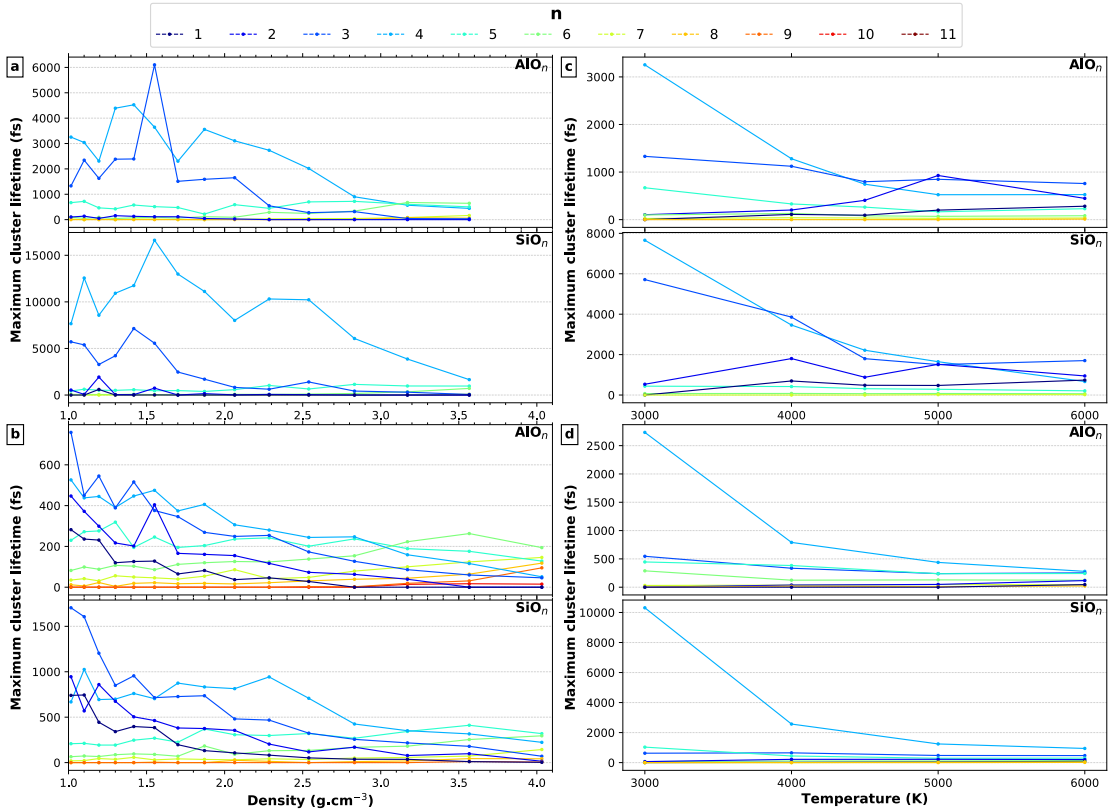

Figure 3.17 – Maximum lifetime of AlO_n and SiO_n coordination polyhedra for $NaAlSi_3O_8$ as a function of density at (a) 3000 K, (b) 6000 K and as a function of temperature at (c) 1.02 g cm^{-3}, (d) 2.29 g cm^{-3}. Can be compared with the same representations for $CaAl_2Si_2O_8$ (figure A.12) or $KAlSi_3O_8$ (figure A.13).

range studied here (for example CaO_{10}).

Also the lifetime of the MO_n coordination polyhedra (M being Na, K or Ca) is considerably shorter than the SiO_n and AlO_n (figure 3.19). From the three interstitial cations, Ca is the one with the highest coordination polyhedra lifetimes. This is possibly explained by its considerably lower diffusion coefficient (see chapter 5).

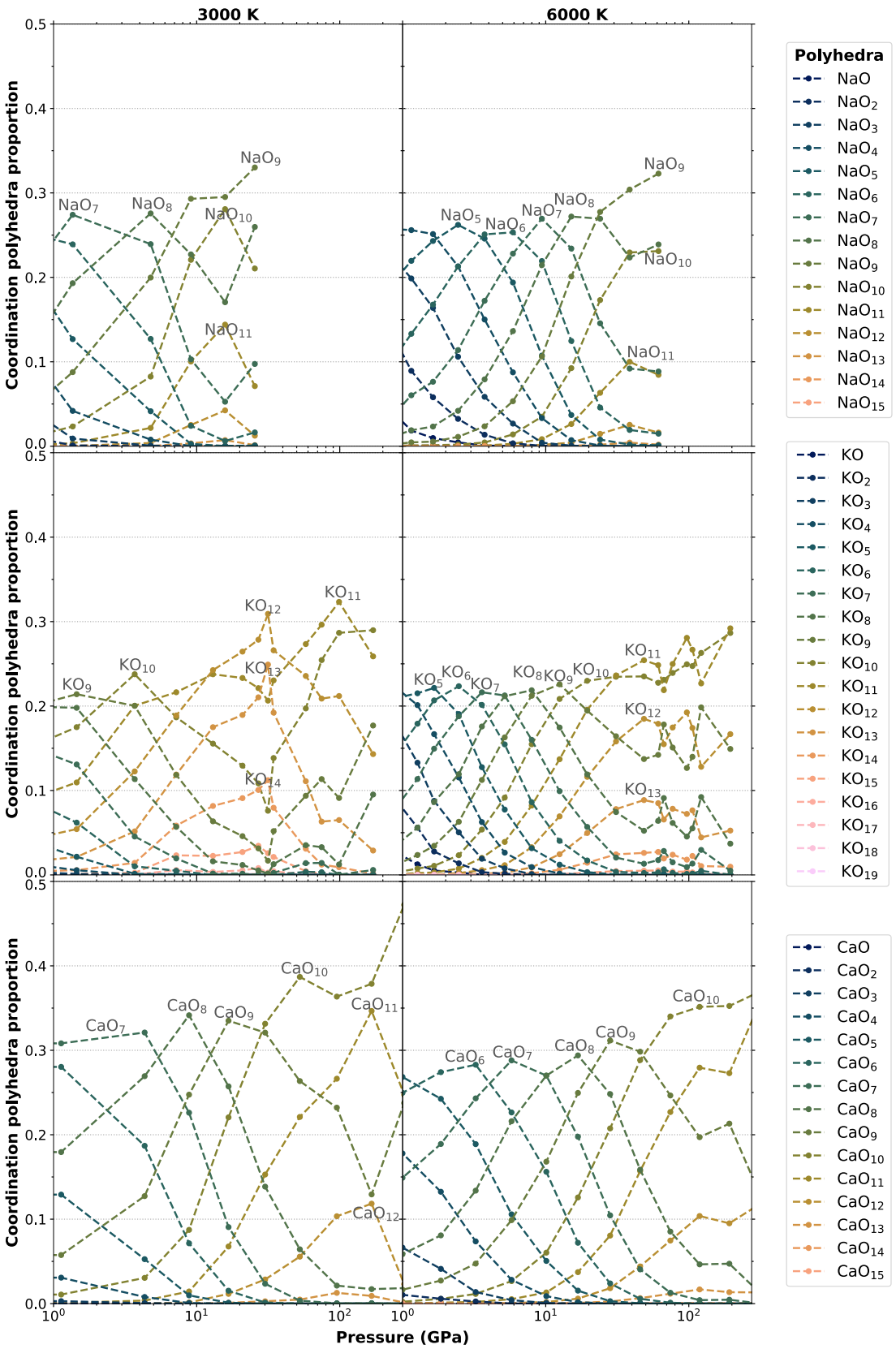

Figure 3.18 – Relative proportion of NaO_n, KO_n and CaO_n coordination species for 3000 K and 6000 K as a function of pressure. The same figure as a function of density is available figure A.14.

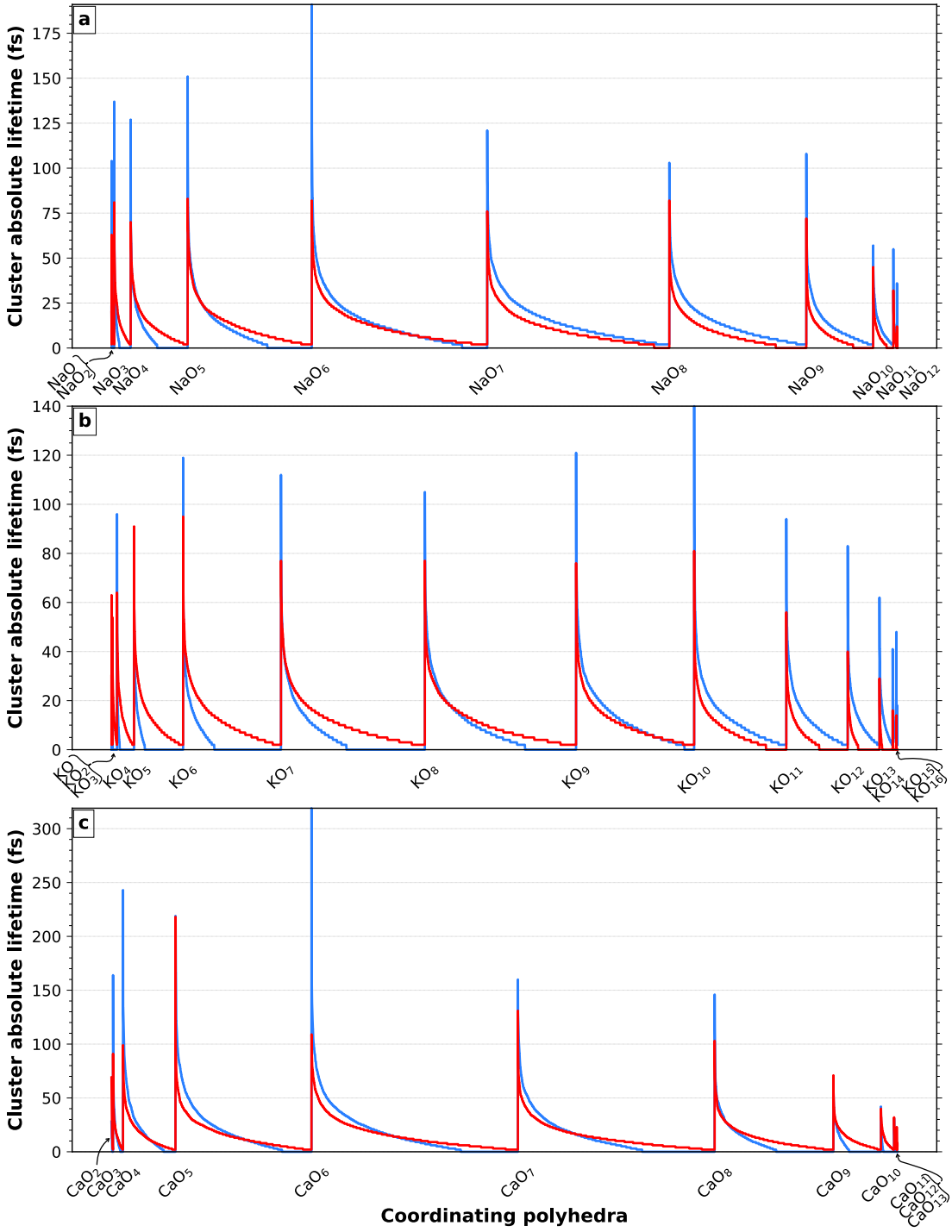

Figure 3.19 – Same as Fig. 3.15 for NaO_n, KO_n and CaO_n coordinating polyhedra.

CHAPTER 4

VOLATILIZATION

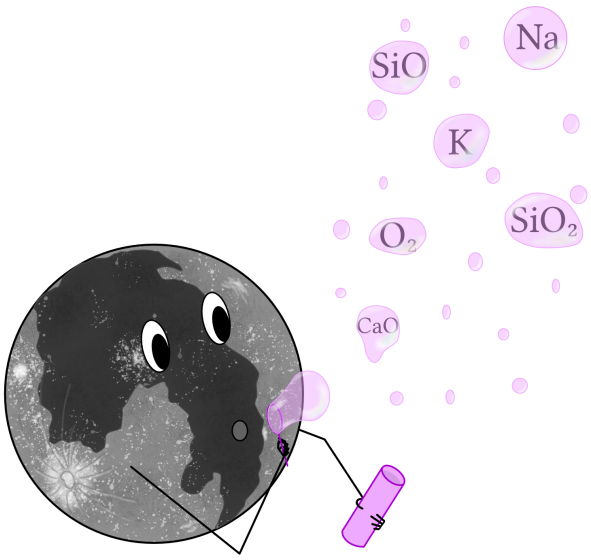

Si l'on porte à ébullition des feldspaths, les minéraux majeurs des croûtes lunaire et terrestre, que se passe-t-il ? Il est probable que les bulles créées soient composées majoritairement de petites espèces comme Na, K, SiO, SiO_2 ou O_2.

Quand les feldspaths bullent...

Prenez une boîte hermétiquement fermée, maintenue à température constante et remplie totalement d'un liquide quelconque. Si vous augmentez le volume de la boîte sans pour autant qu'elle ne s'ouvre que se passe-t-il ? En général, le liquide entre en ébullition (des bulles se forment) et une nouvelle phase apparaît : un gaz. Cela n'est cependant vrai que pour des conditions expérimentales « ordinaires » : si la température dépasse une certaine valeur, la température critique T_c (cf. chapitre 6), le fluide dans la boîte (alors qualifié de supercritique) ne subit pas la transformation décrite ci-dessus. Visuellement, aucune bulle ne se forme et le fluide reste constitué d'une seule phase homogène tout au long de l'augmentation de volume.

Cette expérience de pensée illustre les expériences numériques réalisées ici. La boîte est notre cellule de simulation contenant un feldspath liquide : en tout 208 atomes répartis entre les éléments {Ca, K, Na}, Al, Si et O. Les vides qui apparaissent (figures 4.3, 4.4 et 4.5) représentent les bulles qui commencent à se former à l'échelle microscopique. Indiquer qualitativement la présence de bulles permet de compléter le diagramme de phases du chapitre 6. Les groupements d'atomes qui flottent à l'intérieur des bulles (figures 4.4 et 4.5) représentent les premières espèces gazeuses qui apparaissent au début de l'évaporation du liquide.

La distribution des tailles des espèces chimiques figure 4.6 montre deux ensembles bien séparés : les petites espèces chimiques en bas, formant le gaz et les grosses espèces chimiques en haut, formant le liquide. Pour chaque simulation on a enregistré les temps de vie de chaque petit groupement d'atomes formant le gaz. Ils sont représentés pour $CaAl_2Si_2O_8$ à une seule masse volumique et deux températures en figure 4.7. Chaque sous-figure est un histogramme donnant le temps de vie (axe vertical) de chaque groupement de même composition chimique (chaque barre individuelle). On considère ici qu'un groupement d'atomes forme une espèce chimique gazeuse lorsque sa durée de vie dépasse un certain seuil, fixé à 30 fs.

La proportion en chaque espèce chimique dans le gaz est le temps de vie total des groupements de même composition chimique divisé par le temps de vie total de tous les petits groupements. Représenté en figure 4.10, il montre que le tout premier gaz qui apparaît est composé en majorité de Na, K, SiO, SiO_2 et O_2. On a même des molécules de SiO_3, confirmant ainsi l'observation faite au chapitre précédent. On remarque également que l'élément Al est presque absent des espèces volatiles (qui passent dans la phase gazeuse) à 4000 K et un peu plus présent à 6000 K. La proportion atomique en chacun des éléments (figure 4.11), calculée elle aussi grâce aux temps de vie de chacune des espèces, montre bien ce déficit en Al dans le gaz. La composition atomique du gaz n'est pas la même que celle du liquide, on dit alors que l'évaporation est incongruente.

Brief outline In the previous chapter, we were interested in the short-range structure of the fluids. Now we are searching for the liquid-gas transition. As before, the first section explains the theory and presents the computer codes used to find the individual chemical species, defined in subsection 4.1.1 as the largest chains of connected atoms. It also presents the parameters used to represent the atoms, bonds, etc. in the snapshots (subsection 4.1.3). Then, section 4.2 gives a qualitative analysis of the vaporization occurring in the simulations by means of snapshots. Before presenting the quantitative results and associated discussions (section 4.4), section 4.3 highlights the limits of this analysis and states the definitions used in the discussions that follow. After that, the quantitative results part presents first the lifetime of chemical species (subsection 4.4.1) and then the proportions of chemical species and elements (subsection 4.4.2).

4.1 Post Processing and visualization parameters

4.1.1 Definitions

In this chapter we are interested in the volatilization of the liquid, which includes the chemistry of the liquid and gas phases. We define a chemical species as the largest 3D chain of connected atoms. In a simulation we usually have a mix of chemical species with different chemical compositions χ, each species present in different proportions. As for the coordination polyhedra definition (section 3.1.2), every individual chemical species i is characterized by its atomic composition, in terms of atomic indexes (from 0 to 207), and by the time t (or snapshot number) when it appears (i.e. when the atoms that made the species are in the 1st coordination sphere of their neighbor(s)). We call "chemical species ID" the list of these atomic indexes. Likewise, we define the chemical species index i as the association {chemical species ID,appearance time}: $i = [A_0, ..., A_x, t]$. The lifetime of this species with chemical composition χ, represented by $L_{\chi,i}$, is the difference between its disappearance time (when at least one atom is no more inside the 1st coordination sphere of any atom of the current species) and its appearance time t.

Examples of chemical species indexes i along with a visual explanation of the rules used to define a chemical species are presented in figure 4.1. Each part of the figure correspond to the following rules and/or implications:

1. Atoms are bonded if they are in the 1st coordination sphere of its neighbors.

2. The periodic boundary conditions are used to link atoms across consecutive cells.

3. Two species made of the same atoms in two consecutive snapshots are the same, no matter the bonds between the different atoms.

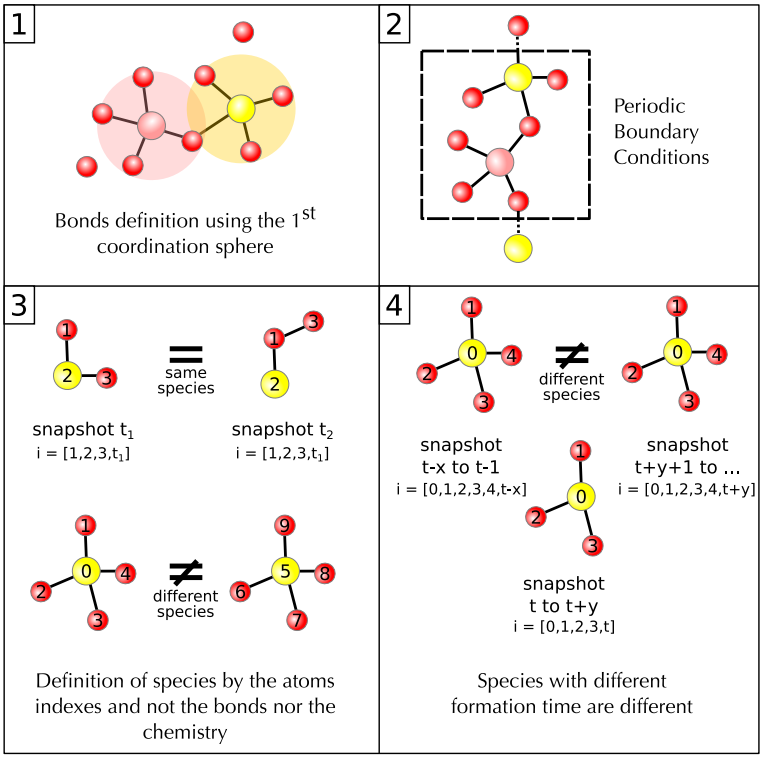

Figure 4.1 – Rules of species definition used in the `speciation_umd.py` script (option `-r 1`). The statements 3 and 4 are implied by the definition of individual species based on the species index i: {chemical species ID,appearance time}: $i = [A_0, ..., A_x, t]$. Species with different indexes i are different.

Two species of the same chemical composition but not atomic composition are different.

4. A species broken at a time t and reforming with the same atoms as before is not the same anymore because of a different appearance time.

As said in section 3.2, we do not think there are bonds between the cations, then we consider only the 1st coordination spheres of T-O and M-O pairs (M=Na,K,Ca;T=Al,Si) for the definition and search of chemical species. For temperatures equal to and above 4000 K, we replace the 1st coordination sphere of O-O (two oxygens sharing the same polyhedra edge) by the first coordination sphere of O_2 (the small additional peak on $g_{O-O}(r)$).

In a given simulation, we compute the total lifetime of a species with chemical composition χ, represented by L_χ, as:

$$L_\chi = \sum_i L_{\chi,i} \tag{4.1}$$

Then, the proportion of a given chemical composition X, represented by R_X is:

$$R_X = \frac{L_X}{\sum_\chi L_\chi} \tag{4.2}$$

Likewise, we compute the total lifetime of a chemical element *elem* as:

$$L_{elem} = \sum_{\chi} \sum_{i} L_{\chi,i} \times N_{\chi,elem} \tag{4.3}$$

with $N_{\chi,elem}$ the number of atoms of this element type *elem* in the chemical composition χ (for example there is 1 Si in SiO_2). Then, the proportion of a given element A is:

$$R_A = \frac{L_A}{\sum_{elem} L_{elem}} \tag{4.4}$$

In the whole system, this proportion is simply equal to $\frac{N_A}{N_{tot}}$, with N_A the number of atoms of this element type A and N_{tot} the total number of atoms. For feldspars we have: R_{Na}=R_K=R_{Ca}=$\frac{16}{208}$=$\frac{1}{13}$=7.7 %, R_O=$\frac{128}{208}$=$\frac{8}{13}$=61.5 %, R_{Si}=R_{Al}=$\frac{32}{208}$=$\frac{2}{13}$=15.4 % in $CaAl_2Si_2O_8$ and R_{Si}=3R_{Al}=$\frac{48}{208}$=$\frac{3}{13}$=23.1 % in $NaAlSi_3O_8$ and $KAlSi_3O_8$.

When we compute these proportions (R_X and R_A), if we only use the lifetimes $L_{\chi,i}$ of species in a given phase, for example in the gaz phase, instead of inside the whole system, then we obtain the proportions in this phase. If the elemental proportions R_A are the same in gaz phase than in the whole system for every elements, then the vaporization is congruent.

4.1.2 Computer implementation details

We use the option `-r 1` of the `speciation_umd.py` script from the UMD package. As for the coordination polyhedra analysis, for a given simulation we record all the species in each snapshot of the simulation (option `-s 1`). We search for species made of any atoms in the simulation (option `-a` or `-c` followed by the complete list of elements in the system). Nevertheless, we only allow bonds between the cations and oxygens or between two oxygens: the *.bonds.inp* file has the values of the 1st coordination sphere for only M-O, T-O and O-O pairs. For the simulations which display the small O_2 peak, we use a linear fit to smooth the xmin values. For each isotherm equal to or above 4000 K, we use the xmin value of the highest density simulation with a visible O_2 peak as the xmin value for higher densities simulations.

The process of the script can be summarized by the figure 4.2, while the actual computing process is summarized in the algorithm 3 in annex. The computational method used to find the individual species in the simulation is based on the mathematics graph theory. Mathematically we construct a finite simple graph, which means we use a finite set of vertices - atoms - and edges - bonds and do not allow self-loop nor multiple edges. In practice we use a recursive loop and the boolean bond presence matrix (a matrix with 0 and 1 inside to indicate whether or not atoms are bonded) as follow. At each snapshot, we first create the bond matrix and add all the isolated atoms to

the cluster list (a list of every species ID at this snapshot). These isolated atoms form the monoatomic gas of this snapshot. Then we enter the recursive search of all the atoms that are linked together. To do this, each time we use a bond in the bond matrix to create the list of linked atoms in the same species, we remove this bond from the bond matrix. We have the complete species ID once every atom that constitute it are link to nothing in the boolean bond matrix. This recursive step is indicated * on the figure 4.2 and corresponds to the function `Neighboring` of the algorithm 3. When the boolean bond presence matrix is filled with zeros it means we found all the species in the snapshot.

4.1.3 Visualization

The visualization of atomic movements during the course of the simulation is the first analysis step. We use the Visual Molecular Dynamics (VMD) software (Humphrey *et al.*, 1996) and two representation methods that are implemented in it. The atoms are represented by spheres using the CPK representation: the radii of the spheres are the scaled-down Van der Waals radii. The bonds are represented by the DynamicBonds method: a bond is drawn if the atoms are within a distance cutoff of eachother.

Following the discussion about bond lengths in section 3.2, we would like to take the 1st coordination sphere as distance cutoff for Si-O and Al-O bonds representation (located around 2.5–2.9 Å, see figure 3.4). Unfortunately the VMD selection panel for representations does not allow the selection of bonds instead of atoms. Then when using a value of about 2.7 Å for Si-O and Al-O bonds representation, the software also uses this value for O-O bonds representation. Since the maximum of the first $g_{O-O}(r)$ peak is located around 2.7–2.8 Å (see figure A.4), a lot of bonds between two oxygens sharing the same polyhedra edge are represented and overload the figure. That is why, for more clarity, we use the xmax as cutoff distance for bonds representation.

For bubble representation, we display the electronic density isosurface at $0.01\,\mathrm{e/\AA^3}$. This value, although arbitrary, provides a good representation of the bubble shape. The electronic density is computed on the selected snapshots using the INCAR file available in annex A.1.2. VASP® produces three charge density files named AECCAR0, AECCAR1 and AECCAR2. To obtain the correct total electronic charge density we use the script `chgsum.pl` from the VASP Transition State Tools (VTST) package (Jónsson group and Henkelman group) to sum the AECCAR0 and AECCAR2 which contained respectively the core and valence electronic density.

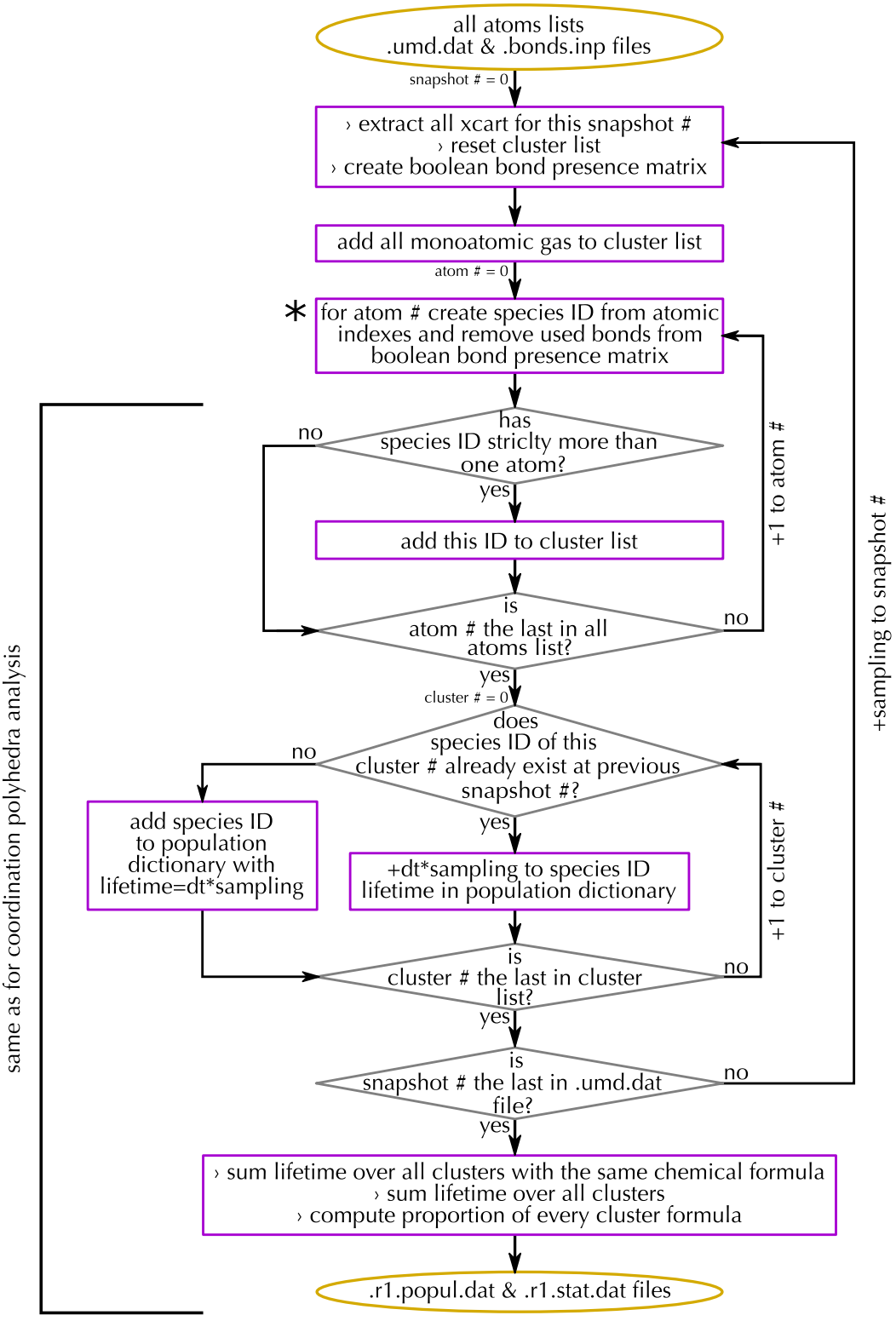

Figure 4.2 – Simplified flowchart of the speciation analysis from the `speciation_umd.py` script (option `-r 1`). dt is the timestep used in the simulations, while "sampling" is the sampling frequency value we indicate in the option `-s`. Here we choose 1 to sample every step. * corresponds to the recursive function `Neighboring` of the algorithm 3. accronyms and definitions: xcart = cartesian coordinates; boolean bond presence matrix = matrix of N atoms side filled with 0 (no bonds) and 1 (bonds between the atoms); species ID = string of atomic indexes present in the chemical species;

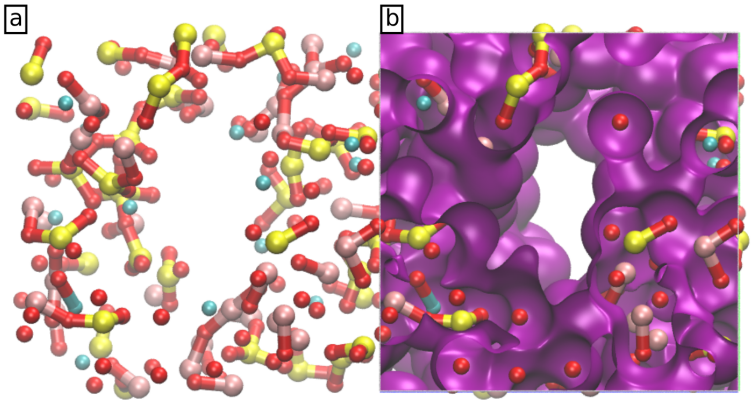

Figure 4.3 – Snapshot of $CaAl_2Si_2O_8$ at 4000 K and 1.81 g cm^{-3} (cell size of 16 Å) with (b) addition of iso-electronic density surface at 0.01 e/Å^3. Colors indicate different elements: cyan - Ca, pink - Al, yellow - Si, red - O.

4.2 Qualitative analysis

As said in chapter 3, feldspar are tectosilicates. At normal to high density, the largest chemical species found in the simulations involve forming chains and rings of alternating cations and oxygens, in ... - oxygen - cation - oxygen - cation - oxygen - ... sequences. At high density all 208 atoms are connected in one infinite cluster which constitutes the liquid.

At low densities and below the critical temperature[1], long lasting cavities appear in the structure, where isolated atoms or clusters of atoms may freely float inside. As said before, we display the electronic density isosurface at 0.01 e/Å^3 in order to differentiate interatomic voids from larger cavities. Figure 4.3 shows a typical snapshot of the first visible cavities. We see all the interconnected atoms surrounding an ellipsoidal cavity large enough to be seen with the iso-electronic density surface drawn. Due to the small size of the cell and of the periodic boundary conditions this cavity appear as an infinite cylinder. These cavities evolve with time. For example, figure 4.4 shows the evolution of the cavity, from a cylinder shape to slab-like along two different axis, and even its disappearance. They also evolve with density. On average we see more cavities with a sphere or cylinder shape for densities close to the ambient one, and more slab-like shapes for the lowest densities reached here. This behavior was also observed and well described by Binder *et al.* (2012) for their study of the phase coexistence region using Monte Carlo simulations (figure 3). Nevertheless, here we see an additional type of cavity which appear after the cylinder type (i.e. for $\rho < \rho_{cylinder}$) and before the slab step (i.e. for $\rho > \rho_{slab}$): two perpendicular cylinder cavities. We also notice that the liquid slabs do not display a truly flat surface (figures 4.4 or 4.5) and tend to spontaneously change shape. Xiao and Stixrude (2018) also noted a tendency of their liquid slab to split in two in their *ab initio* MD simulations. While here we let the system evolve freely, they try to prevent this behavior.

[1] see section 6.1.3 for definition of critical temperature

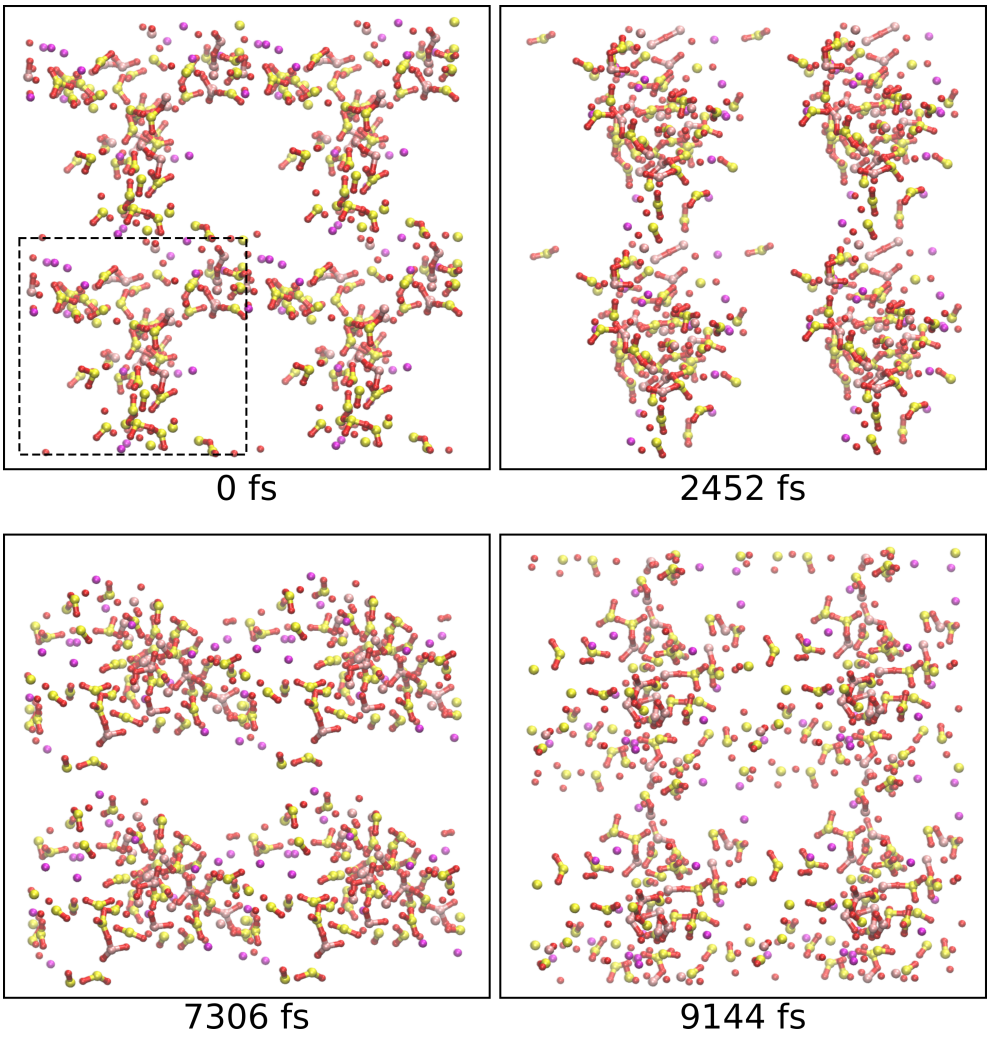

Figure 4.4 – Snapshots of $KAlSi_3O_8$ at 4500 K and 0.61 g cm^{-3} for different times in the simulation. Four simulations cells are represented here using the periodicity, the dashed square indicate the limits of the 23 Å side simulation box. Colors indicate different elements: purple - K, pink - Al, yellow - Si, red - O.

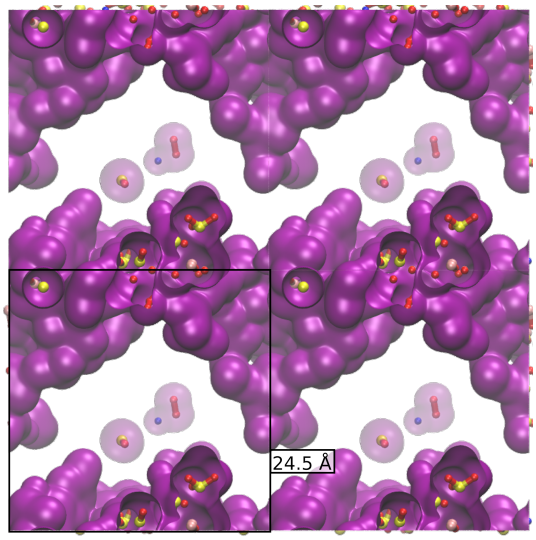

Figure 4.5 – Snapshot of the iso-electronic density surface at 0.01 e/Å^3 in the simulation cell of $NaAlSi_3O_8$ at 4500 K and 0.47 g cm^{-3} (cell size of 24.5 Å). Four simulations cells are represented here. We see a clear bubble with two clusters inside: SiO and NaO_2. Colors indicate different elements: blue - Na, pink - Al, yellow - Si, red - O.

Depending on the simulation, the cavities can be empty (figure 4.3) or have some small clusters floating inside (figures 4.4 or 4.5). We interpret then these cavities as the nucleating gas bubble. Since there are not always clusters inside these cavities we cannot define them as real (macroscopic) bubbles. That is why the free clusters represent only the first volatile species and do not give the complete gas composition. Likewise, we cannot define any partial pressure of the gas nor surface tension. A more realistic gas bubble nucleation would require a much larger number of atoms, something which is not yet possible in *ab initio* MD simulations.

At too high temperature we do not see bubbles anymore since the atoms are too fast to keep a liquid-like structure. We distinguish cavities up to 6000, 6500 and 7500 K for respectively K, Na and Ca-feldspar end-members at densities below $1\,\mathrm{g\,cm^{-3}}$. This qualitative analysis will be useful for the construction of the phase diagram in chapter 6.

4.3 Gas, species... Some warnings

Before we perform any quantitative analysis of the speciation it is mandatory to specify the limits of this study. First, as mentioned in the rule number 3 (section 4.1.1), the species are defined by the atoms, not by the bonds. In this case, we can end up with a SiO_4 as in figure A.15, which is basically an O_2 molecule too close to a SiO_2 molecule. A maybe more accurate speciation analysis should define a species by the bonds. This way it would be possible to follow the lifetime of an O_2 bond, from its formation to its destruction, no matter the additional atoms that may cross its first coordination sphere. One reason why we did not do that is the lack of time to implement this in the `speciation.py` script.

Second, we have to define what is the minimum lifetime of a species. Here, the speciation analysis allows to find all the species with a lifetime as small as the timestep of the simulation, which is about 1 fs. This implies, for example, that a species can exist only for the time an atom B needs to: 1) enter the first coordination sphere of another atom A, 2) bounce on this atom and 3) leave the coordination sphere. In my opinion, if there is a bond between the two atoms A and B, I expect the atom B to be captured by the atom A attraction forces, and then stay longer in the first coordination sphere of A. This idea is highly dependent on the velocity of atoms (and then of the temperature): the faster atoms move, the stronger the attraction field of A should be to capture B (i.e. the stronger a bond should be to form). In Raman spectroscopy, peaks indicate bond vibrations, then we can assume a bond exist if it lasts at least for one vibrational period. This idea was already used by one of the only other *ab initio* MD volatilization study (Xiao and Stixrude, 2018). Here I only want to remove the species that exist only because of the "bouncing" mechanism describe above. Then I want to use a minimum

lifetime criterion as small as possible. In Raman spectra acquired at room temperature, the fastest vibrations in feldspars are located between 900 and 1200 cm^{-1} and involve stretching of Si-O bonds. Using the vibrational theory we can link the Raman shift $\Delta\overline{\nu}$ to the vibration frequency ν:

$$\begin{aligned} E_{\text{vib.}} &= E_{\text{laser}} - E_{\text{emitted}} \\ \Leftrightarrow h\nu &= h\frac{c}{\lambda_{\text{laser}}} - h\frac{c}{\lambda_{\text{emitted}}} \\ \Leftrightarrow \nu &= c\Delta\overline{\nu} \end{aligned} \tag{4.5}$$

Applied to feldspars, we get a vibration period $\frac{1}{\nu}$ of about 30 fs. Then for a first approximation, in the chemical proportion analysis section 4.4.2 we will not count species that live less than 30 fs. I admit that this criterion is arbitrary and has limits, for example the influence of temperature on the vibration period. Nevertheless it is the only reasonable one I can think about.

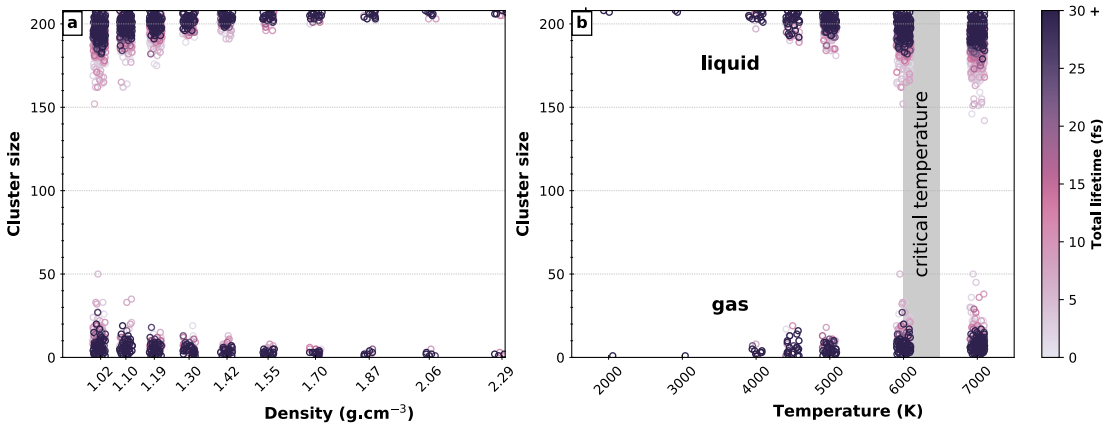

Figure 4.6 – Size distribution of all individual clusters of atoms in $NaAlSi_3O_8$ fluids as a function of (a) density at 6000 K or (b) temperature at 1.02 g cm^{-3}. Each point represents an individual cluster of the corresponding size (y axis). Color scale indicates the lifetime of each cluster. Clusters in the gas with size larger than 13 atoms have lifetimes shorter than 30 fs. In every simulations there is a stable liquid part: big clusters (>200 atoms) living more than 30 fs.

Third, we have to define what is the so-called "gas phase". For each feldspar endmember the distribution of the size of the atomic clusters is bimodal: the large polymerized melt that surrounds the cavities and the small atomic clusters that populate these cavities. It is represented as a function of density for 6000 K (close to the critical temperature) on figure 4.6 (a) and as a function of temperature for 1 g cm^{-1} (below the liquid-gas boundary density) on figure 4.6 (b). We notice there is an upper limit in the size of the small clusters that live more than one vibration period: they are usually made of less than about 10 atoms below the critical temperature. In the speciation analysis, all small clusters, for example with less than 100 atoms in their formula, are considered

to be gas species, while all big clusters, with more than 100 atoms in their formula, form the liquid part. This criterion has a sense only below the critical temperature, in the liquid-gas dome. Above the critical temperature we should see a continuous distribution of cluster sizes. Here we still have a bimodal distribution, maybe due to the large density fluctuations that occur around the critical temperature. We should also keep in mind that due to size limitation of our simulations, the lists of volatile species we will show in the following do not represent the real composition of the gas phase at the same conditions. Nevertheless they give an overview of the composition and highlight the first volatile species.

4.4 Quantitative analysis

4.4.1 Lifetime of species

Figures 4.7, 4.8 and 4.9 show the lifetime of each individual volatile species with less than 8 atoms in their composition in the Ca-, Na- and K-feldspar fluids at very low density ($1\,\mathrm{g\,cm^{-3}}$) and two reference temperatures: 4000 K and 6000 K. The same figures for the species with 9 to 13 atoms in their formula are available in annex, figures A.16, A.17 and A.18.

Each bar of these bar plot represent an individual chemical specie. The height of the bar is the associated lifetime of the species. We represented here all the individual species, including those living less than a vibrational period (30 fs). We see that the lifetime distributions are all very skewed toward short lifetimes, showing the importance of a minimum lifetime for a quantitative analysis.

At 4000 K, during the entire simulations (about 15 ps), most of the species appear less than 10 times. Nevertheless their individual apparition time is usually about 100 fs and can be almost in the order of 500 fs for some species, for example SiO and SiO_2. The two alkali feldspars show more species than $CaAl_2Si_2O_8$. They also show al lot of free Na and K, whereas Ca appear only in three individual species of $CaSiO_3$.

At 6000 K, there are almost no cavities in the alkali feldspar, so we cannot really talk about a gas phase. The speciation becomes more diverse, with many more clusters being composed of 4 to 13 atoms. But at a larger scale the melt is homogenous, as these clusters have short lifetimes and very few occurrences. The major volatile species, as SiO, SiO_2, O_2 and the free Na and K, have long lifetimes in the three feldspar end-members. Free Ca appeared only once and Ca-bearing species are still rare. We can also note some free Al in the two alkali feldspars.

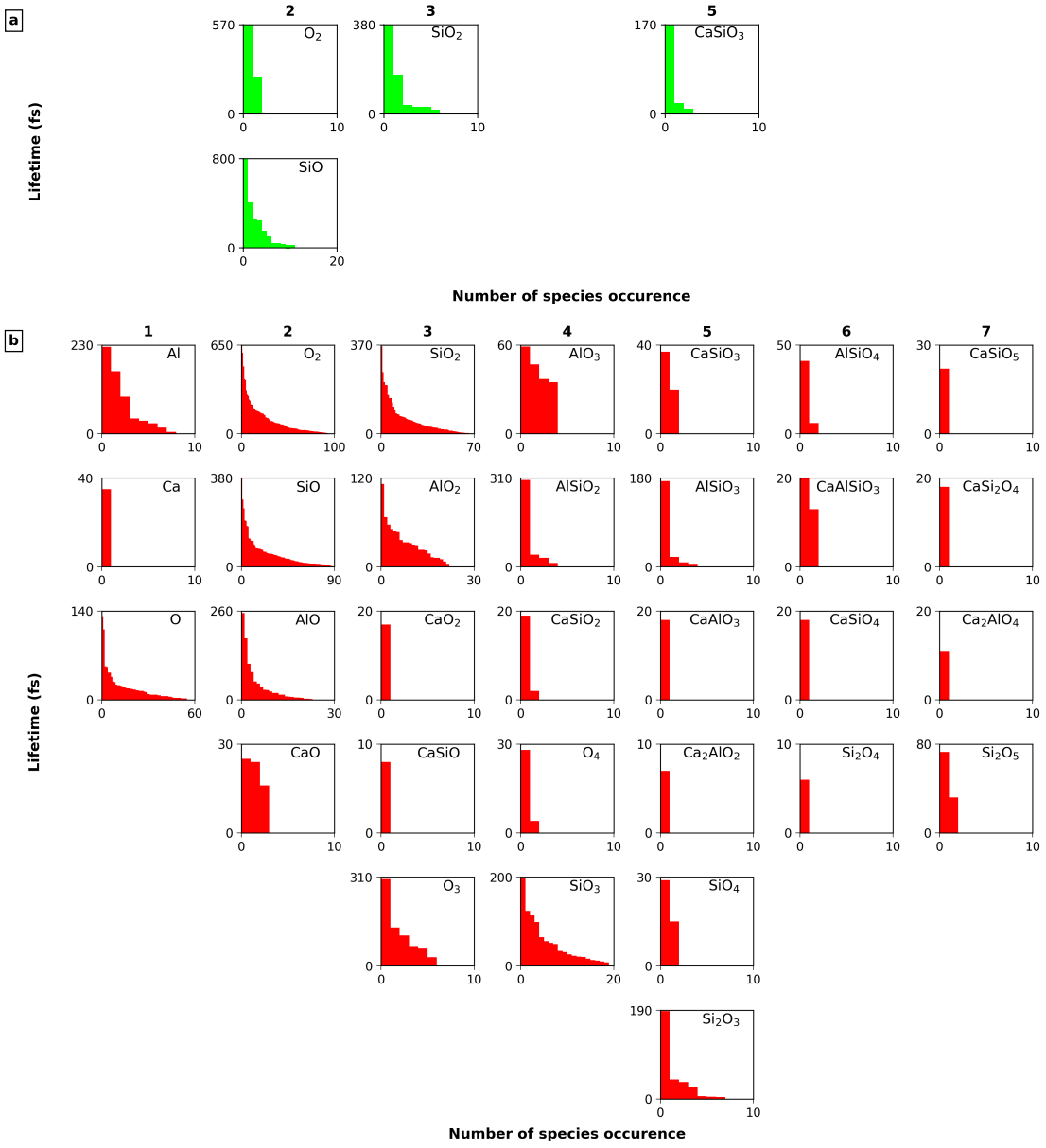

Figure 4.7 – Lifetime of each individual volatile species with less than 8 atoms in $CaAl_2Si_2O_8$ fluids at 1.1 g cm^{-3} and (a) 4000 K, (b) 6000 K. The species with 8 to 13 atoms in their formula are available in annex, figure A.16.

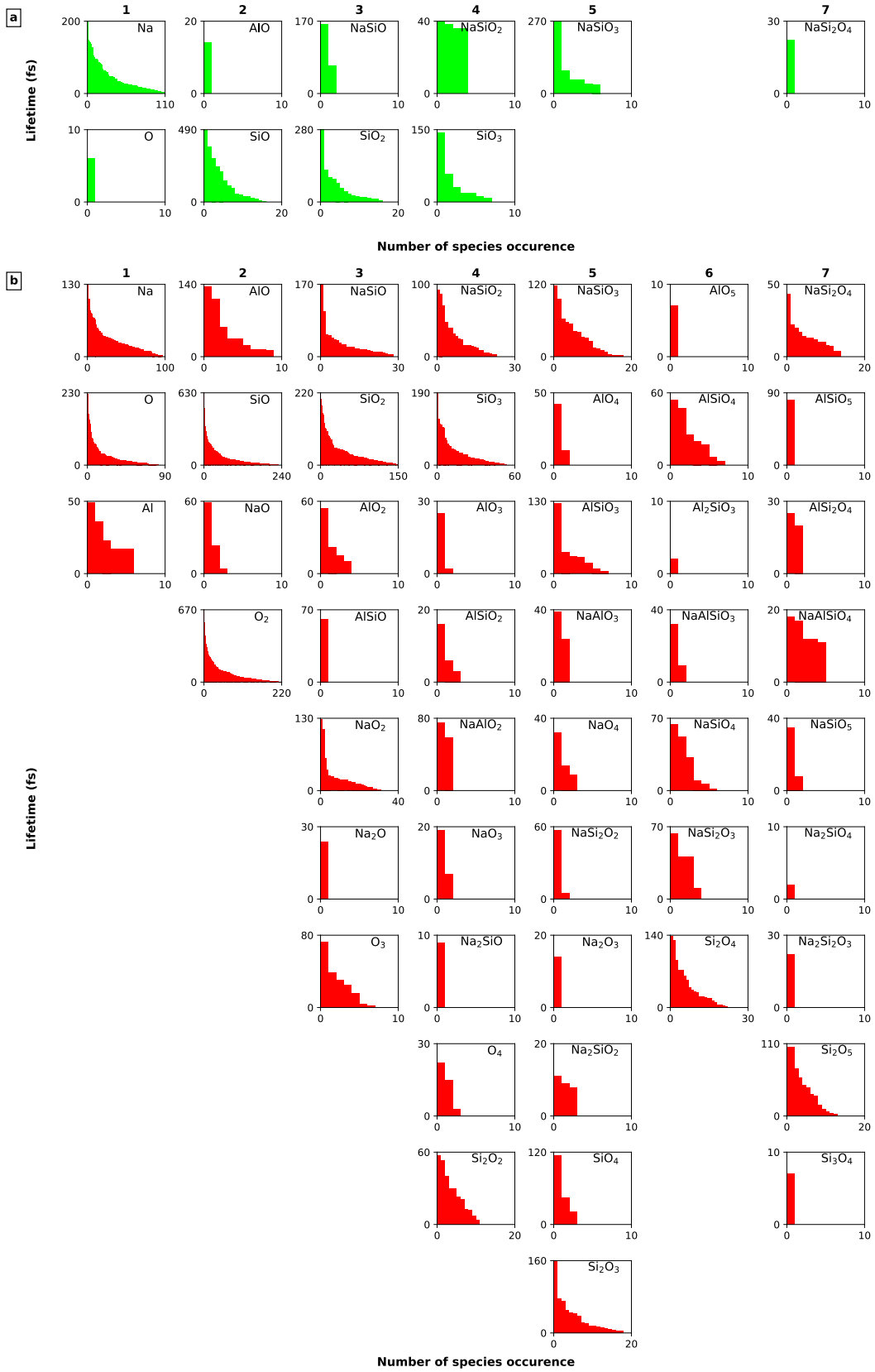

Figure 4.8 – Lifetime of each individual volatile species with less than 8 atoms in $NaAlSi_3O_8$ fluids at 1.1 g cm^{-3} and (a) 4000 K, (b) 6000 K. The species with 8 to 13 atoms in their formula are available in annex, figure A.17.

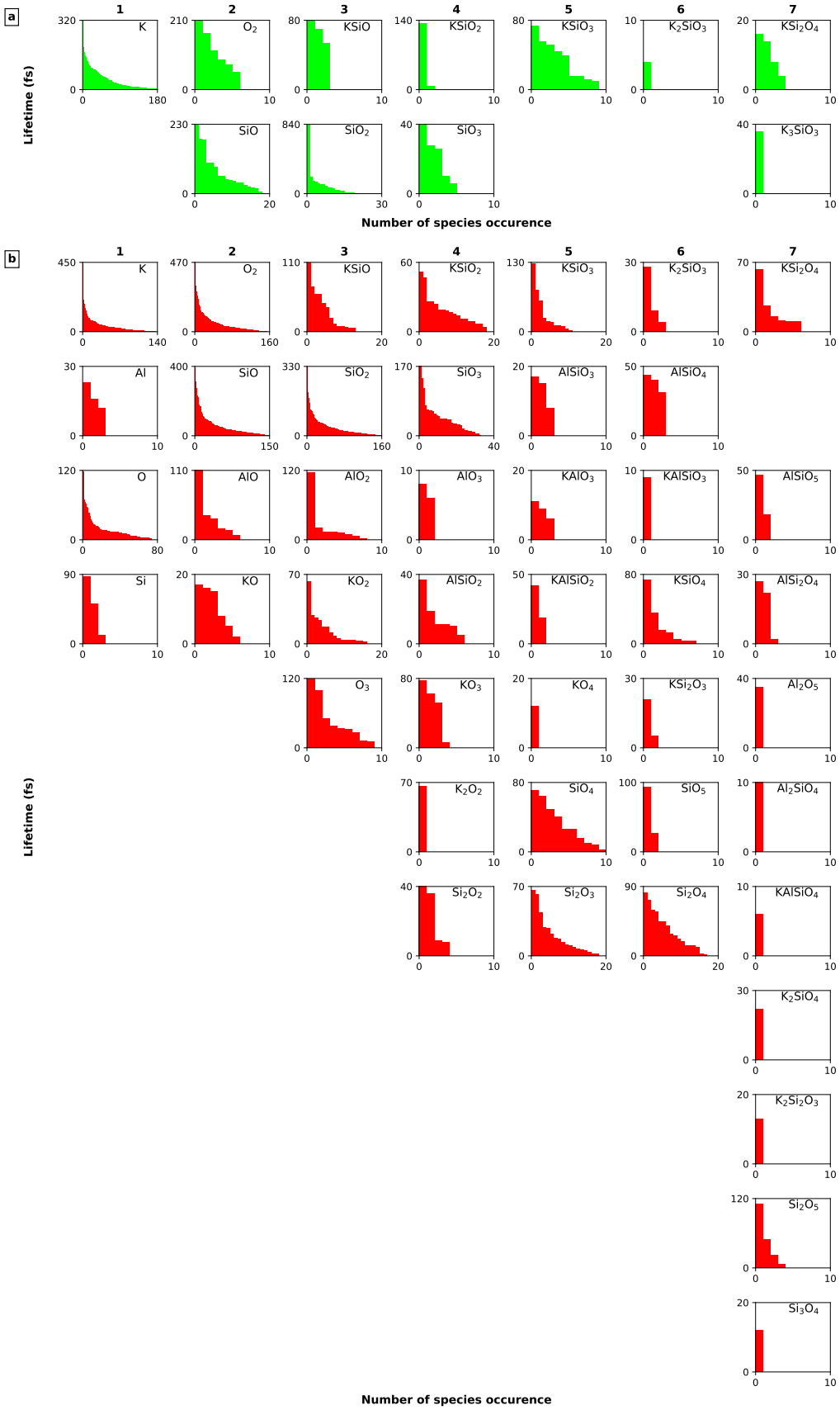

Figure 4.9 – Lifetime of each individual volatile species with less than 8 atoms in $KAlSi_3O_8$ fluids at 1.1 g cm^{-3} and (a) 4000 K, (b) 6000 K. The species with 8 to 13 atoms in their formula are available in annex, figure A.18.

4.4.2 Proportions in the gas phase

As said in section 4.1.1, for each simulation we compute two different proportions: the chemical (or species) proportion (equation 4.2) and the elemental proportion (equation 4.4). As explained before, we use only the individual species which live more than 30 fs in the calculation of these proportions. In section 4.3 we defined the gas phase as all the chemical species which are made of less than 13 atoms. Then, we use only these small species in the calculation of the proportions. In this way, the chemical and elemental proportions, presented in figures 4.10 and 4.11 respectively, represent the chemical and elemental proportion in the gas phase only.

At 4000 K, a limited number of species appear in the gas bubbles. The gas is dominated by free Na and K cations making up for at least half of the gas in alkali feldspar. Second in importance are small volatile species, like O_2, SiO, and SiO_2. In $CaAl_2Si_2O_8$ there is almost no volatilization of Ca, making SiO the major volatile species. Figure 4.11 shows that in every feldspars Al is (almost) not present, which makes the volatilization of feldspars incongruent (see section 4.1.1 for the elemental proportions).

At 6000 K there are fewer isolated Na and K but more free O atoms. The proportion in O_2 is higher than at 4000 K whereas other small species, as SiO and SiO_2, are a bit less abundant. The composition of the "gas" phase is closer to a congruent composition, with for instance the volatilization of Al-bearing species. The proportion of Al among species of less than 100 atoms is now about 1 %.

Figures 4.10 and 4.11 show that Ca and Al-bearing species are much less volatile than other species. This observation is consistent with the composition of the Moon crust: anorthite ($CaAl_2Si_2O_8$) is the major feldspar in the Moon crust and there is almost no sign of albite ($NaAlSi_3O_8$).

Visscher and Fegley Jr. (2013) used the MAGMA code to calculate the composition of the silicate gas phase in the protolunar disk. They explored temperatures from 1800 to 6000 K and included 32 gas species (mono to triatomic species) made of the elements Si, Mg, Fe, Al, Ca, Na, K, Ti, Zn and O. The saturated silicate vapor they obtained is dominated by SiO, O_2 and O at temperatures above 3000 K, whereas it is dominated by more volatile species as Na at lower temperatures. We observe the same phenomenon but in our case it is at higher temperature: between 4000 and 6000 K (figure 4.10). Likewise, they observe the volatilization of refractory elements, such as Al or Ca, when the temperature increase above 3000 or 4000 K.

The mole fraction abundance of O_2 obtained by Visscher and Fegley Jr. (2013) is about 20–30 % of the silicate vapor at all temperatures. In our simulations of the three feldpar end-members, O_2 appears only at 4000 K and very low density. When it is present, its proportion is also in the order of 20–30 %. The two previous FPMD, on pure

SiO_2 (Green *et al.*, 2018) and $MgSiO_3$ (Xiao and Stixrude, 2018), also observed free O_2 above 4500–5000 K. These consistent results suggest that there is potential degassing of O_2 from the silicate melt at high temperatures, independently of the composition of the melt. The process seems to start between 4000 and 4500 K for silicates.

The O=O pairs observed in silica (Green *et al.*, 2018) survived for less than one vibrational period according to the authors. For feldspars, O_2 molecules live up to 650 fs. Although they do not spend the entire time in a bubble, they are still free floating species that are not linked to the big cluster representing the melt. Likewise, in $MgSiO_3$, Xiao and Stixrude (2018) see O_2 molecules live up to about 1000 fs. In both cases this is considerably longer than the vibrational period. It is possible that cations other than Al and Si, like Na, K, Ca or Mg, reduce the polymerization of the melt at these conditions and then enhance the formation and survival of O_2 groups.

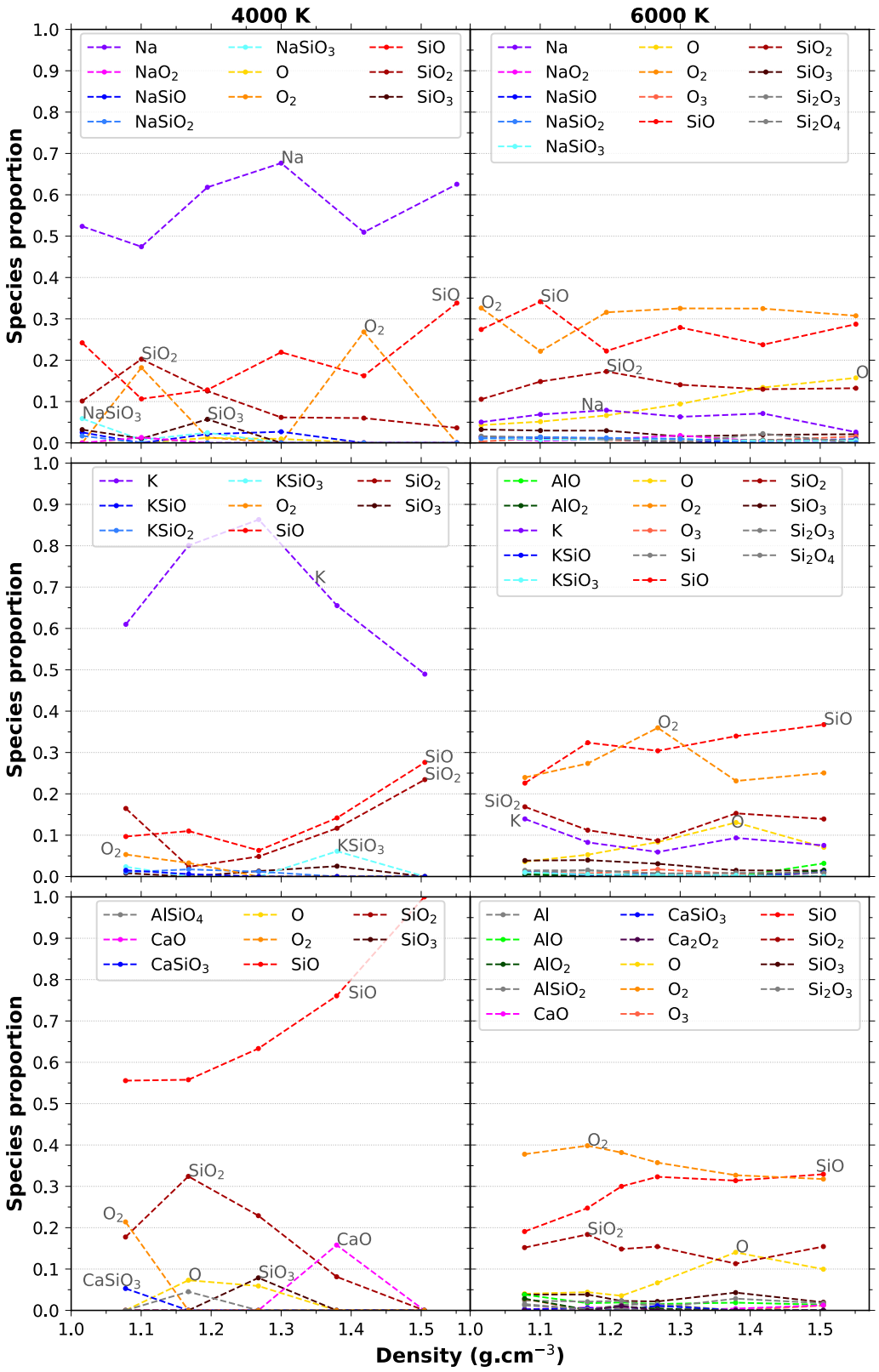

Figure 4.10 – Proportion of chemical species in the "gas" phase (i.e. among all the isolated clusters of length less than 100 atoms) as a function of density at 4000 K and 6000 K for the three feldspar end-members. Species that represent more than 5 % of all the gas species for at least one density point are labeled in the graph. The other species, found in trace amounts are listed in annex A.3.3.

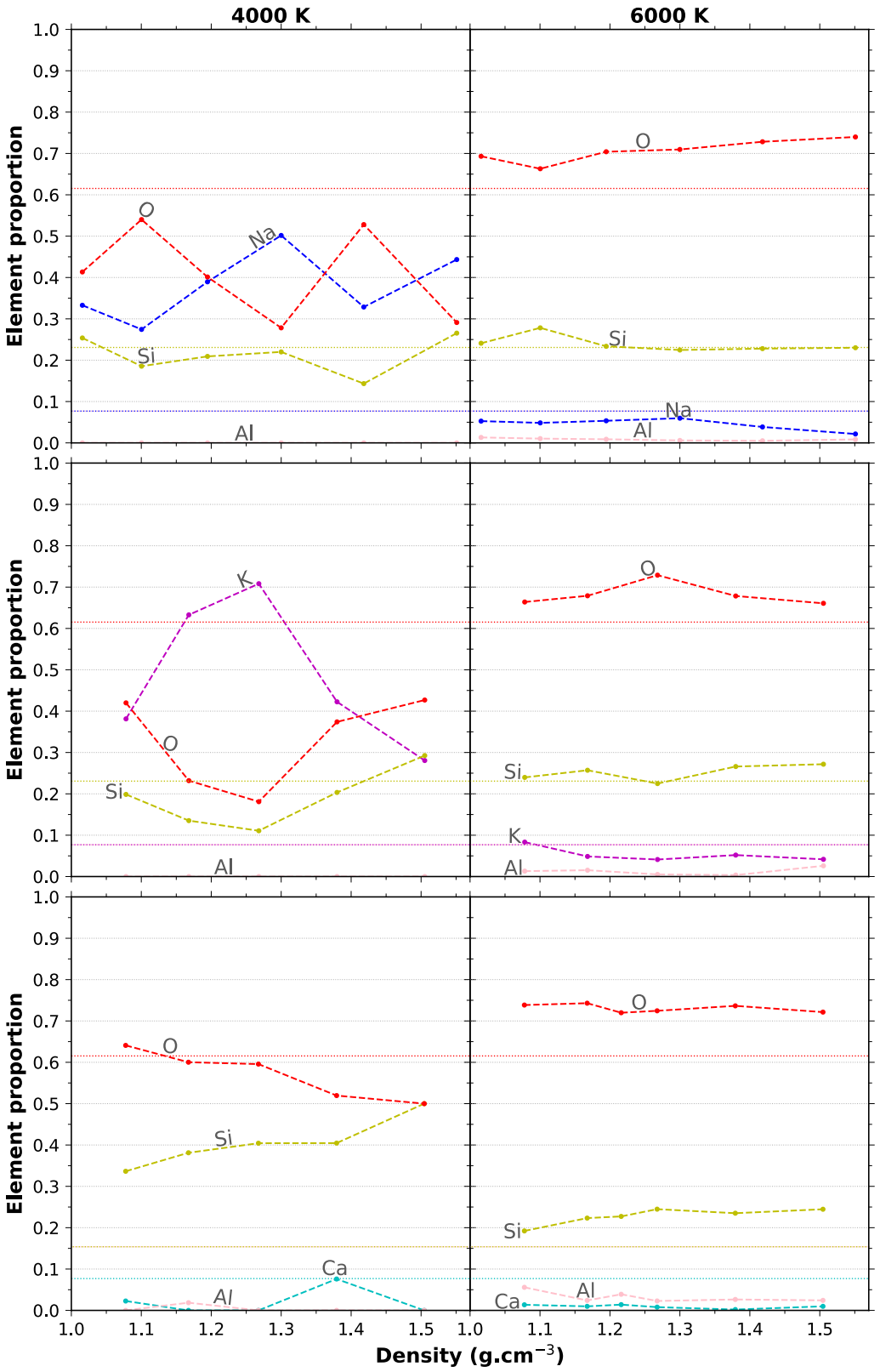

Figure 4.11 – Proportion of each element in the "gas" phase (i.e. among all the species of length less than 100 atoms) as a function of density at 4000 K and 6000 K for each feldspar end-member. Colors indicate the element type: blue - Na, purple - K, cyan - Ca, pink - Al, yellow - Si, red - O. The colored dotted horizontal lines indicate the congruent vaporization proportions: R_{Na}=R_K=R_{Ca}=7.7 %, R_O=61.5 %, R_{Si}=R_{Al}=15.4 % in $CaAl_2Si_2O_8$ and R_{Si}=3R_{Al}=23.1 % in $NaAlSi_3O_8$ and $KAlSi_3O_8$.

CHAPTER 5

TRANSPORT PROPERTIES

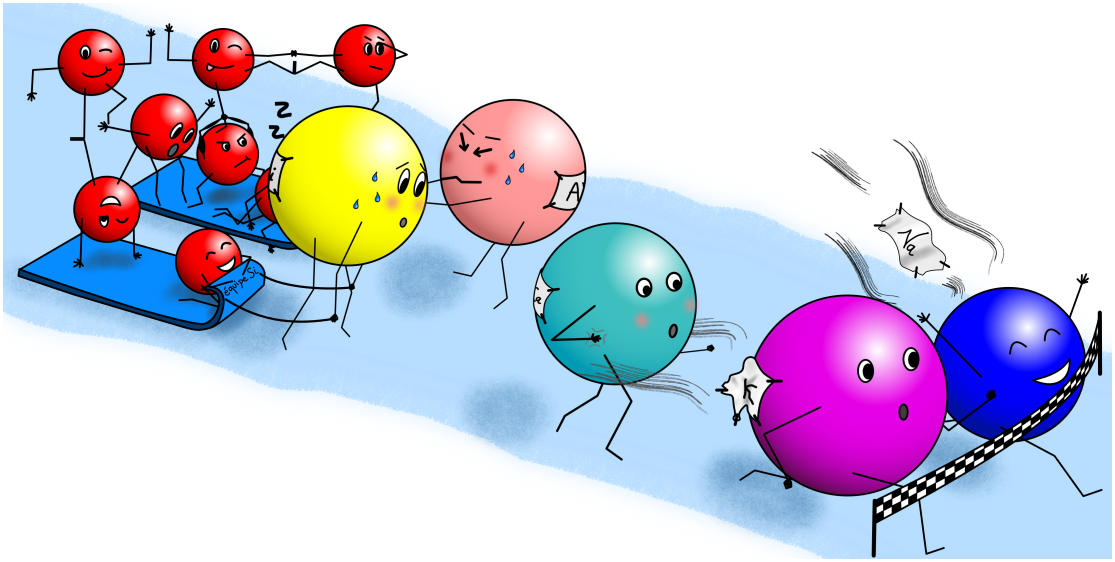

Si les atomes participaient à un marathon, alors Na serait en tête, suivit par K et Ca. Loin derrière, ralenti par tous les atomes d'oxygènes qui leur sont liés, Si et Al peinent à suivre le rythme.

Le déplacement des atomes vu de près

Les atomes et groupements d'atomes constituant la matière sont en permanence en mouvement les uns par rapport aux autres. Dans ce chapitre nous étudions un type de mouvement particulier, les translations, autrement dit le transport des atomes.

Pour analyser ce transport on utilise le "déplacement carré moyen" des atomes en fonction du laps de temps écoulé. Pour chaque atome dans notre simulation on sait ainsi quelle distance moyenne (au carré) il a parcouru en un certain temps donné (figure 5.1). Dans un fluide (liquide ou gaz), plus le temps attendu est long et plus les atomes s'éloignent de leur position de départ (courbe croissante), alors que dans un solide ils restent en moyenne autour de leur position d'équilibre (courbe presque horizontale). Si en moyenne les atomes de silicium (Si) ont eu le temps de se déplacer de leur position d'équilibre à une autre voisine (3 Å plus loin) alors on considère la simulation suffisamment longue pour représenter un fluide. C'est le cas de presque toutes nos simulations au delà de 3000 K. On remarque que les atomes voyagent plus loin lorsque (1) le fluide est moins dense, (2) la température est plus élevée et (3) les atomes sont isolés ou composent de petites molécules. Ce dernier point se voit très bien sur le déplacement carré moyen de chaque atome individuel d'oxygène (figure 5.2). Les atomes d'indice 92, 153 ou 156 (entre autres) se déplacent beaucoup plus loin que les autres. La figure 5.3 montre que ces atomes entrent en général dans la composition de O_2, NaO_2, SiO et SiO_2, de petites molécules formant le gas. Au contraire des atomes se déplaçant peu, comme les numéros 93 ou 160, se trouvent exclusivement dans le liquide, liés à de gros groupements d'atomes. De même, les cations interstitiels (Ca, K, Na) se déplacent en moyenne plus loin que Al, Si ou O car ils sont en général seul à se déplacer, alors que Al, Si et O forment de gros groupements (ils forment la structure des feldspaths).

Pour caractériser efficacement le transport des éléments on utilise le coefficient d'auto-diffusion (en m^2/s) qui se calcule à partir de la pente du déplacement carré moyen. Plus un atome s'éloigne rapidement loin de sa position de départ et plus il aura un coefficient de diffusion élevé. Ainsi il est aisé de comparer les coefficients de diffusion de chaque élément en fonction de la pression et de la température (figure 5.4). Les résultats que l'on obtient ici sont en général cohérents avec ceux obtenus dans d'autres études d'expériences numériques sur les feldspaths ou d'autres minéraux.

Certaines études utilisent les coefficients d'autodiffusion pour calculer la viscosité du minéral fondu, autrement dit la facilité avec laquelle il s'écoule. Par exemple l'eau a une viscosité beaucoup plus faible que le miel. Cependant ces calculs impliquent de réaliser des simulation au moins 100 fois plus longues que ce que nous avons ici. Ce serait bien trop long à réaliser avec la technique utilisée ici, surtout dans le cadre d'une thèse limitée à 3 ans, c'est pourquoi nous ne présentons que les coefficients d'auto-diffusion.

Brief outline In this chapter we present the transport properties using the mean square displacement (MSD) and the self-diffusion coefficients. First, section 5.1 explains the theory, computer codes and parameters used. Then the results and discussions about the MSD and diffusion coefficients are presented in the sections 5.2 and 5.3 respectively.

5.1 Post Processing

5.1.1 Mean square displacement of atoms

The MSD is at the basis of the self-diffusion coefficient calculation. For an atom with index i and vector position $\overrightarrow{r_i}(t) = x_i.\overrightarrow{x} + y_i.\overrightarrow{y} + z_i.\overrightarrow{z}$, it is written as

$$\begin{aligned} MSD(\tau)_i &= \left\langle \left(\overrightarrow{r_i}(t) - \overrightarrow{r_i}(t+\tau)\right)^2 \right\rangle \\ &= \frac{1}{t_{run}/2} \sum_{t=0}^{t_{run}/2} \left(\overrightarrow{r_i}(t) - \overrightarrow{r_i}(t+\tau)\right)^2 \end{aligned} \tag{5.1}$$

with $\langle\ \rangle$ symbolizing the time average and t_{run} the length of the simulation . τ ranges from 0 to $t_{run}/2$. Since the trajectories last at least 16 ps, we obtain mean square displacements of more than 8 ps for each atom. In an orthonormal coordinate system, this equation can be simplified into

$$MSD(\tau)_i = \left\langle \left(x_i(t) - x_i(t+\tau)\right)^2 + \left(y_i(t) - y_i(t+\tau)\right)^2 + \left(z_i(t) - z_i(t+\tau)\right)^2 \right\rangle \tag{5.2}$$

To obtain the MSD of an element type A we only have to average the equation 5.2 over all atoms of the same element type:

$$MSD(\tau)_A = \left\langle \frac{1}{N_A} \sum_{i=1}^{N_A} \left(\overrightarrow{r_{A,i}}(t) - \overrightarrow{r_{A,i}}(t+\tau)\right)^2 \right\rangle \tag{5.3}$$

These two types of MSD are obtained with the scripts from the UMD package `msd_umd_all.py` and `msd_umd.py` respectively. The main options are the "horizontal jump" (`-z`) and the "vertical jump" (`-v`). They correspond to sampling frequencies, the first for the sum over t and the second for the MSD output sampling (i.e. which τ are used). We want these numbers to be not too large, in order to have enough data, but also not too small in order to not make the calculations fast. We choose samplings in the order of 10-20 fs. A quick test using several pairs of sampling frequencies reveals almost identical results in the MSD and self-diffusion coefficient identical to the first three significant figures. Here we used `-z 11` and `-v 13`. Additional information about the choice of these parameters can be found in annex A.3.2.

5.1.2 Self-Diffusion

The MSD curves are usually composed of two distinct parts. The first section of the curve, typical of a few hundred fs, corresponds to the ballistic part of the transport and the second section to the diffusive part. The ballistic part corresponds to the short period of time, right after atoms "bounce" on eachother, when they follow a ballistic trajectory (like billiard balls). The slope of a linear regression over the second section of the curve (diffusive part) is used in the Einstein relation to obtain the self-diffusion coefficient of elements, D_A:

$$D_A = \lim_{\tau \to \infty} \frac{1}{6\tau} MSD(\tau)_A \tag{5.4}$$

We perform linear regressions of the MSD curves without considering the first 500 fs. The error on diffusion coefficients is estimated from the error on the slope of the linear regression.

The self-diffusivities of every element of every simulation is computed with the script `analyze_msd.py`, that gives also the error on the self-diffusion coefficient, the fitted parameters of the linear regression and the coefficient of determination r^2. It also estimate the time for the change of transport regime, from ballistic ($D \propto t^2$) to diffusive ($D \propto t$) regime. It simply fit a 2nd order polynomial ($y = ax^2 + bx$, $b = 0$ by default) to the data between 0 and about 60 fs, a straight line ($y = \alpha x + \beta$) after 500 fs and finds the intersection of these two fitted curves. The time windows for the two fits can be modified with the option `-r`, while the independent option `-s` is used to compute the self-diffusivities with the deletion of the desired number of steps at the beginning of the data.

The self diffusivities can also be computed using the script `vibr_spectrum_umd.py`. It uses the velocities written in the UMD files to compute the velocity-velocity autocorrelation function along with their fast-Fourier transform for each element. From these results the script extract the self-diffusivities of each element as explained in Caracas *et al.* (2020a).

5.2 Mean Square Displacement

The MSD of all elements at every temperature and density is represented for the Na-end-member on figure 5.1. The same figures for the two other end-members are available in annex, figures A.19 and A.20. These log-log representation of the MSD highlight the two transport regime. The first part, from 0 to less than 500 fs, corresponds to the ballistic movement and display a bigger slope than the second part which corresponds to the diffusion movement. We do not see any clear influence of the temperature over the position of the inflection point. At very high density the inflection point, i.e. where

there is a change of slope, is clearly visible around 40-50 fs. As the density decreases the inflection point shifts toward higher times, around 100 fs at about 2.4 g cm^{-3}. It is not possible to estimate with precision the time of ballistic to diffusive regime change at lower densities since the curve smoothen a lot and there is no inflection point visible anymore.

At 5000 K and densities around 1 g cm^{-3} after 8 ps Al travels around 12–15 Å while Si and O travel 15–17 Å, and {Na, K, Ca} travel 25, 22 and 18 Å respectively. At about 2.2 g cm^{-3}, the traveled distances over the same time decrease down to 9 Å for Si, 9–10 Å for Al, 10–11 Å for O, 12 Å for {K, Ca} and 16 Å for Na. At 3000 K and about 1 GPa all atoms travel considerably shorter distances over the same amount of time, on the order of 5–8 and 2–4 Å for {K, Na, Ca} and {Al, Si, O} respectively.

Along the 2000 K and 3000 K isotherms we observe a strong decoupling between the diffusion of {Na,K} and the diffusion of {Si, Al, O} with more than one order of magnitude difference at 1.0 g cm^{-3}. This decoupling is of lesser importance for Ca, meaning it has more difficulties than the two other smaller interstitial cations to travel through the fluid. For densities larger than about 1.7 g cm^{-3} diffusion is very sluggish for Al, Si, and O. Some of the simulations at low temperature may be in the regime of undercooled melt. Spera *et al.* (2009) suggested that in order to be accurate and meaningful, liquid MD simulations must be performed for temperatures above the computer glass transition, estimated around 2800 K for $CaAl_2Si_2O_8$, value that increases when the pressure increases. Other works (e.g. Harvey and Asimow, 2015) suggest that minimum ergodicity is achieved when all atoms in a melt change at least one crystallographic site. For a polymerized silicate melt, this corresponds to a displacement of all Si atoms, the least diffusive species, by at least 3 Å according to the pair distribution function of Si-Si, or a MSD of at least 9 Å^2 within the length of the production run. This value extends beyond the first coordination sphere of Si by Si. This distance can be traveled only by allowing for long simulation times, which is now tractable on the available computational resources. The list of all our simulation not long enough to meet this criteria is indicated in annex A.3.4 and are also indicated on the phase diagrams 6.9 in chapter 6. We took care in chapter 4 to not use them during the interpretation of species proportions. Chapter 6 will show they are long enough to give accurate average values of the pressure, energy and temperature.

The MSD of every feldspar end-member are almost linear with respect to time, with some exceptions for the interstitial cations especially at low density. Unlike Si or Al, they are not strongly linked to O atoms, which is why they move freely inside the melt, from one empty site to another. At low density there is enough space in the structure to allow most of the atoms to move freely outside of the 1st coordination spheres of the atoms constituting the melt.

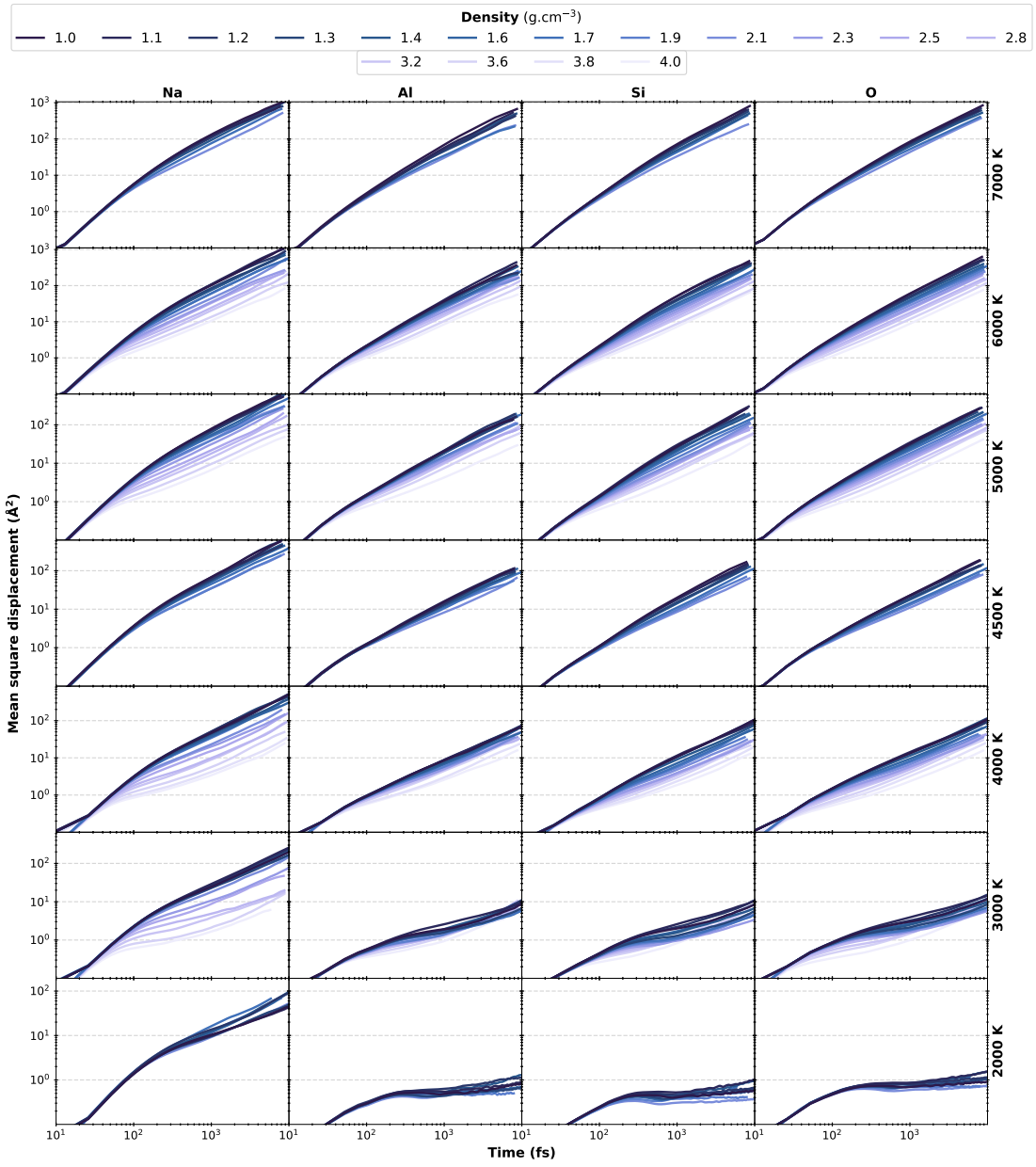

Figure 5.1 – Mean square displacement of Na, Al, Si and O in $NaAlSi_3O_8$ at seven temperatures between 2000 K and 7000 K and up to 15 densities between 1.0 g cm^{-3} and 4.0 g cm^{-3}. The same figure for the two other feldspar end-members are available in annex, figures A.19 and A.20.

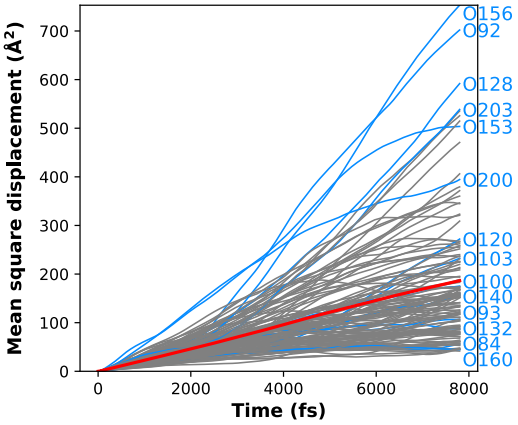

Figure 5.2 – Mean square displacement of every O atom at 4500 K and 1 g cm^{-3} in $NaAlSi_3O_8$. For clarity only some atomic index are indicated in blue. The red line indicate the average MSD of O. Figure 5.3 shows that some very diffusive atoms (e.g. indices 92, 153, 156, 200, 203) are part of the gas phase (they constitute very small species) more often than atoms with a low diffusivity (they are always in the "melt", e.g. indices 132 and 160).

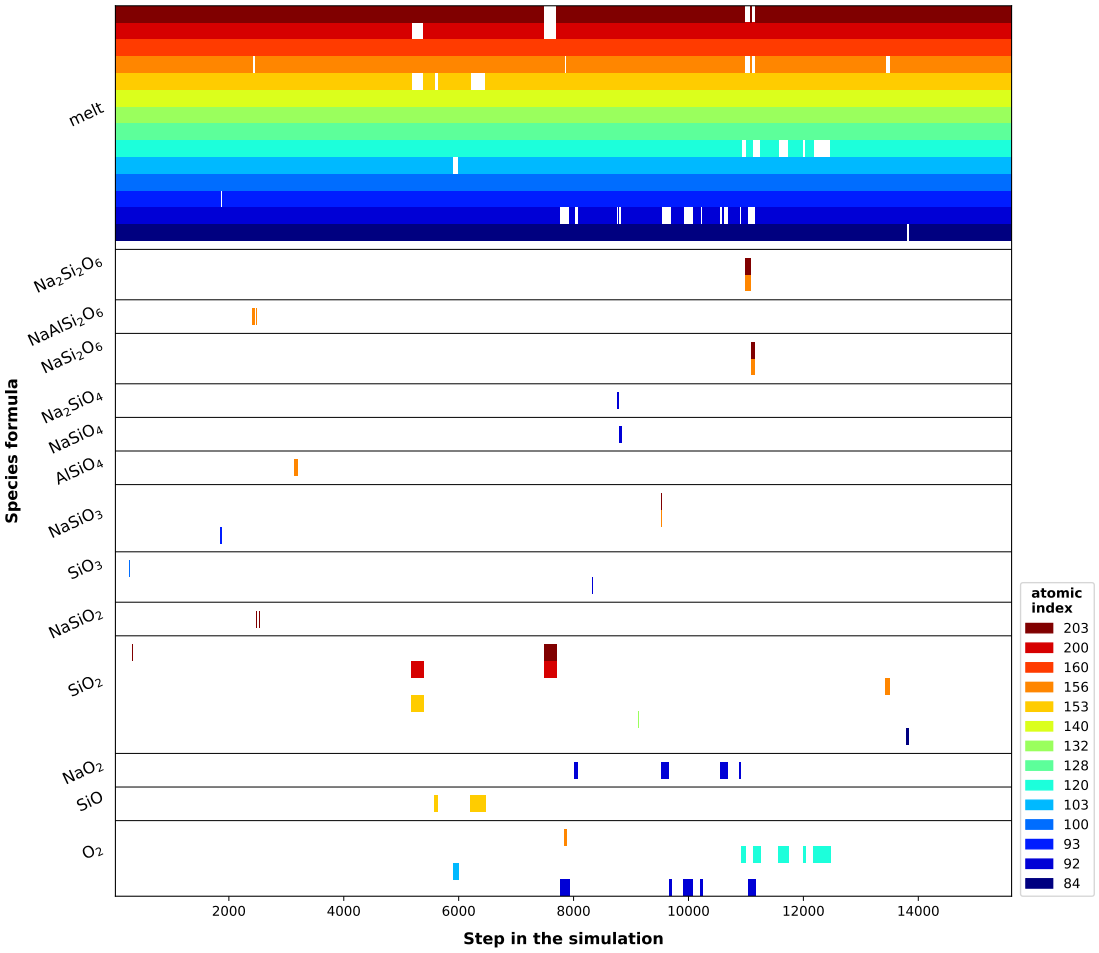

Figure 5.3 – Localization of 14 O atoms in the different chemical species during the course of the simulation of $NaAlSi_3O_8$ at 4500 K and 1 g cm^{-3}. The appearance and existence times of each individual chemical species (which composition is written on the left) are indicated by small vertical bars, color-coded with the index of 14 O atoms (among the 128 in the simulation) that form the species. All the species with more than 13 atoms are grouped under the name "melt". Some very diffusive atoms (figure 5.2) are part of the gas phase more often than some atoms with a very low diffusivity, but there are exceptions: e.g. index 128 is highly diffusive even though it is always located in the "melt" (species with more than 13 atoms).

When we look at the MSD of individual oxygen atoms (figure 5.2) we can distinguish between very diffusive atoms (e.g. indices 92, 128, 153, 156, 200, 203) and all the others with a lower diffusivity. Figure 5.3 shows in which species these atoms are located during the simulation of $NaAlSi_3O_8$ at 4500 K and 1 g cm^{-3}. All the species with more than 13 atoms are grouped under the name "melt". We see for example that atoms n°92 and 120 spend a lot of time as free O_2 or NaO_2 species compared to other atoms. Some very diffusive atoms (e.g. indices 92, 153, 156, 200, 203) are part of the gas phase (they constitute very small species) more often than atoms with a low diffusivity (they are always in the "melt", e.g. indices 132 and 160). There are exceptions to this observation: e.g. index 128 is highly diffusive even though it is always located in the "melt" (species with more than 13 atoms). The high diffusivity of some O atoms in the gas phase only weakly influence the average diffusion of O because most of the atoms are part of the big slow cluster forming the melt. This is a good example of the limit of diffusion coefficient determination in case of systems with two phases.

5.3 Self-Diffusion

As said before, the slope of the MSD yields the self-diffusivity coefficients, which are shown in figure 5.4 for Al, Si, O and the interstitial cations Na, K and Ca as a function of pressure for temperatures between 3000 K and 7000 K. The interstitial cations are always the most diffusive elements at low densities. Ca is less diffusive than Na and K by about half an order of magnitude. The self diffusivities of Al, O and Si are similar along each isotherm, resulting from the polymerized character of the melt. The difference between isotherms is reduced as the temperature increases. At high temperature and low density, the self diffusivity of every element tends toward 1–2 $\times 10^{-7}$ m^2 s^{-1}.

Figure A.22 shows that the self-diffusivities of Al and Si usually show the same trend at each temperature and for each feldspar. Usually Al is slightly more diffusive than Si, especially at 3000 K. Since the method used to obtain these values of self-diffusivities is not very accurate, we cannot say if the variations of the curves are significant or not. Then it seems the Al/Si ratio in the different plagioclase feldspars does not influence the self-diffusivities of Al and Si.

The value for diffusion that we obtain from our simulations are on the same order of magnitude as the values published previously on various other silicate melts. For example D_{Si} at 4000 K and 1 GPa is around 6×10^{-9}–1×10^{-8} m^2 s^{-1} in alkali feldspars and anorthite respectively, compared to about 1.5×10^{-9}–1×10^{-8} m^2 s^{-1} in anorthite using classical and ab-initio MD respectively (de Koker, 2010; Spera *et al.*, 2009), 1×10^{-9} m^2 s^{-1} in silica (Karki *et al.*, 2007), and 8×10^{-9} m^2 s^{-1} in pyrolite (Caracas *et al.*, 2019).

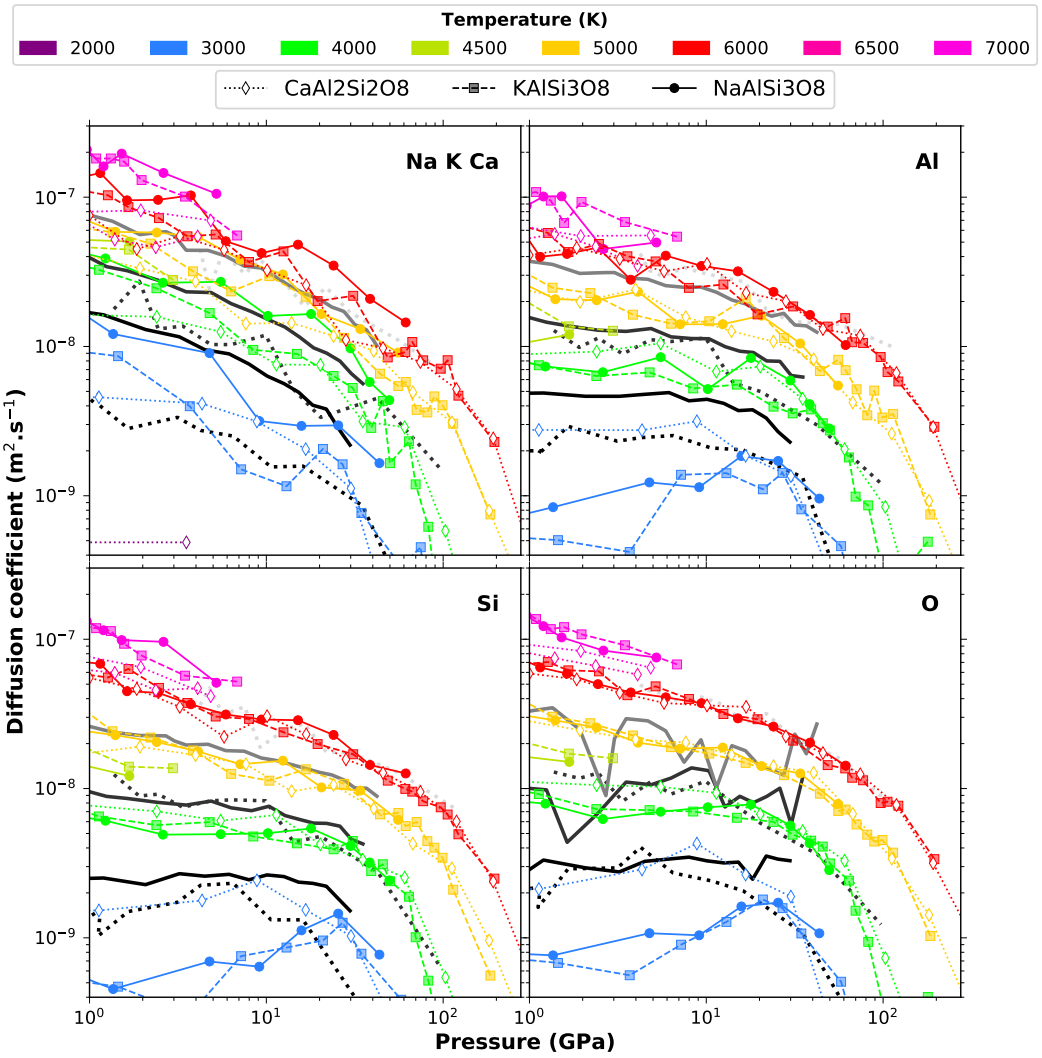

Figure 5.4 – Self-diffusion coefficients for every element as a function of pressure for each feldspar end-member. Colors indicate temperatures. The black to light gray lines are results from de Koker (2010) on $CaAl_2Si_2O_8$ at 3000, 4000 and 6000 K and from Neilson *et al.* (2016) on $NaAlSi_3O_8$ at approximately 3000, 4000 and 5000 K. The same figure as a function of density instead of pressure is presented in annex, figure A.21.

The values of the self diffusivities obtained using vibrational spectrum are in great agreement with those obtained with the MSD (figure 5.5). The largest uncertainty between the two methods is obtained at 3000 K for Al and Si in the two alkali feldspars. This shows that the two methods used to compute the self-diffusivities are correctly implemented and that our simulation may be long enough to give accurate values of the diffusion coefficients. The differences in the diffusion coefficient between the two methods may be due to numerical errors in the calculation of the velocities that are written in the UMD file.

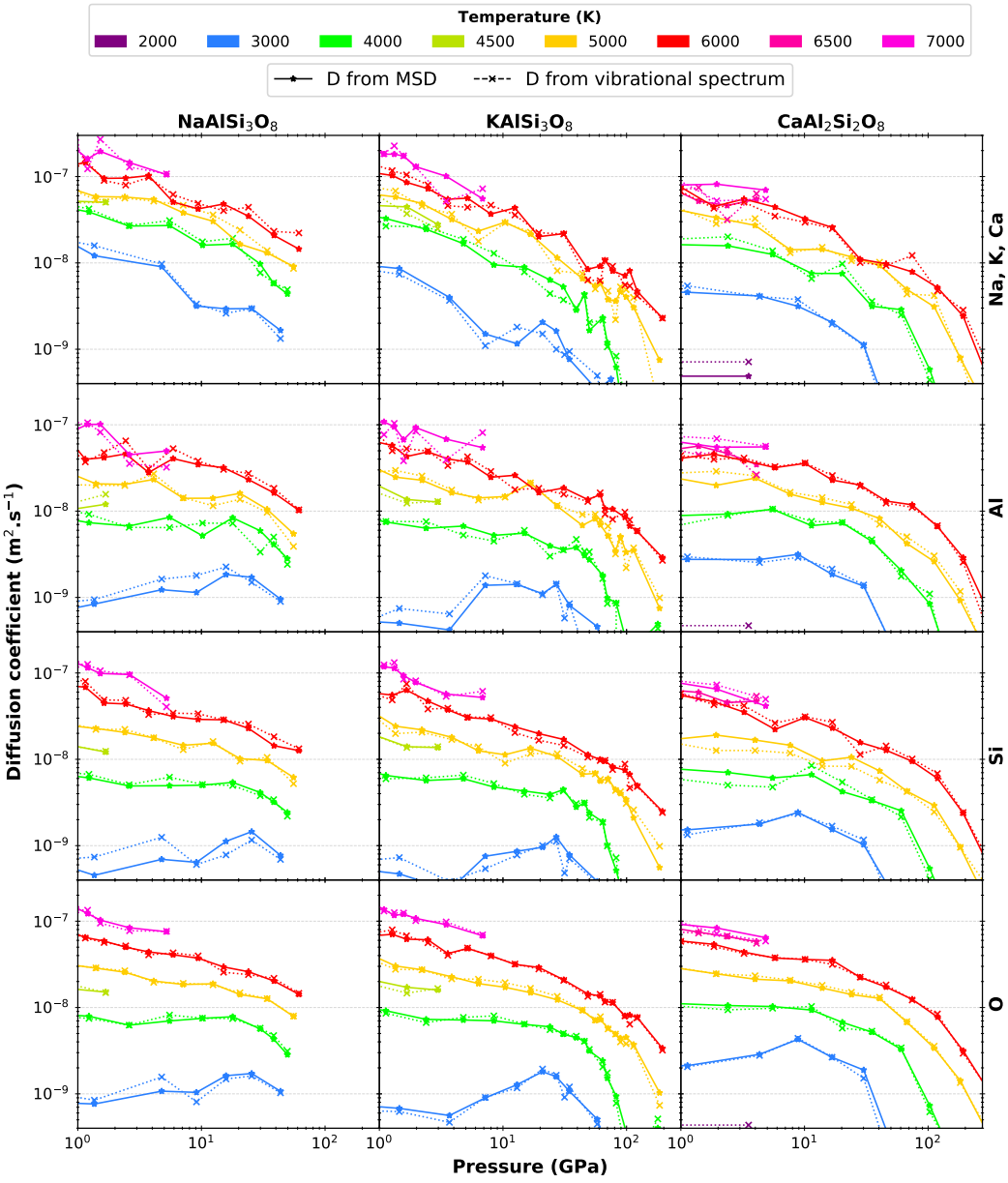

Figure 5.5 – Comparison of the self-diffusion coefficients obtained with two different methods: from the slope of the MSD and from the vibrational spectrum. Colors indicate temperature.

The pressure and temperature dependence of self-diffusivities are usually represented by the Arrhenius equation:

$$D(P,T) = D_0 \exp\left[-\frac{E_A + PV_A}{RT}\right], \tag{5.5}$$

with R the universal gas constant, E_A and V_A the activation energy and volume respectively and D_0 the pre-exponential factor corresponding to the diffusivity in the limit $T \to \infty$.

We have enough data around 1 GPa to perform an Arrhenius fit as a function of temperature. It is displayed on figure 5.6. When this fit is extrapolated to low temperatures (below 2000 K), it yields diffusion coefficients similar to experimental value obtained between 1000 and 2000 K in alkali feldspar melts (Freda and Baker, 1998). The agreement between extrapolated values and experimental results is better for Na than for K. On the contrary, all the experimental measurements of the self-diffusion coefficient summarized by Cherniak (2010) are lower by several orders of magnitude.

Our simulations are performed in the NVT ensemble, which means we have several isotherms and isochores. To perform an Arrhenius fit as a function of temperature at other pressures we need several isobars, which are usually obtained using a NPT ensemble[1]. Then we use an Arrhenius fit as a function of pressure to estimate the self-diffusivities at 25 GPa, 50 GPa and 100 GPa for each element and temperature. For the fits we only use data points between 25 and 150 GPa since they appear to be aligned on a different line than data points below 25 GPa (see figures A.23 and A.24). This analysis is not available for the Na-end-member because the simulations below and above 50 GPa are performed with different sets of pseudopotentials (see section 2.2.2 in chapter 2). At last, an Arrhenius fit as a function of the inverse temperature is performed at 1, 25, 50 and 100 GPa (figures A.25 and A.26). The slope fo the fit gives the activation energies. The values estimated by this mean are indicated in table 5.1. The activation energy at 1 GPa is bigger than those at 25 or in some cases at 50 GPa. The activation energies computed from self diffusivities estimated at 25, 50 and 100 GPa increase with increasing pressure, their values double between 25 and 100 GPa. Every value computed here is always much smaller than values obtained by the previous numerical and experimental studies (e.g Adjaoud *et al.*, 2008; de Koker, 2010; Karki *et al.*, 2011; Spera *et al.*, 2009). It is most probable that the activation energies estimated here are not reliable, given the uncertainty of the Arrhenius fits (see figures A.25 and A.26) and the use of estimated diffusivities from a previous fit to obtain the pressure dependence of the activation energy.

[1]Nevertheless in an NPT ensemble the calculation of the MSD as presented here is not correct anymore.

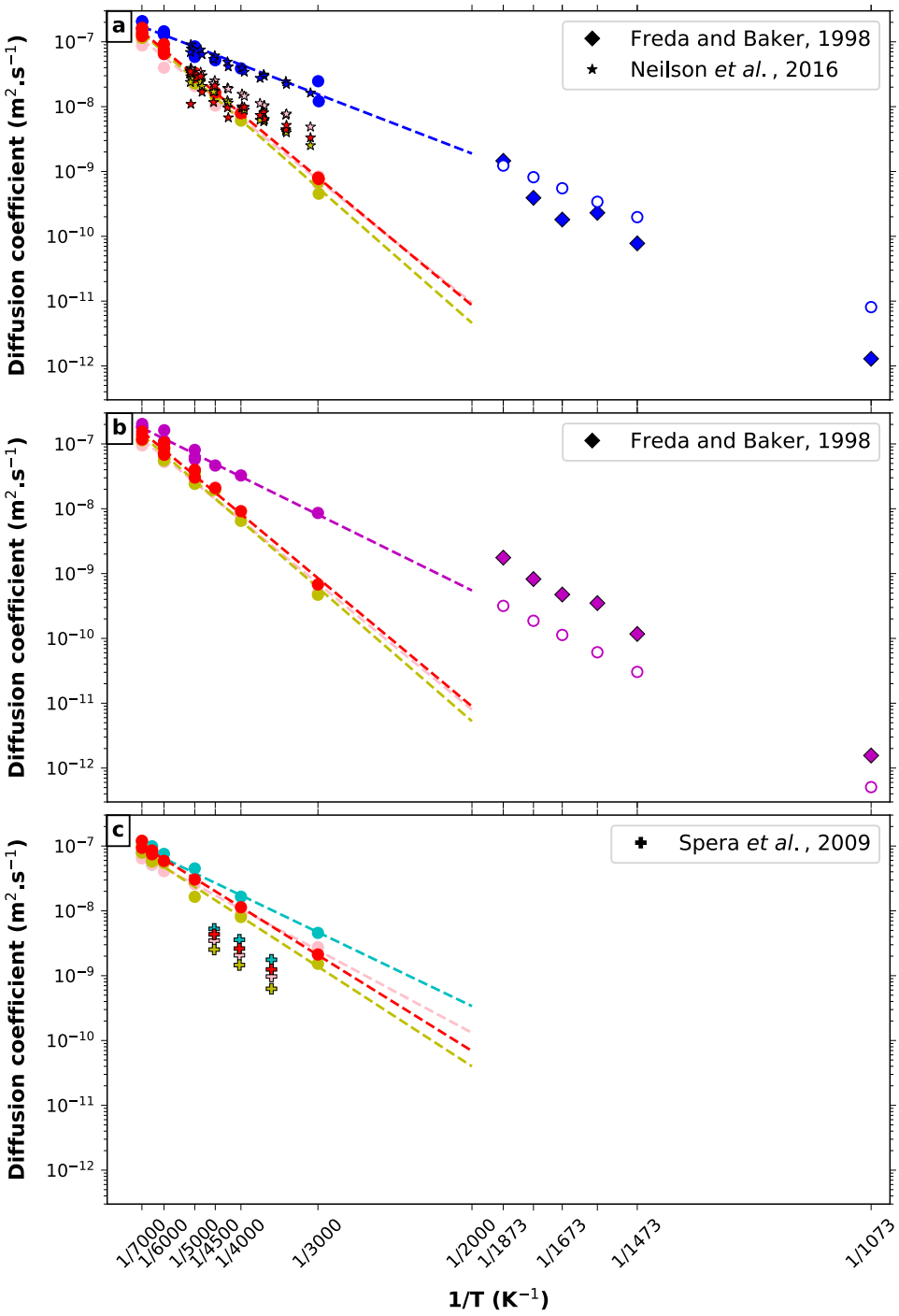

Figure 5.6 – Self diffusion coefficients for (a) Na- (b) K- and (c) Ca-feldspar end-members at 1 GPa as a function of the inverse temperature (filled circles), and fit of the Arrhenius law (dashed lines). Colors indicate elements: red - O, yellow - Si, pink - Al, blue - Na, purple - K, cyan - Ca. The stars and crosses indicate results from classical MD simulations on respectively molten albite (Neilson *et al.*, 2016) and anorthite (Spera *et al.*, 2009), and diamonds are experimental results on albite-orthoclase melts Freda and Baker (1998). Empty circles are the extrapolated diffusivities at the experimental temperatures using the Arrhenius fit of our data.

Table 5.1 – Activation energies estimated at four different pressures in K- and Ca-feldspar end-members.

	E_A (kJ/mol)					E_A (kJ/mol)			
	1 GPa	25 GPa	50 GPa	100 GPa		1 GPa	25 GPa	50 GPa	100 GPa
K	58	44	69	120	Ca	57	54	82	138
Al	97	53	76	123	Al	63	52	78	132
Si	103	53	73	112	Si	77	54	77	124
O	99	49	72	118	O	74	56	79	125

5.4 Viscosity

The viscosity of a melt with a given composition is a very important parameter in hydrodynamics simulations, whether they are about convection in magma oceans or evolution of the protolunar disk. The shear viscosity η is usually computed by the Green-Kubo relation which is the integration over time of the autocorrelation function of the stress tensor σ_{ij}:

$$\eta = \frac{V}{k_B T} \int_0^{t_{max}} \left\langle \sigma_{ij}(t + t_0)\sigma_{ij}(t_0) \right\rangle \tag{5.6}$$

with k_B the Boltzmann constant. An accurate calculation of this parameters is possible only for very long simulations, of at least 100 ps (e.g Adjaoud *et al.*, 2008; Karki *et al.*, 2011) or on the order of several nanoseconds (e.g Spera *et al.*, 2009). For our systems of 208 atoms modeled by FPMD it is not possible to reach such long simulations in a reasonable amount of time. Then we prefer to not compute the shear velocity of feldspars.

CHAPTER 6

THERMODYNAMIC PROPERTIES

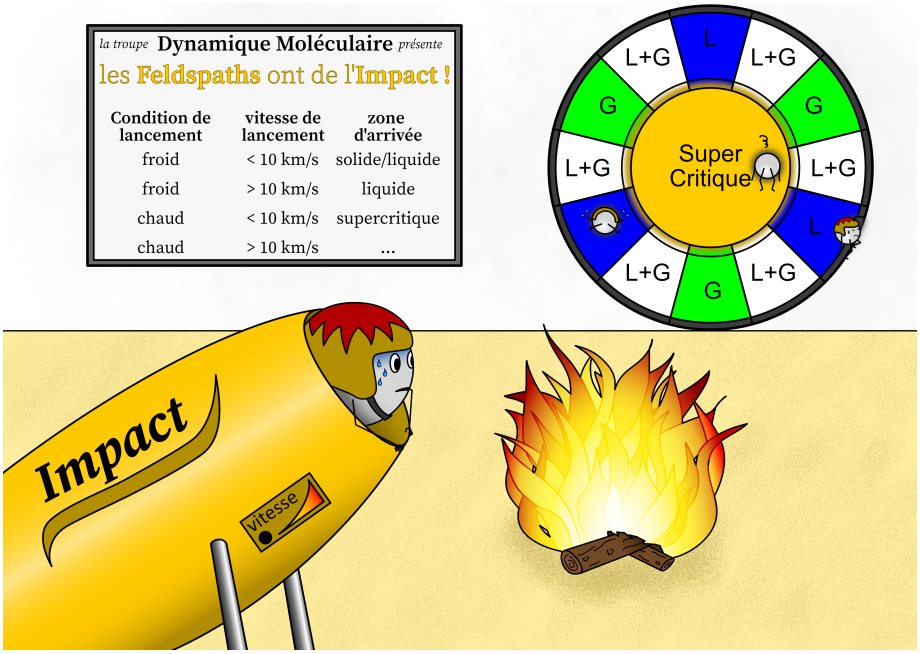

Lorsqu'un feldspath est projeté sur une cible, autrement dit quand il subit un impact, il atteint de hautes pressions et températures qui peuvent le faire changer d'état physique et devenir liquide ou supercritique s'il est initialement assez chaud.

La thermodynamique (des feldspaths) dans tous ses états

Après avoir étudié les propriétés microscopiques des trois feldspaths, passons maintenant à l'étude des propriété macroscopiques, comme la masse volumique (ρ), la température (T), la pression (P) et l'énergie (E). Au cours de nos simulations, ces trois dernières fluctuent. D'après la physique statistique, la moyenne de ces fluctuations nous donne une estimation correcte de ces grandeurs thermodynamiques. Les analyser va nous permettre de répondre à certaines questions posées dans l'introduction, comme « où se trouve l'état supercritique ? » ou bien « quel est l'état de la matière lors de l'Impact Géant ? ».

Pour répondre à la première question, traçons la pression au sein de notre fluide en fonction de la masse volumique pour différentes températures (figure 6.7). Chaque courbe, ensemble de points de température constante, est appelée isotherme. La théorie prédit que ces isothermes montrent un minimum et un maximum en dessous d'une température, appelée température critique, autrement dit lorsqu'elles traversent un changement de phase (figure 6.2). L'isotherme à la température critique est la seule à présenter un point d'inflexion (en ce point la courbe admet une tangente horizontale qui la traverse). Dans le cas présent du changement liquide vers gaz, nous identifions des minima, aussi appelés spinodal liquides, jusqu'à 5000, 6000 et 7000 K pour les trois pôles purs des feldspaths, respectivement K, Na et Ca. Pour les températures supérieures, les isothermes ne montrent plus de minima et continuent uniquement de décroître quand la masse volumique diminue. Ainsi pour chaque feldspath, la température critique est encadrée par l'isotherme avec et celle sans minimum, séparées de 500 K. La masse volumique du point critique est encadrée par les masses volumiques du dernier maximum et du dernier minimum visibles. Pour les feldspaths, cela correspond approximativement à 0.5-0.8 $\mathrm{g\,cm^{-3}}$.

La deuxième question trouve sa réponse en combinant les diagrammes de phases avec les équations d'état des feldspaths. Un diagramme de phase est un graphique selon deux grandeurs thermodynamiques (ex. P *vs* ρ, T *vs* ρ) dans lequel est indiqué l'état physique de la matière (liquide, gaz...) pour chaque point, ainsi que les courbes délimitant les zones de changement de phase. La figure 6.9 est un diagramme de phase indicatif car nous n'avons pas pu obtenir la courbe délimitant la zone de mélange liquide-gaz. Une équation d'état est une relation entre les grandeurs thermodynamiques nécessaires à la description du système. Lors d'un impact (par exemple de météorite), l'état thermodynamique de la surface de la planète est soumis à l'équation d'état appelée Hugoniot. Selon la vitesse d'impact on obtient des températures, pressions et énergies au moment du choc différentes. Pour des impacts très énergétiques, comme celui de l'Impact Géant, on trouve par exemple des températures dépassant les 7500 K, garantissant la fonte des feldspaths voire leur passage en état supercritique.

Brief outline This chapter is about the thermodynamic properties of the fluids. Section 6.1 gives the definitions, computer codes and theories behind the thermodynamic concepts used in the results sections that follow. First section 6.2 presents some results about equations of state. Then the main work of this thesis is presented in section 6.3 about the spinodal analysis. This leads to an attempt of phase diagrams shown in section 6.4, which are used in the discussion about impacts and shock states described in section 6.5.

6.1 Post Processing

6.1.1 Averages, standard deviation and errors

As said in section 2.1.1, we obtain the value of a macroscopic parameter A by performing a time-average of the value $A(t)$ over the entire MD simulation. This section explains how the script `fullaverages.py` computes the averages, spread of the data and errors on the means of the pressure (P), temperature (T) and energy (E) along with the heat capacity for each *.umd.dat* file available.

Pressure, Temperature, Energy

We use the arithmetic average of all the instantaneous values $X(t)$ as an estimator of the expected value $E(X)$, also represented by $\overline{X}$. Likewise, we compute the spread of the instantaneous values using the population standard deviation, σ_X. As explained in section 2.2.1, we made sure each simulation was thermalized, i.e. reached equilibrium of the thermodynamic parameters of interest (P, E, T). This is even true for simulations which are not fully ergodic (see the list in annex A.3.4) or that are very short, as shown in example figure A.27.

The statistical error on the mean, represented by $\sigma_{\overline{X}}$, is computed using the blocking method as described by Flyvbjerg and Petersen (1989). The core of the method can be decomposed into two steps.

1. From a data set $\{x_1, ..., x_n\}$ of length n we compute the quantity $\sqrt{\frac{Var(X)}{n-1}}$, with $Var(X)$ being the variance of the data set.

2. We transform the data set into a new data set, of length $n' = \frac{n}{2}$ if n is even, or $n' = \lfloor \frac{n}{2} \rfloor + 1$ if n is odd, $\lfloor x \rfloor$ being the floor function of x. To do so, each new data point is an average of two consecutive old data points, that is to say each $x_{i'}$ of the new data set is defined by

$$x_{i'} = \frac{1}{2}(x_{2i-1} + x_{2i}). \tag{6.1}$$

Then we perform a loop on these steps 1 and 2, using each time the new data set to replace the old one, until the data set has only two elements left. Finally we obtain a sequence of all the quantities $\sigma_{\overline{X}} = \sqrt{\frac{Var(X)}{n-1}}$ as a function of the number of block transformation. These values are represented in figure 6.1 with their associated error bars drawn to $\pm 1\sigma_{error} = \sqrt{\frac{1}{2(n-1)}}$. The first point (with its error bar) which is included in the error bars of every following points is the value we choose to estimate the statistical error on the mean $\sigma_{\overline{X}}$. The length of our simulations is around 15 000 steps, which corresponds to about 13 block transformations. Then, for the value of the error on the mean $\sigma_{\overline{X}}$, we choose to use the first point which is included in the error bars of the next 6 points (about half the number of maximal block transformations).

If we cannot find a point which is included in the error bars of at least 6 following consecutive points, then we use the point with the highest value (i.e. the maximum if the series $\sqrt{\frac{Var(x)}{n-1}}$) to estimate the lower bound of the statistical error on the mean $\sigma_{\overline{X}}$. For example this is the case for the temperature on figure 6.1[1]. In the result table produced by the `fullaverages.py` script, the value $\sigma_{\overline{X}}$ is preceded by the sign '>'.

Heat capacity

In the NVT ensemble and for insulators, the isochoric heat capacity (in J/K) can be obtained by the equation

$$\sigma^2_{Etot} = k_B \overline{T}^2 Cv, \tag{6.2}$$

with $\overline{T}$ the average temperature, k_B the Boltzmann constant and σ^2_{Etot} being the standard deviation of the total internal energy. As presented in the equation 2.4, this energy is the sum of the potential and kinetic energies. It is this quantity that is always used in this thesis. In theory, the contribution of the kinetic part to the heat capacity should equal $\frac{3}{2}Nk_B$, with N the total number of atoms in the system (Allen and Tildesley, 1989). Then, for users who do not extract the kinetic energy of ions in their calculation of the total internal energy, we implemented the following equation for the calculation of the heat capacity

$$Cv = \frac{\sigma^2_E}{k_B \overline{T}^2} + \frac{3}{2} N k_B. \tag{6.3}$$

To compute the statistical error on the heat capacity we need the statistical error on the variance σ^2_E. We choose to use the bootstrap method, described by Newman and Barkema (1999). The core of this method can be decomposed again into two steps.

1. From the total internal energy data set of length n we create a sample of the same length n with elements randomly drawn with replacement from the initial data set of instantaneous values.

[1] figure created by the script `fullaverages.py`

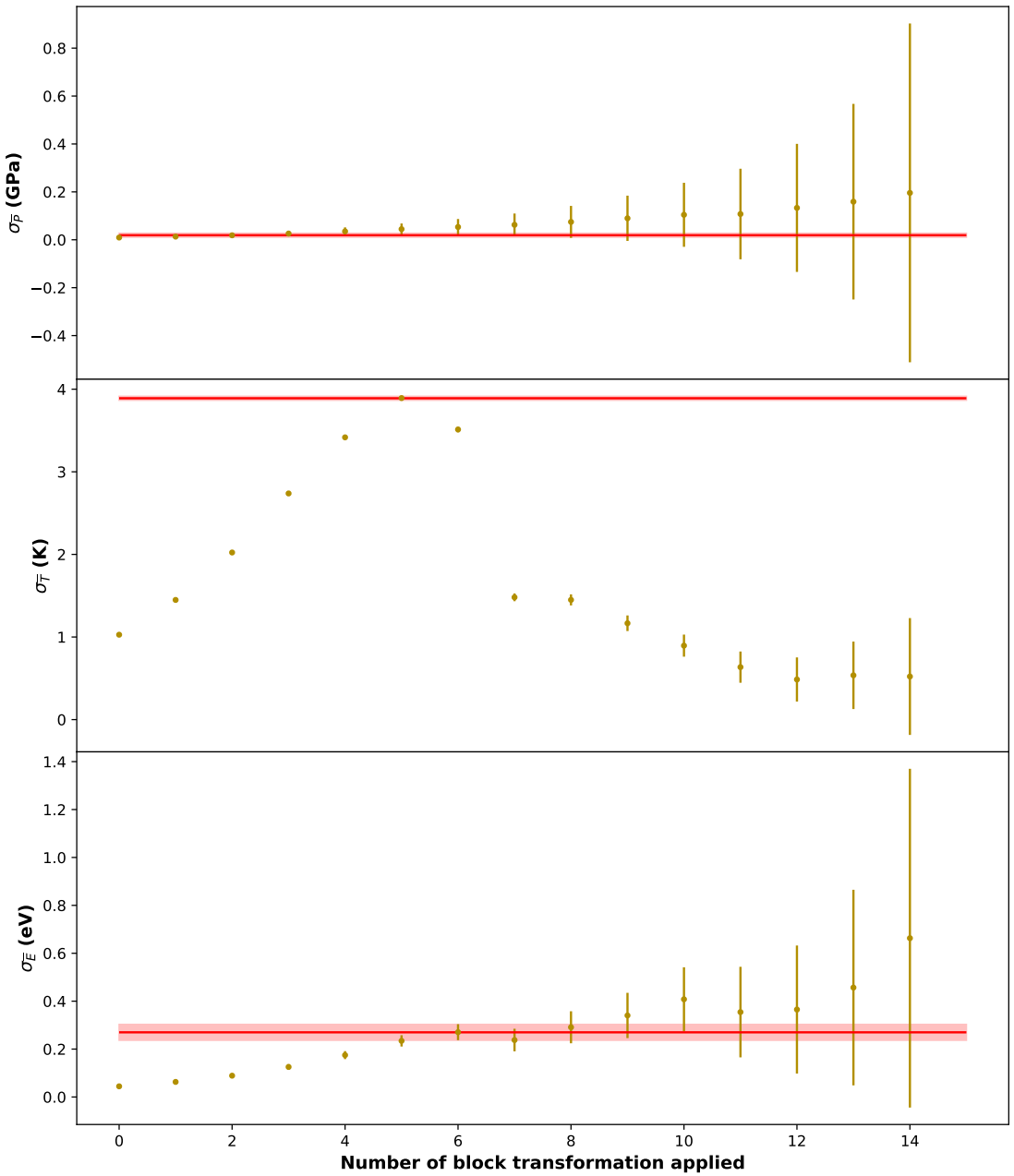

Figure 6.1 – Statistical error analysis applied to $CaAl_2Si_2O_8$ at 3000 K and 3.36 g cm^{-3}. The values $\sigma_{\overline{X}} = \sqrt{\frac{Var(X)}{n-1}}$ (X being P, T or E) are represented as a function of the number of block transformation. Their errors bars are drawn to $\pm 1_{error} = \sqrt{\frac{1}{2(n-1)}}$. The selected values for the errors on the mean $\sigma_{\overline{X}}$ are indicated by the red lines. The light red areas that surround them indicate the range $\pm 1\sigma_{error} = \sqrt{\frac{1}{2(n-1)}}$ around this value. For this simulation, the values selected for $\sigma_{\overline{P}}$ and $\sigma_{\overline{E}}$ are included in the error bars of the next 6 points. This was not the case for the temperature, then $\sigma_{\overline{T}} > \max(\sqrt{\frac{Var(X)}{n-1}})$.

2. We compute the specific heat capacity of this sample. We call it Cv_1.

We perform a loop on these steps 1 and 2 over more than a 1000 iterations. At each iteration we save the specific heat capacity of the created sample. Finally we obtain a set of values $\{Cv_1, ..., Cv_B\}$ of length $B > 1000$. From this set we can compute the empirical mean

$$\overline{Cv} = \frac{1}{B}\sum_{b=1}^{B} Cv_b, \tag{6.4}$$

which is another estimator of the mean specific heat capacity. We choose to use this estimation instead of the value obtained directly using equation 6.2. The error in the value of Cv is the standard deviation of the distribution of Cv_b, which is

$$\sigma_{Cv} = \sqrt{\overline{Cv^2} - \overline{Cv}^2}. \tag{6.5}$$

In the literature we can see reported the heat capacity in Nk_B units or the specific heat capacity in R units. Annex A.3.5 explains the unit conversions and the link between the two units.

6.1.2 Equations of state and compressibility

Equations of state

The thermodynamic behavior of material is characterized by its equation of state, which relates at least two thermodynamic variables (P, V, E, T). Several types of equations of state exist for solid materials and can describe their thermodynamic evolution quite accurately in their range of application. Likewise, there is the ideal gas law

$$PV = nRT \tag{6.6}$$

with R the gas constant to describe ideal gas and there is also the van der Waals equation

$$\left(P + a\frac{n^2}{V^2}\right)(V - nb) = nRT \tag{6.7}$$

based on a more realistic model of gas. Nevertheless, there is no equation of state that is valid for every real fluids, either liquids or gases. In this section, we want to obtain thermodynamic parameters, such as the compressibility, for the liquids only. Many previous studies (e.g. Ghiorso *et al.*, 2009; Karki *et al.*, 2011; Neilson *et al.*, 2016) used equations of state developed for solids to fit their liquid simulation results. Then to allow a comparison of the fitted parameters with those previously obtained, we use the 3rd and 4th order of the Birch-Murnaghan equations of state, respectively equations 6.8

and 6.9.

$$P(\rho) = \frac{3K_0}{2}\left[\left(\frac{\rho}{\rho_0}\right)^{\frac{7}{3}} - \left(\frac{\rho}{\rho_0}\right)^{\frac{5}{3}}\right]\left\{1 + \frac{3}{4}(K_0' - 4)\left[\left(\frac{\rho}{\rho_0}\right)^{\frac{2}{3}} - 1\right]\right\} \tag{6.8}$$

$$\begin{aligned} P(\rho) = \frac{3K_0}{2}&\left[\left(\frac{\rho}{\rho_0}\right)^{\frac{7}{3}} - \left(\frac{\rho}{\rho_0}\right)^{\frac{5}{3}}\right]\left\{1 + \frac{3}{4}(K_0' - 4)\left[\left(\frac{\rho}{\rho_0}\right)^{\frac{2}{3}} - 1\right]\right. \\ &\left. + \frac{3}{8}\left[K_0 K_0'' + (K_0' - 3)(K_0' - 4) + \frac{35}{9}\right]\left[\left(\frac{\rho}{\rho_0}\right)^{\frac{2}{3}} - 1\right]^2\right\} \end{aligned} \tag{6.9}$$

To fit these equations to our liquid data, we first selected only the points with either a pressure above 1 GPa or a density above 1.6 g cm^{-3} in order to have only the liquid phase. No consistent thermodynamic parameters can be found when very high pressure data are included. Then, the results presented in section 6.2 are obtained from the data with a pressure below 100 GPa. The fitting step is performed using the orthogonal distance regression (ODR) method from the Python® package *scipy* (Boggs *et al.*, 1992).

Isobaric expansivity and isothermal compressiblity

Following the calculation process described by Spera *et al.* (2009), we use our pressure-temperature-density data points to compute the thermal pressure coefficient (TPC),

$$\frac{\partial P}{\partial T}\Big)_V = \frac{\alpha}{\beta}, \tag{6.10}$$

which links the isobaric expansivity $\alpha = \frac{1}{\rho}\frac{\partial \rho}{\partial T}\Big)_P$ to the isothermal compressibility $\beta = -\frac{1}{\rho}\frac{\partial \rho}{\partial P}\Big)_T$. In a pressure-temperature diagram the isochores are close to straight lines. We perform a linear fit to each individual isochore and extract the slope which is the TPC. Then in a density-pressure diagram we plot each isotherm. We obtain β for each temperature and density by performing central finite differences along each isotherm. For the lowest and highest density-pressure data points (i.e. at the end of the isotherms), we perform forward and backward difference respectively. Finally the isobaric expansivity α is obtained using the equation 6.10. The complete analysis along with the figure and table production is performed by the script `analyze_compressibility.py`.

6.1.3 Spinodal search

The figure 6.2 shows the isotherms of a real fluid on a pressure-density diagram spanning the liquid and gas regions. The Van der Waals theory states that every state on the isotherms is at the equilibrium, but it is an unstable equilibrium when the slope of the

P-ρ isotherm is negative. The states with a zero slope, the maxima and minima of the isotherms, define the vapor and liquid spinodal points respectively. When these points are linked over all isotherms they define the vapor and liquid spinodal lines respectively. They both meet at the critical point. When the complete isotherms, i.e. equations of state, are known, the Maxwell construction can be used to determine the saturated liquid and gas states. When linked over all isotherms they define the saturated liquid and vapor curves respectively. Once again these two curves meet at the critical point and define the binodal curve. The pressure-density states comprised between the saturated liquid and the liquid spinodal or between the saturated vapor and vapor spinodal are metastable states. In our simulations, we obtain states in the liquid, metastable and unstable regions. We reach the vapor region only in the vicinity of the critical point. Therefore, we cannot use the Maxwell construction to construct the binodal line. Nevertheless, we obtain the liquid spinodal points and then an estimation of the critical point.

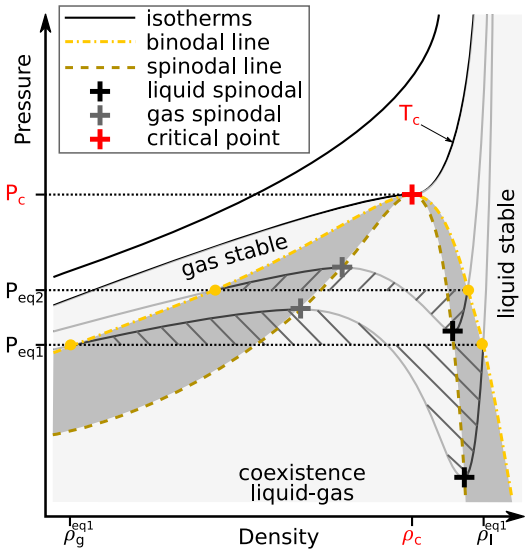

Figure 6.2 – Schematic of the pressure variations as a function of density for several isotherms in a real fluid. The spinodal curve (dashed dark yellow) is found using the extrema of the isotherms, whereas the binodal or saturation curve (dashed-dot yellow) is found using the Maxwell equal-area construction (stripped areas). Both curves have the critical point as a common maximum. The dark gray areas indicate the regions of metastable equilibrium.

To do so, we need to fit our data to a curve representing the isotherm. As said before, there is no equation of state that is valid for every real fluids and even less for a mixture of real fluids. Then, we decided to use a simple function to approximate the isotherms and especially the minimum. The van der Waals equation (number 6.7) can be written in the form $P = f(\rho)$:

$$P = \frac{\frac{ab}{M^3}\rho^3 - \frac{a}{M^2}\rho^2 + \frac{RT}{M}\rho}{1 - \frac{b}{M}\rho} \tag{6.11}$$

with M the molar mass of the material. When the density is small, i.e. $\frac{b}{M}\rho \ll 1$, this equation can be approximated by a 3rd order polynomial with the constant coefficient equal to 0. Nevertheless, since our fluid, as modeled by ab initio MD, is not a van der Waals gas, we consider first a 3rd order polynomial with a non zero constant term. If 0 is in the uncertainty range of this constant term obtained from the fit, then the constrained polynomial fit would be a better choice. The fitting process and the choice of polynomial fit is implemented in the script `plot_thermo_rho.py`.

This method to find the liquid spinodal is based on the theory of real fluid thermodynamics. Binder *et al.* (2012) pointed out that the minima we see in the pressure-density curves obtained via MD simulations are not the thermodynamic spinodals but are only due to finite size effect and should correspond to the apparition of bubbles in our fluid. Nevertheless, bubbles can only appear inside the binodal dome that is located below the critical isotherm. Then the minima in the pressure-density isotherms still indicate a two-phase region. Above the critical temperature, there is no minima anymore in the isotherms and the pressure decreases continuously with the density. This method to find the critical point was successfully used by Green *et al.* (2018) in the case of pure SiO_2. It is also the best approximation for the spinodal curve we have up-to-date.

6.1.4 Hugoniot equation of state and shock conditions

When a material is hit by another one, compression waves propagate into both materials and change their thermodynamic properties as pressure, energy, density, etc. To estimate the new values of these properties right after the impact we use the shock wave physics. We explain here the basics and detail the equations used in this thesis. For a more complete list of all the assumptions made and examples on shock wave treatment, the reader can refer to the book by Forbes (2012).

We assume the shock waves are one-dimensional (1D) plane waves that propagate into a continuum fluid. By definition, each point (of a material) hit by a shock wave undergoes a change from low to high stress and compression level in an almost discontinuous jump as a function of time. We assume then that the shocked material is in thermodynamic equilibrium. For a 1D plane wave that travel through a material in the +x direction with a velocity u_s as in figure 6.3a, we can define two states. The number 1 ahead of the shock wave, for the unshocked material and the number 2 behind the shock wave, for the shocked material. The pressure (P), specific internal energy (e), density (ρ) and particle velocity (u_p) in each state are linked by three conservation equations

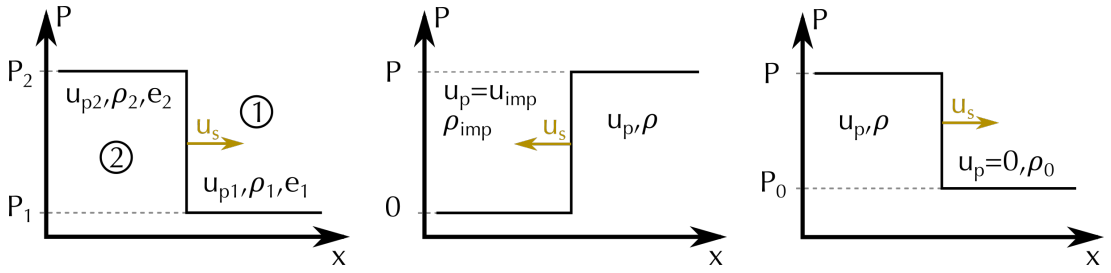

(a) General case.

(b) Applied to the impactor with initial state P_{imp},ρ_{imp} and u_{imp}.

(c) Applied to the crust with initial state P_0,ρ_0 and u_{p0}.

Figure 6.3 – Schematics of the pressure state of a material ahead and behind a 1D plane shock wave for different cases. In the impedance match method, we consider the shock velocity (yellow) to be equal in (b) and (c).

defining the Rankine-Hugoniot equations:

$$\text{conservation of mass} \qquad \rho_1(u_s - u_{p1}) = \rho_2(u_s - u_{p2}) \tag{6.12}$$

$$\text{conservation of momentum} \qquad \rho_1(u_s - u_{p1})^2 + P_1 = \rho_2(u_s - u_{p2})^2 + P_2 \tag{6.13}$$

$$\text{conservation of energy} \qquad e_1 + \frac{(u_s - u_{p1})^2}{2} = e_2 + \frac{(u_s - u_{p2})^2}{2} \tag{6.14}$$

When we combine the conservation equation of mass (6.12) and momentum (6.13) to eliminate the velocities in the conservation equation of energy (6.14), then we obtain the Hugoniot equation

$$\underbrace{E_1 - E_2 + \tfrac{1}{2}(P_2 + P_1)(\tfrac{1}{\rho_1} - \tfrac{1}{\rho_2})}_{\mathrm{Hg}(\rho)} = 0 \ . \tag{6.15}$$

For each temperature, we find the density ρ for which $\mathrm{Hg}(\rho) = 0$. To obtain the pressure corresponding to this density we need a second equation. We choose to fit a 3rd order Birch-Murnaghan equation of state to the isotherm (equation 6.8) to obtain the pressure. The energy can then be obtained from the Hugoniot relation (equation 6.15). For each temperature of interest, the {P, ρ (, E)} ensemble verifying the Hugoniot equation 6.15 defines the thermodynamic shock state of the material (labeled 2 on figure 6.3a), for a given initial state 1.

To obtain the shock state a material, for example a planet crust, as a function of the impactor velocity u_{imp}, we use the impedance match method as follow:

1. We obtain the {P, ρ} point verifying the equation 6.15 for the crust (figure 6.3c). The initial pressure P_0 and density ρ_0 used in this calculation are detailed in section 6.5.

2. Same process for the impactor (figure 6.3b), which is assumed to be made of the

same material as the crust.

3. We assume that at the impact, two shock waves of the same velocity u_s appear and travel on opposite direction, one in the crust, one in the impactor. Combining the equations 6.12 and 6.13 with the notation in figures 6.3b and 6.3c, we obtain the following equations for the particle velocities of the crust and the impactor respectively:

$$crust \quad u_p = \sqrt{(P - P_0)\frac{(\rho - \rho_0)}{\rho\rho_0}} \tag{6.16}$$

$$impactor \quad u_p = -\sqrt{P\frac{(\rho - \rho_{imp})}{\rho\rho_{imp}}} \tag{6.17}$$

4. We assume there is no discontinuity in the particle velocity on the two sides of the impact interface, meaning u_p(crust) = u_p(impactor) at the impact time and location. Then the intersection of the equations 6.16 and 6.17 gives the shock pressure and particle velocity.

5. Using the Hugoniot equation of the crust we obtain the corresponding shock temperature and density for the selected impactor velocity u_{imp}.

The selection of the impactor velocities is detailed in section 6.5. The calculation of Hugoniot curves is performed by the script `analyze_Hugoniot.py` and the impedance match method is done by the script `plot_Hugoniot_impedance-match.py`.

6.2 Equations of state and thermodynamic parameters

Equations of state

In the liquid region, in other words approximately for densities larger than 1.6 g cm^{-3} and pressures below 100 GPa, we fit 3rd and 4th order Birch-Murnaghan equations of state to the pressure - density points along each isotherm. We only present the results of the fit for 3000 and 4000 K isotherms for the alkali feldspars since no consistent values for the bulk modulus and its derivatives can be found at higher temperatures. For $CaAl_2Si_2O_8$, we can obtain results with both equations of state up to 5000 K and up to 6000 K with only the 3rd order equation. This is partly due to the inappropriateness of the Birch-Murnaghan equations of state to describe the behavior of liquids at high temperatures and low pressures where bulk modulus is small. Table 6.1 shows the results and the comparison to existing data in the literature, both experimental Lange (2007); Tenner *et al.* (2007) and calculated Bajgain and Mookherjee (2020); de Koker (2010); Ghiorso *et al.* (2009); Karki *et al.* (2011). The ρ_0 values extrapolated from our

Table 6.1 – Parameters of 3rd order Birch-Murnaghan equations of state fitted to our computed pressure-density values along the different isotherms and comparison with the available experimental data or theoretical results (FPMD) from the literature. No consistent data for the bulk modulus and its derivatives can be found at 5000 K and higher for alkali feldspars.

	Temperature (K)	ρ_0 ($g\,cm^{-3}$)	K_0 (GPa)	K_0'	other studies
$NaAlSi_3O_8$	298	2.615	56.4	3.9	crystalline albite Tenner *et al.* (2007)
	1373	2.326	17.5	11	liquid Tenner *et al.* (2007)
	2500	2.31	12	5.3	FPMD Bajgain and Mookherjee (2020)
	3000	2.01(7)	11(3)	4.9(5)	
	4000	1.82(3)	7(1)	5.8(2)	
$KAlSi_3O_8$	295	2.554	57	4	crystalline sanidine Lange (2007)
	1473	2.298	15.8	12	liquid Lange (2007)
	3000	1.8(1)	5(2)	6.5(8)	
	4000	1.70(4)	5(1)	5.9(2)	
$CaAl_2Si_2O_8$	1830	2.56(7)	17.4(3)	3.18	FPMD de Koker (2010)
	3000	2.13(3)	7(4)	8(2)	
		2.39(2)	11.5(3)	6.8(6)	FPMD Karki *et al.* (2011)
	3500	2.31	9.93	9.88	Classical MD Ghiorso *et al.* (2009)
	4000	2.09(4)	11(2)	5.9(3)	
		2.27	10.40	9.47	Classical MD Ghiorso *et al.* (2009)
	4500	2.21	9.82	9.27	Classical MD Ghiorso *et al.* (2009)
	5000	1.85(3)	7(1)	6.1(2)	
		2.19	10.78	8.85	Classical MD Ghiorso *et al.* (2009)
	5500	2.14	10.52	8.68	Classical MD Ghiorso *et al.* (2009)
	6000	1.55(7)	3(1)	6.7(7)	
			10.19	8.55	Classical MD Ghiorso *et al.* (2009)

simulations using a second-order polynomial are $2.26\,g\,cm^{-3}$ at 1373 K for $NaAlSi_3O_8$, i.e. about 2.7 % smaller than the experimental values Lange (2007). As seen in chapter 3, the major coordination polyhedra SiO_x and AlO_x become larger as the pressure increase, starting from 4-fold coordinated at ambient conditions to up to 8 fold-coordinated above 200 GPa. Maybe it would be of importance to fit a different equation of state per region of dominant coordination, i.e. per structure but we do not have enough data point per region to do so.

Heat capacity

The specific heat capacity Cv is computed for each simulation using the equations 6.2 and 6.4. All the values are available in annex B.1.1. Nevertheless, these values can be trusted only if the fluctuations of temperature are correct. For example, in a canonical ensemble the relative variance should obey

$$\frac{\sigma_T^2}{\overline{T}^2} = \frac{2}{3N} \tag{6.18}$$

with $N = 208$ the number of particles in the system (Frenkel and Smit, 2002c). Figure 6.4 represents these relative variance for each simulation. In this figure, we computed their statistical errors (SE) using the same bootstrap scheme as described in section 6.1.1. About 30 % of the simulations obey the relation 6.18 within $\pm 2 * SE$ (and about 45 % within $\pm\ 3 * SE$). They are plotted in bright colors in figures 6.4 and 6.5. Figure 6.5 shows all the Cv values as a function of density and temperature. They are similar to those obtained by other *ab-initio* MD simulations on various silicates (e.g. de Koker, 2010; de Koker *et al.*, 2008; Green *et al.*, 2018; Stixrude and Lithgow-Bertelloni, 2005). On the contrary, values obtained by classical MD are larger by a factor 10 (e.g. Morgan and Spera, 2001; Neilson *et al.*, 2016; Spera *et al.*, 2009), even though they seem to be consistent with old experiments (Richet and Bottinga, 1984; Stebbins *et al.*, 1983).

Some studies found a linear temperature dependence of the isobaric and/or isochoric heat capacity (e.g. Adjaoud *et al.*, 2008; Lange, 2007), but our results do not display such relationship. The heat capacities we obtain increase with temperature up to about 5000 K. Above this temperature it decreases to values sometimes even smaller than those obtained at 3000 K. Nevertheless it is difficult to conclude on the temperature-dependence of the heat capacity of feldspars since more than half of our data may not be trusted.

Thermoelastic parameters

The isobaric expansivity α and isothermal compressibility β are displayed on figure 6.6. The results previously obtained by two classical MD studies on the Na-feldspar (Neilson *et al.*, 2016) and on the Ca-feldspar (Spera *et al.*, 2009) are also indicated for comparison purposes. Our values are on the same order of magnitude as those obtained in the classical MD simulations. We have a better agreement for β than for α and also for the Na- end-member compared to the Ca- end-member. We see the same change in the order of isotherms as observed by Neilson *et al.* (2016): at low pressures the isobaric expansivity increase with increasing temperature while at high pressure it decreases with increasing temperature. The pressure which delimits these two regimes is lower in our study than for Neilson *et al.* (2016). This behavior is also seen in the two other feldspars and in the study of Spera *et al.* (2009).

6.3 Spinodal and critical point

As seen before, we performed the calculations along several isotherms, ranging from 2000 K, corresponding to a hot magma, up to 7500 K. At each temperature we started at high density and decreased the density of the melt by expanding the volume of the simulation box. Since the pressure rises with the temperature of the isotherm, we

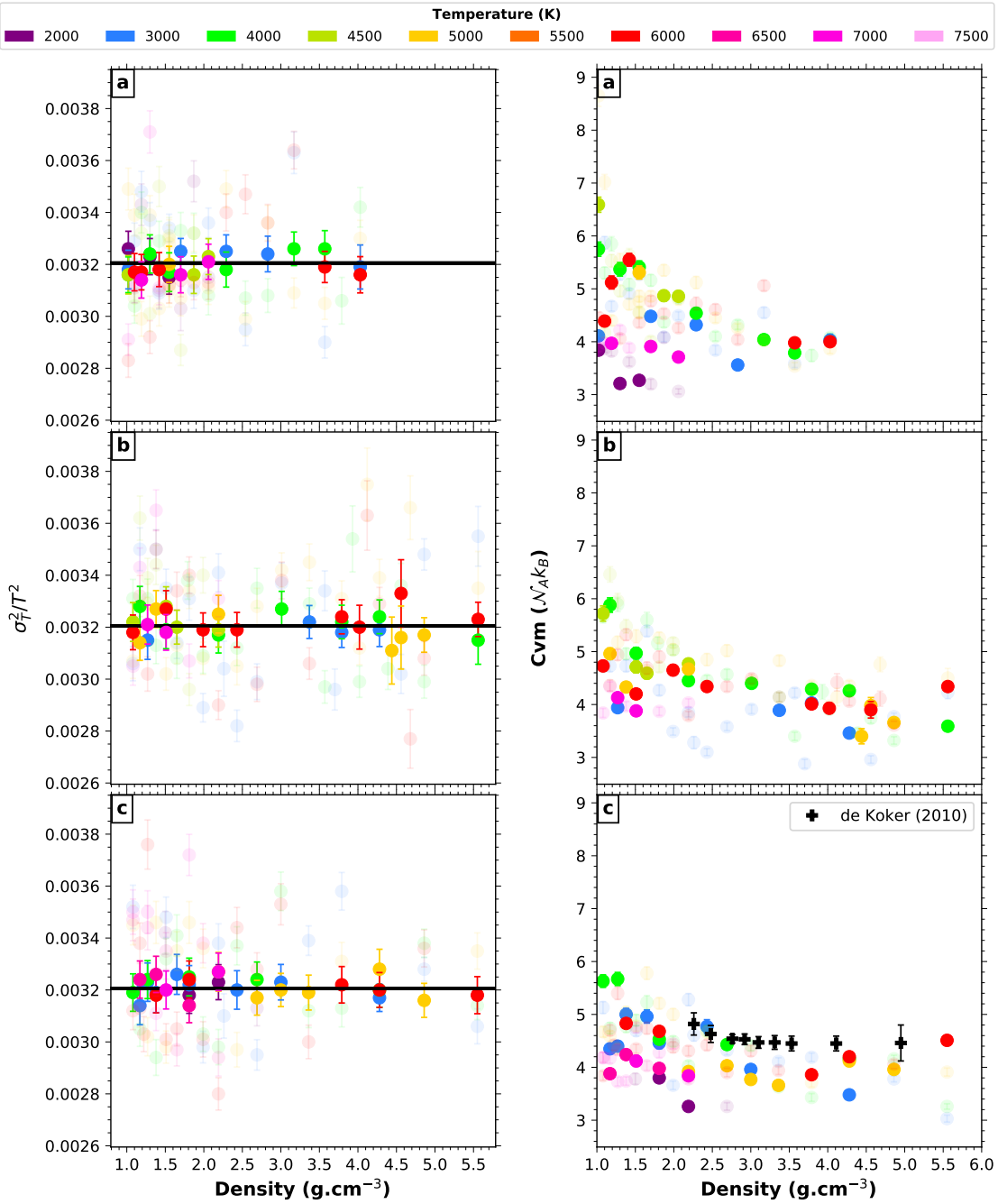

Figure 6.4 – Relative temperature variance as a function of density for the (a) Na- (b) K- and (c) Ca-feldspar end-members. The error bars are plotted to $\pm\ 2 * SE$, with SE being the statistical error on $\frac{\sigma_T^2}{T^2}$, computed using the same bootstrap scheme as for Cv. Only the simulations which are equal to $\frac{2}{3N}$ (black line) in the range of their errors are plotted in bright colors. The others cannot be trusted. Numerical values are available in annex B.1.1.

Figure 6.5 – Specific heat capacity Cv_m as a function of density and temperature for the (a) Na- (b) K- and (c) Ca-feldspar end-members. Only the simulations which obey the equation 6.18 are plotted in bright colors. Numerical data are available in annexes B.1.1.

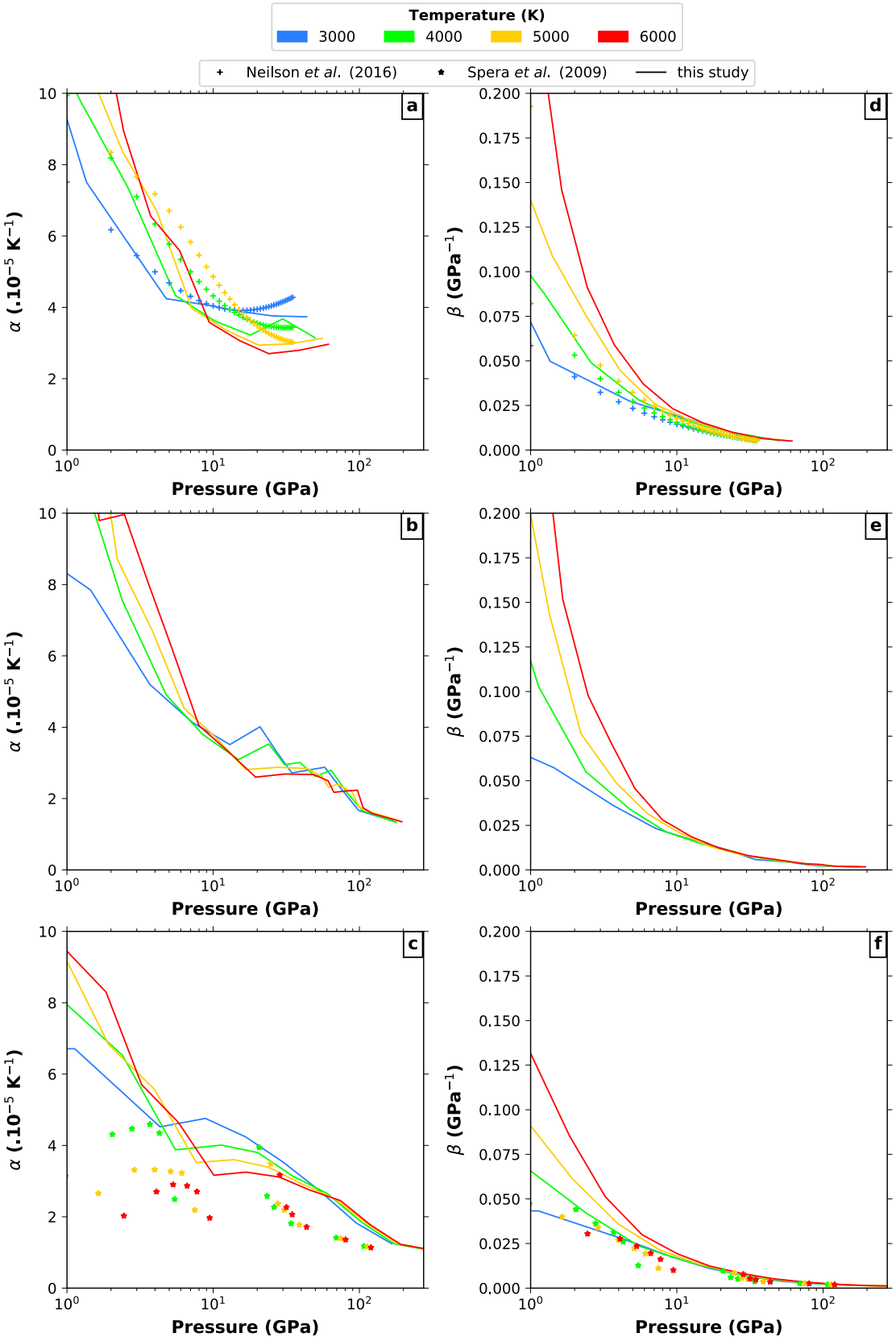

Figure 6.6 – Isobaric expansivity α and isothermal compressibility β as a function of pressure for the (a,d) Na-, (b,e) K- and (c,f) Ca-feldspar end-members. Colors indicate temperature. Data previously obtained by two classical MD simulations on the same end-members (Neilson *et al.*, 2016; Spera *et al.*, 2009) are also indicated for comparison. The same figure as a function of density is available in annex, figure A.28.

reach ambient pressure at lower and lower densities up to a temperature for which the isotherm always displays positive pressures. The last ambient pressure is seen at 4500 K and 1.3 g cm^{-3} for K-feldspars, 5000 K and 1.1 g cm^{-3} for Na end-member and 6500 K and 1.0 g cm^{-3} for Ca-feldspars. At lower temperature, as we perform simulations at lower densities we go into extension regime and the pressure drops below zero, where the melts are metastable.

Figure 6.7 shows the variation of pressure as a function of density for the three feldspar end-members along all computed isotherms. The statistical errors on the mean are included in the size of the points. Due to the large number of steps in each simulation runs, we obtain small uncertainties for the mean pressure even at very low densities. These values, of the order of 10^{-3}–10^{-2} GPa, are smaller or about the same order of magnitude as those obtained by Green *et al.* (2018) who used the same method to estimate them. The spread of the pressure values during the simulation is about 1.6 GPa, which is typical for FPMD simulations. The numerical results for pressure, temperature, density and internal energy are available in annex B.1.1.

As said in section 6.1.3, we approximate the P-T variation around the liquid spinodal with 3rd order pressure-density polynomials. We perform the fits along each isotherm with and without constraining the constant term to 0 (figures A.29 and 6.7 respectively). The minima of these curves show the position of the liquid spinodals and the numerical values can be found in annex B.1.2. As explained in section 2.2.2, we used two different sets of pseudopotentials to perform the simulations: one set for densities above 1 g cm^{-3} ("main study") and another set for densities between 0.5 and 2.5 g cm^{-3} ("low densities", see table 2.1). Figure 6.8(a,b,c) shows the position of the minima obtained with both datasets and type of fit. The two sets of pseudopotentials yield a slightly different position of the liquid spinodal. The data sets down to 1.0 g cm^{-3} appear to have enough data for a correct determination of spinodals located at density higher than 1.3 g cm^{-3}. This is the case for temperatures up to 3000, 4000 and 5000 K for respectively K, Na and Ca-end-member. Above these temperatures we used the data sets extended to low-enough densities to observe a local maximum, corresponding to the gas spinodal (figures 6.7 and A.29 d, e and f). For the case of the 4000 K isotherm of Na, available in both types of pseudopotentials, we choose to average the two values obtained for the minima as an estimation of the liquid spinodal.

The position of the minima obtained by constrained fits are very similar to the unconstrained ones except for the last values. For the alkali feldspars, the constrained fit finds a minimum for the first isotherm which did not displayed one with unconstrained fit (i.e. 6000 K for Na- and 5500 K for K-feldspars). Following the discussion in section 6.1.3, we choose to use the spinodals given by the constrained fit when 0 is comprised in the uncertainty range of the constant term of the unconstrained polynomial fit. This leads

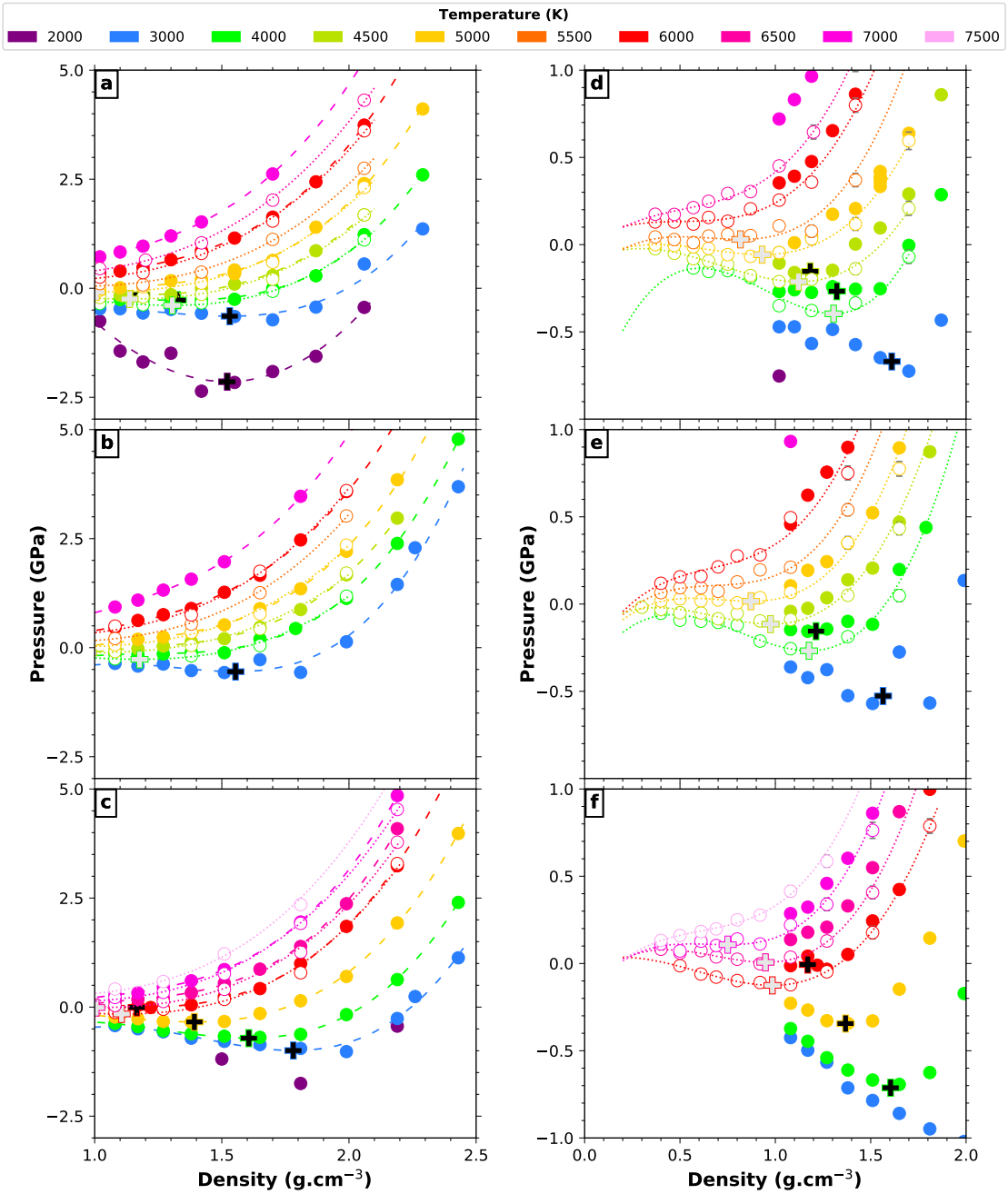

Figure 6.7 – Computed pressure as a function of density for the (a) Na-, (b) K- and (c) Ca-feldspar end-members and their respective enlarged view on the low density region, (d), (e) and (f). Open and solid symbols indicate values obtained with the two sets of pseudopotentials described in table 2.1 ("low density" and "main study" respectively). Dashed and dotted lines represent unconstrained 3rd order polynomial curve fits corresponding to the respective two sets of pseudopotentials. The gray and black crosses indicate the liquid spinodals corresponding respectively to the open and solid datasets. The statistical errors on the mean are included in the size of the points. Numerical data are available in annexes B.1.1 and B.1.2. The same figure for constrained fits is available in annex, figure A.29.

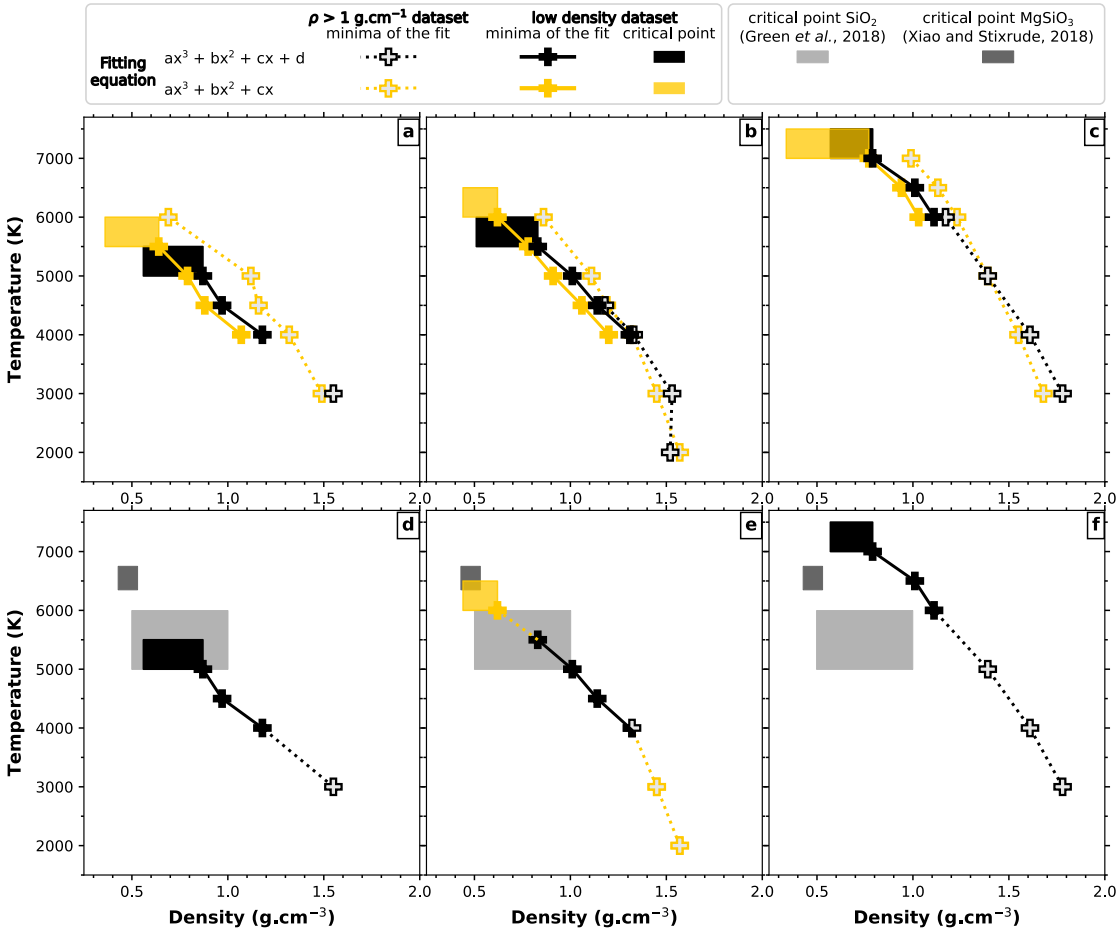

Figure 6.8 – Liquid spinodals obtained for the (a,d) Na-, (b,e) K- and (c,f) Ca-feldspar end-members using 3rd order polynomial fits. Colors indicate which equation is used for the fit. The symbol and line types (solid/empty/dotted) indicate which set of simulations is used in the fit (low density or above 1 g cm^{-3}). The rectangles indicate the position of the critical points. Subfigures (d), (e) and (f) summarize which spinodals and critical point estimations are selected here, and compare these results with critical point previously obtained on silica (Green *et al.*, 2018) and $MgSiO_3$ (Xiao and Stixrude, 2018). For numerical data, the reader can refer to the annex B.1.2.

to slightly different values for the Na end-member at 2000 and 3000 K, but increases by 500 K the position of the last spinodal, now located at 6000 K and 0.62 g cm^{-3} instead of 5500 K and 0.83 g cm^{-3}. All the selected values used as estimation of the liquid spinodals are summarized in the table 6.2 and displayed on figure 6.8(d,e,f).

For each feldspar end-member, the minima are less and less pronounced as the isotherms approach the critical temperature. Along the isotherms above this temperature, the pressure only decreases monotonously. The position of the critical point lies in density between the gas and the liquid spinodals and in temperature between the last isotherm that shows minima and maxima and the first isotherm that shows a monotonous decrease of pressure. The gas spinodals are estimated with the maxima of the 3rd order polynomial fits. For information they are indicated in the phase diagrams

Table 6.2 – Selected values for the estimation of the liquid spinodals in feldspars. The "origin" column states which data set and fit is used to select the spinodal value. See text for selection rules. *NaN* indicates that no minima could be found by the fitting process. These values are displayed on figure 6.8(d,e,f).

T	$NaAlSi_3O_8$			$KAlSi_3O_8$			$CaAl_2Si_2O_8$		
(K)	ρ ($g\,cm^{-3}$)	P (GPa)	origin	ρ ($g\,cm^{-3}$)	P (GPa)	origin	ρ ($g\,cm^{-3}$)	P (GPa)	origin
2000	1.57	-2.17	cf; m						
3000	1.45	-0.67	cf; m	1.55	-0.55	uf; m	1.78	-1	uf; m
4000	1.32	-0.33	uf; a	1.18	-0.27	uf; l	1.61	-0.71	uf; m
4500	1.14	-0.25	uf; l	0.97	-0.12	uf; l			
5000	1.01	-0.08	uf; l	0.87	0.02	uf; l	1.39	-0.34	uf; m
5500	0.83	0.03	uf; l	*NaN*	*NaN*	uf; l			
6000	0.62	0.13	cf; l	*NaN*	*NaN*	uf; l	1.11	-0.16	uf; l
6500	*NaN*	*NaN*	cf; l				1.01	-0.01	uf; l
7000							0.79	0.11	uf; l
7500							*NaN*	*NaN*	uf; l

cf: constrained fit; uf: unconstrained fit; l: low densities dataset (down to $0.5\,g\,cm^{-3}$); m: "main study" dataset (above $1\,g\,cm^{-3}$); a: average of values from the two datasets

figure 6.9 but their values are not entirely reliable since we do not have data at low enough density to obtain reliable fits of the maxima in this region (the values we have now are highly dependent on the equation used for the fit). Hence using the selected values for the liquid spinodals (table 6.2) we obtain the following ranges for the critical point of the three feldspar end-members:

$\mathbf{NaAlSi_3O_8}$ $6000 \leq T_c(\mathrm{K}) \leq 6500$; $0.44 \leq \rho_c(g\,cm^{-3}) \leq 0.62$; $0.1 < P_c(\mathrm{GPa}) \leq 0.2$

$\mathbf{KAlSi_3O_8}$ $5000 \leq T_c(\mathrm{K}) \leq 5500$; $0.56 \leq \rho_c(g\,cm^{-3}) \leq 0.87$; $0 < P_c(\mathrm{GPa}) \leq 0.1$

$\mathbf{CaAl_2Si_2O_8}$ $7000 \leq T_c(\mathrm{K}) \leq 7500$; $0.57 \leq \rho_c(g\,cm^{-3}) \leq 0.79$; $0.1 < P_c(\mathrm{GPa}) \leq 0.2$

To date there are no experimental determinations of the position of the critical point of feldspars. Recently, two studies computed the critical point of SiO_2 (Green *et al.*, 2018) and $MgSiO_3$ (Xiao and Stixrude, 2018) using FPMD. Green *et al.* (2018) found a supercritical temperature located between 5000 and 6000 K, and a supercritical density around 0.5–1.0 $g\,cm^{-3}$ by searching for minima in the pressure-density curves. The critical point of silica has been estimated before by Melosh (2007) to 5400 K and 0.55 $g\,cm^{-3}$ based on thermodynamic calculations from ANEOS. Xiao and Stixrude (2018) modeled a slab of liquid at the center of a very elongated empty simulation box and computed the liquid and gas densities by locating the liquid-vapor interface. They obtained a supercritical temperature around 6600 ± 150 K and a supercritical density around $0.48 \pm 0.05\,g\,cm^{-3}$.

6.4 Phase Diagram attempt

With all the information gathered in the previous sections and chapters, we attempt to build an indicative phase diagram, represented in figure 6.9. Each point corresponds to one simulation at a fixed volume and temperature. For clarity purposes, the simulations performed with two sets of pseudopotentials are represented by only one point with the average pressure from the two sets. Simulations are sorted into two physical states, fluid and mix liquid + gas, determined by visual analysis (see section 4.2). When the simulation did not reach the minimum ergodicity (see section 5.2 and annex A.3.4) we superimpose a gray cross to the simulation point. For long enough simulations, as for the 2000 K isotherm of $NaAlSi_3O_8$, we can consider this indicates a very viscous fluid. The liquid spinodals selected in table 6.2 are also indicated in this diagram down to 2000 K. We determine the position of the gas spinodals only for the isotherms with densities down to 0.5 g cm^{-3}. They are the maxima of the 3rd order fit used in the determination of the liquid spinodals. The line which links all the spinodal points together is only a guide to the eye for the spinodal curve. We place the critical point as the maximum of the spinodal curve.

6.5 Behavior of a feldspathic crust during impacts

The early part of the Hadean was dominated by impacts as the main phase of the accretion unfolded. The Giant Impact marked the end of this major part of the Earth history; it happened not later than 100 million years after the formation of the solar system. By this time, there could have been several partial melting and partial freezing episodes, which could have led to the formation of some primitive crust. In a terrestrial-like planet, even if we cannot know precisely what would have been the extent of the crust nor the temperature at the surface of the proto-planet, feldspars must have been one of the major components of this crust.

In order to model the behavior of the major feldspathic components of the crust during shock as generated by large impacts we build the Hugoniot equations of state, using our computed density-volume-temperature points. We consider three possible thermal initial states: cold (0 K), warm (1932 K) and hot (3000 K).

For the first scenario, temperatures are close to ambient. The crust is solid, made of feldspar crystals. As an extreme case, we infer a thickness of up to 50 km since current values are an average of about 30 km for the Earth and about 50 km on the Moon (Taylor and McLennan, 2008). According to the estimated variations of the pressure as a function of depth inside terrestrial planets (Warren, 1985), the pressure at the bottom of such a crust would be less than 2 GPa. This pressure corresponds to the

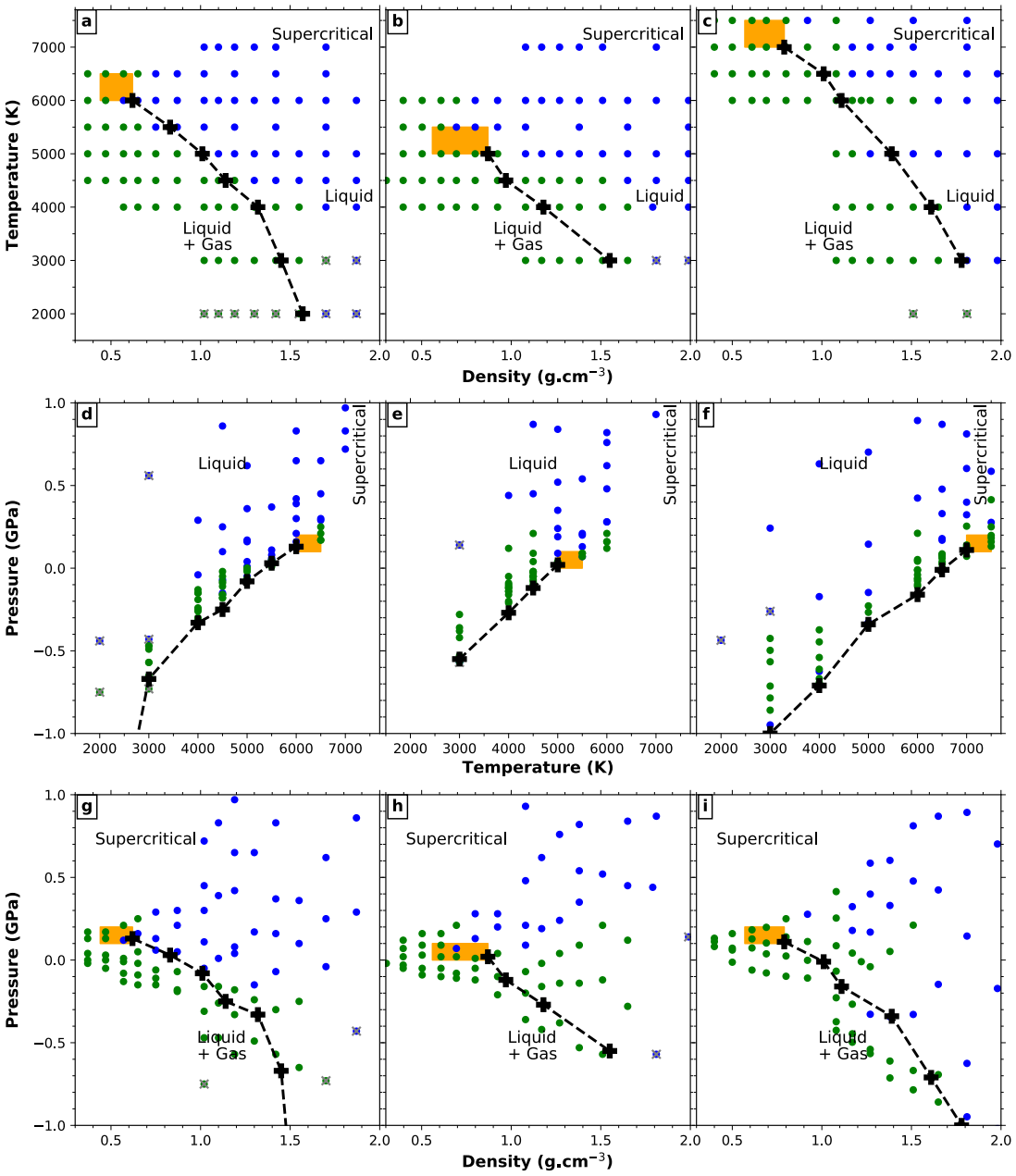

Figure 6.9 – Phase diagram for the (a, d, g) Na-, (b, e, h) K- and (c, f, i) Ca-feldspar end-members in the three different reference axis. Colors indicate the physical state of feldspars in the simulation: blue - fluid, green - mixture of liquid and gas, gray crosses - viscous fluid/simulation which did not reached the minimum ergodicity. The black crosses indicate the liquid spinodals as summarized in the table 6.2. The dashed black line is a guide to the eye for the spinodal curve. Critical point lies in the orange rectangles, see the previous section for numerical values.

2.5–2.7 g cm^{-3} density range for feldspars. We model the initial state using standard static calculations on ideal triclinic feldspar crystals. The effect on the Hugoniot lines of the temperature variations due to the thickness of the crust or to the possible presence of a shallow atmosphere are negligible.

For the second scenario, we assume the surface temperature to be close to the melting temperature of feldspars, as if a magma ocean has just crystallized. The melting temperature of feldspars varies with the composition. It ranges from 1383 K for albite to 1823 K for anorthite (Bowen, 1913), and is around 1473 K for the K-end-member (Lange, 2007). We choose to use 1932 K as initial temperature in order to compare our results with those obtained experimentally by Asimow and Ahrens (2010) on anorthite. This scenario is particularly relevant for the crystallization of the Moon. Feldspars float in the lunar magma ocean but they may behave differently in magma oceans of other terrestrial bodies (Taylor, 1982). For this scenario the Hugoniot curve lies at higher temperatures and pressures than in the previous case.

For the third scenario, temperatures are similar to those at the surface of a hot magma ocean, as covered for example by a thick silicate atmosphere. The density of a liquid feldspar is much lower than its corresponding solid form. This effect combined with the thermal expansion of liquids leads to a density of 2.26 g cm^{-3} at a temperature of 3000 K in the case of the K-end-member (Lange, 2007). The calculated Hugoniot line is the highest in both temperature and pressure from all the three scenarii.

As shown in figure 6.10(a,c), up to 5000 K the three feldspars have similar Hugoniot equations of state. At higher temperatures the Hugoniot pressure of the Ca- and K-feldspars deviates by up to 75 GPa above that of the Na-feldspar and the Hugoniot temperature by about 5000 K above that of the Na-feldspar. For all feldspars, the initial temperature has weak to moderate influence on the final Hugoniot pressure and temperature respectively, but decreasing the initial density leads to considerably higher Hugoniot temperatures. The pressure-density projection (figure 6.10b,d) shows that our cold Hugoniot curves are shifted by at most 10 GPa towards higher pressures compared to the experimental shock data on feldspars (Ahrens, 1973; Ahrens *et al.*, 1969; Boslough *et al.*, 1986a,b; McQueen *et al.*, 1967). The same observation can be made between the shock experiments performed by Asimow and Ahrens (2010) after heating an anorthite at 1932 K and our orange Hugoniot curve corresponding to the same thermal initial state (1932 K). Like us, their data do not show any difference between the different feldspar compositions. We do not capture the curve of the Hugoniot below 75 GPa (highlighted by the experimental data and represented here with a cubic interpolation) since the first high density isotherm we have is located at 3000 K.

We do not specifically calculate the Hugoniot equations of state beyond 20 000 K since the pseudopotentials are missing electronic states that might be occupied at such

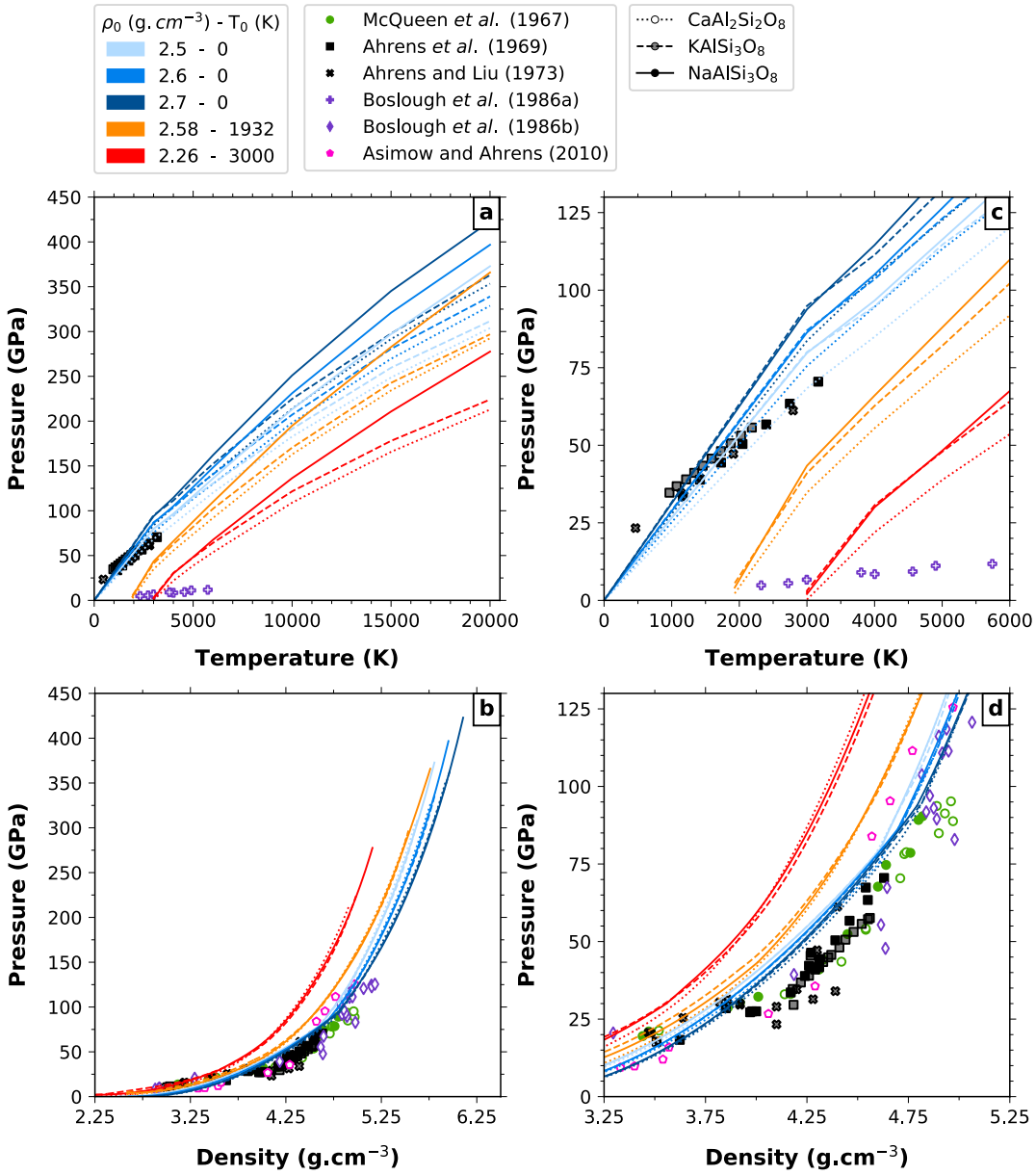

Figure 6.10 – Hugoniot curves for each initial temperature and density of the crust (colors) on several projections: (a) pressure-temperature, (b) pressure-density and their associated zoom on the low pressure range (c) and (d). Data from experiments on feldspars are indicated by the colored markers. The feldspars composition is represented by the line styles for the Hugoniot curves and by the markers filling for the experimental data: solid symbols - $NaAlSi_3O_8$, half transparent symbols - $KAlSi_3O_8$, open symbols - $CaAl_2Si_2O_8$. A cubic interpolation is used to smooth the Hugoniot curves in the pressure-density projection. The same figure for the last projection (temperature-density) is available in annex, figure A.30.

high temperatures. However we are able to provide an extrapolated estimate based on the computed lower temperatures (see tables B.3, B.4 and B.5 in annex).

To infer the shock state under large impacts for the Earth crust we choose velocities for the impactor of 12.9, 15.2 and 18.1 km s^{-1}. These values correspond respectively to the first, second and third quartile of the Earth impactor velocities obtained on a basis of 1487 impacts generated for the Earth in the work of Raymond *et al.* (2013) (personal communication) on planetary impacts during the late veneer (figure 6.11a). We employ the formalism from Raymond *et al.* (2013) (Eq. 3, 4 and 5) to compute the two-body escape velocities along with the impact velocities on the Moon from the same impact distribution. Then, for the impacts on the Moon, we obtain velocities of 8.3, 11.5 and 15.2 km s^{-1} (figure 6.11b). We consider all the impactors to have a density of 3.0 g cm^{-3} regardless of their possible composition, as in Raymond *et al.* (2013), and 0 K temperature.

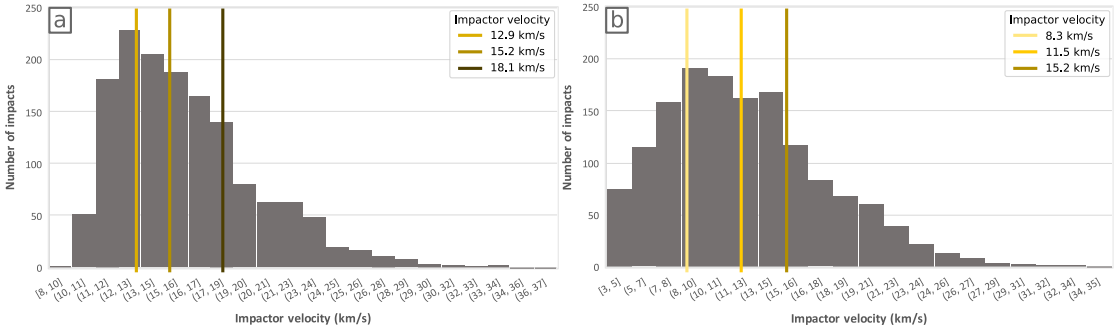

Figure 6.11 – Impact distributions for (a) Earth and (b) Moon during the late veneer obtained on a basis of 1487 impacts generated for the Earth in the work of Raymond *et al.* (2013) (personal communication). The impact velocities used in the impedance match method figure 6.12 are the first, second and third quartile of these distributions (yellow shades).

Then we compute the peak pressure at the moment of impact after the first shock wave using the impedance match method (Forbes, 2012) presented in figure 6.12 and described in section 6.1.4. For this we intersect the cold Hugoniot of the impactor, computed using the results of this study, with the various Hugoniot equations of the cold, hot, or molten feldspar crust, as described above. We consider the impact velocities described before to anchor the state of the impactor. Figure 6.13 illustrates the results of the different scenarios for each impactor velocity and feldspar.

For impact velocities lower than about 10 km s^{-1} in a cold crust the peak temperatures would remain below 4500 K and pressures below about 125 GPa; at these conditions the crust would enter a pre-melting regime or might even melt. At impact velocities larger than 10 km s^{-1} but still in a cold crust, the peak conditions would exceed 7500 K in temperature and about 200 GPa in pressure. At these conditions the crust would melt to participate in local magma ponds or magma seas.

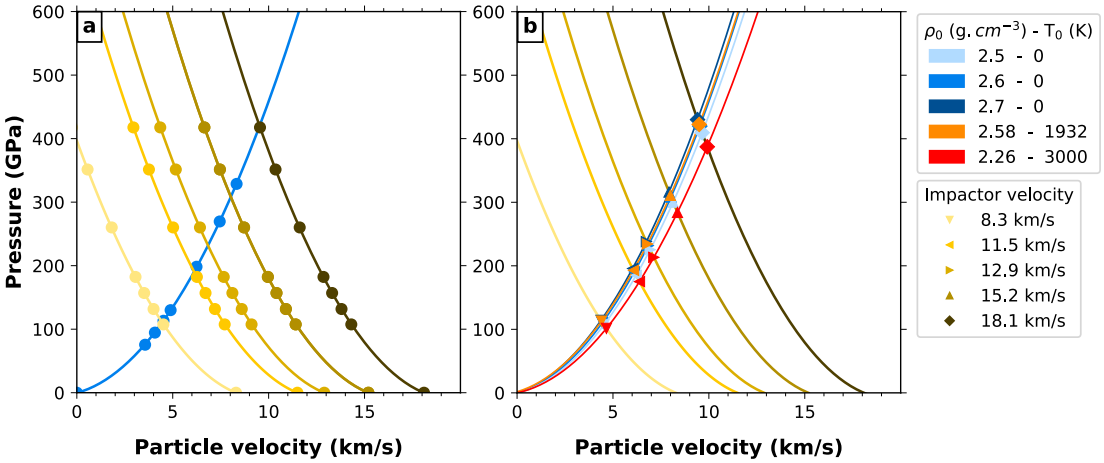

Figure 6.12 – Example of impedance match method applied to $CaAl_2Si_2O_8$. (a) shows the construction of the P-u_p curves from the equations 6.16 and 6.17 using the Hugoniot points (dots) for each impactor velocities and only one initial state of the crust. The intersection between these curves gives the shock pressures and particle velocities, represented in (b) by the colored symbols for every crustal initial state and impactor velocity.

However impacts in hot crust, or even where local magma ponds may exist, see a very different outcome. In this case the temperatures can reach between 10 000 K and up to 30 000 K depending on the impactor velocity. At these conditions the integrity of the crust would be completely erased, as all materials would melt and reach supercritical state. The crust would be entirely part of the protolunar disk, bringing a silica- and alkali-rich contribution. This was the case of the Giant Impact.

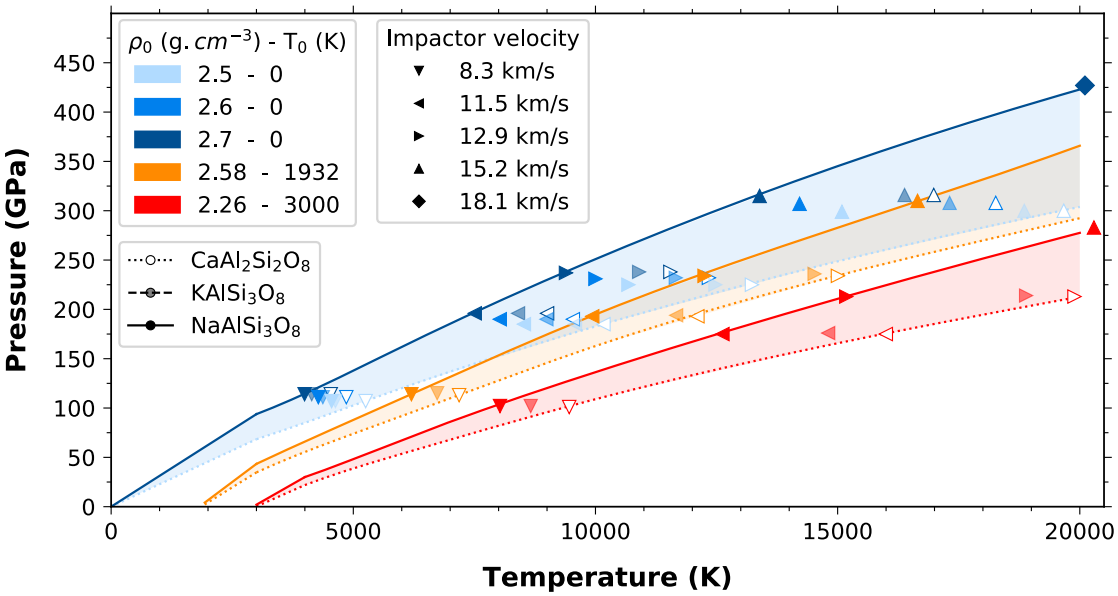

Figure 6.13 – Using the impedance match method (figure 6.12 and section 6.1.4), we represented the peak conditions for each impactor velocity (symbol shapes) and initial temperature and density of the crust (colors) on the pressure-temperature projection. For clarity only ranges of the Hugoniot curves for the three feldspars are represented here for the three scenarios. The filling of symbols correspond to each feldspar end-member: solid symbols - $NaAlSi_3O_8$, half transparent symbols - $KAlSi_3O_8$, open symbols - $CaAl_2Si_2O_8$. For individual Hugoniot lines refer to the figure 6.10.

CHAPTER 7

CONCLUSION

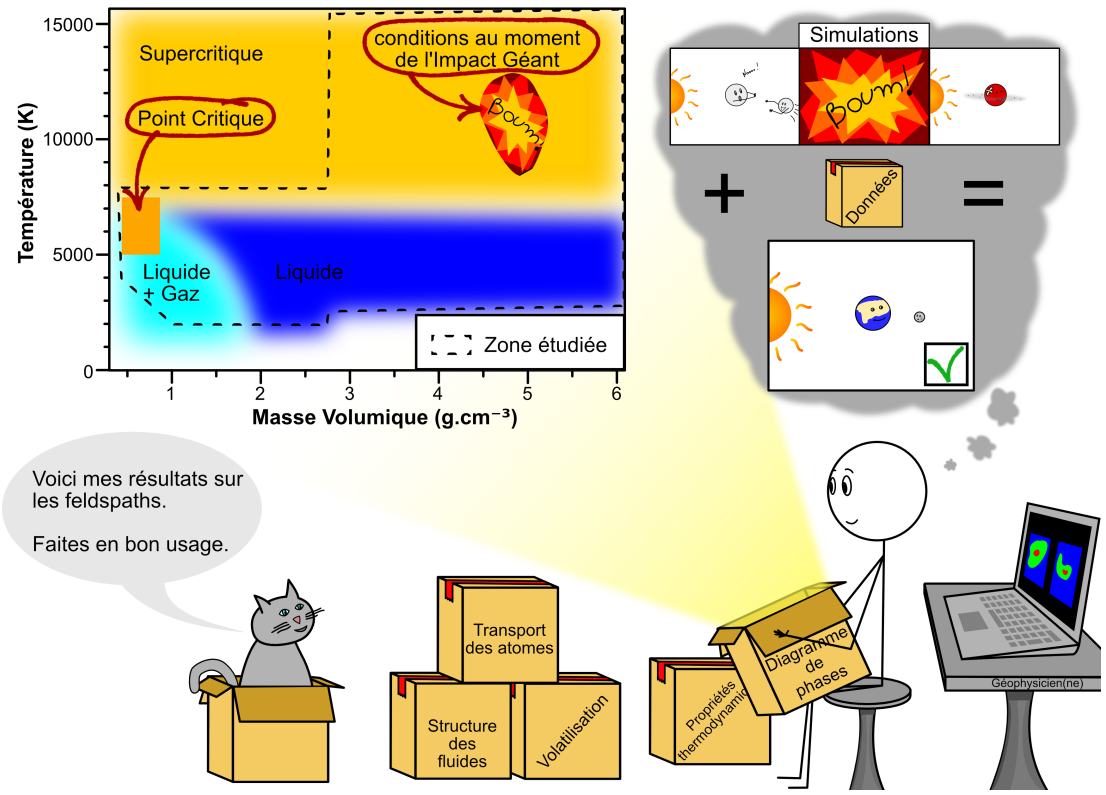

J'ai obtenu un grand nombre de données sur les feldspaths et en particulier la position du point critique. Si les géophysiciens travaillant sur les simulations d'impacts géants utilisent mes données, peut-être pourront-ils améliorer leurs simulations.

Un petit mot pour finir

Ce travail de thèse avait principalement deux buts : 1) améliorer notre connaissance des propriétés des feldspaths dans une large gamme de masses volumiques et températures typiques des impacts météoritiques et du disque protolunaire et 2) étudier l'état physique des feldspaths pendant l'Impact Géant.

Les expériences par ordinateur réalisées entre 2000 et 7500 K et entre 0.5 et 6 g cm^{-3} nous ont ainsi permis d'obtenir un diagramme de phases indicatif des feldspaths, figure 7.1, autour de la transition liquide-gaz sur lequel on peut superposer les zones indiquant combien d'atomes O se trouvent autour des atomes Si (la coordinence dominante de Si avec O). Nous avons obtenu une estimation de la température (T_c), pression (P_c) et masse volumique (ρ_c) du point critique (point de contact entre les zones "liquide", "gaz" et "mélange liquide-gaz" dans le diagramme de phases) :

NaAlSi$_3$O$_8$ $6000 \leq T_c(\mathrm{K}) \leq 6500\,;\ 0.44 \leq \rho_c(\mathrm{g\,cm^{-3}}) \leq 0.62\,;\ 0.1 < P_c(\mathrm{GPa}) \leq 0.2$

KAlSi$_3$O$_8$ $5000 \leq T_c(\mathrm{K}) \leq 5500\,;\ 0.56 \leq \rho_c(\mathrm{g\,cm^{-3}}) \leq 0.87\,;\quad 0 < P_c(\mathrm{GPa}) \leq 0.1$

CaAl$_2$Si$_2$O$_8$ $7000 \leq T_c(\mathrm{K}) \leq 7500\,;\ 0.57 \leq \rho_c(\mathrm{g\,cm^{-3}}) \leq 0.79\,;\ 0.1 < P_c(\mathrm{GPa}) \leq 0.2$

Nous avons vu, par exemple, la formation de bulles dans les feldspaths liquides en dessous de la température critique et d'environ 1.5 g cm^{-3}. Parfois, de petites espèces chimiques flottent librement dans ces bulles et constituent un début de phase gazeuse. On retrouve majoritairement des ions Na et K, mais aussi de petites molécules comme SiO, SiO_2 et O_2. Il y a très peu, voire pas du tout, d'espèces chimiques contenant des éléments Ca et Al dans la phase gazeuse. On dit alors que la vaporisation du liquide est incongruente (le gaz n'a pas la même composition en éléments chimiques que le liquide).

L'étude des feldspaths à très hautes masses volumiques et températures (jusqu'à 20 000 K) nous permet d'estimer l'état physique qu'une croûte planétaire composée de feldspaths pourrait avoir lors d'un impact météoritique. Lorsque l'impact se produit sur une croûte froide (0 K) il pourrait au maximum faire fondre la croûte. Au contraire, lorsque l'impact a lieu sur une croûte chaude (2000 K) voire sur un océan de magma (3000 K), les températures atteintes lors d'un impact du type Impact Géant sont d'au moins 10 000 K et peuvent monter jusqu'à 30 000 K. Dans ces cas, toute la partie de la croûte composée de feldspaths serait transformée en fluide supercritique.

L'ensemble des données (thermodynamique, structure, etc.) produites dans cette thèse seront disponibles en libre accès. Elle seront bientôt accompagnées de données sur d'autres matériaux géologiques d'intérêt comme le fer, SiO_2 ou MgO dans le cadre du projet IMPACT de Razvan Caracas. Ainsi nous espérons que les géophysiciens pourront améliorer leurs modèles d'impacts géants et de formation de la Lune à partir du disque protolunaire.

Brief reminder The goals of this thesis, presented in section 1.4, can be summarized into two categories, each associated to one of the following sections:

1. Improve our knowledge of feldspar minerals properties (structure, thermodynamics, etc.) over a wide range of temperatures and densities typical of meteoric impacts and of the protolunar disc.

2. Investigate the physical state of feldspars during the Giant Impact.

7.1 Main results

We investigated feldspar properties between 2000 and 7500 K and between 0.5 and 6 g cm^{-3}, which corresponds to a pressure range of about 300 GPa. Most of the main results obtained in this thesis can be summarized in a single "phase diagram", shown in figure 7.1.

The spinodal analysis was applied on our low densities data sets to obtain the following estimations for the position of the critical points:

NaAlSi$_3$O$_8$ $6000 \leq T_c(\mathrm{K}) \leq 6500$; $0.44 \leq \rho_c(\mathrm{g\,cm^{-3}}) \leq 0.62$; $0.1 < P_c(\mathrm{GPa}) \leq 0.2$

KAlSi$_3$O$_8$ $5000 \leq T_c(\mathrm{K}) \leq 5500$; $0.56 \leq \rho_c(\mathrm{g\,cm^{-3}}) \leq 0.87$; $0 < P_c(\mathrm{GPa}) \leq 0.1$

CaAl$_2$Si$_2$O$_8$ $7000 \leq T_c(\mathrm{K}) \leq 7500$; $0.57 \leq \rho_c(\mathrm{g\,cm^{-3}}) \leq 0.79$; $0.1 < P_c(\mathrm{GPa}) \leq 0.2$

Below the critical temperatures and at low densities (below about 1.5 g cm^{-3}), we identify the formation of cavities inside the big cluster of atoms forming the melt. We also see small chemical species free-floating inside these cavities. We interpret this as gas bubble nucleation. The very first gas is mostly made of free Na or K and of SiO, SiO_2 and O_2 molecules. We see only very few species containing Al or Ca, which makes the vaporization incongruent. The liquid is then enriched in Al and Ca relative to the other cations. This may explain why the Na and K end-members are almost absent of the Moon crust. The incongruent volatilization of feldspar also implies that the search of spinodals and of the phase diagrams are more complex than initially thought, since another dimension with composition should be taken into account. For the alkali feldspars, about 50 % of the gas is made of the free floating interstitial cations at 4000 K, whereas at 6000 K they only represent about 10 % of the gas species (i.e. small species in the bimodal distribution of the species sizes). At high temperatures SiO, SiO_2 and O_2 become the major species. Visscher and Fegley Jr. (2013) observe the same phenomenon but at lower temperatures. We notice also an O_2 degassing of the fluids above 4000 K at all densities, including in the liquid phase where no bubbles can be seen. When O_2 appears, it represents about 20–30 % of the small species, which is consistent with the

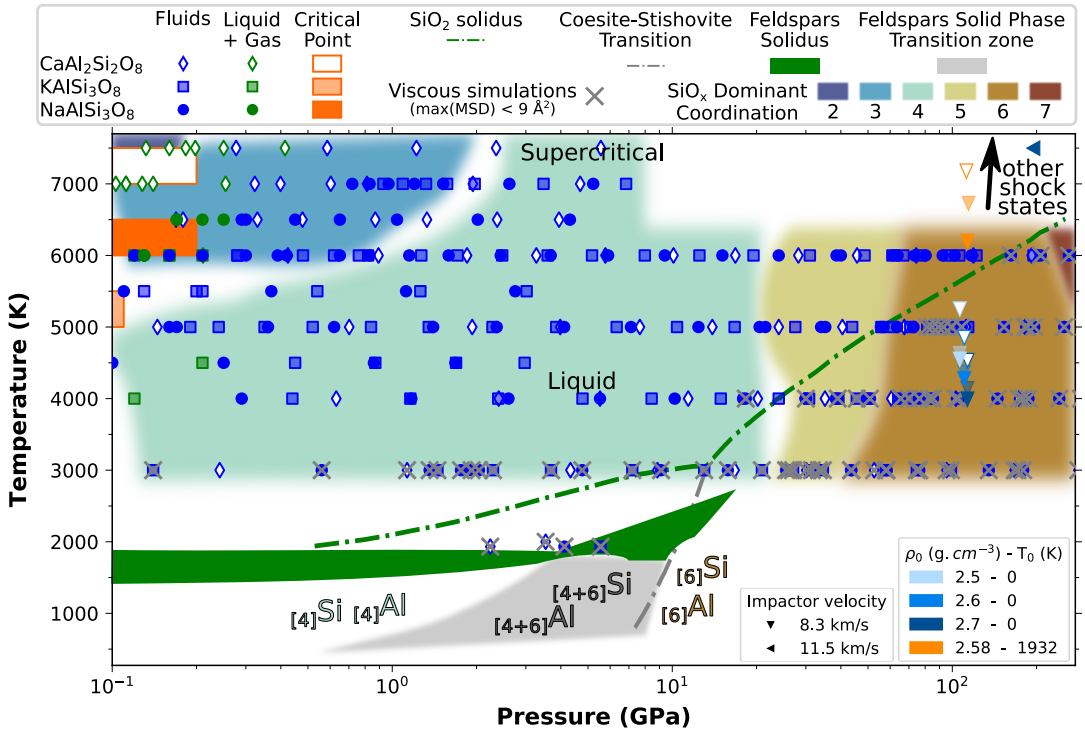

Figure 7.1 – Summary of most of the major results obtained here in the temperature-density projection for the three feldspars. The symbols are our simulation points. They are green if bubbles are visible in the simulation, blue else. The green and the gray regions respectively represent all the feldspars solidus and the solid-solid phase transitions from Akaogi *et al.* (2004); Bell and Roseboom Jr. (1969); Lindsley (1966); Litvin and Gasparik (1993); Newton and Smith (1967); Urakawa *et al.* (1994). Dash-dotted lines are solidus (green) and coesite-stishovite phase transition (gray) for silica from Tsuchiya and Tsuchiya (2011); Zhang *et al.* (1996). Background colors indicate the number of O atoms in the SiO_x coordination polyhedra that dominates the structure of our computed melt. These regions are obtained by combining those presented in figure 3.14 for the three end-members. The viscous simulations are those for which the least diffusive element (Si) did not jump to the next crystallographic site withing the length of the simulation, i.e. the MSD did not reach at least 9 $Å^2$ at the end of the simulation (see table A.5). The shock states are obtained from figure 6.13.

mole fraction abundance of the silicate vapor obtained by Visscher and Fegley Jr. (2013). This degassing is also seen in $MgSiO_3$ (Xiao and Stixrude, 2018) and in silica (Green *et al.*, 2018) even though O_2 molecules do not live more than tens of femtoseconds in silica.

In the liquid state, the three-dimensional framework of AlO_n and SiO_n polyhedra, inherited from the crystal structure, is conserved. Around 3000 K and 1 GPa, close to the conditions of a hot magma, the coordination of the melt is dominated by tetrahedra of AlO_4 and SiO_4. The coordination increases continuously with pressure and the melts are dominated by AlO_6 and SiO_6 around 100 GPa. Below 2.5 g cm^{-3} and at 3000 K, in other words in the extension regime corresponding to negative pressures (not shown on figure 7.1) we see AlO_3 and SiO_3 appear. Around or above the critical temperature we

also see AlO_3 and SiO_3 and even smaller coordination polyhedra.

The self-diffusion coefficients show the same temperature and density dependence as seen before with several numerical experiments (e.g de Koker, 2010; Neilson *et al.*, 2016): the self-diffusivity of feldspars increases as temperature increases and density decreases. Below about $3\,\mathrm{g\,cm^{-3}}$, interstitial cations are more diffusive than the other elements, especially at 3000 K. Ca is the less diffusive of the three interstitial cations and even shows a decrease of its self-diffusivity below 5000 K as the system enters the two-phases region (about $2\,\mathrm{g\,cm^{-3}}$ at 3000 K and $1.5\,\mathrm{g\,cm^{-3}}$ at 4000 K). Around the critical temperature this decreases of self-diffusivity disappear. The very viscous simulations, i.e. those for which the least diffusive element (Si) did not jump to the next crystallographic site withing the length of the simulation, seem to approximately follow the solidus. They may indicate a transition zone between the solid and the liquid state, especially if the simulations are long enough.

We performed additional simulations at very high densities and temperatures (up to 20 000 K) in order to obtain the shock state of feldspars, modeled by Hugoniot equations of state. We considered three initial thermal states of a planetary crust made of feldspars: cold (0 K), warm (1932 K) and hot (3000 K). We obtained the shock pressure, temperature and density for several impact velocities typical of meteoric impacts during the late veneer. We combined these data with the indicative phase diagrams of feldspars we produced in order to obtain the physical state of a feldspathic crust during impacts. This shows that impacts in a cold crust would at most locally melt the crust. On the contrary, impacts in a hot crust or where magma ponds may exist would bring the crust into supercritical state.

7.2 Implications for the Giant Impact

The Giant Impact is usually thought to have happened in the early history of Earth, after the differenciation started and with an initial surface temperature of about 2000 K (e.g Canup, 2004). Recently, a global magma ocean was even assumed to exist at the surface of the proto-Earth at the moment of impact (Hosono *et al.*, 2019). This corresponds to the second and third scenarii (warm and hot crust) we used to compute the shock state of feldspars. For an initial impact velocity around Earth's escape velocity this leads to shock temperatures of about 10 000 K for the second scenario and up to about 15 000 K for the third scenario. In these cases, the feldspathic part of the crust would be totally molten and even in a supercritical state. Recent studies on $MgSiO_3$ (Xiao and Stixrude, 2018) and silica (Green *et al.*, 2018) showed critical temperatures similar to those obtained for feldspars. Thus, it is likely that a substantial part of the crust would have been in a supercritical state. This particular state of the matter may have played

a key role in the evolution of the protolunar disk or the synestia (Lock *et al.*, 2018).

On the density profiles of the protolunar disk obtained by smooth particle hydrodynamic (SPH) simulations (e.g Canup, 2012; Canup and Asphaug, 2001) we see that most of the disk has a density smaller than the critical density estimated here. This means the disk is mainly only made of one phase, which is either gas or supercritical depending on the temperature profile. To say more about the physical state of the disk we would need both density and temperature profile in the disk.

7.3 To be continued...

Even if the crusts of the two proto-planets constitute the protolunar disk, they would represent only a very small portion. Most of the material from the protolunar disk came from the mantles of the proto-planets and in a lesser amount from the core of the proto-Earth. That is why it is important to perform similar studies as this one on many other materials, typical of the whole planet. This is already an on-going work with the IMPACT project (see Razvan Caracas webpage). Following this work on feldspars, studies on other material such as pyrolite, iron, silica with water or MgO will soon be completed. We trust that all the data that will be available in open access will help geophysicists improving impact simulations and disk accretion models.

BIBLIOGRAPHY

O. Adjaoud, G. Steinle-Neumann, and S. Jahn. Mg_2SiO_4 liquid under high pressure from molecular dynamics. Chemical Geology, 256(3–4):185–192, 2008.

T. J. Ahrens. A shock-induced phase change in orthoclase. Journal of Geophysical Research, 78(8):1274–1278, 1973.

T. J. Ahrens, C. F. Petersen, and J. T. Rosenberg. Shock compression of feldspars. Journal of Geophysical Research, 74(10):2727–2746, 1969.

M. Akaogi, N. Kamii, A. Kishi, and H. Kojitani. Calorimetric study on high-pressure transitions in $KAlSi_3O_8$. Physics and Chemistry of Minerals, 31(2):85–91, 2004.

M. P. Allen and D. J. Tildesley. Computer Simulation of Liquids (Oxford Science Publications). Clarendon Press, 1989.

D. L. Anderson. 2 Earth and Moon. In Theory of the Earth, pages 27–45. Boston, MA, blackwell scientific publications edition, 1989. ISBN 0-86542-335-0.

R. J. Angel. Feldspars at High Pressure. In I. Parsons, editor, Feldspars and Their Reactions, NATO ASI Series, pages 271–312. Springer Netherlands, Dordrecht, 1994. ISBN 978-94-011-1106-5.

R. J. Angel, M. A. Carpenter, and L. W. Finger. Structural variation associated with compositional variation and order-disorder behavior in anorthite-rich feldspars. American Mineralogist, 75:150–162, 1990.

R. M. G. Armytage, R. B. Georg, H. M. Williams, and A. N. Halliday. Silicon isotopes in lunar rocks: Implications for the Moon's formation and the early history of the Earth. Geochimica et Cosmochimica Acta, 77:504–514, 2012.

P. D. Asimow and T. J. Ahrens. Shock compression of liquid silicates to 125 GPa: The anorthite-diopside join. Journal of Geophysical Research: Solid Earth, 115(B10), 2010.

E. Asphaug. Impact Origin of the Moon? Annual Review of Earth and Planetary Sciences, 42(1):551–578, 2014.

S. K. Bajgain and M. Mookherjee. Structure and Properties of Albite Melt at High Pressures. ACS Earth and Space Chemistry, 4(1):1–13, 2020.

A. C. Barr. On the origin of Earth's Moon. Journal of Geophysical Research: Planets, 121(9):1573–1601, 2016.

P. M. Bell and E. H. Roseboom Jr. Melting relationships of jadeite and albite to 45 kilobars with comments on melting diagrams of binary systems at high pressures. Mineralogical Society of America Special Paper, 2(Pyroxenes And Amphiboles: Crystal Chemistry And Phase Petrology):151–162, 1969.

M. Benoit, S. Ispas, and M. E. Tuckerman. Structural properties of molten silicates from ab initio molecular-dynamics simulations: Comparison between CaO-Al_2O_3-SiO_2 and SiO_2. Physical Review B, 64:224205–224205, 2001.

A. B. Binder. On the origin of the moon by rotational fission. The moon, 11(1):53–76, 1974.

K. Binder, B. J. Block, P. Virnau, and A. Tröster. Beyond the Van Der Waals loop: What can be learned from simulating Lennard-Jones fluids inside the region of phase coexistence. American Journal of Physics, 80(12):1099–1109, 2012.

P. E. Blöchl. Projector augmented-wave method. Physical Review B, 50:17953–17979, 1994.

P. T. Boggs, R. H. Byrd, J. E. Rogers, and R. B. Schnabel. User's Reference Guide for ODRPACK Version 2.01 Software for Weighted Orthogonal Distance Regression, 1992.

M. Born and R. Oppenheimer. Zur Quantentheorie der Molekeln. Annalen der Physik, 389(20):457–484, 1927.

M. B. Boslough, T. J. Ahrens, and A. C. Mitchell. Shock temperatures in anorthite glass. Geophysical Journal of the Royal Astronomical Society, 84(3):475–489, 1986a.

M. B. Boslough, S. M. Rigden, and T. J. Ahrens. Hugoniot equation of state of anorthite glass and lunar anorthosite. Geophysical Journal of the Royal Astronomical Society, 84(3):455–473, 1986b.

N. L. Bowen. The melting phenomena of the plagioclase feldspars. American Journal of Science, Series 4 Vol. 35(210):577–599, 1913.

A. G. W. Cameron and W. R. Ward. The Origin of the Moon. In Abstracts of Papers Submitted to the Seventh Lunar Science Conference, volume 7, page 120, 1976.

R. M. Canup. Dynamics of Lunar Formation. Annual Review of Astronomy and Astrophysics, 42(1):441–475, 2004.

R. M. Canup. Forming a Moon with an Earth-like Composition via a Giant Impact. Science, 338(6110):1052–1055, 2012.

R. M. Canup and E. Asphaug. Origin of the Moon in a giant impact near the end of the Earth's formation. Nature, 412(6848):708–712, 2001.

R. Caracas. Giant Impact project. razvancaracas.info/impact/.

R. Caracas, K. Hirose, R. Nomura, and M. D. Ballmer. Melt–crystal density crossover in a deep magma ocean. Earth and Planetary Science Letters, 516:202–211, 2019.

R. Caracas, A. Kobsch, N. V. Solomatova, Z. Li, F. Soubiran, and J.-A. Hernandez. Analyzing melts and fluids from ab initio molecular dynamics simulations. Journal of Visualized Experiments, accepted, 2020a.

R. Caracas, A. Kobsch, N. V. Solomatova, Z. Li, F. Soubiran, and J.-A. Hernandez. rcaracas/umd_package 1.0.0, 2020b. URL https://doi.org/10.5281/zenodo.3710978.

R. Caracas, A. Kobsch, N. V. Solomatova, Z. Li, F. Soubiran, and J.-A. Hernandez. UMD package. github.com/rcaracas/UMD_package/releases/tag/1.0.0, 2020c.

Frédéric Caupin and Eric Herbert. Cavitation in water: A review. Comptes Rendus Physique, 7(9):1000–1017, 2006.

S. Charnoz and C. Michaut. Evolution of the protolunar disk: Dynamics, cooling timescale and implantation of volatiles onto the Earth. Icarus, 260:440–463, 2015.

D. J. Cherniak. Cation Diffusion in Feldspars. Reviews in Mineralogy and Geochemistry, 72(1):691–733, 2010.

M. Ćuk and S. T. Stewart. Making the Moon from a Fast-Spinning Earth: A Giant Impact Followed by Resonant Despinning. Science, 338(6110):1047–1052, 2012.

G. Darwin. On the Bodily Tides of Viscous and Semi-Elastic Spheroids, and on the Ocean Tides upon a Yielding Nucleus. Philosophical Transactions of the Royal Society of London, 170:1–35, 1879.

N. de Koker. Structure, thermodynamics, and diffusion in $CaAl_2Si_2O_8$ liquid from first-principles molecular dynamics. Geochimica et Cosmochimica Acta, 74(19):5657–5671, 2010.

N. P. de Koker, L. Stixrude, and B. B. Karki. Thermodynamics, structure, dynamics, and freezing of Mg_2SiO_4 liquid at high pressure. Geochimica et Cosmochimica Acta, 72(5):1427–1441, 2008.

T. S. Duffy and R. F. Smith. Ultra-High Pressure Dynamic Compression of Geological Materials. Frontiers in Earth Science, 7, 2019.

C. Fiolhais, F. Nogueira, and M. A. L. Marques, editors. A Primer in Density Functional Theory. Lecture Notes in Physics 620. Springer-Verlag Berlin Heidelberg, first edition, 2003. ISBN 978-3-540-03083-6.

H. Flyvbjerg and H. G. Petersen. Error estimates on averages of correlated data. The Journal of Chemical Physics, 91(1):461–466, 1989.

J. W. Forbes. Shock Wave Compression of Condensed Matter: A Primer. Shock Wave and High Pressure Phenomena. Springer, Heidleberg, 2012. ISBN 978-3-642-32534-2.

C. Freda and D. R Baker. Na-K interdiffusion in alkali feldspar melts. Geochimica et Cosmochimica Acta, 62(17):2997–3007, 1998.

D. Frenkel and B. Smit. Chapter 2 - Statistical Mechanics. In D. Frenkel and B. Smit, editors, Understanding Molecular Simulation (Second Edition), pages 9–22. Academic Press, 2002a.

D. Frenkel and B. Smit. Chapter 4 - Molecular Dynamics Simulations. In D. Frenkel and B. Smit, editors, Understanding Molecular Simulation (Second Edition), pages 63–107. Academic Press, 2002b.

D. Frenkel and B. Smit. Chapter 6 - Molecular Dynamics in Various Ensembles. In D. Frenkel and B. Smit, editors, Understanding Molecular Simulation (Second Edition), pages 139–163. Academic Press, 2002c.

M. S. Ghiorso, D. Nevins, I. Cutler, and F. J. Spera. Molecular dynamics studies of $CaAl_2Si_2O_8$ liquid. Part II: Equation of state and a thermodynamic model. Geochimica et Cosmochimica Acta, 73(22):6937–6951, 2009.

E. C. R. Green, E. Artacho, and J. A. D. Connolly. Bulk properties and near-critical behaviour of SiO_2 fluid. Earth and Planetary Science Letters, 491:11–20, 2018.

A. N. Halliday. The Origin of the Moon. Science, 338(6110):1040–1041, 2012.

Y. Hariya and G. C. Kennedy. Equilibrium study of anorthite under high pressure and high temperature. American Journal of Science, 266(3):193–203, March 1968.

W. K. Hartmann and D. R. Davis. Satellite-sized planetesimals and lunar origin. Icarus, 24(4):504–515, 1975.

J.-P. Harvey and P. D. Asimow. Current limitations of molecular dynamic simulations as probes of thermo-physical behavior of silicate melts. American Mineralogist, 100: 1866–1882, 2015.

W. M. Haynes, editor. CRC Handbook of Chemistry and Physics. Taylor and Francis Group, LLC, ninety-second edition, 2011. ISBN 978-1-4398-5511-9.

E. R. Hernández, J. Brodholt, and D. Alfè. Structural, vibrational and thermodynamic properties of Mg_2SiO_4 and $MgSiO_3$ minerals from first-principles simulations. Physics of the Earth and Planetary Interiors, 240:1–24, 2015.

P. Hohenberg and W. Kohn. Inhomogeneous Electron Gas. Physical Review, 136:B864–B871, 1964.

W. G. Hoover. Canonical dynamics: Equilibrium phase-space distributions. Physical Review A, 31(3):1695–1697, 1985.

N. Hosono, S. Karato, J. Makino, and T. R. Saitoh. Terrestrial magma ocean origin of the Moon. Nature Geoscience, page 1, 2019.

W. Humphrey, A. Dalke, and K. Schulten. VMD – Visual Molecular Dynamics. Journal of Molecular Graphics, 14:33–38, 1996.

Jónsson group and Henkelman group. Transition State Tools for VASP. theory.cm.utexas.edu/vtsttools/index.html.

B. B. Karki, D. Bhattarai, and L. Stixrude. First-principles simulations of liquid silica: Structural and dynamical behavior at high pressure. Physical Review B, 76(10): 104205, 2007.

B. B. Karki, B. Bohara, and L. Stixrude. First-principles study of diffusion and viscosity of anorthite ($CaAl_2Si_2O_8$) liquid at high pressure. American Mineralogist, 96(5-6): 744–751, 2011.

B. B. Karki, D. B. Ghosh, and S. K. Bajgain. Chapter 16 - Simulation of Silicate Melts Under Pressure. In Y. Kono and C. Sanloup, editors, Magmas Under Pressure, pages 419–453. Elsevier, Amsterdam, 2018. ISBN 978-0-12-811301-1.

A. Kobsch. Complements to the UMD package. github.com/Astranais/MD_postprocessing, 2020.

A. Kobsch and R. Caracas. Thermodynamics data of Alkali Feldspars from FPMD simulations, 2020. URL https://doi.org/10.5281/zenodo.3860527.

W. Kohn and L. J. Sham. Self-Consistent Equations Including Exchange and Correlation Effects. Physical Review, 140:A1133–A1138, 1965.

R. G. Kraus, S. T. Stewart, D. C. Swift, C. A. Bolme, R. F. Smith, S. Hamel, B. D. Hammel, D. K. Spaulding, D. G. Hicks, J. H. Eggert, and G. W. Collins. Shock vaporization of silica and the thermodynamics of planetary impact events. Journal of Geophysical Research: Planets, 117:E09009–E09009, 2012.

G. Kresse and J. Furthmüller. Efficiency of ab-initio total energy calculations for metals and semiconductors using a plane-wave basis set. Computational Materials Science, 6(1):15–50, 1996a.

G. Kresse and J. Furthmüller. Efficient iterative schemes for ab initio total-energy calculations using a plane-wave basis set. Physical Review B, 54(16):11169–11186, 1996b.

G. Kresse and J. Hafner. Ab initio molecular dynamics for liquid metals. Physical Review B, 47(1):558–561, 1993.

G. Kresse and D. Joubert. From ultrasoft pseudopotentials to the projector augmented-wave method. Physical Review B, 59:1758–1775, 1999.

R. A. Lange. The density and compressibility of $KAlSi_3O_8$ liquid to 6.5 GPa. American Mineralogist, 92(1):114–123, 2007.

Dien Li, R. A. Secco, G. M. Bancroft, and M. E. Fleet. Pressure induced coordination change of Al in silicate melts from Al K edge XANES of high pressure $NaAlSi_2O_6$-$NaAlSi_3O_8$ glasses. Geophysical Research Letters, 22(23):3111–3114, 1995.

D. H. Lindsley. Melting relations of $KAlSi_3O_8$: Effect of pressures up to 40 kilobars. American Mineralogist, 51(11-12):1793–1799, 1966.

Y. A. Litvin and T. Gasparik. Melting of jadeite to 16.5 GPa and melting relations on the enstatite-jadeite join. Geochimica et Cosmochimica Acta, 57(9):2033–2040, 1993.

S. J. Lock, S. T. Stewart, M. I. Petaev, Z. M. Leinhardt, M. T. Mace, S. B. Jacobsen, and M. Ćuk. The origin of the Moon within a terrestrial synestia. Journal of Geophysical Research: Planets, 123(4):910–951, 2018.

S.-N. Luo, J. A. Akins, T. J. Ahrens, and P. D. Asimow. Shock-compressed $MgSiO_3$ glass, enstatite, olivine, and quartz: Optical emission, temperatures, and melting. Journal of Geophysical Research: Solid Earth, 109(B05205):1–14, 2004.

R. M. Martin. Electronic Structure: Basic Theory and Practical Methods. Cambridge University Press, 2004. ISBN 978-0-511-80576-9.

W. F. McDonough. Earth's Core. In W. M. White, editor, Encyclopedia of Geochemistry: A Comprehensive Reference Source on the Chemistry of the Earth, Encyclopedia of Earth Sciences Series, pages 418–429. Springer International Publishing, 1st edition, 2018. ISBN 978-3-319-39311-7 978-3-319-39312-4.

R. G. McQueen, S. P. Marsh, and J. N. Fritz. Hugoniot equation of state of twelve rocks. Journal of Geophysical Research, 72(20):4999–5036, 1967.

H. J. Melosh. A hydrocode equation of state for SiO_2. Meteoritics & Planetary Science, 42(12):2079–2098, 2007.

N. D. Mermin. Thermal Properties of the Inhomogeneous Electron Gas. Physical Review, 137(5A):A1441–A1443, 1965.

N. A. Morgan and F. J. Spera. Glass transition, structural relaxation, and theories of viscosity: A molecular dynamics study of amorphous $CaAl_2Si_2O_8$. Geochimica et Cosmochimica Acta, 65(21):4019–4041, 2001.

R. T. Neilson, F. J. Spera, and M. S. Ghiorso. Thermodynamics, self-diffusion, and structure of liquid $NaAlSi_3O_8$ to 30 GPa by classical molecular dynamics simulations. American Mineralogist, 101(9):2029–2040, 2016.

H. Nekvasil. Ternary Feldspar/Melt Equilibria: A Review. In Ian Parsons, editor, Feldspars and Their Reactions, NATO ASI Series, pages 195–219. Springer Netherlands, Dordrecht, 1994. ISBN 978-94-011-1106-5.

M. E. J. Newman and G. T. Barkema. Monte Carlo Methods in Statistical Physics. Clarendon Press; Oxford University Press, 1999. ISBN 0-19-851797-1 978-0-19-851797-9 978-0-585-48400-6 0-19-851796-3.

R. C. Newton and J. V. Smith. Investigations concerning the Breakdown of Albite at Depth in the Earth. The Journal of Geology, 75(3):268–286, 1967.

S. Nosé. A unified formulation of the constant temperature molecular dynamics methods. The Journal of Chemical Physics, 81(1):511–519, 1984.

J. A. O'Keefe and E. S. Sullivan. Fission origin of the Moon: Cause and timing. Icarus, 35(2):272–283, 1978.

K. Pahlevan and D. J. Stevenson. Equilibration in the aftermath of the lunar-forming giant impact. Earth and Planetary Science Letters, 262(3):438–449, 2007.

Kaveh Pahlevan, David J. Stevenson, and John M. Eiler. Chemical fractionation in the silicate vapor atmosphere of the Earth. Earth and Planetary Science Letters, 301 (3–4):433–443, 2011.

J. P. Perdew, K. Burke, and M. Ernzerhof. Generalized Gradient Approximation Made Simple. Physical Review Letters, 77(18):3865–3868, 1996.

M. Perfit. Earth's Oceanic Crust. In W. M. White, editor, Encyclopedia of Geochemistry: A Comprehensive Reference Source on the Chemistry of the Earth, Encyclopedia of Earth Sciences Series, pages 430–438. Springer International Publishing, 1st edition, 2018. ISBN 978-3-319-39311-7 978-3-319-39312-4.

S. N. Raymond, H. E. Schlichting, F. Hersant, and F. Selsis. Dynamical and collisional constraints on a stochastic late veneer on the terrestrial planets. Icarus, 226(1):671–681, 2013.

A. Reufer, M. M. M. Meier, W. Benz, and R. Wieler. A hit-and-run giant impact scenario. Icarus, 221(1):296–299, 2012.

P. Richet and Y. Bottinga. Glass transitions and thermodynamic properties of amorphous SiO_2, NaAlSinO2n+2 and $KAlSi_3O_8$. Geochimica et Cosmochimica Acta, 48 (3):453–470, 1984.

A. B. Ronov and A. A. Yaroshevsky. Chemical Composition of the Earth's Crust. In The Earth's Crust and Upper Mantle, pages 37–57. American Geophysical Union (AGU), 1969. ISBN 978-1-118-66897-9.

S. Root, L. Shulenburger, R. W. Lemke, D. H. Dolan, T. R. Mattsson, and M. P. Desjarlais. Shock Response and Phase Transitions of MgO at Planetary Impact Conditions. Physical Review Letters, 115(19):198501, 2015.

E. L. Ruskol. The Origin of the Moon. I. Formation of a Swarm of Bodies Around the Earth. Soviet Astronomy-AJ, 4:657, 1960.

S. K. Saxena and Y. Wang. Chapter Thirteen - Determintation of Pressure-Dependent Phase Diagrams. In J. C. Zhao, editor, Methods for Phase Diagram Determination, pages 412–441. Elsevier Science Ltd, Oxford, 2007. ISBN 978-0-08-044629-5.

S. F. Singer. Origin of the moon by tidal capture and some geophysical consequences. The moon, 5(1):206–209, 1972.

J. V Smith and W. L Brown. Feldspar Minerals. Springer-Verlag, Berlin; New York, 1988. ISBN 978-0-387-17692-5 978-3-540-17692-3.

J. V. Smith, A. T. Anderson, R. C. Newton, E. J. Olsen, P. J. Wyllie, A. V. Crewe, M. S. Isaacson, and D. Johnson. Petrologic history of the moon inferred from petrography, mineralogy, and petrogenesis of Apollo 11 rocks. In A. A. Levinson, editor, Proceedings of the Apollo 11 Lunar Science Conference, pages 897–925. Pergamon Press, New York, NY, 1970. ISBN 978-0-08-016392-5.

N. V. Solomatova and R. Caracas. Pressure-induced coordination changes in a pyrolitic silicate melt from ab initio molecular dynamics simulations. Journal of Geophysical Research: Solid Earth, 124(11), 2019.

F. J. Spera, D. Nevins, M. Ghiorso, and I. Cutler. Structure, thermodynamic and transport properties of $CaAl_2Si_2O_8$ liquid. Part I: Molecular dynamics simulations. Geochimica et Cosmochimica Acta, 73(22):6918–6936, 2009.

J. F. Stebbins, I. S. E. Carmichael, and D. E. Weill. The high temperature liquid and glass heat contents and the heats of fusion of diopside, albite, sanidine and nepheline. American Mineralogist, 68:717–730, 1983.

D. J. Stevenson. Origin of the Moon-The Collision Hypothesis. Annual Review of Earth and Planetary Sciences, 15(1):271–315, 1987.

L. Stixrude and B. Karki. Structure and Freezing of $MgSiO_3$ Liquid in Earth's Lower Mantle. Science, 310(5746):297–299, 2005.

L. Stixrude and C. Lithgow-Bertelloni. Thermodynamics of mantle minerals — I. Physical properties. Geophysical Journal International, 162(2):610–632, 2005.

A. Stracke. Mantle Geochemistry. In W. M. White, editor, Encyclopedia of Geochemistry: A Comprehensive Reference Source on the Chemistry of the Earth, Encyclopedia of Earth Sciences Series, pages 867–877. Springer International Publishing, 1st edition, 2018. ISBN 978-3-319-39311-7 978-3-319-39312-4.

N. Sun, L. Stixrude, N. de Koker, and B. B. Karki. First principles molecular dynamics simulations of diopside ($CaMgSi_2O_6$) liquid to high pressure. Geochimica et Cosmochimica Acta, 75(13):3792–3802, 2011.

D. Sykes, B. T. Poe, P. F. McMillan, R. W. Luth, and R. K. Sato. A spectroscopic investigation of anhydrous $KAlSi_3O_8$ and $NaAlSi_3O_8$ glasses quenched from high pressure. Geochimica et Cosmochimica Acta, 57(8):1753–1759, April 1993.

M. Taylor and G. E. Brown. Structure of mineral glasses—I. The feldspar glasses $NaAlSi_3O_8$, $KAlSi_3O_8$, $CaAl_2Si_2O_8$. Geochimica et Cosmochimica Acta, 43(1):61–75, 1979.

S. R. Taylor. Planetary Science: A Lunar Perspective. Lunar and Planetary Institute, Houston, 1982.

S. R. Taylor. The unique lunar composition and its bearing on the origin of the Moon. Geochimica et Cosmochimica Acta, 51(5):1297–1309, 1987.

S. R. Taylor and S. McLennan. A primary crust: The highland crust of the Moon. In Planetary Crusts: Their Composition, Origin and Evolution, Cambridge Planetary Science, pages 32–60. Cambridge University Press, 2008.

S. R. Taylor and S. M. McLennan. The geochemical evolution of the continental crust. Reviews of Geophysics, 33(2):241–265, 1995.

T. J. Tenner, R. A. Lange, and R. T. Downs. The albite fusion curve re-examined: New experiments and the high-pressure density and compressibility of high albite and $NaAlSi_3O_8$ liquid. American Mineralogist, 92(10):1573–1585, 2007.

S. L. Thompson and H. S. Lauson. Improvements in the CHART D radiation-hydrodynamic code III: Revised analytical equation of state. Technical Report SC-RR-710714, Sandia National Laboratories, Albuquerque, 1972.

J. H. Tillotson. Metallic equations of state for hypervelocity impact. Technical Report GA-3216, General Dynamics San Diego Ca General Atomic Div, 1962.

Taku Tsuchiya and Jun Tsuchiya. Prediction of a hexagonal SiO_2 phase affecting stabilities of $MgSiO_3$ and $CaSiO_3$ at multimegabar pressures. Proceedings of the National Academy of Sciences, 108(4):1252–1255, 2011.

S. Urakawa, T. Kondo, N. Igawa, O. Shimomura, and H. Ohno. Synchrotron radiation study on the high-pressure and high-temperature phase relations of $KAlSi_3O_8$. Physics and Chemistry of Minerals, 21(6):387–391, 1994.

C. Visscher and B. Fegley Jr. Chemistry of Impact-generated Silicate Melt-vapor Debris Disks. The Astrophysical Journal Letters, 767(1):L12–L12, 2013.

J. T. K. Wan, T. S. Duffy, S. Scandolo, and R. Car. First-principles study of density, viscosity, and diffusion coefficients of liquid $MgSiO_3$ at conditions of the Earth's deep mantle. Journal of Geophysical Research: Solid Earth, 112(B03208):1–7, 2007.

W. R. Ward. On the vertical structure of the protolunar disk. The Astrophysical Journal, 744(2):140, 2012.

P. H. Warren. The Magma Ocean Concept and Lunar Evolution. Annual Review of Earth and Planetary Sciences, 13(1):201–240, 1985.

J. A. Wood. Moon over Mauna Loa: A review of hypotheses of formation of Earth's moon. In W. K. Hartmann, R. J. Phillips, and G. J. Taylor, editors, Origin of the Moon, pages 17–56. Lunar & Planetary Institute, Houston, 1986. ISBN 978-0-942862-03-4.

B. Xiao and L. Stixrude. Critical vaporization of $MgSiO_3$. Proceedings of the National Academy of Sciences, 115(21):5371–5376, 2018.

T. Yagi, T. Sakai, H. Kadobayashi, and T. Irifune. Review: High pressure generation techniques beyond the limit of conventional diamond anvils. High Pressure Research, 40(1):148–161, 2020.

J. Zhang, B. Li, W. Utsumi, and R. C. Liebermann. In situ X-ray observations of the coesite-stishovite transition: Reversed phase boundary and kinetics. Physics and Chemistry of Minerals, 23(1):1–10, 1996.

J. Zhang, N. Dauphas, A. M. Davis, I. Leya, and A. Fedkin. The proto-Earth as a significant source of lunar material. Nature Geoscience, 5(4):251–255, 2012.

List of Figures

☾

List of Tables

GLOSSARY

.bonds.inp Bonds file used as input in the `speciation_umd.py` script and containing the first coordination sphere radius for each pair of atoms in the simulation. Is obtained by one of the following scripts: `analyze_gofr_semi_automatic.py` or `plot_distances+analysis_xmin.py`.

.gofr.dat Output file of the `gofrs_umd.py` script giving the pair distribution function of each atomic pair for the input UMD file.

1D one-dimensional

CN coordination number

DAC diamond anvil cell

DFT density functional theory

FPMD first principles molecular dynamics

g(r) Pair distribution function.

gofrs.txt Output file of the `analyze_gofr_semi_automatic.py` script giving the values of xmax,ymax,xmin,coord,bond for each atomic pair selected and each *.gofr.dat* file located in the corresponding subfolder.

INCAR VASP input file.

LCM least common multiple

MD molecular dynamics

MSD mean square displacement

NPT ensemble Isothermal-isobaric ensemble (the number of atoms N, the average pressure P and the average temperature T are kept constant).

NVE ensemble Microcanonical ensemble (the number of atoms N, the volume V and the energy E are kept constant).

NVT ensemble Canonical ensemble (the number of atoms N, the volume V and the average temperature T are kept constant).

ODR orthogonal distance regression

option Option of a python script as defined in section 2.3.2.

OUTCAR VASP ouput file.

SPH smooth particle hydrodynamic

UMD Name for the post-processing package of molecular dynamics simulations developped by our team (Caracas *et al.*, 2020c). Also refers to the *.umd.dat* files created from the OUTCAR file with the `VaspParser.py` script.

VASP® Vienna Ab-initio Simulation Package

VMD Visual Molecular Dynamics

VTST VASP Transition State Tools

GLOSSAIRE FRANÇAIS

diagramme de phases Graphique selon au moins deux grandeurs thermodynamiques (ex. P *vs* ρ, T *vs* ρ) dans lequel est indiqué l'état physique de la matière (liquide, gaz...) pour chaque point, ainsi que les courbes délimitant les zones de changement de phase.

disque Disque protolunaire = disque de débris en orbite autour de la proto-Terre formé à la suite de l'Impact Géant.

feldspath Minéral de formule générale $(Ca,K,Na)(Al,Si)_2O_8$ (aluminosilicate de calcium, potassium ou sodium) très présent dans les croûtes lunaire et terrestre.

Impact Géant Scénario communément accepté par les scientifiques pour expliquer la formation de la Lune impliquant l'impact géant d'une planète en formation, appelée Théïa, avec la Terre en cours de formation, appelée Gaïa. Suite à cet impact un disque de débris provenant des deux planètes est mis en orbite autour de la proto-Terre. C'est l'agglomération (accrétion) des débris de ce disque qui forme la Lune.

K Unité de température appelée le Kelvin. Pour obtenir la température en degrés Celcius (°C) il suffit de retrancher 273.25 à la température exprimée en Kelvins (K).

masse volumique Masse par unité de volume. Masse que possède un matériau qui occupe un certain volume unitaire. Généralement exprimée en $\mathrm{kg\,m^{-3}}$ ou $\mathrm{g\,cm^{-3}}$. Exemple : l'eau a une masse volumique de $1000\,\mathrm{kg\,m^{-3}}$ soit $1\,\mathrm{g\,cm^{-3}}$.

moment angulaire Grandeur physique quantifiant la rotation d'un système (vitesse, axe...). Il est l'analogue de la quantité de mouvement pour la rotation.

supercritique État de la matière existant à des températures et pressions supérieures aux température et pression critiques (T_c,P_c) et ayant les propriétés d'un fluide intermédiaire entre liquide et gaz.

APPENDIX A

ADDITIONAL INFORMATION AND FIGURES

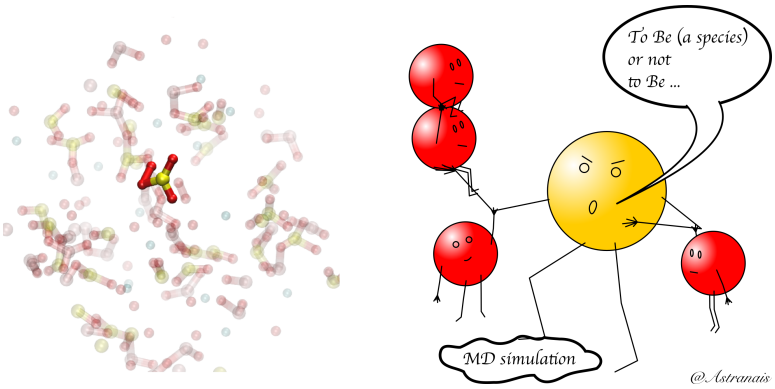

Cartoon inspiré du problème de définition d'une espèce chimique apparu pendant ma thèse : est-ce un SiO_4 ou un SiO_2 un peu trop proche d'un O_2 ? Dilemme...

A.1 INCAR files

A.1.1 Production run

The following file shows the parameters used for a typical production run. When all the MD steps are completed, the same input file can be reused to continue the production run from the last position of atoms.

```
SYSTEM = feldspar_long-run

ISTART  = 1
ISYM = 0
ENCUT = 550                    #change depending on the pseudopotential set
ENAUG = 800                    #change depending on the pseudopotential set

ALGO = Very_Fast
EDIFF = 1.0E-03
LREAL = Auto
PREC = High

NSW = 5000                     #change depending on the simulation
IBRION = 0
SMASS = 4
ISMEAR = 1
TEBEG = 4000            #change depending on the simulation
TEEND = 4000            #change depending on the simulation
SIGMA = 0.3447          #change depending on the simulation
POTIM = 1                      #change depending on the simulation
ISIF = 2
MDALGO = 2

NSIM = 4
NPAR = 16

LWAVE = .TRUE.
LCHARG = .FALSE.
```

A.1.2 Electronic density calculation

The following input files gives the typical parameters used in the electronic density calculations which produces three AECCAR files. The AECCAR0 and AECCAR2 containing respectively the core and valence electron charge density, can be summed by the script `chgsum.pl` (Jónsson group and Henkelman group). The produced output file can be imported into VMD to plot the electronic density isosurface of our choice.

```
SYSTEM = feldspar_electronic_densities

ISTART  = 1
ISYM = 0
ENCUT = 550             #change depending on the pseudopotential set
ENAUG = 800             #change depending on the pseudopotential set

ALGO = Very_Fast
EDIFF = 1.0E-04
LREAL = Auto
PREC = High

NSW = 1
IBRION = 0
ISMEAR = 1
SMASS = 4
TEBEG = 4000            #change depending on the simulation
TEEND = 4000            #change depending on the simulation
SIGMA = 0.3447          #change depending on the simulation
POTIM = 1               #change depending on the simulation
ISIF = 2
MDALGO = 2

NSIM = 4
NPAR = 16

#Electronic densities calculation
LORBIT = 11
LWAVE = .FALSE.
LCHARG = .TRUE.
LAECHG = .TRUE.
NGXF = 150
NGYF = 150
NGZF = 150
```

A.2 Algorithms

Here are presented simplified algorithms for some python scripts used in the post processing of our MD simulations.

Algorithm 1 `analyze_gofr_semi_automatic.py` (simplified version). "atompairs" (`-a`) is the list of atomic pairs (e.g. 'Si-O,O-O') we want to analyze. `-b` takes the value 1 or 0 whether we want to write *.bonds.inp* files or not.

```
procedure MAIN(b,atompairs)
    for all directories ∈ current_directory do
        files ← list of sorted .gofr.dat files
        allatomicpairs ← list of all the atomic pairs from one .gofr.dat file
        if atompairs is empty then   ▷ default behavior ⟹ take all atomic pairs
            atompairs ← allatomicpairs − reversepairs   ▷ without the reverse pairs
        end if
        create the new directory_gofrs.txt file
        initialize the guesses variable for all pairs   ▷ dictionary with xmax, xmin ∀ AB
        for all gofr_file ∈ files do
            initialize the results variable for all pairs
            for all AB ∈ atompairs do
                if file = files[0] then
                    results, guesses ← INTERACT.ANALYSIS(file, AB, results, guesses)
                else
                    results, guesses ← AUTO.ANALYSIS(file, AB, results, guesses)
                end if
            end for
            complete the results with [0,0,0,0,0] for each AB (and BA) pairs not analyzed
            add a line with the results to the directory_gofrs.txt file
            if b = 1 then   ▷ if we want to print .bonds.inp files
                create the filename.bonds.inp file with the selected results
            end if
        end for
    end for
end procedure
```

Functions algorithm for `analyze_gofr_semi_automatic.py`.

procedure INTERAC.ANALYSIS(file,AB,results,guesses)
  extract r, $g_{AB}(r)$, $Int(g_{AB}(r))$ and $Int(g_{BA}(r))$ from file
  $xmax\_click \leftarrow$ r value of the mouse when clicked on 1st peak
  select a portion of $g_{AB}(r)$ data around $xmax\_click$
  fit a 3rd order polynomial in this portion using $xmax\_click$ as initial guess
  $xmin\_click \leftarrow$ r value of the mouse when clicked on 1st min
  select a portion of $g_{AB}(r)$ data around $xmin\_click$
  fit a 3rd order polynomial in this portion using $xmin\_click$ as initial guess
  show the fits and decision buttons
  if click on "Good" button **then**
    $results, guesses \leftarrow$ fitted $xmax, ymax, xmin$ for AB, BA and computed $coord, bond$
  else
    $results, guesses \leftarrow 0$ for AB and BA
  end if
end procedure

procedure AUTO.ANALYSIS(file,AB,results,guesses)
  if guesses $= 0$ for AB **then**
    INTERACT.ANALYSIS($file, AB, results, guesses$)
  else
    extract r, $g_{AB}(r)$, $Int(g_{AB}(r))$ and $Int(g_{BA}(r))$ from file
    select a portion of $g_{AB}(r)$ data around $guesses[AB][xmax]$
    fit a 3rd order polynomial in this portion using $guesses[AB][xmax]$ as initial guess
    select a portion of $g_{AB}(r)$ data around $guesses[AB][xmin]$
    fit a 3rd order polynomial in this portion using $guesses[AB][xmin]$ as initial guess
    $results, guesses \leftarrow$ fitted $xmax, ymax, xmin$ for AB, BA and computed $coord, bond$
  end if
end procedure

Algorithm 2 `speciation_umd.py` with option `-r 0` (simplified version). "cations" (`-c`) and "anions" (`-a`) are lists of element symbols for atoms inside and on the vertices of the coordination polyhedra respectively. "sampling" (`-s`) is the sampling frequency of snapshots.

procedure MAIN(cations,anions,sampling,*.umd.dat*,*.bonds.inp*)
  $AllSnapshots \leftarrow$ Cartesian coordinates of all atoms and snapshots from *.umd.dat* file
  $Timestep \leftarrow$ timestep written in *.umd.dat* file
  $BondTable \leftarrow$ matrix of xmin^2 for every bond defined in *.bonds.inp*
  $CentralAtoms \leftarrow$ list of cations atom indices
  $OuterAtoms \leftarrow$ list of anions atom indices
  $ligands \leftarrow$ list of cations + anions atom indices, each only once
  for all $0 \leq istep \times sampling \leq \tau_{run}$ **do**
    $BooleanMap \leftarrow$ COMPUTEBONDMAP($AllSnapshots[istep], ligands, BondTable$)
    $clusters \xleftarrow{append}$ CLUSTERINGNORINGS($BooleanMap, CentralAtoms, OuterAtoms$)
  end for
  ANALYSISCLUSTERS($clusters, ligands, sampling, Timestep$)
end procedure

Functions algorithm for `speciation_umd.py` with option `-r 0` and `-r 1`.

procedure ComputeBondMap($AllSnapshots[istep], ligands, BondTable$) ▷ create the boolean matrix of bond presence using atom indices
  initialize $BooleanMap$ matrix with 0
  for all $i \in ligands$ **do**
    for all $i+1 \leq j \in ligands$ **do**
      compute d_{ij}^2
      if $d_{ij}^2 < xmin_{ij}^2$ **then**
        $BooleanMap_{ij} = BooleanMap_{ij} = 1$
      end if
    end for
  end for
end procedure

procedure AnalysisClusters($clusters, ligands, sampling, Timestep$)
  initialize the population dictionary to store every information of all clusters
  for all $istep \in AllSnapshots$ **do** ▷ this is also the *clusters* matrix line #
    for all $j \in clusters_{istep}$ **do** ▷ for every coordination polyhedra (or chemical species) at timestep *istep*
      $ClusterName \leftarrow$formula_PolyhedraID
      $ClusterIndex \leftarrow$ formula_PolyhedraID_istep
      $flagalive = 0$ ▷ indicate if we add the cluster to the population dictionary
      for all index $\in$ *population* **do** ▷ for every entry in dictionary
        if $ClusterName =$ clustername of $population_{index}$ **then**
          if $istep - 1 =$ cluster end-life step of $population_{index}$ **then** ▷ this cluster already existed at the previous timestep
            +1 to end-life step of $population_{index}$
            +1 to lifetime of $population_{index}$
            $flagalive = 1$
          end if
        end if
      end for
      if $flagalive = 0$ **then** ▷ this is the first time we see this cluster
        add $ClusterIndex$ to *population* dictionary and initialize lifetime, start-life and end-life step to 1
      end if
    end for
  end for
  for all index $\in$ *population* **do**
    lifetime $\times sampling \times Timestep$, start-life and end-life step $\times sampling$
    write this line to *.popul.dat* file
  end for
  sum lifetime of every cluster with same formula
  sum all lifetimes
  compute presence ratio for every cluster formula
  write *.stat.dat* file
end procedure

Function algorithm for `speciation_umd.py` with option `-r 0`.

procedure ClusteringNoRings($BooleanMap, CentralAtoms, OuterAtoms$) ▷ add the coordination polyhedra list for the current istep to the clusters list
  initialize $AllPolyhedra$ list
  for all $i \in CentralAtoms$ **do** ▷ create its coordination polyhedra (PolyhedraID)
    initialize $PolyhedraID$ list and add i atomic index
    for all $j \in OuterAtoms$ **do**
      if $BooleanMap_{ij} = 1$ **then**
        add index j to the $PolyhedraID$ list
      end if
    end for
    if $PolyhedraID$ has more than one atom **then**
      add this $PolyhedraID$ to the $AllPolyhedra$
    end if
  end for
end procedure

Algorithm 3 `speciation_umd.py` with option `-r 1` (simplified version). For this version, we indicate with "ions" the list of element symbols in the simulation (without duplicates) either using `-a` or `-c` option. "sampling" (`-s`) is the sampling frequency of snapshots.

procedure main(ions,sampling,*.umd.dat*,*.bonds.inp*)
  $AllSnapshots \leftarrow$ Cartesian coordinates of all atoms and snapshots from *.umd.dat* file
  $Timestep \leftarrow$ timestep written in *.umd.dat* file
  $BondTable \leftarrow$ matrix of xmin^2 for every bond defined in *.bonds.inp*
  $ligands \leftarrow$ list of ions atom indices, each only once
  for all $0 \leq istep \times sampling \leq \tau_{run}$ **do**
    $BooleanMap \leftarrow$ ComputeBondMap($AllSnapshots[istep], ligands, BondTable$)
    $clusters \xleftarrow{append}$ Clustering($BooleanMap, ligands$)
  end for
  AnalysisClusters($clusters, ligands, sampling, Timestep$)
end procedure

Function algorithm for `speciation_umd.py` with option `-r 1`.

procedure CLUSTERING($BooleanMap, ligands$) ▷ add the $ClusterID$ list for the current istep to the clusters list
  initialize $AllClusters$ list
  for all $i \in ligands$ **do** ▷ find monoatomic gas species
    if $\sum_j BooleanMap_{ij} = 0$ **then**
      add this monoatomic species i to the $AllClusters$
    end if
  end for
  for all $i \in ligands$ **do** ▷ find all other species and remove used bonds in $BooleanMap$
    if $\sum_j BooleanMap_{ij} > 0$ **then**
      initialize $NewCluster$ list
      $ClusterID \leftarrow$ NEIGHBORING($BooleanMap, ligands, i, NewCluster$)
      sort by numbers the atomic indexes in $ClusterID$
      if $ClusterID$ has more than one atom **then**
        add this $ClusterID$ to the $AllClusters$ list
      end if
    end if
  end for
end procedure

procedure NEIGHBORING($BooleanMap, ligands, i, NewCluster$) ▷ graph creation: recursive search of all atoms linked together
  add current atom index i to the $NewCluster$ list
  for all $j \in ligands$ **do**
    if $BooleanMap_{ij} = 1$ **then**
      $BooleanMap_{ij} = BooleanMap_{ji} = 0$ ▷ remove bond between i and j
      $NewCluster \leftarrow$ NEIGHBORING($BooleanMap, ligands, j, NewCluster$)
    end if
  end for
end procedure

A.3 Additional text

A.3.1 Methodology

Part of the post-processing, especially when it comes to produce figures, is facilitated by a good choice of naming the different output files. It is even more crucial here since there are 3 feldspar compositions, between 10 and 13 different temperatures and up to 18 cell size per temperature. The choice we made for naming the output file is `mineralname_TY_nvt_aX.outcar`, replacing Y by the temperature in thousands of degrees (for ex. 3 for 3000 K, 4.5 for 4500 K), and replacing X by the size of the cubic simulation cell in angstroms (for ex. 15.0, 12.85 etc.). Figure A.1 is a simplified version of the directories tree used for performing the calculations here.

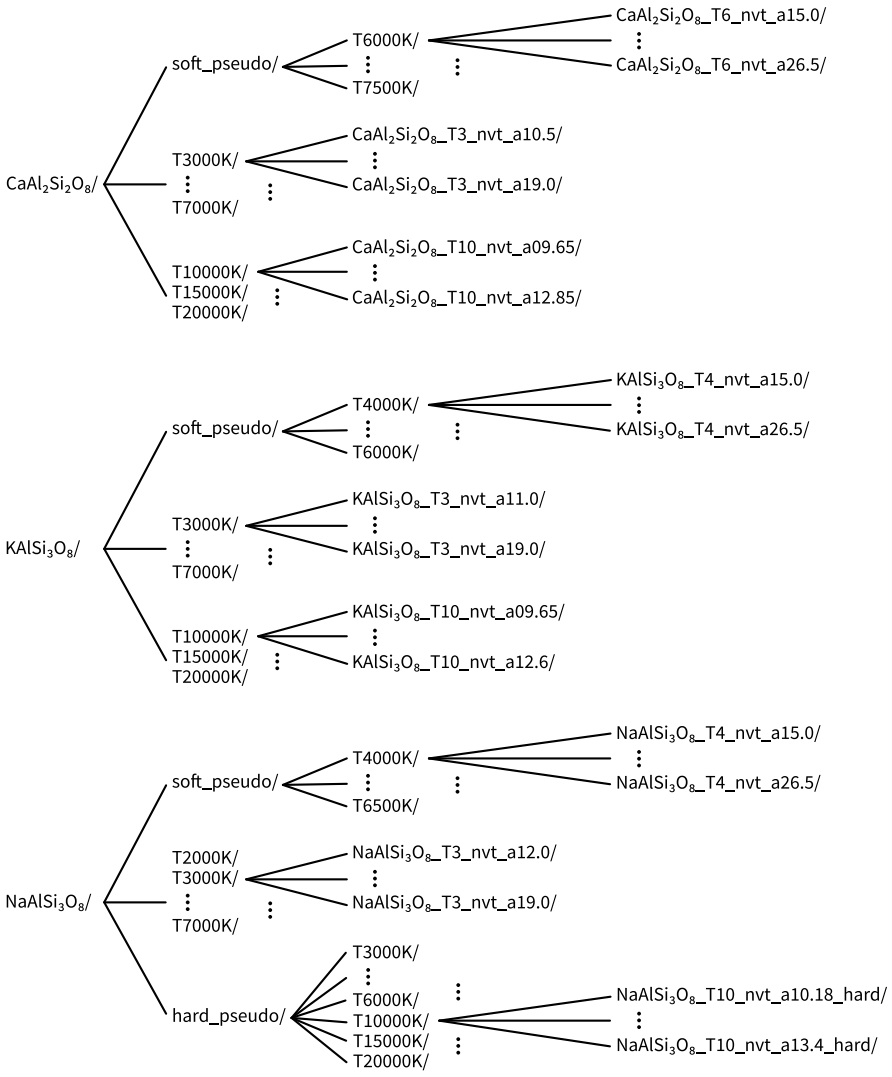

Figure A.1 – Simplified directories tree used for organization of computational experiments here.

A.3.2 MSD sampling

The MSD is computed using the equations 5.2 or 5.3 with two sampling frequencies, over t and τ. This means first not all the snapshots are used in the calculation, and second we cycle through the same snapshot for the calculation of the MSD at different values of τ. For example we represented in the table A.1 the snapshot number that are used in the calculation of the five first values of the MSD for a UMD file made of 100 snapshots with sampling parameters of `-z 3` and `-v 5`. We see the same snapshot are used again beyond $\tau = 16$. This is because the least common multiple (LCM) of 3 and 5 is 15, i.e. every 15 snapshots the same snapshots are used. Of course each calculation $\overrightarrow{r_i}(t) - \overrightarrow{r_i}(t+\tau)$ will be different, but I wanted to see if using more different snapshots in the MSD calculation influence the final results. The figure A.2 represent the LCM values for each pair of sampling frequencies between 10 and 20. The highest multiples are located for sampling frequencies of 11, 13, 17 or 19. At fixed 1st sampling frequency, the LCM increase linearly with the 2nd sampling frequency. To compare the effect of the LCM value on the MSD I computed the MSD of the same UMD file using sampling frequencies with very different LCM: 15,10 (LCM = 30) ; 15,13 (LCM = 195) ; 15,19 (LCM = 285). No difference in the MSD can be seen, and the self-diffusion coefficient are the same within three significant figures. The influence is negligible.

Table A.1 – Example of the snapshot number used in the MSD calculation for the first five τ and an initial UMD file of 100 snapshots. The sampling frequencies used are `-z 3` and `-v 5`.

τ \ t	1	4	7	10	13	16	19	22	25	28	31	34	37	40	43	46	49	⋯ 100
1	6	9	12	15	18	21	24	27	30	33	36	39	42	45	48	51	54	
6	11	14	17	20	23	26	29	32	35	38	41	44	47	50	53	56	59	
11	16	19	22	25	28	31	34	37	40	43	46	49	52	55	58	61	64	
16	21	24	27	30	33	36	39	42	45	48	51	54	57	60	63	66	69	
21	26	29	32	35	38	41	44	47	50	53	56	59	62	65	68	71	74	

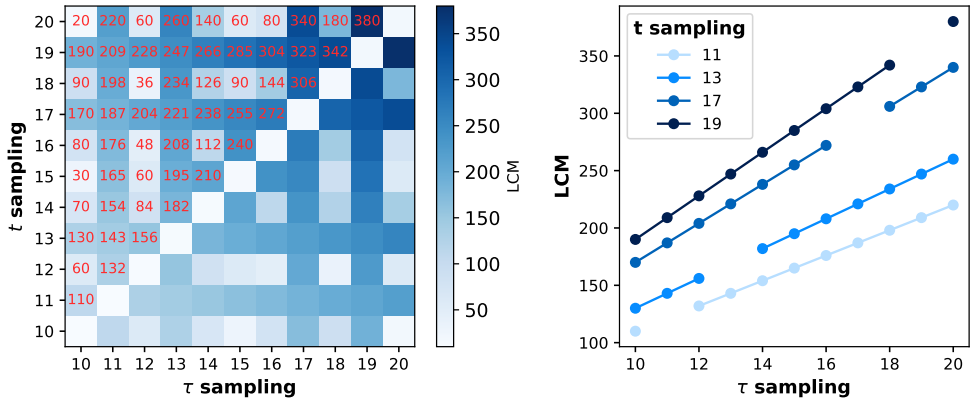

Figure A.2 – Left: LCM values for each pair of sampling frequencies between 10 and 20. Right: variation of LCM values with the sampling frequency.

A.3.3 Trace amount chemical species

The speciation analysis performed in chapter 4 allows to find every isolated species that appear in the simulations. For clarity we represented on figure 4.10 only the proportions for species which represent at least 1 % of all the small isolated species in one or more of the simulations studied. At 4000 K, the Na-feldspar end-member shows presence of Na_2SiO_3 and Si_2O_5. For the K-feldspar end-member we have more species: KSi_2O_4; KSi_2O_5; $K_2Si_3O_7$; K_3SiO_3; O; Si_2O_4. The tables A.2, A.3, and A.4 list all the species which amounts are always below 1 % in the density range studied at 6000 K.

Table A.2 – List of species in the "gas" phase of Na-feldspar which amount is always below 1 % in the density range studied at 6000 K.

$Na_xSi_yO_z$

x \ y	0	1	2	3	4
0	O_4	Si; SiO_4; SiO_5	Si_2O_2; Si_2O_5; Si_2O_6	Si_3O_4; Si_3O_5; Si_3O_6; Si_3O_7; Si_3O_8	
1	NaO; NaO_4	$NaSiO_4$; $NaSiO_5$; $NaSiO_6$	$NaSi_2O_2$; $NaSi_2O_3$; $NaSi_2O_4$; $NaSi_2O_5$; $NaSi_2O_6$	$NaSi_3O_5$; $NaSi_3O_6$; $NaSi_3O_7$; $NaSi_3O_8$	$NaSi_4O_8$
2	Na_2O_3	Na_2SiO_4		$Na_2Si_3O_8$	

$Na_xAlSi_yO_z$

x \ y	0	1	2	3	4
0	Al; AlO; AlO_2; AlO_4	AlSiO; $AlSiO_2$; $AlSiO_3$; $AlSiO_4$; $AlSiO_5$	$AlSi_2O_4$; $AlSi_2O_5$; $AlSi_2O_6$	$AlSi_3O_6$; $AlSi_3O_7$	
1	$NaAlO_2$; $NaAlO_3$	$NaAlSiO_3$; $NaAlSiO_4$	$NaAlSi_2O_4$; $NaAlSi_2O_6$; $NaAlSi_2O_7$		

Table A.3 – List of species in the "gas" phase of K-feldspar which amount is always below 1 % in the density range studied at 6000 K.

$K_xSi_yO_z$

x \ y	0	1	2	3	4
0		SiO_4; SiO_5	Si_2O_2; Si_2O_5;	Si_3O_5; Si_3O_6; Si_3O_7	Si_4O_7
1	KO; KO_2; KO_3	$KSiO_2$; $KSiO_4$	KSi_2O_4; KSi_2O_5; KSi_2O_6		
2	K_2O_2;	K_2SiO_3; K_2SiO_5		$K_2Si_3O_6$	

$K_xAlSi_yO_z$

x \ y	0	1	2	3	4
0	Al; AlO_3	$AlSiO_2$; $AlSiO_3$; $AlSiO_4$; $AlSiO_5$	$AlSi_2O_4$; $AlSi_2O_5$; $AlSi_2O_6$	$AlSi_3O_6$	
1	$KAlO_2$	$KAlSiO_2$; $KAlSiO_3$; $KAlSiO_4$; $KAlSiO_5$	$KAlSi_2O_5$; $KAlSi_2O_6$		

Al_2O_5, Al_2SiO_5

Table A.4 – List of species in the "gas" phase of Ca-feldspar which amount is always below 1 % in the density range studied at 6000 K.

$Ca_xSi_yO_z$

x \ y	0	1	2	3	4
0	O_4	Si; SiO_4	Si_2O_2; Si_2O_4; Si_2O_5		
1	Ca; CaO_2;	$CaSiO_2$; $CaSiO_6$		$CaSi_3O_5$	
2			$Ca_2Si_2O_5$;		

$Ca_xAlSi_yO_z$

x \ y	0	1	2	3	4
0	AlO_3;	AlSiO; $AlSiO_3$; $AlSiO_4$	$AlSi_2O_5$; $AlSi_2O_6$; $AlSi_2O_7$		
1	$CaAlO_2$;	$CaAlSiO_3$;	$CaAlSi_2O_5$; $CaAlSi_2O_7$		
2			$Ca_2AlSi_2O_6$	$Ca_2AlSi_3O_7$	

Al_2O_2; Al_2O_3; Al_2SiO_5

A.3.4 Not ergodic simulations

After the discussion in section 5.2, we stated a simulation has reached the minimum ergocity when the MSD of Si reached at least 9 $Å^2$ within the length of the production run. In the table A.5 are listed all the simulations which do not fulfill this requirement, along with the last value of MSD and the corresponding time.

Table A.5 – Simulations which do not have reached the minimum ergodicity, i.e. with a maximal Si MSD value of less than 9 $Å^2$. They are indicated by a gray cross in the phase diagrams figure 6.9.

Simulation name	MSD duration (fs)	max MSD ($Å^2$)
NaAlSi3O8_T1.932_nvt_rho2.585_hard	2210	0.5
NaAlSi3O8_T2_nvt_a15.0	30654	0.5
NaAlSi3O8_T2_nvt_a15.5	7891	0.4
NaAlSi3O8_T2_nvt_a16.0	5850	0.7
NaAlSi3O8_T2_nvt_a16.5	18356	0.9
NaAlSi3O8_T2_nvt_a17.0	17680	1.4
NaAlSi3O8_T2_nvt_a17.5	17004	0.9
NaAlSi3O8_T2_nvt_a18.0	16640	0.7
NaAlSi3O8_T2_nvt_a18.5	23504	1.3
NaAlSi3O8_T2_nvt_a19.0	18408	0.6
NaAlSi3O8_T3_nvt_a10.5_hard	4589	0.2
NaAlSi3O8_T3_nvt_a10.75_hard	3900	0.3
NaAlSi3O8_T3_nvt_a11.0_hard	4550	0.4
NaAlSi3O8_T3_nvt_a11.5_hard	3575	0.4
NaAlSi3O8_T3_nvt_a11.75_hard	4771	1.2
NaAlSi3O8_T3_nvt_a12.0_hard	2678	1.5
NaAlSi3O8_T3_nvt_a12.0	5746	2.9
NaAlSi3O8_T3_nvt_a12.25_hard	3471	1.9
NaAlSi3O8_T3_nvt_a12.5_hard	2639	2.7
NaAlSi3O8_T3_nvt_a12.5	8749	7.8
NaAlSi3O8_T3_nvt_a13.0	8749	6.3
NaAlSi3O8_T3_nvt_a13.5	8749	3.9
NaAlSi3O8_T3_nvt_a14.0	8567	4.7
NaAlSi3O8_T3_nvt_a14.5_hard	3133	2.3
NaAlSi3O8_T3_nvt_a14.5	10270	3.5
NaAlSi3O8_T3_nvt_a14.6_hard	1625	1
NaAlSi3O8_T3_nvt_rho2.246_hard	1079	1.2
NaAlSi3O8_T3_nvt_a15.0	13364	6
NaAlSi3O8_T3_nvt_a15.5	8138	4.6
NaAlSi3O8_T3_nvt_a16.0	15574	7.3
NaAlSi3O8_T4_nvt_a10.5_hard	4381	0.5
NaAlSi3O8_T4_nvt_a10.75_hard	4043	0.7

Table A.5 – (continued)

Simulation name	MSD duration (fs)	max MSD (Å^2)
NaAlSi3O8_T4_nvt_a11.0_hard	3614	2
NaAlSi3O8_T4_nvt_a11.5_hard	2652	2.5
NaAlSi3O8_T4_nvt_a11.6_hard	3029	3.8
NaAlSi3O8_T4_nvt_a11.75_hard	3146	5.4
NaAlSi3O8_T4_nvt_a12.0_hard	2691	7
NaAlSi3O8_T4_nvt_a12.25_hard	2860	6.8
NaAlSi3O8_T4_nvt_a12.5_hard	2626	8.2
NaAlSi3O8_T4_nvt_a13.0_hard	2496	6.8
NaAlSi3O8_T5_nvt_a10.5_hard	4251	2
NaAlSi3O8_T5_nvt_a10.75_hard	3744	3
NaAlSi3O8_T5_nvt_a11.0_hard	3653	4.4
NaAlSi3O8_T5_nvt_a11.35_hard	2418	5.3
NaAlSi3O8_T5_nvt_a11.5_hard	2535	6.3
NaAlSi3O8_T5_nvt_a11.6_hard	2743	8.4
NaAlSi3O8_T6_nvt_a10.5_hard	4108	5.7
NaAlSi3O8_T6_nvt_a10.75_hard	3627	6.2
NaAlSi3O8_T6_nvt_a11.0_hard	2782	6.7
NaAlSi3O8_T10_nvt_a10.18_hard	559	4.6
NaAlSi3O8_T10_nvt_a10.5_hard	559	5.8
KAlSi3O8_T1.932_nvt_rho2.585	2496	0.4
KAlSi3O8_T3_nvt_a11.0	4615	0.3
KAlSi3O8_T3_nvt_a11.5	13039	0.6
KAlSi3O8_T3_nvt_a11.75	6448	0.8
KAlSi3O8_T3_nvt_a12.0	9243	2.3
KAlSi3O8_T3_nvt_a12.5	11856	6.2
KAlSi3O8_T3_nvt_a12.6	5863	2
KAlSi3O8_T3_nvt_a12.75	8788	6.8
KAlSi3O8_T3_nvt_a13.0	9880	6.4
KAlSi3O8_T3_nvt_a13.5	8463	5
KAlSi3O8_T3_nvt_a14.0	8320	4.6
KAlSi3O8_T3_nvt_a14.5	8749	2.3
KAlSi3O8_T3_nvt_rho2.26	3406	1.1
KAlSi3O8_T3_nvt_a15.0	8268	3
KAlSi3O8_T3_nvt_a15.5	10764	5.2
KAlSi3O8_T3_nvt_a16.0	9178	4.7
KAlSi3O8_T4_nvt_a11.0	4667	1.2
KAlSi3O8_T4_nvt_a11.5	9438	1.1
KAlSi3O8_T4_nvt_a11.75	6214	2.4
KAlSi3O8_T4_nvt_a11.9	6253	4.3

Table A.5 – (continued)

Simulation name	MSD duration (fs)	max MSD (Å^2)
KAlSi3O8_T4_nvt_a12.35	2743	5.6
KAlSi3O8_T5_nvt_a11.0	1989	1.2
KAlSi3O8_T5_nvt_a11.65	3744	7.9
KAlSi3O8_T5_nvt_a11.75	2743	6.9
KAlSi3O8_T5_nvt_a11.85	2392	6.7
KAlSi3O8_T10_nvt_a09.65	968	3.4
KAlSi3O8_T10_nvt_a10.9	474	4.1
KAlSi3O8_T10_nvt_a11.5	474	8.4
KAlSi3O8_T10_nvt_a11.85	474	8.2
KAlSi3O8_T15_nvt_a09.65	474	6.4
CaAl2Si2O8_T1.932_nvt_rho2.585	10842	0.5
CaAl2Si2O8_T2_nvt_a14.0	9750	1.2
CaAl2Si2O8_T2_nvt_a15.0	9087	1.4
CaAl2Si2O8_T2_nvt_a16.0	10920	0.7
CaAl2Si2O8_T2_nvt_a17.0	12792	2.3
CaAl2Si2O8_T3_nvt_a10.5	12922	0.1
CaAl2Si2O8_T3_nvt_a11.0	8749	0.4
CaAl2Si2O8_T3_nvt_a11.5	19591	0.6
CaAl2Si2O8_T3_nvt_a12.0	15015	2.6
CaAl2Si2O8_T3_nvt_a12.5	8684	5.7
CaAl2Si2O8_T3_nvt_a14.5	8164	8.1
CaAl2Si2O8_T3_nvt_a15.0	8281	6.5
CaAl2Si2O8_T4_nvt_a10.5	11336	0.8
CaAl2Si2O8_T4_nvt_a11.0	13949	1.1
CaAl2Si2O8_T4_nvt_a11.5	15626	5.6
CaAl2Si2O8_T5_nvt_a10.5	9763	1.7
CaAl2Si2O8_T5_nvt_a11.0	8684	5.3
CaAl2Si2O8_T6_nvt_a10.5	10478	4.3
CaAl2Si2O8_T10_nvt_a09.65	1001	2
CaAl2Si2O8_T15_nvt_a09.65	721	7.8

A.3.5 Unit conversion for the heat capacity

We can compare the heat capacity of different systems using the specific heat capacity (in J/K/g), or the molar heat capacity (in J/K/mol) defined respectively by

$$Cv_{mass} = \frac{Cv}{m} = Cv\frac{\mathcal{N}_A}{MN} \tag{A.1}$$

$$Cv_{molar} = \frac{Cv}{n} = Cv\frac{\mathcal{N}_A}{N} \tag{A.2}$$

with $\mathcal{N}_A$ the Avogadro constant and m, M and n the mass, molar mass and amount of substance of the material respectively. The isochoric heat capacity Cv can be expressed in Nk_B units, while the molar heat capacity Cv_m can be expressed in R units (with R the ideal gas constant equal to the product of $\mathcal{N}_A$ and k_B). This means we only have to multiply by Nk_B and R the values obtained in these units to convert them to J/K and J/K/mol respectively. Then, by combining these conversions with the equation A.2 we find that both units give the same numerical value, and then can be directly compared together.

A.4 Additional figures

A.4.1 Structure

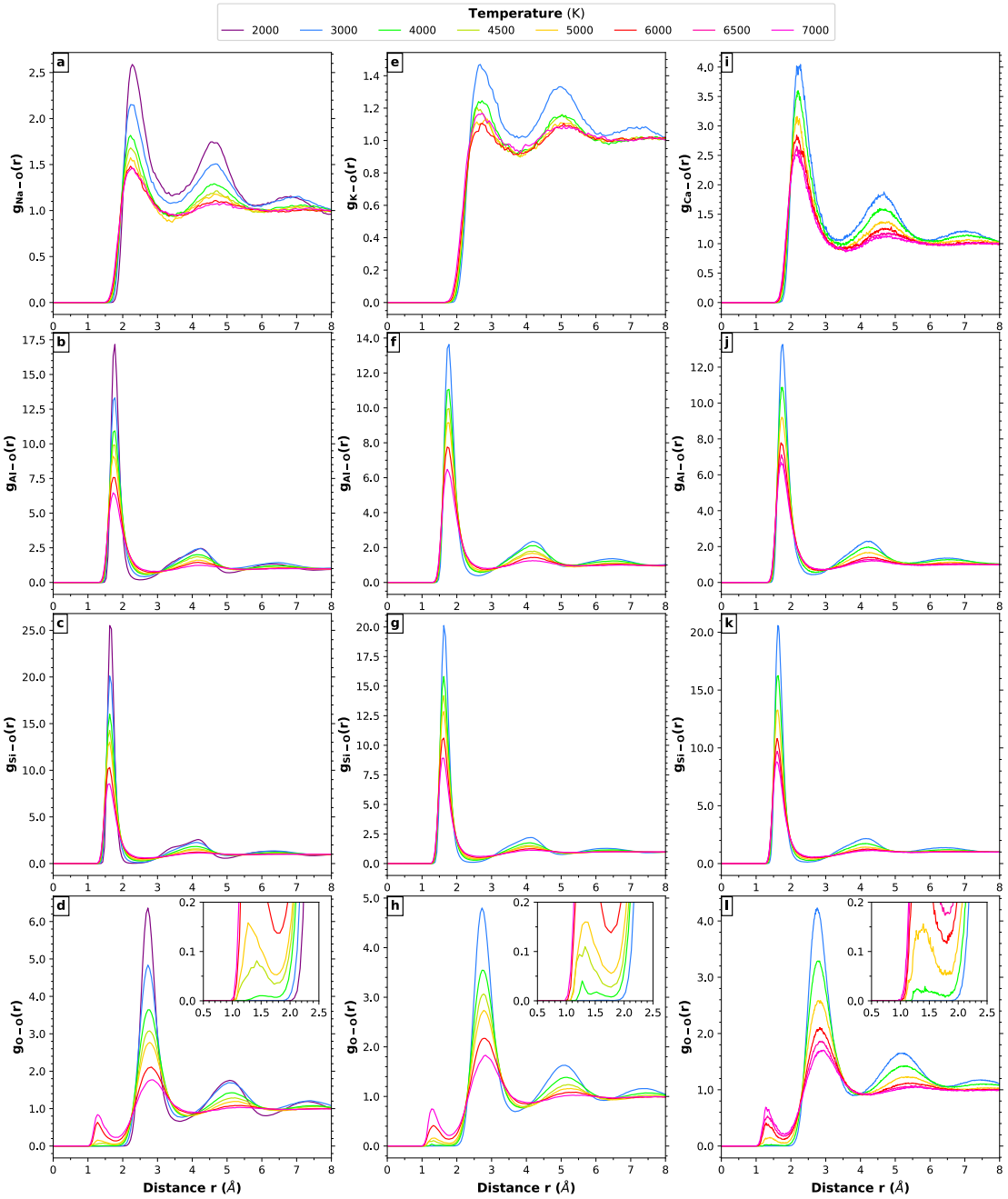

Figure A.3 – Pair distribution functions of X-O (X being Na, K, Ca, Al, Si and O) in $NaAlSi_3O_8$ (a,b,c,d), $KAlSi_3O_8$ (e,f,g,h) and $CaAl_2Si_2O_8$ (i,j,k,l) at $1\,g\,cm^{-1}$. Colors indicate temperatures. The insert shows a zoom on the region 0.5–2.5 Å. The small peak located around 1.4 Å marks the presence of O_2 molecules. The same plot at $2\,g\,cm^{-1}$ is available in figure 3.6.

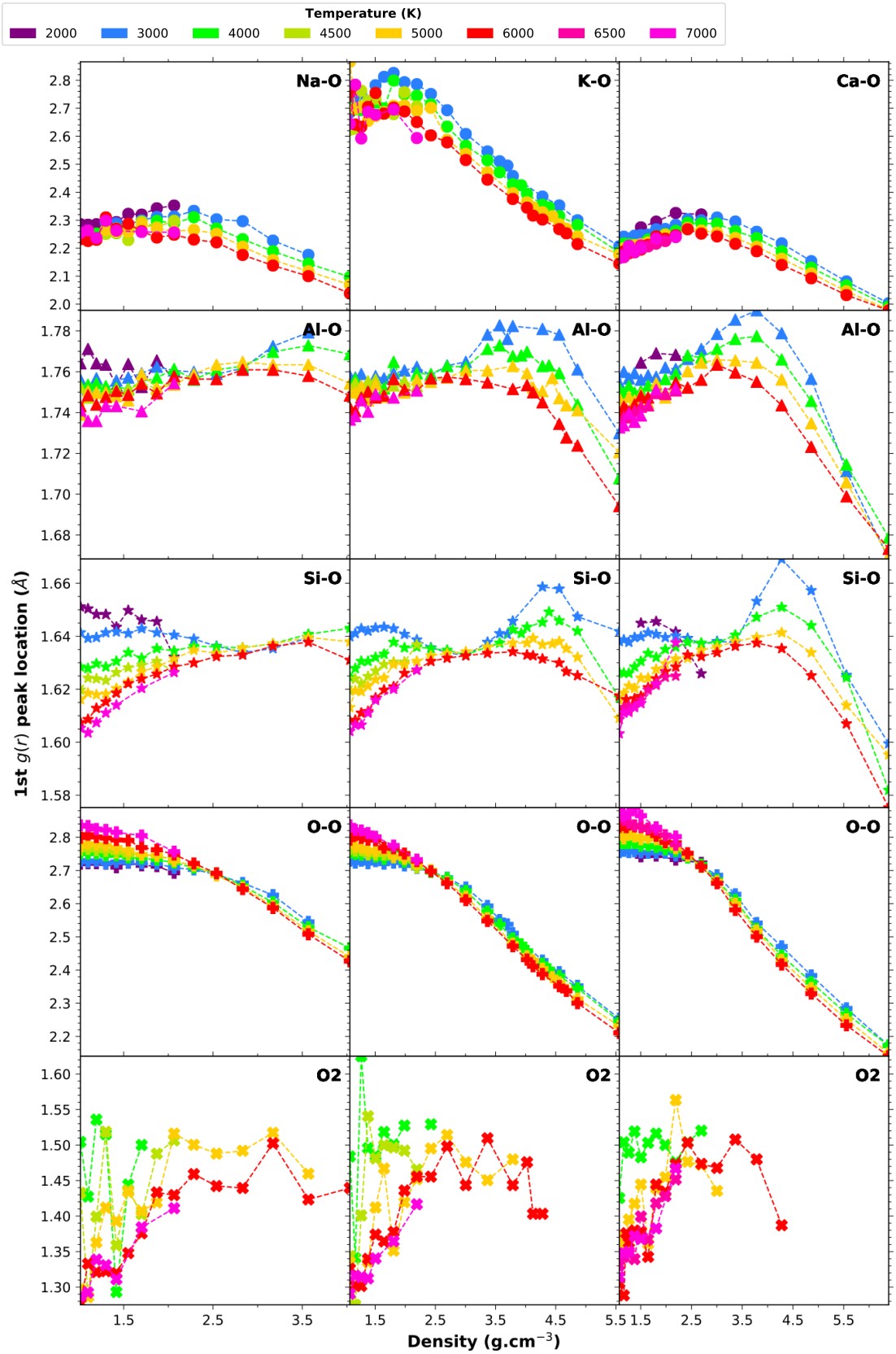

Figure A.4 – Position of the first *g(r)* peak for each feldspar end-member (columns) as a function of density and temperature (colors) for T-O and M-O pairs. O2 corresponds to the small additional peak seen on the $g_{O-O}(r)$. The same figure as a function of pressure instead of density is presented figure 3.7.

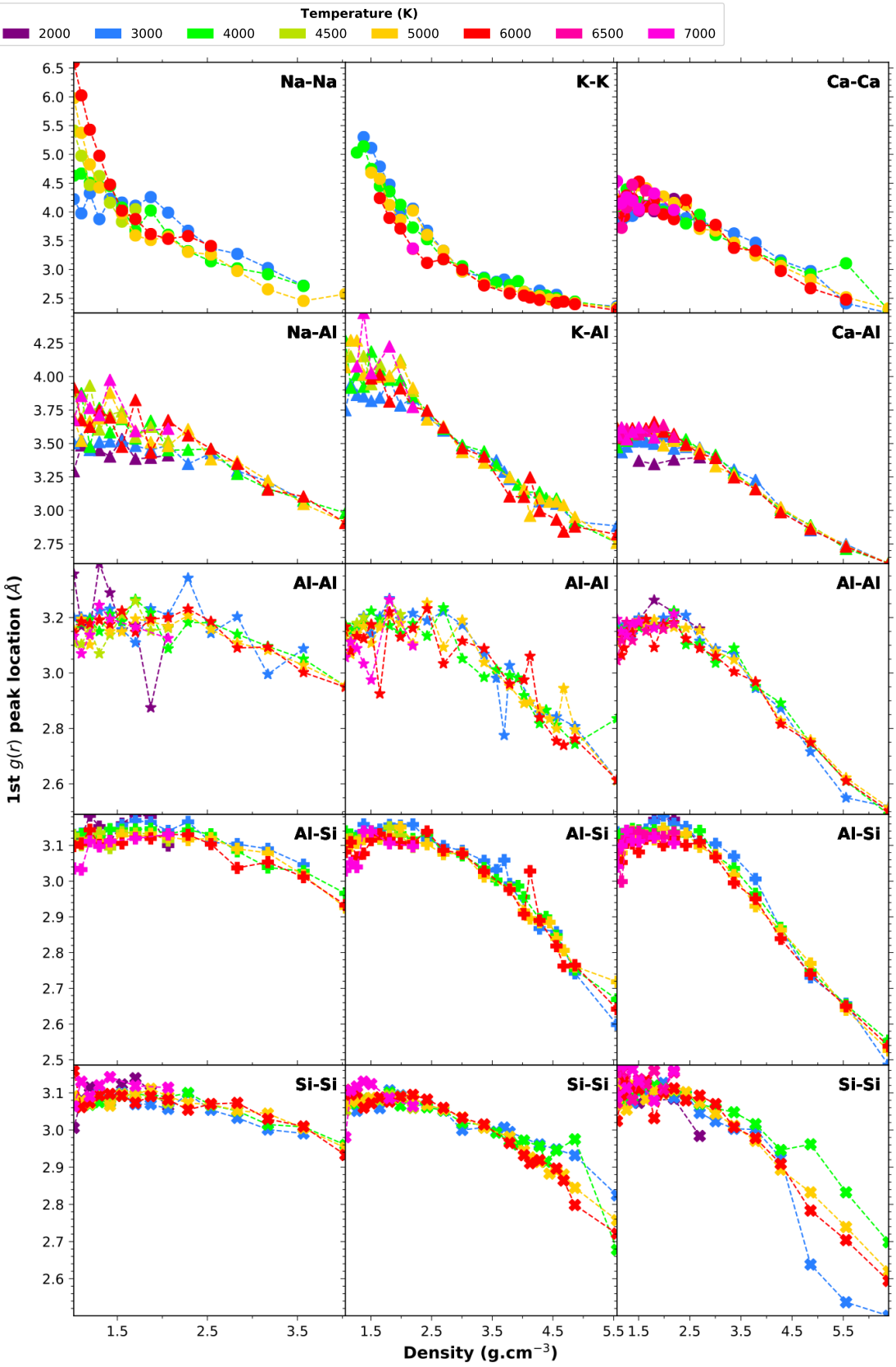

Figure A.5 – Position of the first *g(r)* peak for each feldspar end-member (columns) as a function of density and temperature (colors) for five cation pairs. The same figure as a function of pressure instead of density is presented figure 3.8.

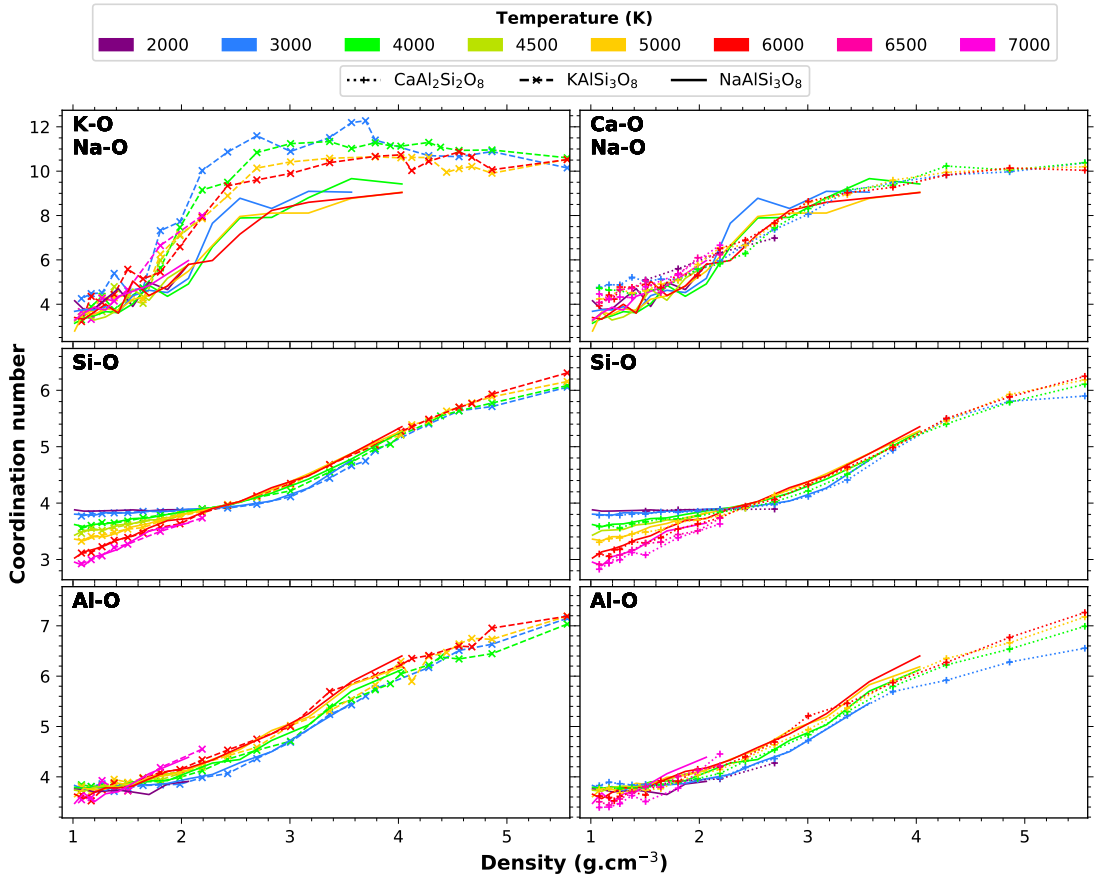

Figure A.6 – Average coordination number of Ca, K, Na, Al and Si by O as a function of density and temperature. Ca- (+ and dotted lines) and K- (x and dashed lines) are both compared with Na-feldspar (solid lines). Colors indicate temperatures. The same plot as a function of pressure is displayed figure 3.9.

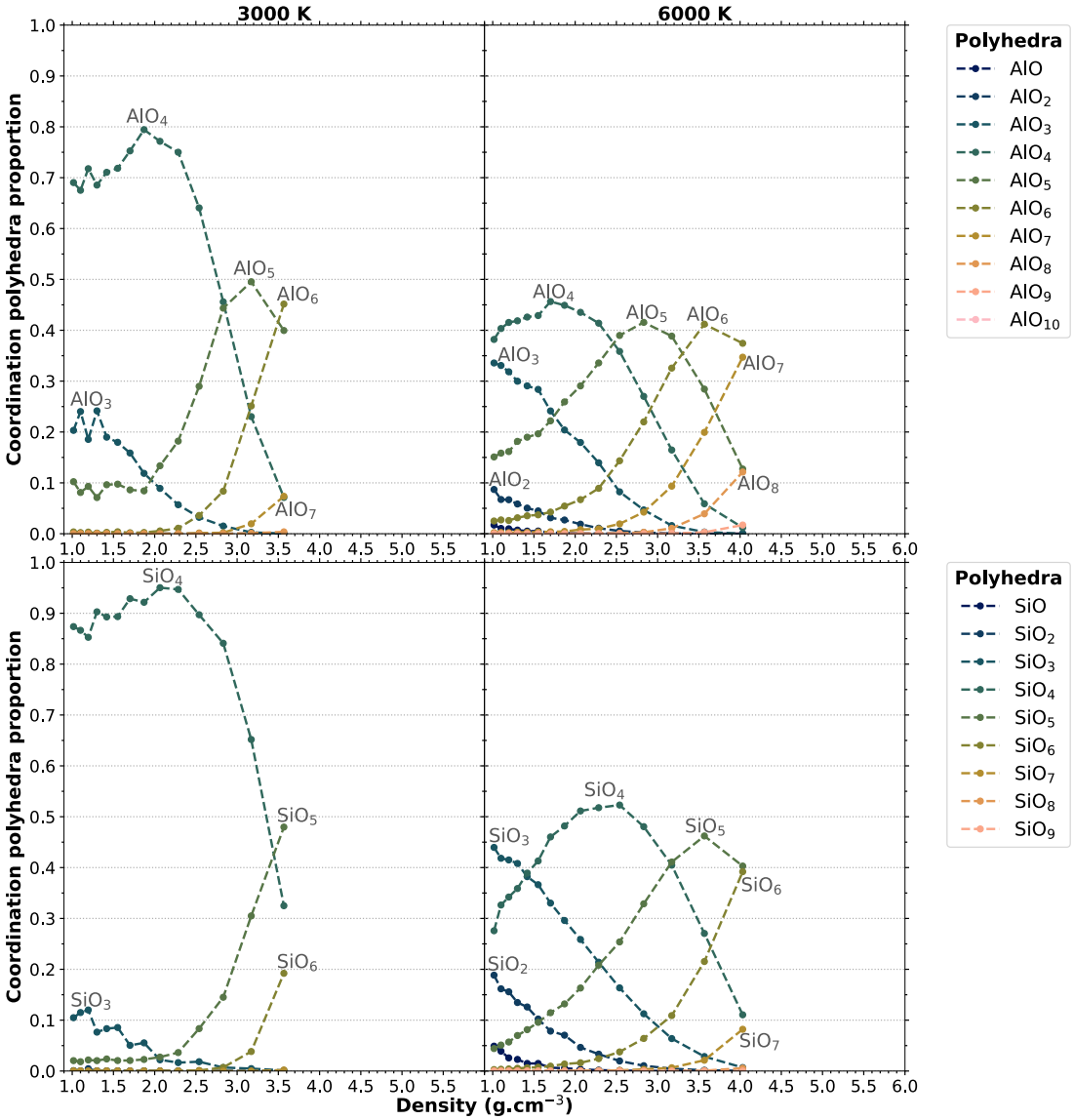

Figure A.7 – Relative proportion of SiO_n and AlO_n coordination species in $NaAlSi_3O_8$ for 3000 K and 6000 K as a function of density. The same figure as a function of pressure is displayed figure 3.11.

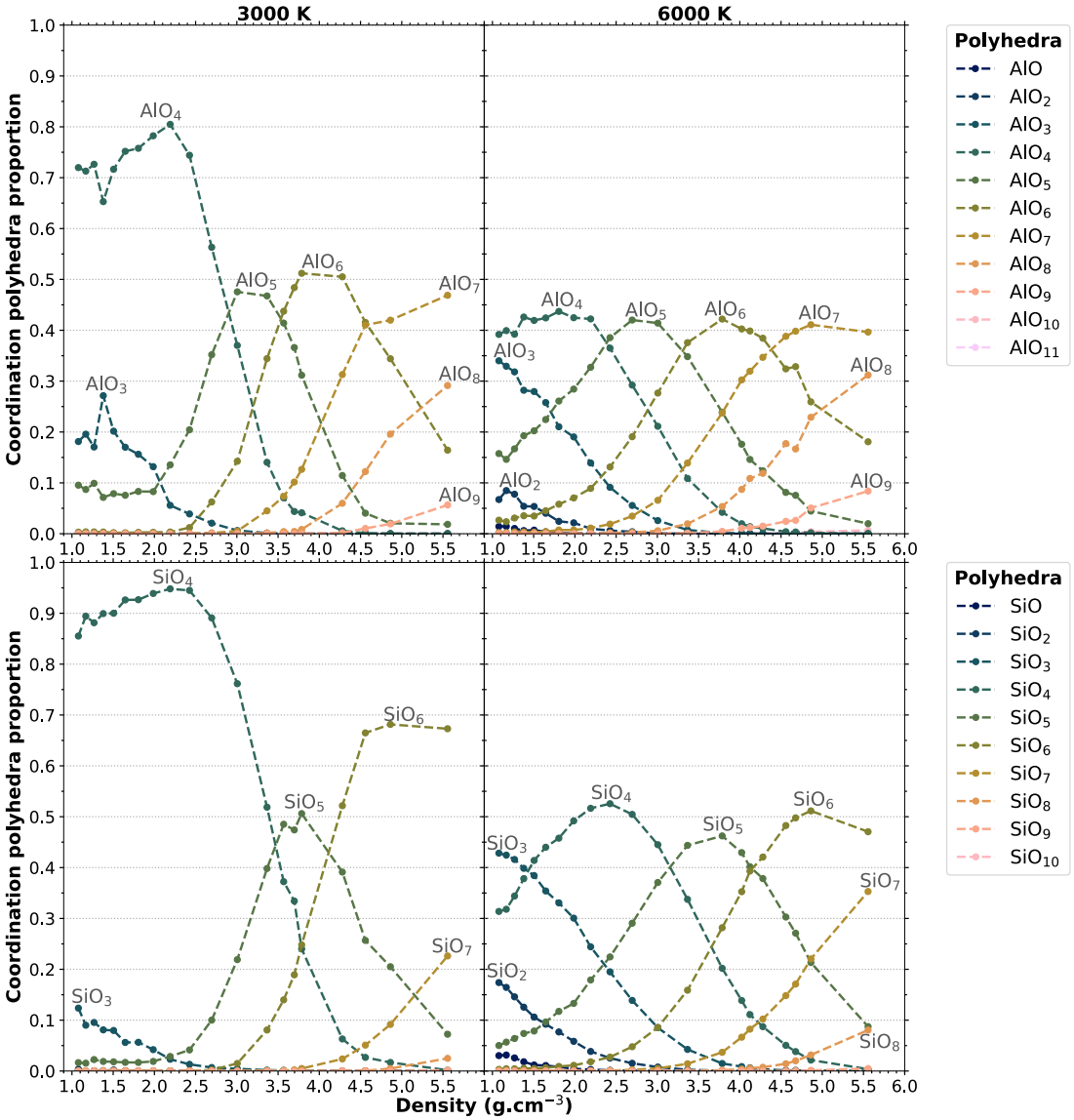

Figure A.8 – Relative proportion of SiO_n and AlO_n coordination species in $KAlSi_3O_8$ for 3000 K and 6000 K as a function of density. The same figure as a function of pressure is displayed figure 3.12.

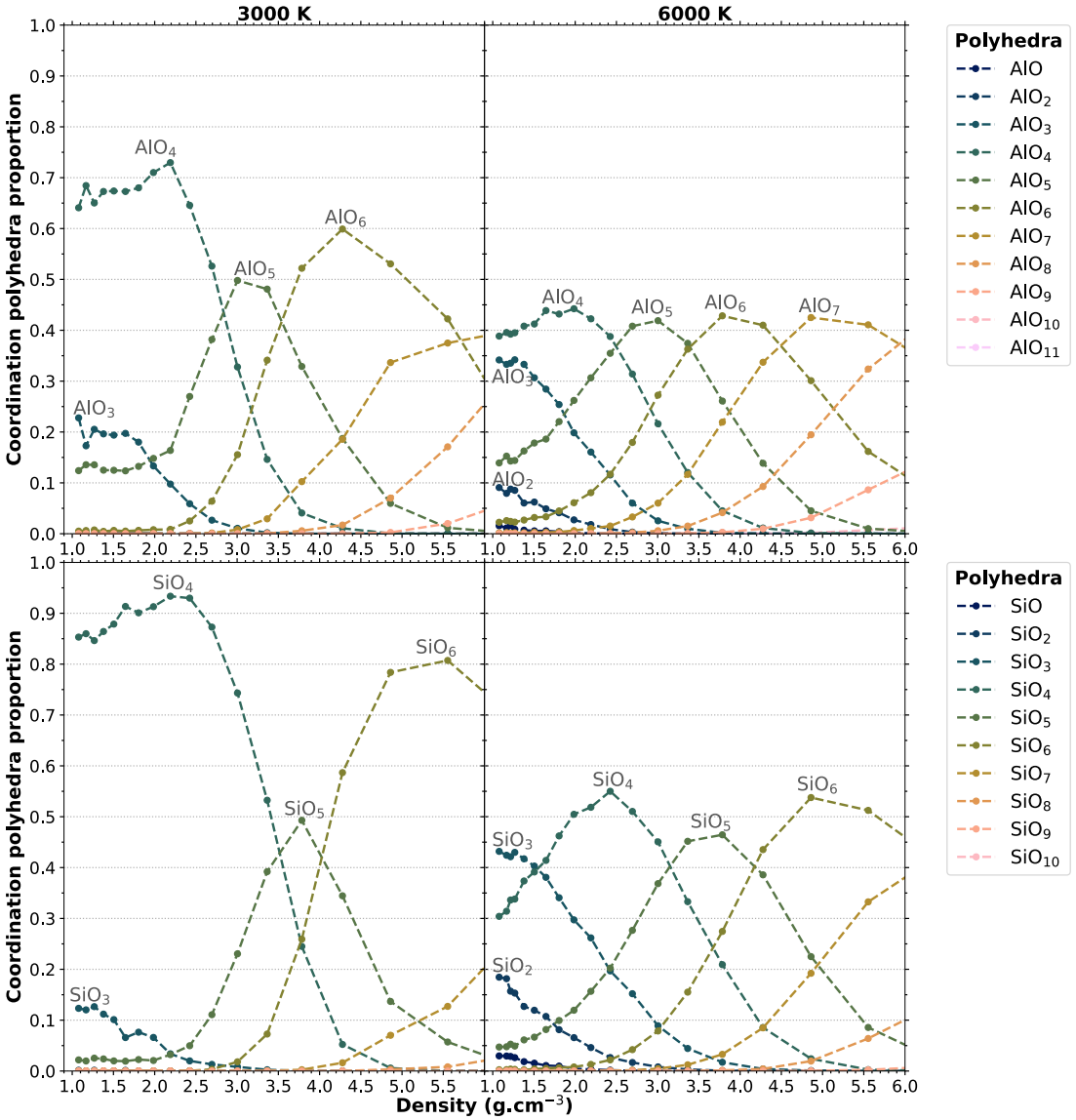

Figure A.9 – Relative proportion of SiO_n and AlO_n coordination species in $CaAl_2Si_2O_8$ for 3000 K and 6000 K as a function of density. The same figure as a function of pressure is displayed figure 3.13.

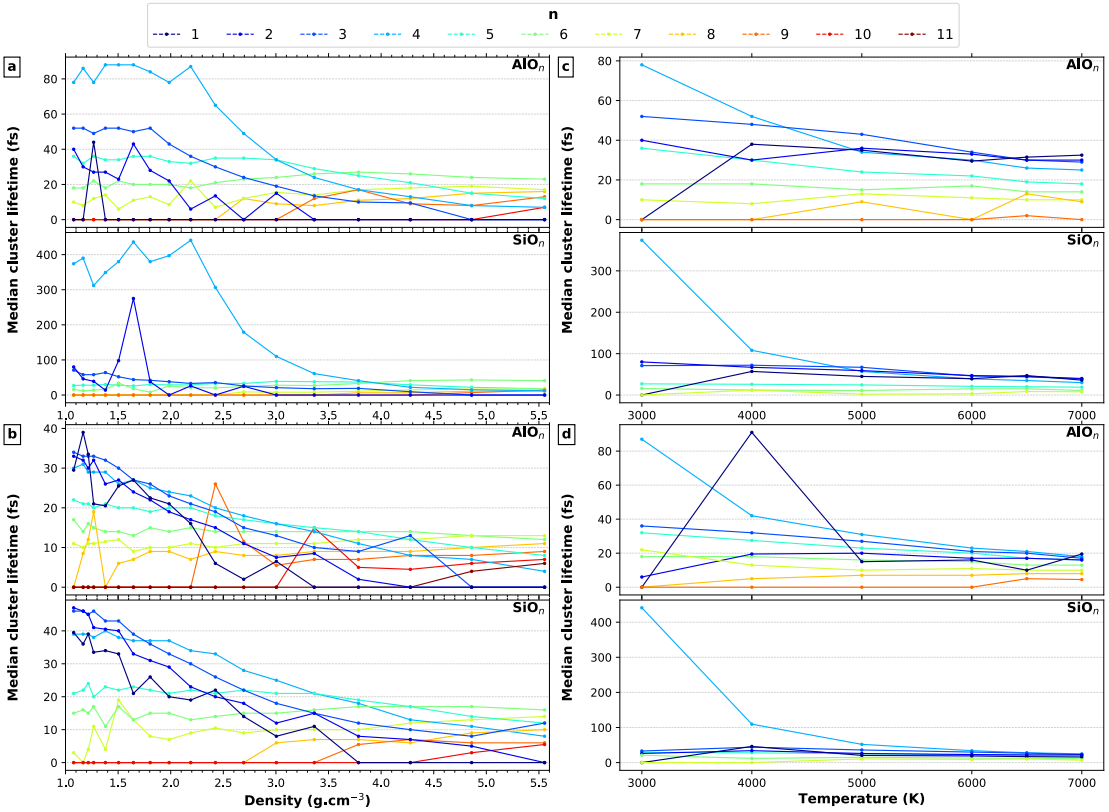

Figure A.10 – Median lifetime of AlO_n and SiO_n coordination polyhedra for $CaAl_2Si_2O_8$ as a function of density at (a) 3000 K, (b) 6000 K and as a function of temperature at (c) 1.08 g cm^{-3}, (d) 2.19 g cm^{-3}. Can be compared with the same representation for $NaAlSi_3O_8$ in figure 3.16.

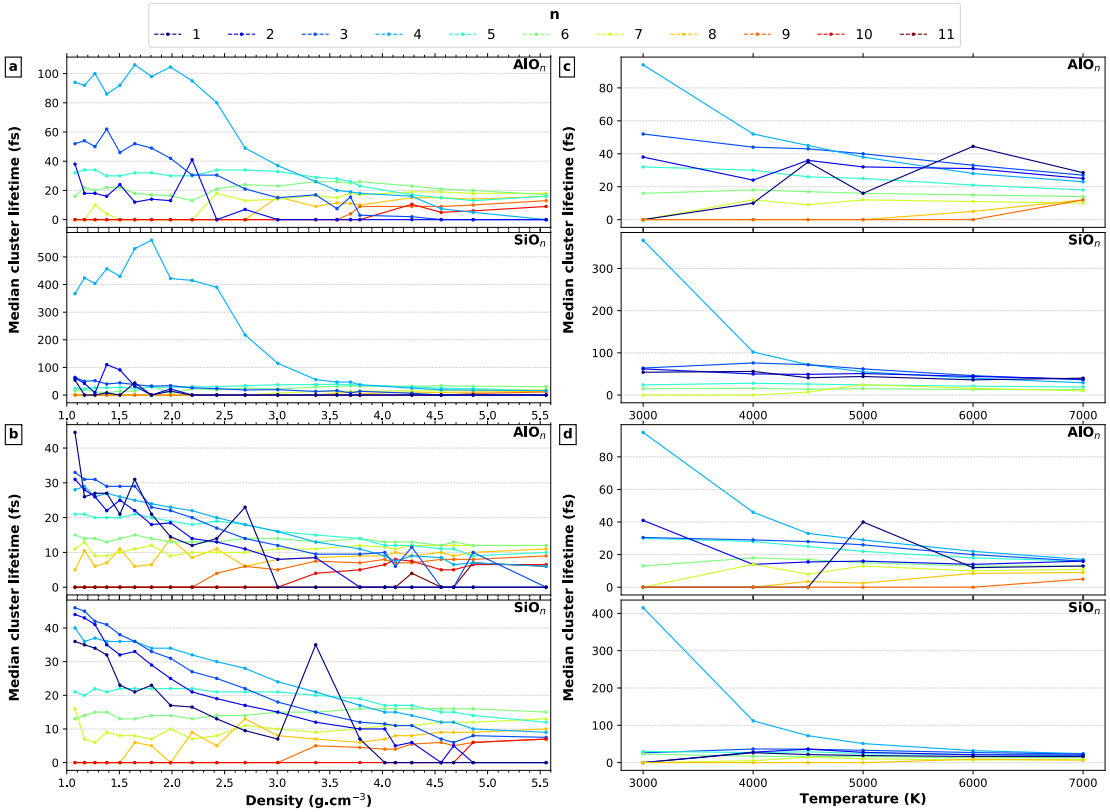

Figure A.11 – Median lifetime of AlO_n and SiO_n coordination polyhedra for $KAlSi_3O_8$ as a function of density at (a) 3000 K, (b) 6000 K and as a function of temperature at (c) 1.08 g cm^{-3}, (d) 2.19 g cm^{-3}. Can be compared with the same representation for $NaAlSi_3O_8$ in figure 3.16.

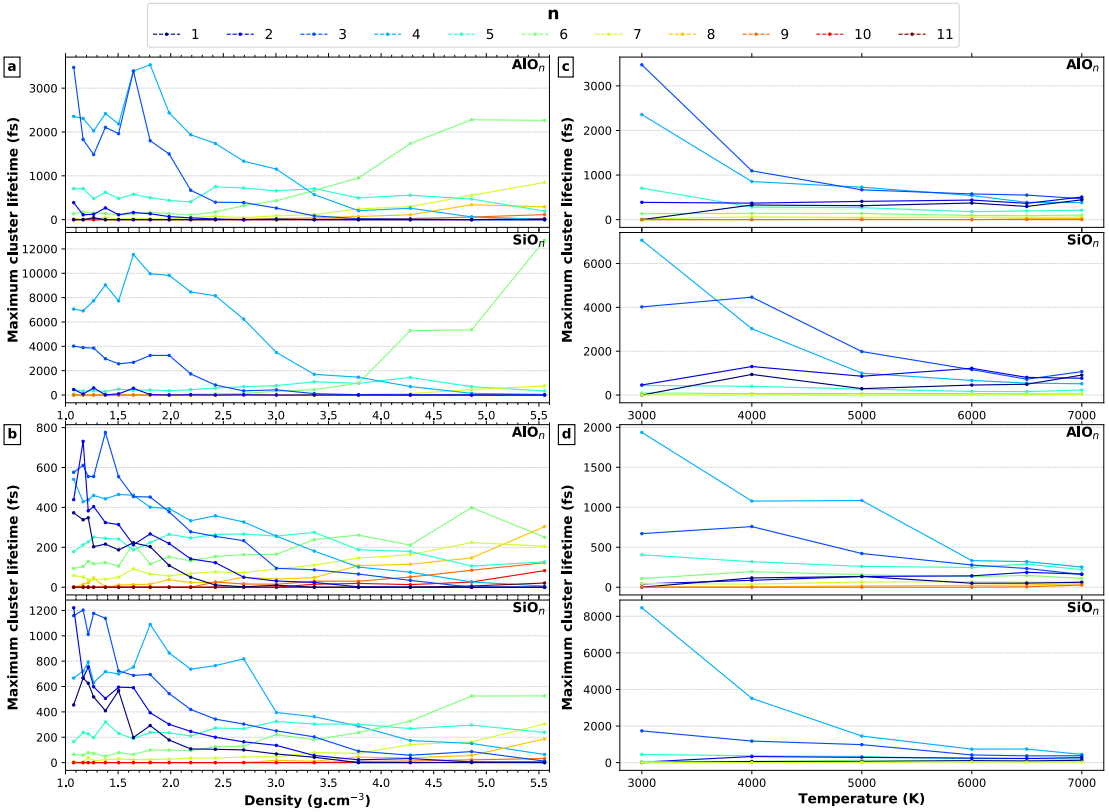

Figure A.12 – Maximum lifetime of AlO_n and SiO_n coordination polyhedra for $CaAl_2Si_2O_8$ as a function of density at (a) 3000 K, (b) 6000 K and as a function of temperature at (c) 1.08 g cm^{-3}, (d) 2.19 g cm^{-3}. Can be compared with the same representation for $NaAlSi_3O_8$ in figure 3.17.

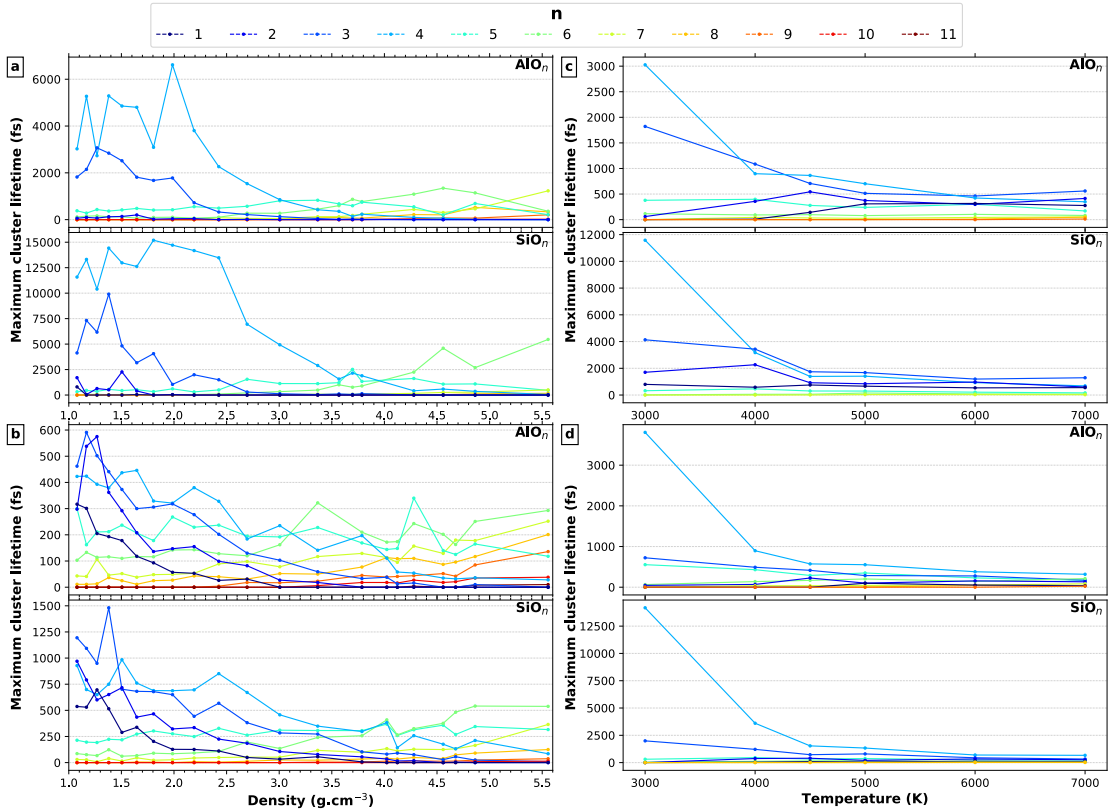

Figure A.13 – Maximum lifetime of AlO_n and SiO_n coordination polyhedra for $KAlSi_3O_8$ as a function of density at (a) 3000 K, (b) 6000 K and as a function of temperature at (c) 1.08 g cm^{-3}, (d) 2.19 g cm^{-3}. Can be compared with the same representation for $NaAlSi_3O_8$ in figure 3.17.

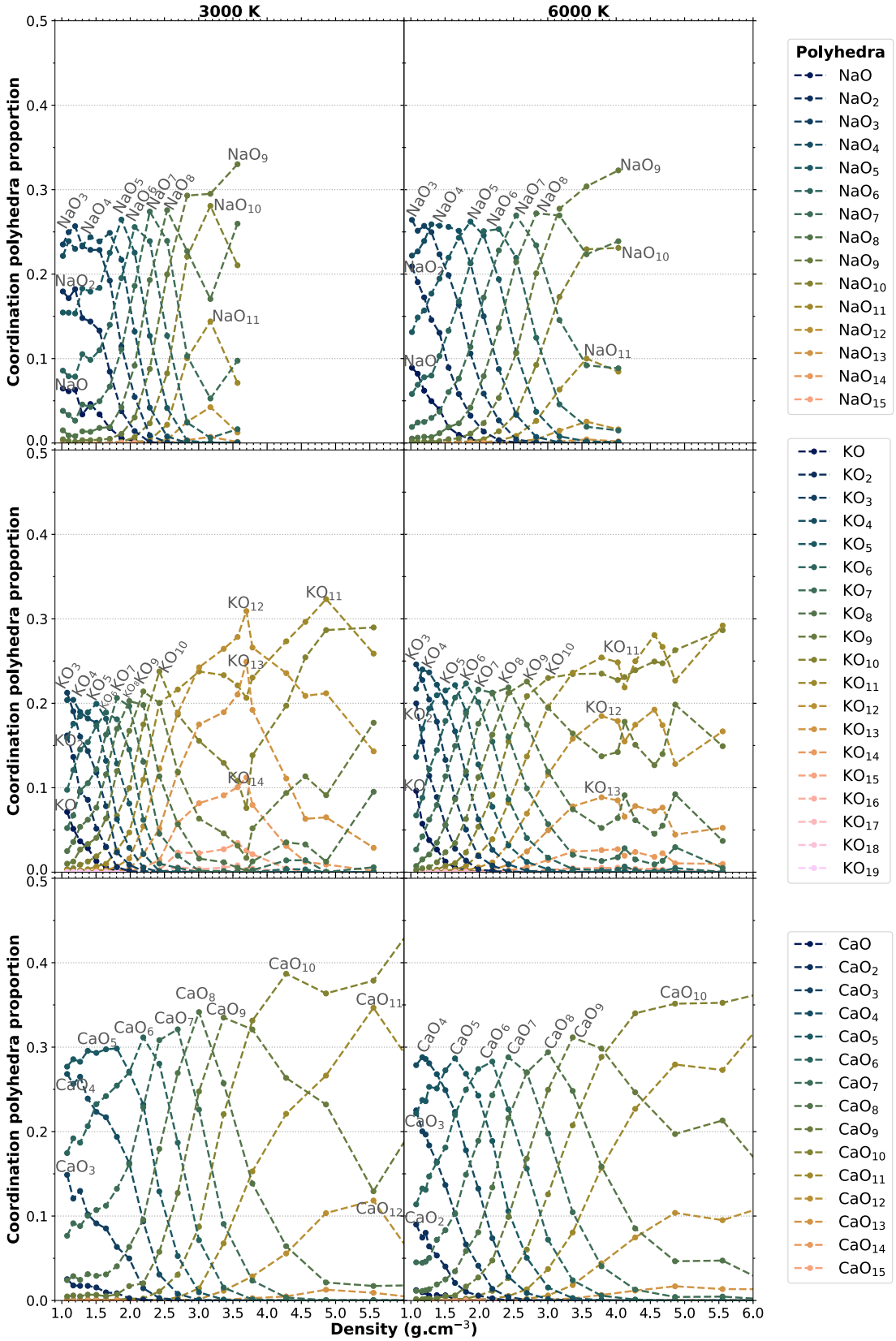

Figure A.14 – Relative proportion of NaO_n, KO_n and CaO_n coordination species for 3000 K and 6000 K as a function of density. The same figure as a function of pressure is presented figure 3.18.

A.4.2 Volatilization

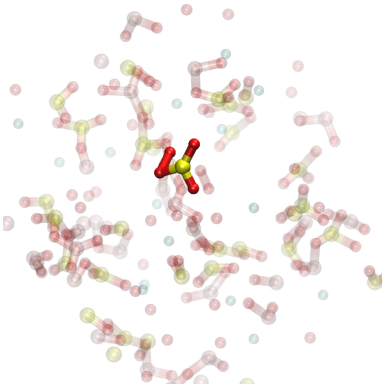

Figure A.15 – Snapshot of "SiO_4" in $CaAl_2Si_2O_8$ at 6000 K and 1.2 g cm^{-3}.

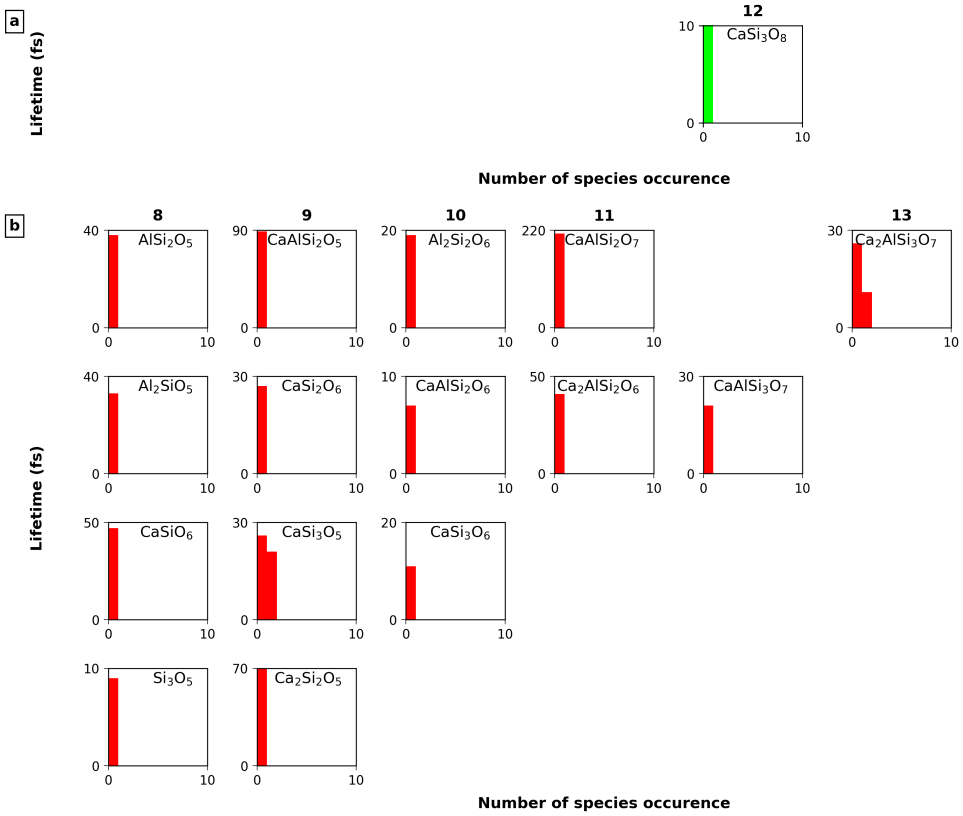

Figure A.16 – Lifetime of each individual volatile species with 8 to 13 atoms in their formula in $CaAl_2Si_2O_8$ fluids at 1.1 g cm^{-3} and (a) 4000 K, (b) 6000 K. The species with less than 8 atoms in their formula are available in figure 4.7.

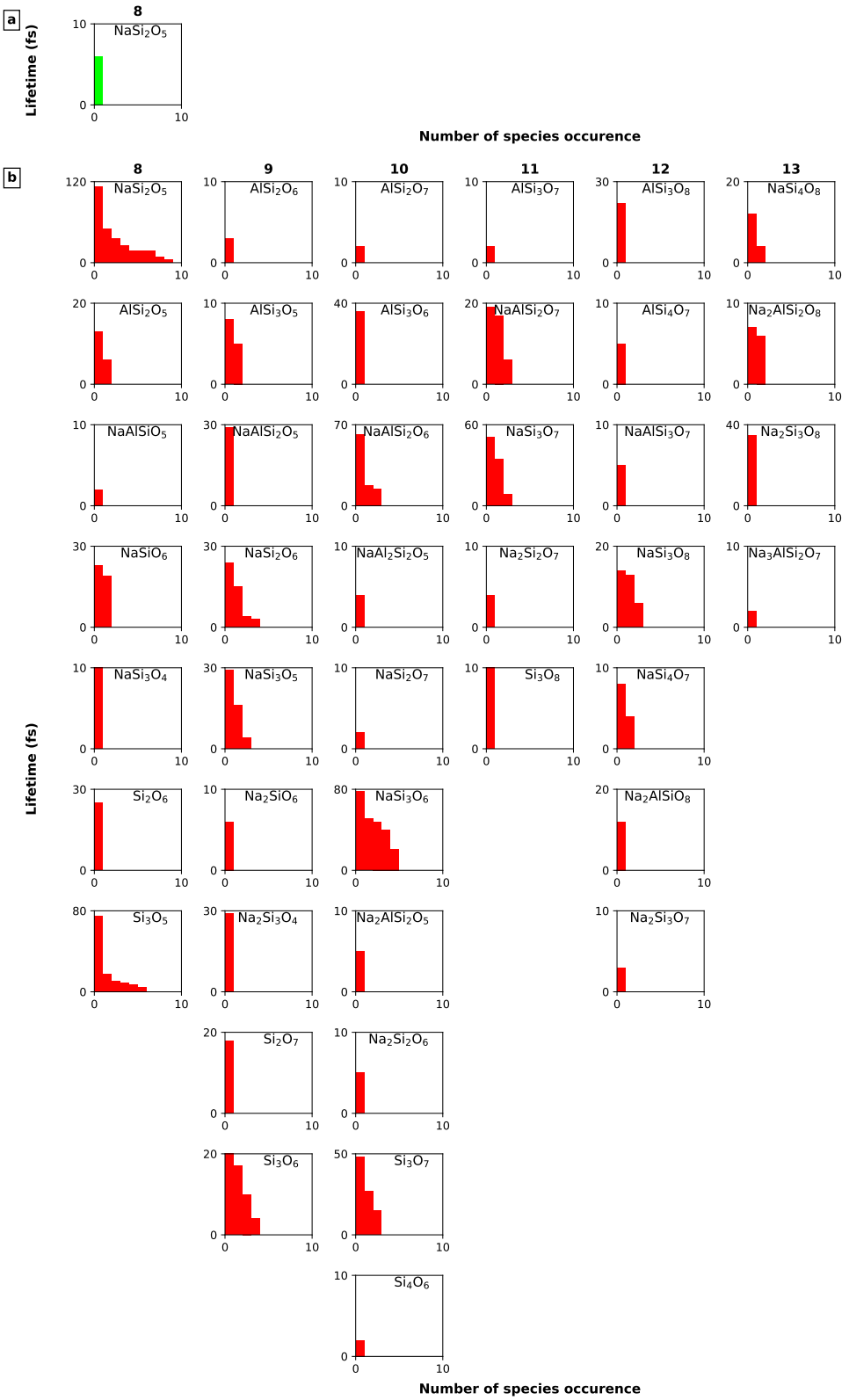

Figure A.17 – Lifetime of each individual volatile species with 8 to 13 atoms in their formula in $NaAlSi_3O_8$ fluids at 1.0 g cm^{-3} and (a) 4000 K, (b) 6000 K. The species with less than 8 atoms in their formula are available in figure 4.8.

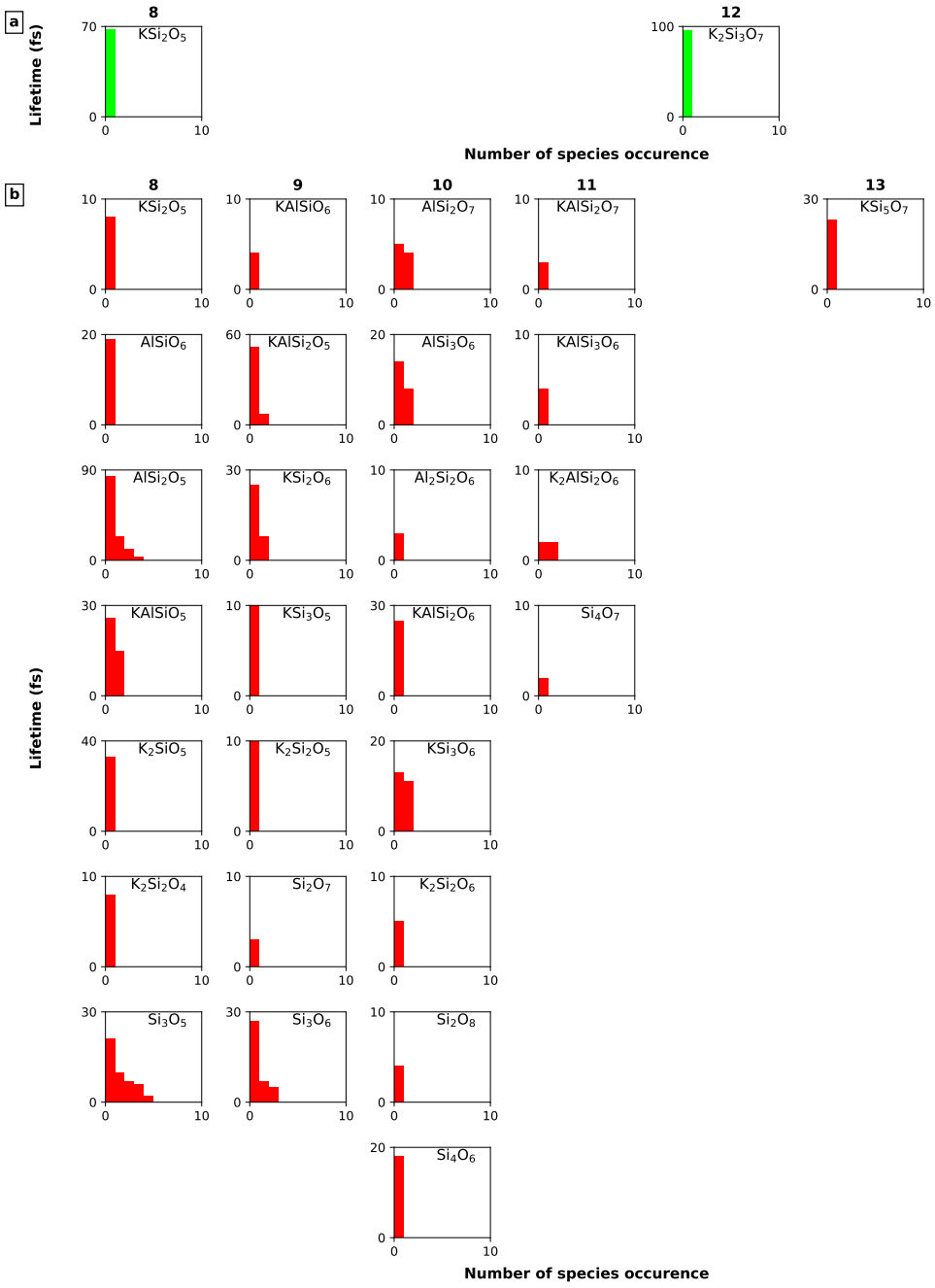

Figure A.18 – Lifetime of each individual volatile species with 8 to 13 atoms in their formula in $KAlSi_3O_8$ fluids at 1.1 g cm^{-3} and (a) 4000 K, (b) 6000 K. The species with less than 8 atoms in their formula are available in figure 4.9.

A.4.3 Transport

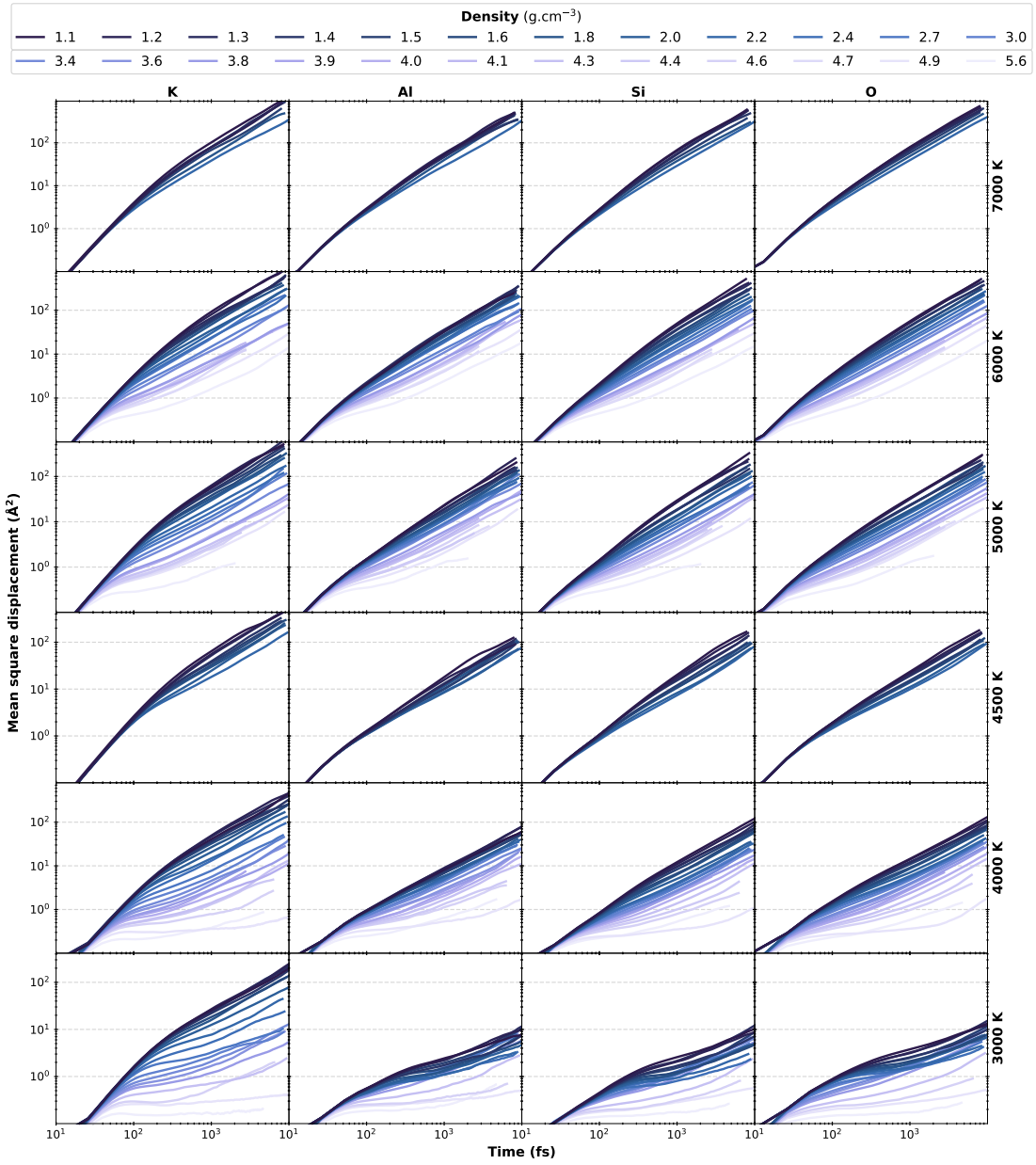

Figure A.19 – Mean square displacement of K, Al, Si and O in $KAlSi_3O_8$ at six temperatures between 3000 K and 7000 K and more than 20 densities between 1.1 g cm^{-3} and 5.6 g cm^{-3}.

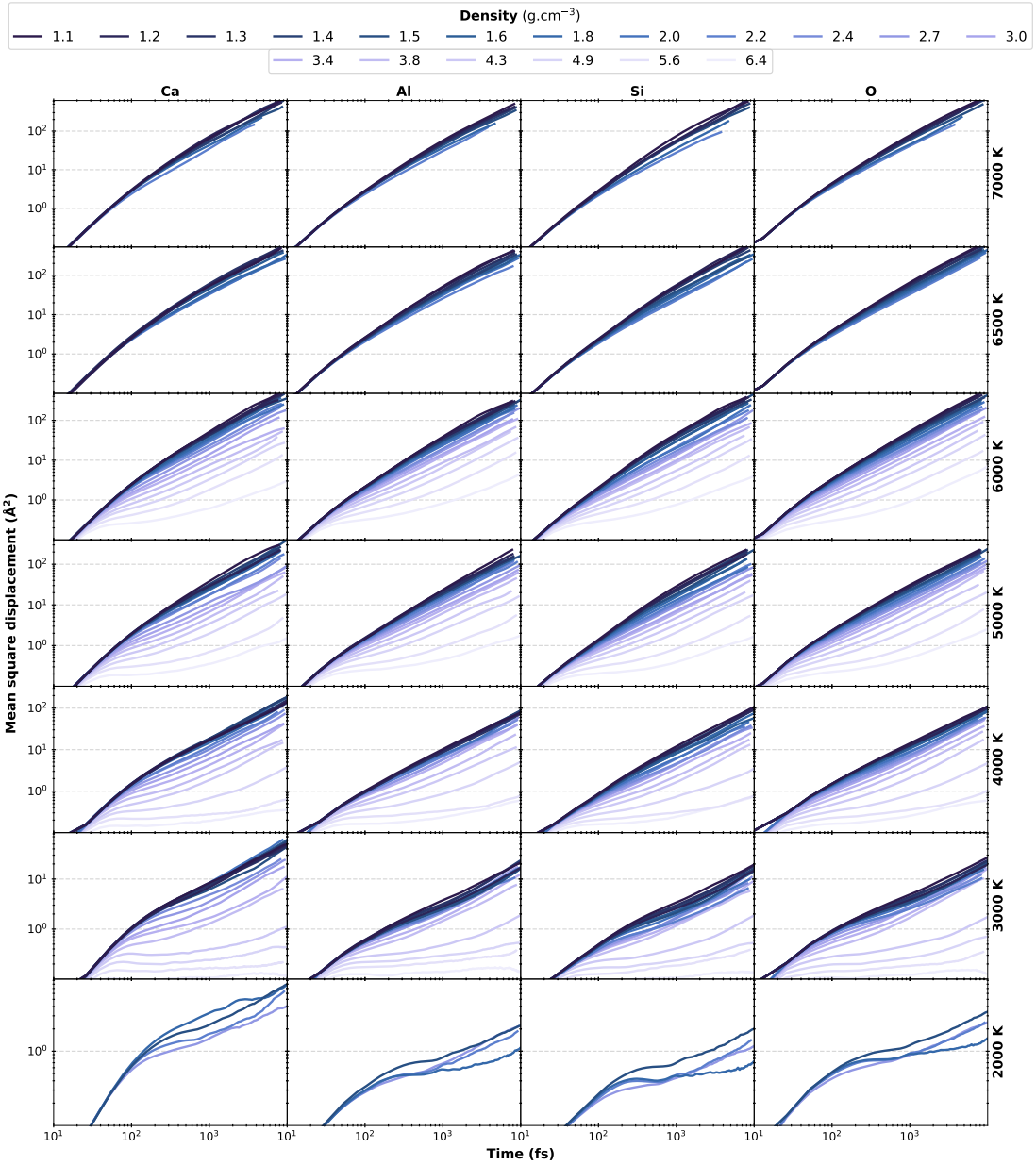

Figure A.20 – Mean square displacement of Ca, Al, Si and O in $CaAl_2Si_2O_8$ at seven temperatures between 2000 K and 7000 K and up to 18 densities between 1.1 g cm^{-3} and 6.4 g cm^{-3}.

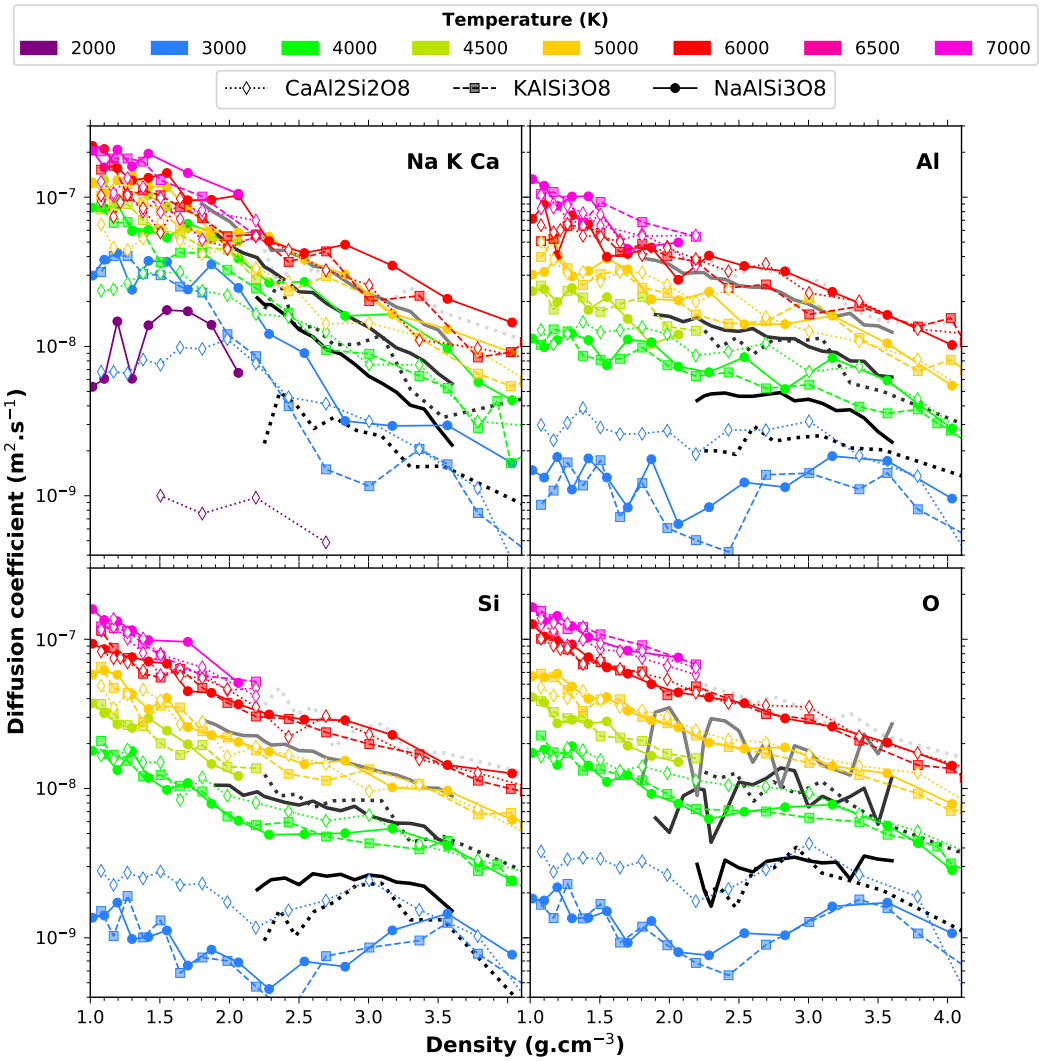

Figure A.21 – Self-diffusion coefficients for every element as a function of density for each feldspar end-member. Colors indicate temperatures. The black to light gray lines are results from de Koker (2010) on $CaAl_2Si_2O_8$ at 3000, 4000 and 6000 K and from Neilson *et al.* (2016) on $NaAlSi_3O_8$ at approximately 3000, 4000 and 5000 K. The same figure as a function of pressure instead of densities is presented figure 5.4.

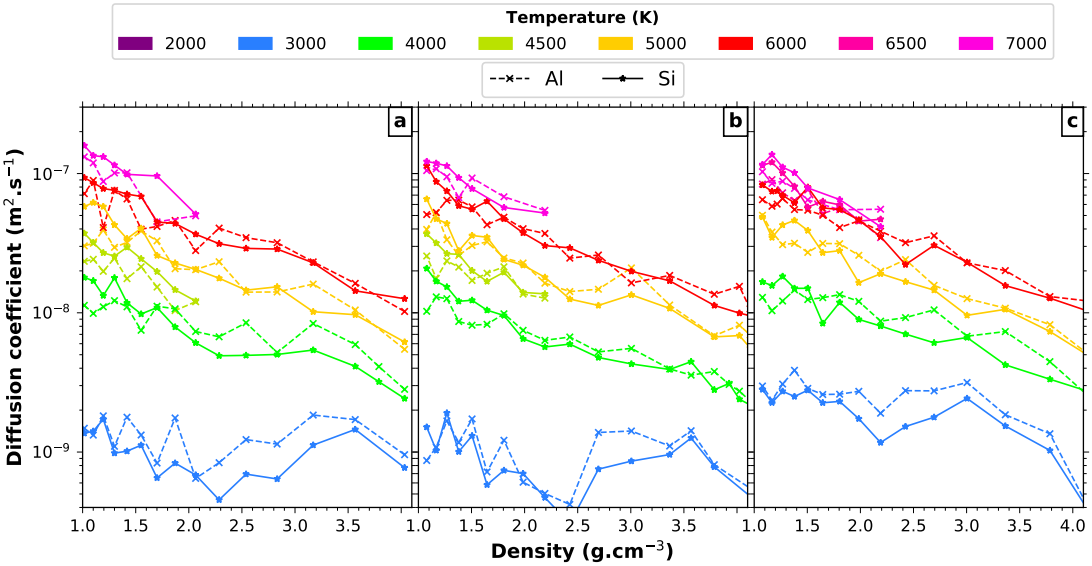

Figure A.22 – Self-diffusion coefficients for Al and Si as a function of density for (a) Na- (b) K and (c) Ca-feldspar end-members. Colors indicate temperatures.

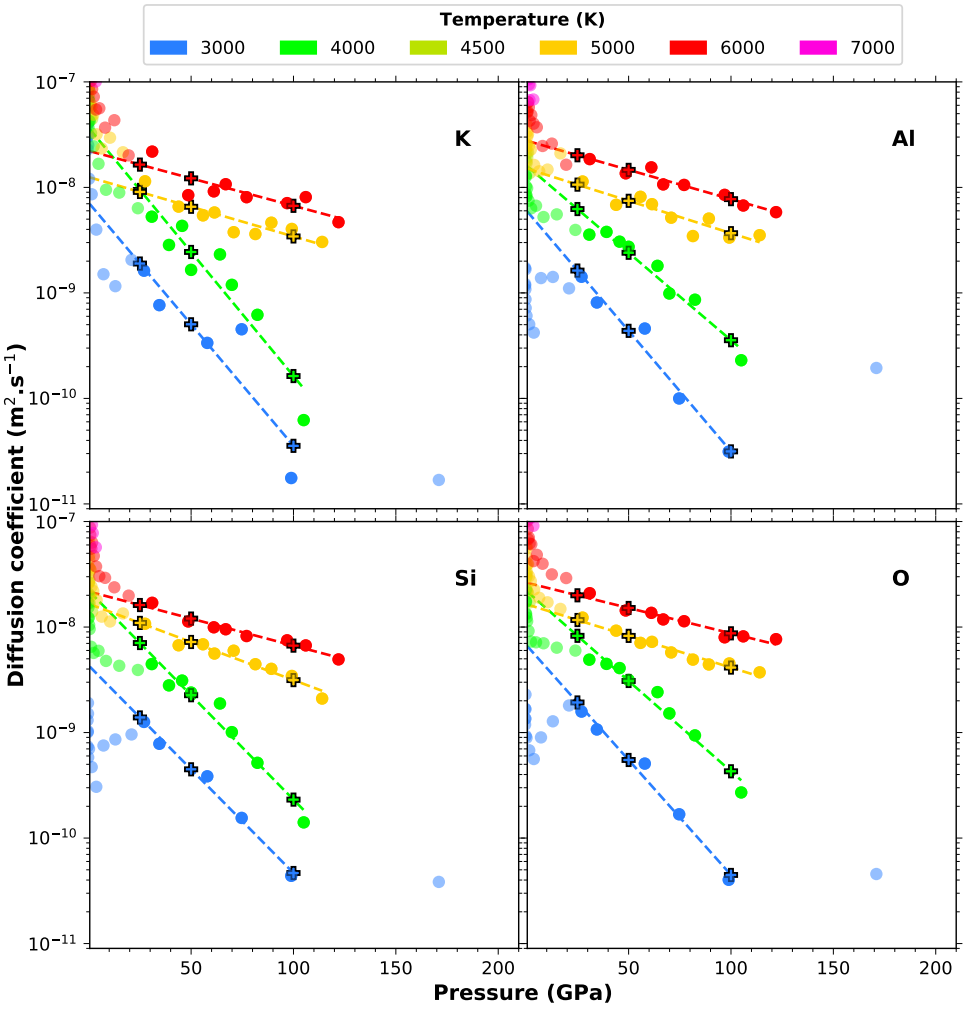

Figure A.23 – Self-diffusion coefficients in $KAlSi_3O_8$ as a function of pressure and Arrhenius fit in the 25–150 GPa range. Colors indicate temperatures. Crosses indicates the diffusion values estimated from the fit at 25, 50 and 100 GPa.

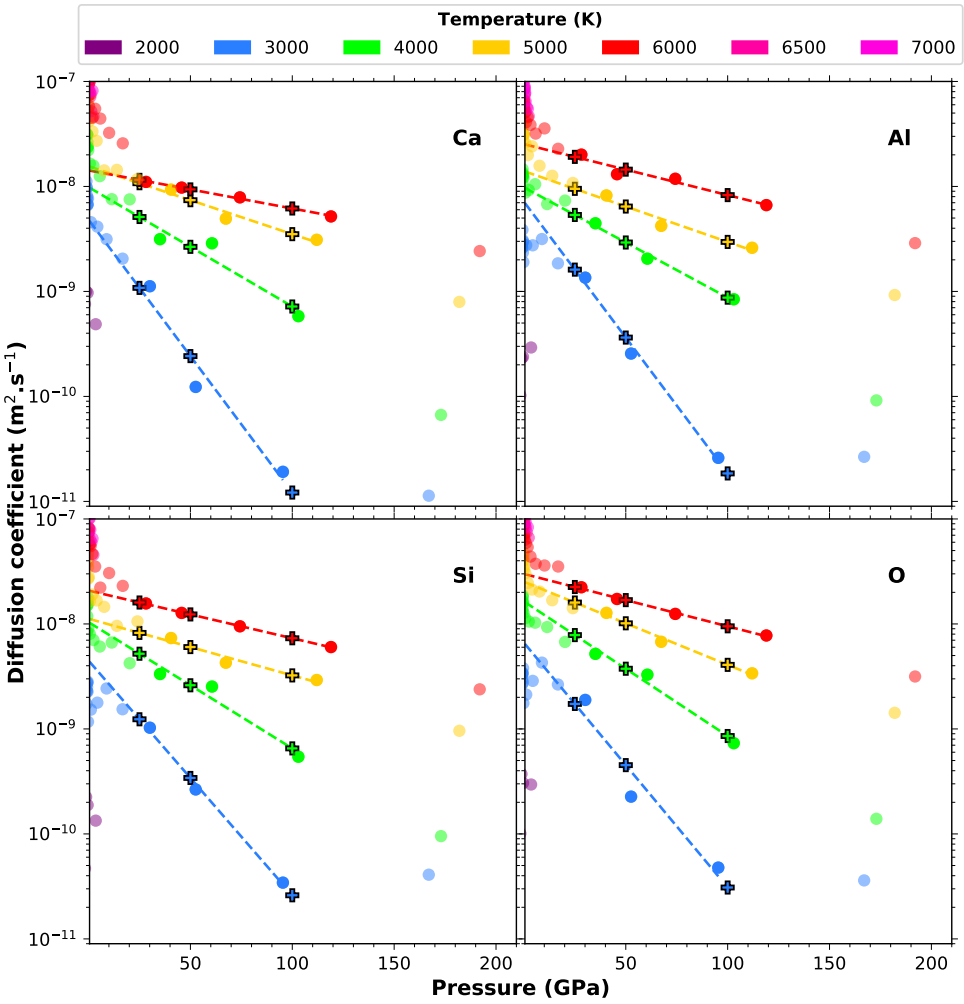

Figure A.24 – Self-diffusion coefficients in $CaAl_2Si_2O_8$ as a function of pressure and Arrhenius fit in the 25–150 GPa range. Colors indicate temperatures. Crosses indicates the diffusion values estimated from the fit at 25, 50 and 100 GPa.

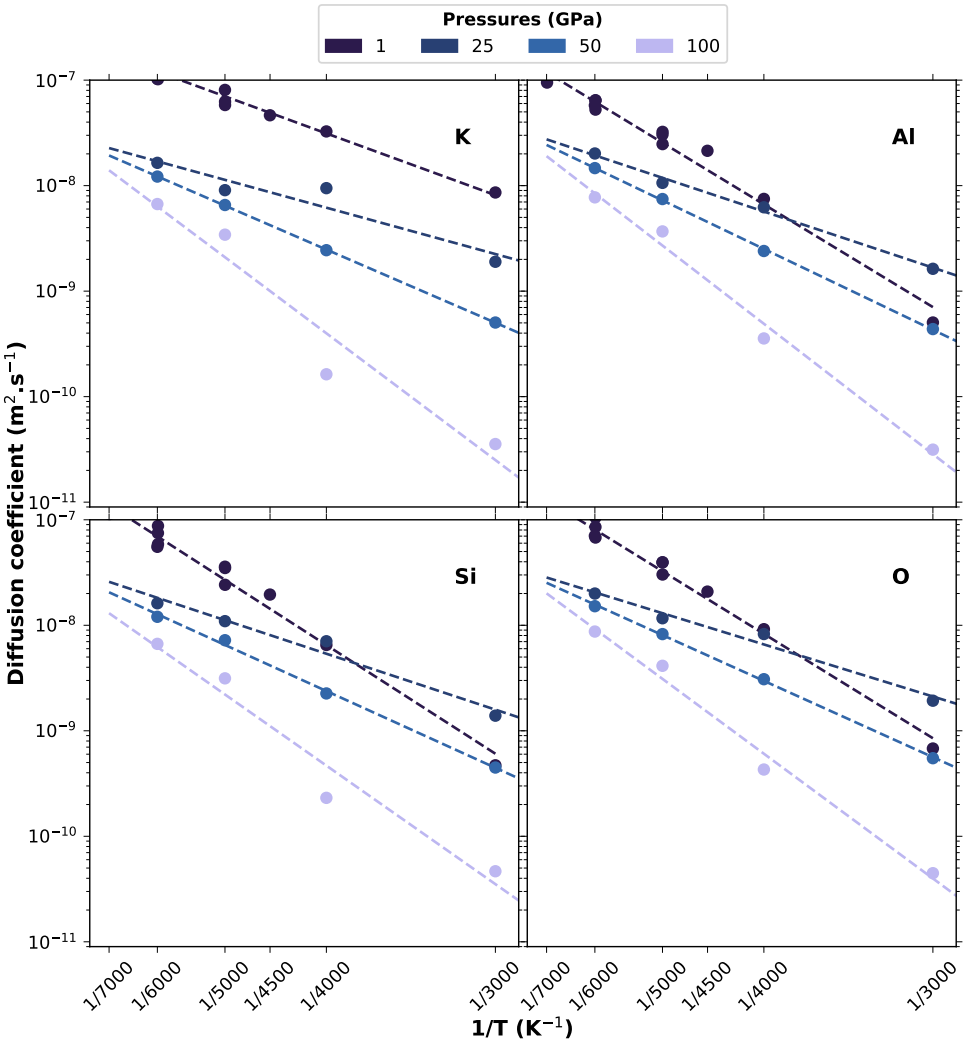

Figure A.25 – Self-diffusion coefficients in $KAlSi_3O_8$ as a function of the inverse temperature and Arrhenius fits to the data estimated in figure A.23 at 25, 50 and 100 GPa (colors).

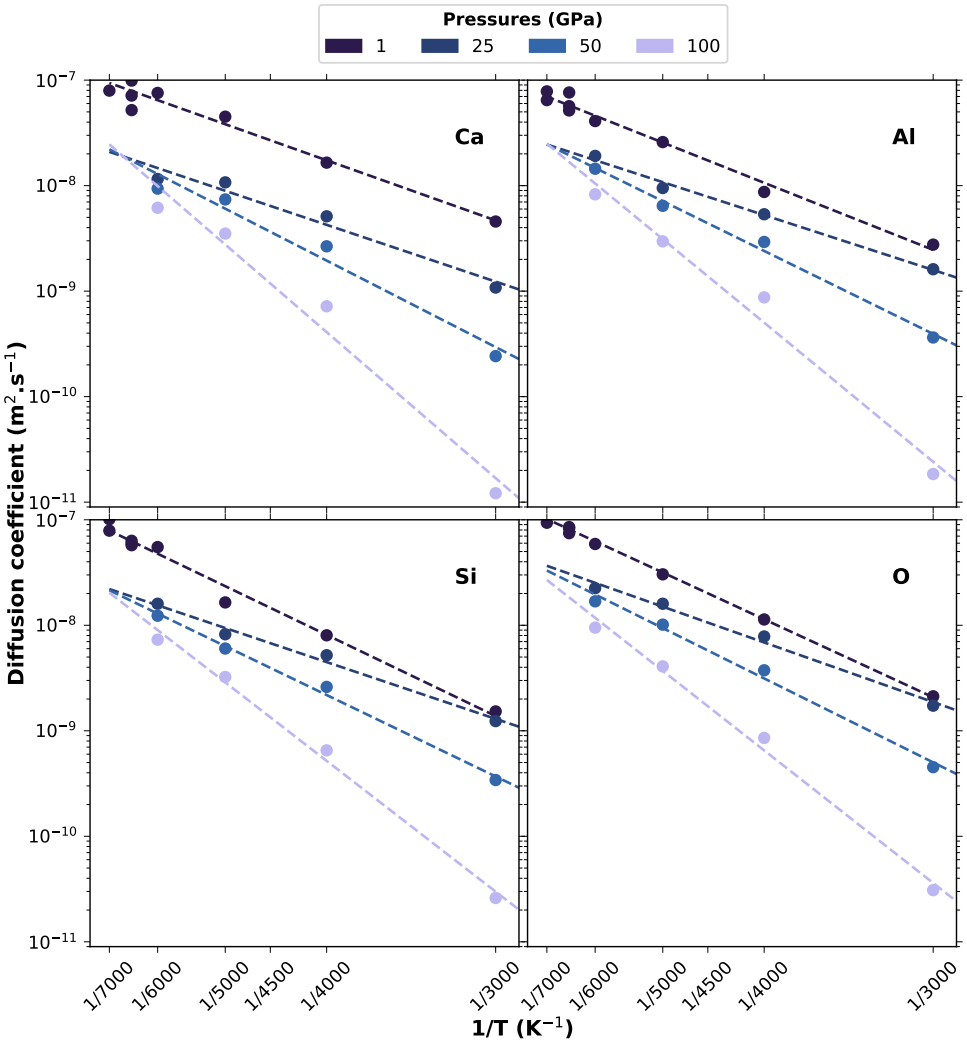

Figure A.26 – Self-diffusion coefficients in $CaAl_2Si_2O_8$ as a function of the inverse temperature and Arrhenius fits to the data estimated in figure A.24 at 25, 50 and 100 GPa (colors).

A.4.4 Thermodynamics

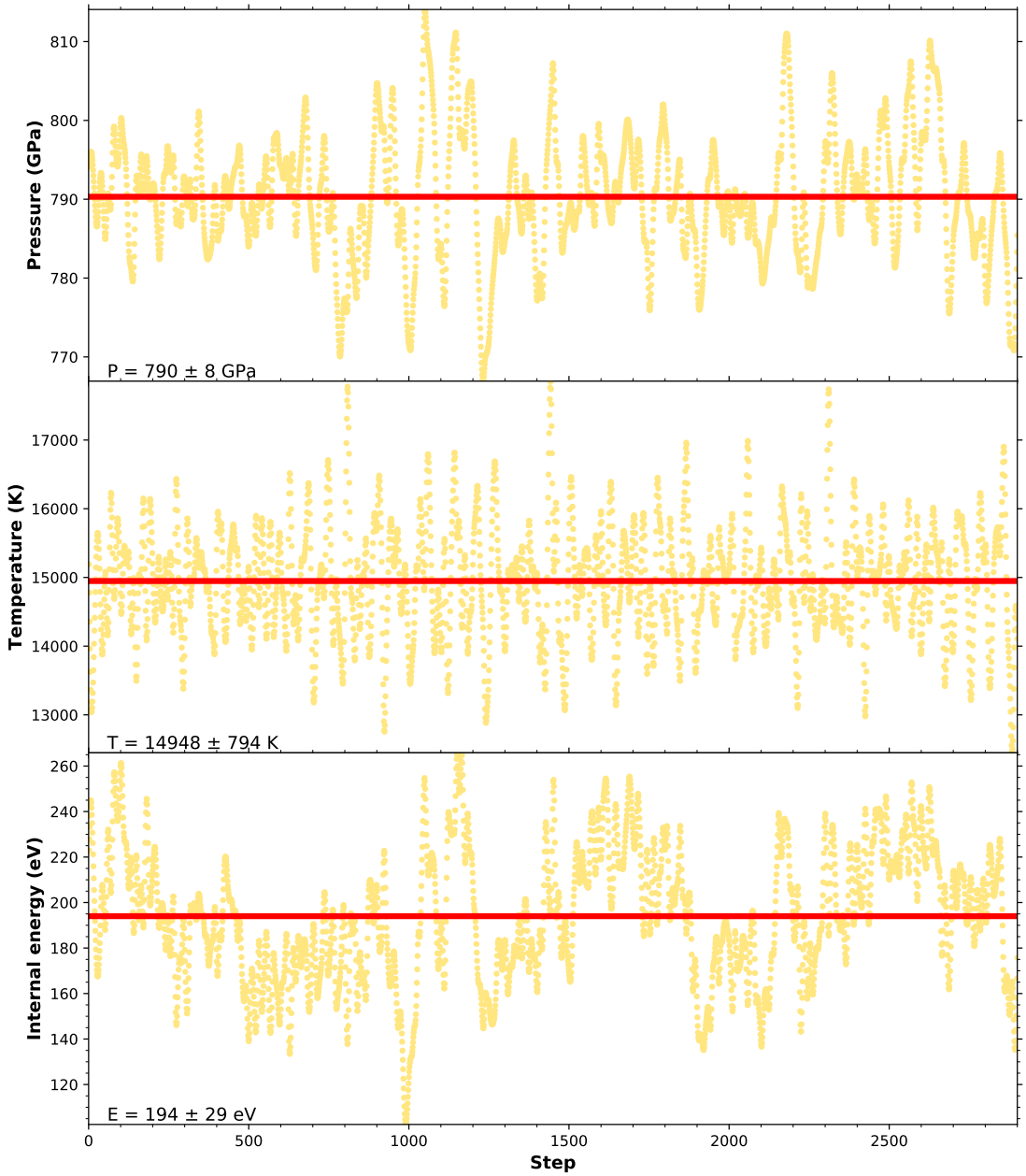

Figure A.27 – Instantaneous pressure, temperature and energy in the short simulation of $CaAl_2Si_2O_8$ at 15 000 K and 8.23 g cm^{-3}. The red line indicates the arithmetic average of the thermodynamic parameters and the numerical value of the average are indicated $\pm\sigma$, σ being the population standard deviation.

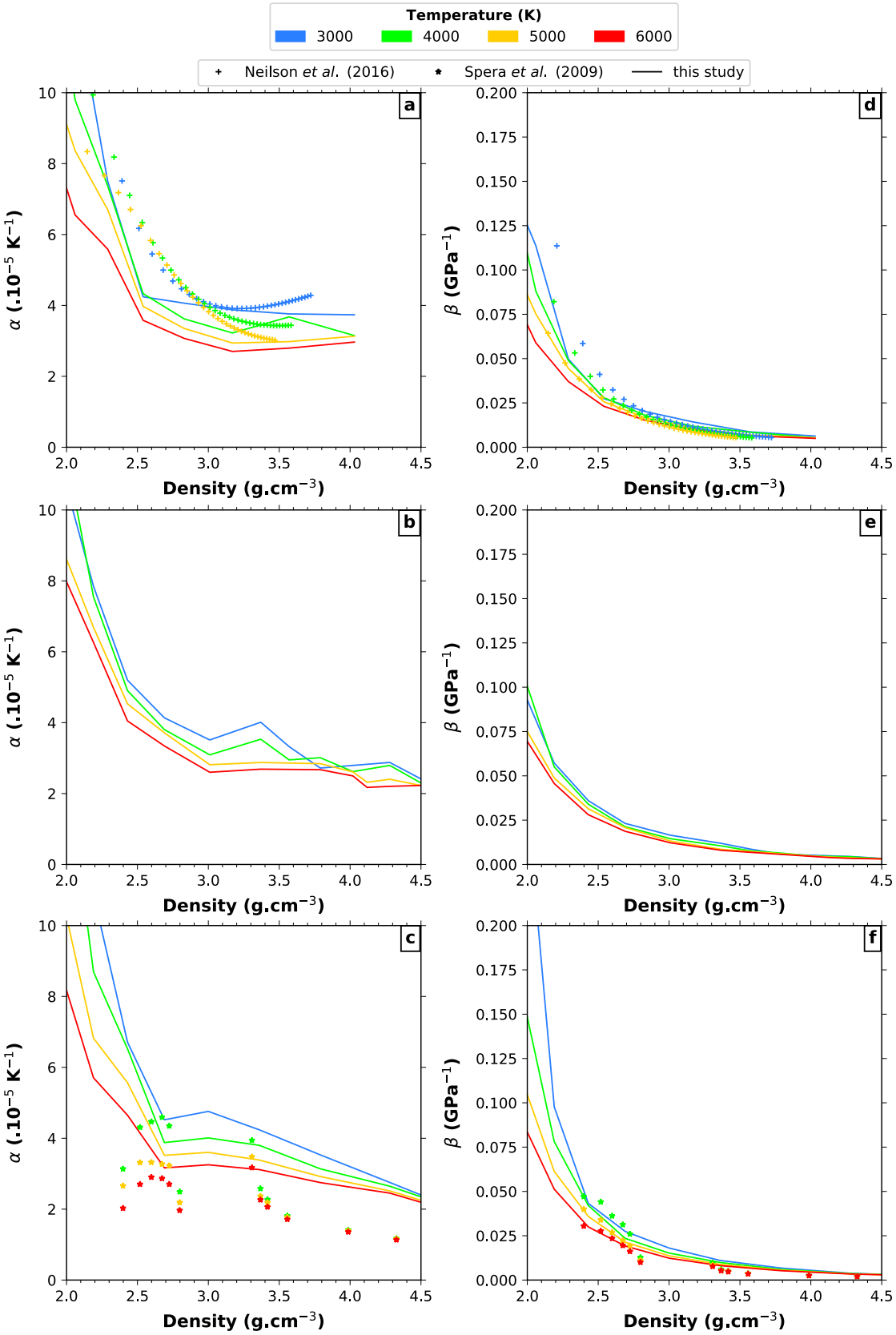

Figure A.28 – Isobaric expansivity α and isothermal compressibility β as a function of density for the (a,d) Na-, (b,e) K- and (c,f) Ca-feldspar end-members. Colors indicate temperature. Data previously obtained by two classical MD simulations on the same end-members (Neilson *et al.*, 2016; Spera *et al.*, 2009) are also indicated for comparison. The same figure as a function of pressure instead of density is presented figure 6.6.

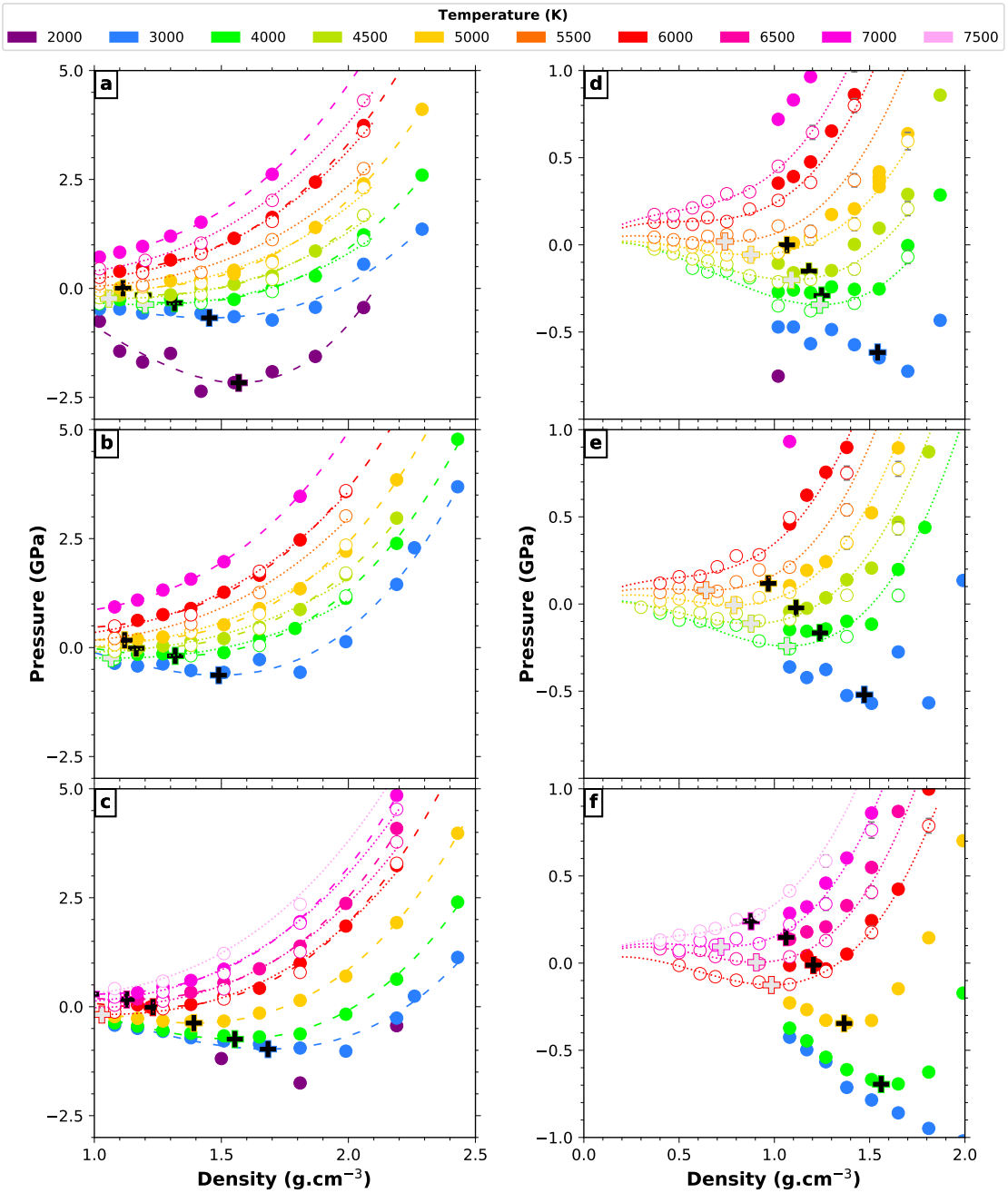

Figure A.29 – Computed pressure as a function of density for the (a) Na- (b) K- and (c) Ca-feldspar end-members and their respective enlarged view on the low density region, (d), (e) and (f). Open and solid symbols indicate values obtained with the two sets of pseudopotentials described in table 2.1 ("low density" and "main study" respectively). Dashed and dotted lines represent constrained 3rd order polynomial curve fits corresponding to the respective two sets of pseudopotentials. The gray and black crosses indicate the liquid spinodals corresponding respectively to the open and solid datasets. The statistical errors on the mean are included in the size of the points. Numerical data are available in annexes B.1.1 and B.1.2. The same figure for unconstrained fits is presented in chapter 6, figure 6.7.

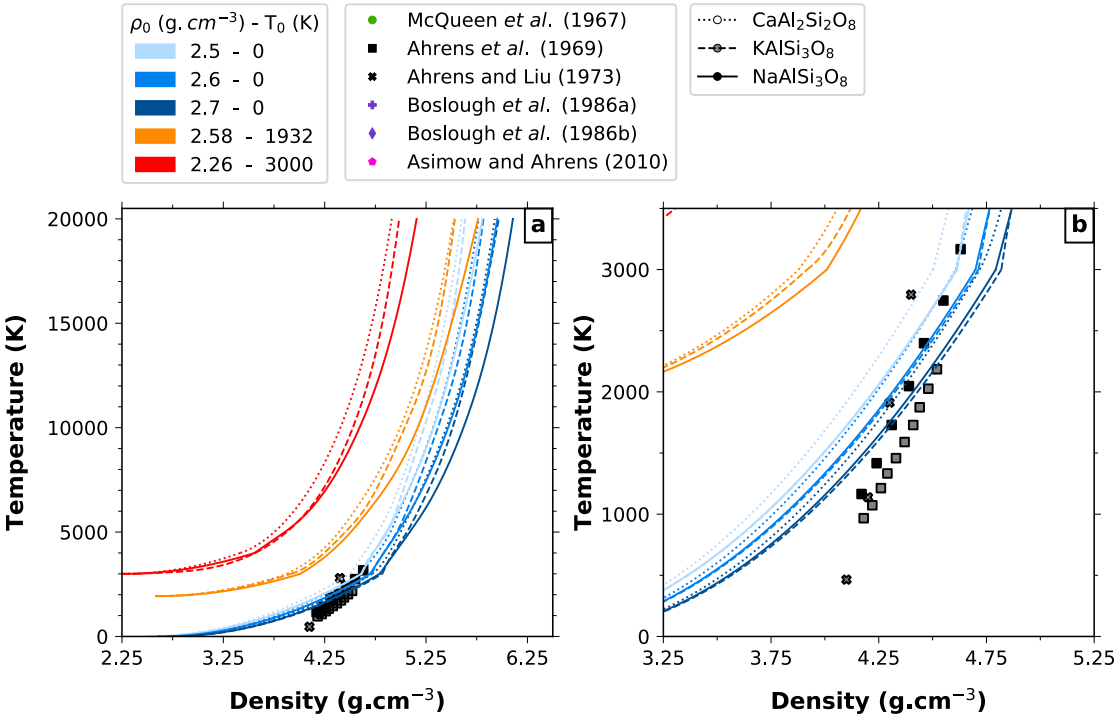

Figure A.30 – Hugoniot curves for each initial temperature and density of the crust (colors) on the temperature-density projection and its associated zoom on the low temperatures range (b). Data from experiments on feldspars are indicated by the colored markers. The feldspars composition is represented by the line styles for the Hugoniot curves and by the markers filling for the experimental data: solid symbols - $NaAlSi_3O_8$, half transparent symbols - $KAlSi_3O_8$, open symbols - $CaAl_2Si_2O_8$. A cubic interpolation is used to smooth the Hugoniot curves. The other projections are presented in figure 6.10.

APPENDIX B

TABLES OF DATA

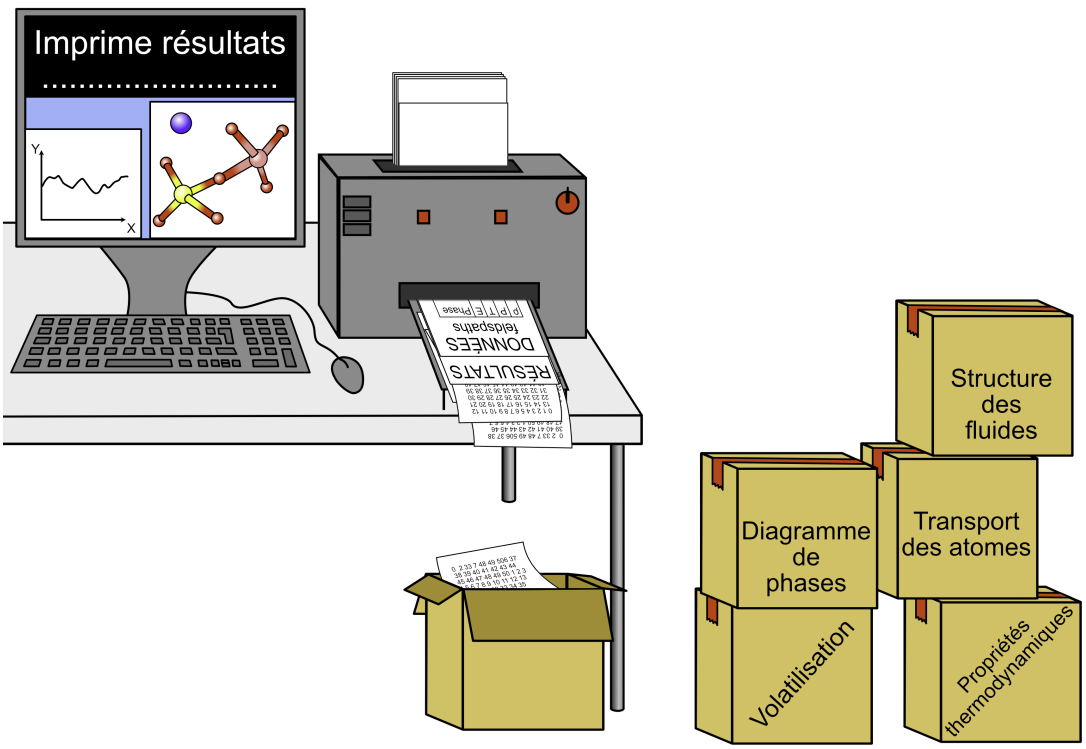

Heureusement que l'on imprime pas réellement tous les résultats de nos simulations, sinon il faudrait plus que quelques cartons pour les stocker !

B.1 Thermodynamics data

B.1.1 Averages

The data on alkali feldspar are already available in the Zenodo repository "Thermodynamics data of Alkali Feldspars from FPMD simulations" (Kobsch and Caracas, 2020). There are five *.txt* files corresponding to different datasets (see below for descriptions). Each file contains the following information:

Thermodynamic properties (pressure, temperature, internal energy, heat capacity) and thermoelastic coefficients (isobaric expansivity, isothermal compressibility, thermal pressure coefficient) computed from our ab-initio molecular dynamics simulations.

Arithmetic time averages of the pressure (P), temperature (T) and internal energy (E) are performed over the entire simulations. The standard deviation of the data to the mean is indicated by $stdev\_X$, where X is P, T or E. The statistical error to the mean (err_X) is computed using the blocking method as described by Flyvbjerg and Petersen (1989). The sign '>' is indicated before the value of the statistical error when no convergence was reached during the estimation of this error. The heat capacity Cv is computed using fluctuations on both potential and kinetic energies Allen and Tildesley (1989) and its statistical error $stdev\_Cv$ is computed using the bootstrap method.

We computed the thermoelastic coefficients only for densities above $1.5\,\mathrm{g\,cm^{-3}}$. The thermal pressure coefficient (TPC $= \frac{\partial P}{\partial T}|_V$) is the slope of linear fit of P vs. T isochores. The isothermal compressibility ($\beta = -\frac{1}{\rho}\frac{\partial \rho}{\partial P}|_T$) is computed using central finite differences on our P vs. ρ isotherms. The isobaric expansivity ($\alpha = \frac{1}{\rho}\frac{\partial \rho}{\partial T}|_P$) is computed using the previously computed β and TPC.

kobsch-ds01.txt Simulations on $NaAlSi_3O_8$ with the standard set of pseudopotentials ("main study" in table 2.1)

kobsch-ds02.txt Simulations on $NaAlSi_3O_8$ with pseudopotentials which require a lower plane wave energy cutoff, set to 370 eV ("low density" in table 2.1)

kobsch-ds03.txt Simulations on $NaAlSi_3O_8$ with hard pseudopotentials in order to reduce the overlap of electronic spheres, in particular for Na-Na pairs. The energy cutoff for this set of pseudopotentials is 950 eV ("high density (h1)" in table 2.1)

kobsch-ds04.txt Simulations on $KAlSi_3O_8$ with the standard set of pseudopotentials ("main study" in table 2.1)

kobsch-ds05.txt Simulations on $KAlSi_3O_8$ with pseudopotentials which require a lower plane wave energy cutoff, set to 370 eV ("low density" in table 2.1)

Data on $CaAl_2Si_2O_8$ are not yet published online.

B.1.2 Spinodal

Table B.1 – Minima of the 3rd order polynomial curves fitted to our P-ρ data for the two datasets (down to $0.5\,\mathrm{g\,cm^{-3}}$ and above $1\,\mathrm{g\,cm^{-3}}$). d and σ_d are the constant term and its standard deviation obtained after the least square fit.

		Main data set (above $1\,\mathrm{g\,cm^{-3}}$)					Low densities data set (down to $0.5\,\mathrm{g\,cm^{-3}}$)				
	T	ρ	P	reduced	d	σ_d	ρ	P	reduced	d	σ_d
	(K)	($\mathrm{g\,cm^{-3}}$)	(GPa)	χ^2	(GPa)	(GPa)	($\mathrm{g\,cm^{-3}}$)	(GPa)	χ^2	(GPa)	(GPa)
$NaAlSi_3O_8$	2000	1.52	-2.14	0.189	8.223	10.752					
	3000	1.53	-0.64	0.026	-4.72	3.319					
	4000	1.33	-0.27	0.003	-4.416	1.259	1.31	-0.39	0.003	-0.997	0.237
	4500	1.18	-0.15	0.002	-0.612	1.753	1.14	-0.25	0.004	-0.296	0.086
	5000	*NaN*	*NaN*	0.003	-3.333	1.294	1.01	-0.08	0.005	-0.317	0.096
	5500						0.83	0.03	0.005	-0.23	0.102
	6000	*NaN*	*NaN*	0.001	-2.35	0.594	*NaN*	*NaN*	0.003	-0.099	0.076
	6500						*NaN*	*NaN*	0.003	-0.157	0.08
	7000	*NaN*	*NaN*	0	-1.746	0.509					
$KAlSi_3O_8$	3000	1.55	-0.55	0.039	-8.165	4.04					
	4000	*NaN*	*NaN*	0.003	-5.044	1.221	1.18	-0.27	0.005	-0.427	0.116
	4500	*NaN*	*NaN*	0.001	-4.634	0.948	0.97	-0.12	0.005	-0.183	0.059
	5000	*NaN*	*NaN*	0.002	-4.044	1.129	0.87	0.02	0.003	-0.339	0.102
	5500						*NaN*	*NaN*	0.004	-0.33	0.107
	6000	*NaN*	*NaN*	0.002	-2.348	1.129	*NaN*	*NaN*	0.008	-0.343	0.155
	7000	*NaN*	*NaN*	0	-2.898	0.78					
$CaAl_2Si_2O_8$	3000	1.78	-1	0.012	-7.784	2.254					
	4000	1.61	-0.71	0.001	-4.604	0.585					
	5000	1.39	-0.34	0.001	-2.518	0.736					
	6000	1.17	-0.01	0.002	-1.795	1.031	1.11	-0.16	0.01	-0.656	0.273
	6500	*NaN*	*NaN*	0.001	-4.338	1.264	1.01	-0.01	0.004	-0.333	0.091
	7000	*NaN*	*NaN*	0	-2.996	0.99	0.79	0.11	0.004	-0.266	0.107
	7500						*NaN*	*NaN*	0.004	-0.403	0.103

Table B.2 – Minima of the constrained 3rd order polynomial curves (constant term set to 0) fitted to our P-ρ data for the two datasets (down to $0.5\,g\,cm^{-3}$ and above $1\,g\,cm^{-3}$).

		Main data set (above $1\,g\,cm^{-3}$)			Low densities data set (down to $0.5\,g\,cm^{-3}$)		
	T (K)	ρ ($g\,cm^{-3}$)	P (GPa)	reduced χ^2	ρ ($g\,cm^{-3}$)	P (GPa)	reduced χ^2
$NaAlSi_3O_8$	2000	1.57	-2.17	0.176			
	3000	1.45	-0.67	0.03			
	4000	1.32	-0.33	0.008	1.2	-0.37	0.012
	4500	1.19	-0.15	0.002	1.06	-0.23	0.009
	5000	1.11	0	0.004	0.91	-0.09	0.01
	5500				0.78	0.01	0.008
	6000	0.86	0.35	0.002	0.62	0.13	0.003
	6500				*NaN*	*NaN*	0.004
	7000	*NaN*	*NaN*	0			
$KAlSi_3O_8$	3000	1.49	-0.63	0.054			
	4000	1.32	-0.19	0.009	1.07	-0.24	0.014
	4500	1.16	-0.02	0.003	0.88	-0.11	0.009
	5000	1.12	0.17	0.006	0.79	-0.01	0.008
	5500				0.64	0.08	0.009
	6000	0.69	0.42	0.003	*NaN*	*NaN*	0.012
	7000	*NaN*	*NaN*	0.001			
$CaAl_2Si_2O_8$	3000	1.68	-0.97	0.029			
	4000	1.55	-0.74	0.006			
	5000	1.39	-0.38	0.002			
	6000	1.23	-0.01	0.002	1.03	-0.18	0.017
	6500	1.13	0.17	0.003	0.94	-0.03	0.009
	7000	0.99	0.29	0.002	0.77	0.08	0.007
	7500				*NaN*	*NaN*	0.013

B.1.3 Hugoniot equation of state and shock conditions

Table B.3 – Shock states parameters for five different ground states and impactor velocities for the Ca-feldspar. All the results with a temperature higher than 20 000 K are extrapolated from fits of the Hugoniot data points. We choose velocities for the impactor of 12.9, 15.2 and 18.1 km s^{-1} for the impacts with the Earth, and of 8.3, 11.5 and 15.2 km s^{-1} for the impacts with the Moon. These values correspond respectively to the first, second, and third quartile of the 1487 impacts generated for the Earth in the work of Raymond *et al.* (2013) on planetary impacts during the late veneer. All their impactors had a density of 3.0 g cm^{-3}. Without information on their composition we consider them to be made of the same material as the crust.

$U_{impactor}$ (km s^{-1})	ρ_0 (g cm^{-3})	T_0 (K)	ρ (g cm^{-3})	T (K)	P (GPa)	U_p (km s^{-1})
8.3	2.26	3000	4.34	9458	101	4.66
8.3	2.585	1932	4.68	7185	113	4.4
8.3	2.5	0	4.80	5255	107	4.53
8.3	2.6	0	4.88	4856	111	4.45
8.3	2.7	0	4.95	4534	114	4.38
11.5	2.26	3000	4.76	15995	175	6.38
11.5	2.585	1932	5.13	12105	193	6.07
11.5	2.5	0	5.19	10165	185	6.21
11.5	2.6	0	5.28	9533	190	6.11
11.5	2.7	0	5.36	9001	196	6.02
12.9	2.26	3000	4.93	19890	213	7.13
12.9	2.585	1932	5.32	15006	234	6.8
12.9	2.5	0	5.34	13231	225	6.94
12.9	2.6	0	5.45	12342	232	6.84
12.9	2.7	0	5.54	11547	238	6.74
15.2	2.26	3000	5.28	26699	284	8.36
15.2	2.585	1932	5.61	21257	311	7.99
15.2	2.5	0	5.59	19669	300	8.14
15.2	2.6	0	5.71	18264	308	8.03
15.2	2.7	0	5.82	16984	316	7.92
18.1	2.26	3000	5.79	36640	387	9.91
18.1	2.585	1932	6.08	29870	423	9.5
18.1	2.5	0	5.98	28574	409	9.65
18.1	2.6	0	6.10	26829	420	9.53
18.1	2.7	0	6.21	25307	430	9.41

Table B.4 – Same as in Table B.3 for the K-feldspar.

$U_{impactor}$ ($km\,s^{-1}$)	ρ_0 ($g\,cm^{-3}$)	T_0 (K)	ρ ($g\,cm^{-3}$)	T (K)	P (GPa)	U_p ($km\,s^{-1}$)
8.3	2.26	3000	4.38	8663	102	4.65
8.3	2.585	1932	4.71	6732	115	4.37
8.3	2.5	0	4.81	4631	107	4.54
8.3	2.6	0	4.88	4371	111	4.46
8.3	2.7	0	4.94	4141	114	4.38
11.5	2.26	3000	4.81	14804	176	6.38
11.5	2.585	1932	5.15	11665	194	6.05
11.5	2.5	0	5.20	9577	185	6.21
11.5	2.6	0	5.29	8987	190	6.12
11.5	2.7	0	5.38	8401	196	6.03
12.9	2.26	3000	4.95	18892	214	7.13
12.9	2.585	1932	5.34	14524	236	6.78
12.9	2.5	0	5.36	12477	225	6.95
12.9	2.6	0	5.46	11658	232	6.85
12.9	2.7	0	5.56	10902	238	6.75
15.2	2.26	3000	5.27	25714	284	8.36
15.2	2.585	1932	5.62	20968	312	7.97
15.2	2.5	0	5.60	18854	300	8.15
15.2	2.6	0	5.73	17312	308	8.04
15.2	2.7	0	5.82	16382	316	7.93
18.1	2.26	3000	5.74	35753	387	9.91
18.1	2.585	1932	6.06	29764	423	9.48
18.1	2.5	0	5.98	27825	408	9.66
18.1	2.6	0	6.11	25846	419	9.53
18.1	2.7	0	6.19	24698	429	9.41

Table B.5 – Same as in Table B.3 for the Na-feldspar.

$U_{impactor}$ (km s^{-1})	ρ_0 (g cm^{-3})	T_0 (K)	ρ (g cm^{-3})	T (K)	P (GPa)	U_p (km s^{-1})
8.3	2.26	3000	4.35	8029	102	4.65
8.3	2.585	1932	4.70	6200	114	4.39
8.3	2.5	0	4.80	4552	107	4.54
8.3	2.6	0	4.87	4278	111	4.46
8.3	2.7	0	4.94	3994	114	4.38
11.5	2.26	3000	4.78	12621	175	6.38
11.5	2.585	1932	5.16	9933	193	6.06
11.5	2.5	0	5.19	8522	185	6.21
11.5	2.6	0	5.28	8024	190	6.12
11.5	2.7	0	5.38	7507	196	6.02
12.9	2.26	3000	4.95	15179	213	7.13
12.9	2.585	1932	5.32	12253	234	6.79
12.9	2.5	0	5.36	10681	225	6.94
12.9	2.6	0	5.47	10000	231	6.84
12.9	2.7	0	5.56	9391	237	6.74
15.2	2.26	3000	5.20	20292	283	8.36
15.2	2.585	1932	5.59	16650	310	7.98
15.2	2.5	0	5.61	15089	299	8.14
15.2	2.6	0	5.72	14214	307	8.03
15.2	2.7	0	5.82	13389	315	7.92
18.1	2.26	3000	5.61	27502	385	9.92
18.1	2.585	1932	5.97	23142	420	9.48
18.1	2.5	0	5.92	22008	406	9.65
18.1	2.6	0	6.03	21087	417	9.52
18.1	2.7	0	6.13	20106	427	9.4

APPENDIX C

ARTICLE

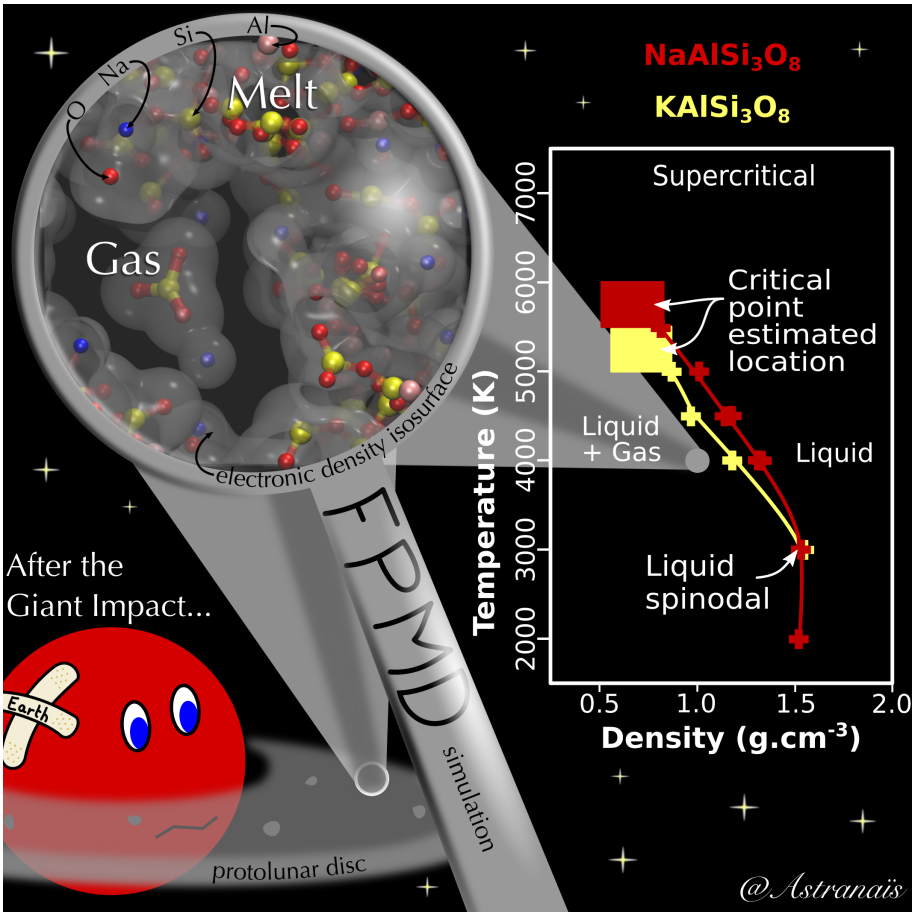

Image proposée au journal JGR pour être l'image de couverture du numéro où parait l'article.

The critical point and the supercritical state of alkali feldspars: implications for the behavior of the crust during impacts

Anaïs Kobsch[1], **Razvan Caracas**[1,2]

[1]CNRS, École Normale Supérieure de Lyon, Laboratoire de Géologie de Lyon UMR 5276, 46 allée d'Italie, 69364 Lyon, France
[2]The Centre for Earth Evolution and Dynamics (CEED), University of Oslo, Postbox 1028 Blindern, N-0315 Oslo, Norway

Key Points:

- First-principles molecular-dynamics simulations of feldspars at low-density and high-temperature
- Free Na, K and O_2, SiO or SiO_2 constitute the first gas when the vaporization starts
- The critical point of alkali feldspars is between 0.5-0.9 g/cm^3 and 5000-6000 K

Corresponding author: Anaïs Kobsch, anais.kobsch@ens-lyon.org

Abstract

The position of the vapor-liquid dome and of the critical point determine the evolution of the outermost parts of the protolunar disk during cooling and condensation after the Giant Impact. The parts of the disk in supercritical or liquid state evolve as a single thermodynamic phase; when the thermal trajectory of the disk reaches the liquid-vapor dome, gas and melt separate leading to heterogeneous convection and phase separation due to friction. Different layers of the proto-Earth behaved differently during the Giant Impact depending on their constituent materials and initial thermodynamic conditions. Here we use first-principles molecular dynamics to determine the position of the critical point for $NaAlSi_3O_8$ and $KAlSi_3O_8$ feldspars, major minerals of the Earth and Moon crusts. The variations of the pressure calculated at various volumes along isotherms yield the position of the critical points: 0.5–0.8 $g\,cm^{-3}$ and 5500–6000 K range for the Na-feldspar, 0.5–0.9 $g\,cm^{-3}$ and 5000–5500 K range for the K-feldspar. The simulations suggest that the vaporization is incongruent, with a degassing of O_2 starting at 4000 K and gas component made mostly of free Na and K cations, O_2, SiO and SiO_2 species for densities below 1.5 $g\,cm^{-3}$. The Hugoniot equations of state imply that low velocity impactors ($< 8.3\,km\,s^{-1}$) would at most melt a cold feldspathic crust, whereas large impacts in molten crust would see temperatures raise up to 30 000 K.

Plain Language Summary

The Moon was formed after the cooling and aggregation of the debris disk produced by the Giant Impact between a small planet in formation and the early Earth. To understand completely this process of cooling and aggregation we need thermodynamic information about the constituents of the disk, like the position of the liquid-vapor dome and also of the critical point, located at the top of this dome. Here we use a technique called first-principles molecular dynamics and based on quantum chemistry to perform computational experiments on $NaAlSi_3O_8$ and $KAlSi_3O_8$ feldspars, major minerals of the Earth and Moon crusts. We performed calculations of the fluids evolution at temperatures typical of those of the debris disk (from 2000 to 7000 K) and at densities covering the liquid-gas transition for these temperatures. We find the position of the critical points: 0.5–0.8 $g\,cm^{-3}$ and 5500–6000 K range for the Na-feldspar, 0.5–0.9 $g\,cm^{-3}$ and 5000–5500 K range for the K-feldspar. The simulations suggest that the liquid and the gas have different compositions, mainly due to a degassing of O_2 starting at 4000 K, and free components like Na, K, O_2, SiO and SiO_2 which go preferentially inside the gas phase. The behavior of liquid feldspars at high density shows also that impacts from a low-velocity object would at most melt a cold crust, whereas impacts in molten crust would see temperatures raising up to 30 000 K.

1 Introduction

For more than twenty years, the simulations of formation of the Moon from an impact-generated disk have made huge progress and went through many different models, from the canonical impact (Canup & Esposito, 1996) to the high-energy high-angular-momentum impact (Ćuk & Stewart, 2012; Canup, 2012) and more recently to the formation of a synestia (Lock et al., 2018). They tend to reproduce better and better the observed features of the actual Earth-Moon system, like the angular momentum or the fractionation of some isotopes and elements. Even if each simulation uses different parameters, they all model the mantle and the core using respectively particles of dunite or forsterite and of iron, with the equations of state provided by the M-ANEOS package (Melosh, 2007).

For many years shock experiments improved equations of state, which are major parameters of the hydrodynamics simulations, on a variety of major geological materials, like $MgSiO_3$ glass, enstatite and olivine (Luo et al., 2004), silica (Kraus et al., 2012) and MgO (Root et al., 2015). These experiments sample points along the shock Hugo-

niot equations of state, at high temperatures and pressures, typical for the peak conditions attained during the shock. In the laboratory their timescales are on the order of nanoseconds, which makes many measurements hard to realize. Moreover, they can rarely follow the evolution of the sample after the shock release, when the pressure and temperature decrease along quasi-isentropic lines over time scales on the order of minutes. Combined with long sample and apparatus preparation times and few available shock facilities, such experiments are relatively scarce. Here we take a numerical approach and employ first-principles molecular dynamics (FPMD) simulations. We study the behavior of two feldspar end-members terms in this regime.

Feldspars are aluminosilicates with general formula $(Ca,Na,K)(Al,Si)_4O_8$. Based on the major-element composition of the current terrestrial bulk continental crust, its normative mineralogy would consist of 58.9 % feldspars by weight. The Moon highland crust is made of at least 80 % of ferroan anorthosite, a rock composed almost entirely of Ca-end-member plagioclase (Taylor & McLennan, 2008). On Venus spectroscopic studies show the presence of a mixture of phases that includes albite. This should be a relatively stable phase compared to Ca-bearing minerals, like anorthite, which would easily react with the atmosphere (Gilmore et al., 2017). Surface models of Mercury show the presence of up to 70 % of Na-rich plagioclase feldspar (Warell et al., 2010). Feldspar minerals are also widely present in eucrites, on Vesta, etc. (e.g. Szurgot, 2014). Thus feldspars represent major mineral components of the crust of terrestrial bodies.

Because of their importance, feldspars have been widely studied for more than a century. The first melting experiments were done in the beginning of the last century on plagioclase feldspars (Bowen, 1913), in which Ca- and Na- end-members melted at about 1823 and 1373 K respectively. Ever since a plethora of experiments, e.g. Bell and Roseboom Jr. (1969); Newton and Smith (1967); Urakawa et al. (1994); Lindsley (1966); Akaogi et al. (2004), determined the melting curves of the entire series, investigated the behavior of the melt in various assemblages and analyzed the compressibility of feldspathic glasses up to at least 128 GPa.

The Hugoniot equations of state for the three end-members and several intermediate compositions were investigated through shock experiments (e.g. McQueen et al., 1967; Ahrens et al., 1969; Asimow & Ahrens, 2010).The maximum shock conditions reached in these experiments were about 120 GPa and 6000 K.

More recently, molecular dynamics (MD) simulations gave access to a series of thermodynamic properties, including the structure and the dynamics of the melts over a large range of temperatures (2500–6100 K) and pressures (0–160 GPa), using either classical MD (e.g. Spera et al., 2009; Neilson et al., 2016) or FPMD (e.g. Karki et al., 2011). However, despite all this effort at high pressures and temperatures, to date, no experiment nor simulation has been done on feldspars in the low-pressure and high-temperature region, which is of interest for the evolution of the protolunar disk.

Here we investigate the two alkali feldspar end-members, $NaAlSi_3O_8$ and $KAlSi_3O_8$, in the low density region by performing FPMD simulations. We compute thermodynamic data as well as transport and structural properties over a wide range of densities and temperatures that are relevant for the synestia or the protolunar disk, as suggested by smooth particle hydrodynamics (SPH) simulations.

2 Material and Methods

2.1 Computational Parameters

We perform first-principle molecular dynamics simulations as implemented in the Vienna *ab initio* simulation package (VASP) (Kresse & Hafner, 1993; Kresse & Furthmüller, 1996a, 1996b; Kresse & Joubert, 1999). We use the projector augmented-wave (PAW)

formulation (Blöchl, 1994) of the density-functional theory (DFT) (Hohenberg & Kohn, 1964; Kohn & Sham, 1965; Mermin, 1965) to compute energy and forces, with the Perdew-Burke-Ernzerhof parametrization of the generalized gradient approximation (Perdew et al., 1996) for the exchange correlation term. We employ an energy cutoff of 550 eV for the plane waves and of 800 eV inside the augmentation sphere; we sample the reciprocal space in the Gamma point. Simulations are performed in the canonical NVT ensemble where the temperature (T) is controlled by the Nosé-Hoover thermostat (Nosé, 1984; Hoover, 1985) around an average fixed value, and the volume (V) and the number of particles (N), are kept constant. At each timestep the energy is converged to 1×10^{-3} eV, which corresponds to at least 7 representative digits in the absolute value of the energy.

We model the feldspar end-members in cubic cells containing 208 atoms (16 formula units) and 1024 or 1152 electrons for the Na- and K-feldspars respectively. A cubic cell of 14 Å side (volume of V_0=2744 Å^3) corresponds to a density of 2.54 g cm^{-3} for the Na feldspar and of 2.69 g cm^{-3} for the K-feldspar. The size of our simulations cells is typical for such FPMD studies on silicates. The relatively small number of atoms is compensated by the long trajectories, which allows for a good sampling of the configurational space. Chemical species have the time to form and break several times during the same simulation. Convergence tests carried out using 416 atoms for two temperature-density couples (5000 K–2.1 g cm^{-3} and 4000 K–1.2 g cm^{-3}) give a pressure difference of less than 0.12 GPa and a difference in the internal energy of less than 10 meV/atom between the two cell sizes. The pair distribution functions are invariant when changing between the simulations cells with 208 and 416 atoms. The relative proportions of coordination polyhedra remain constant within 1-2% between the two cells.

Production simulations are performed in the 2000–7000 K range and 1–6 g cm^{-3} range in order to bracket the critical temperature and density. This also spans both liquid and liquid-gas regions. This corresponds to a ρ/ρ_0 range of about 2.4–0.4, ρ_0 being close to ambient density (corresponds to V_0=2744 Å^3). We use a timestep of 1 fs in all simulations above 4500 K and 1.6 g cm^{-3} and of 2 fs below these conditions. The initial liquid state is obtained by heating a static configuration up to 4000 K for 8 ps and thermalizing it for 2 ps. This time lapse is enough to equilibrate the velocities of the atoms and to reduce the energy fluctuations. The other temperatures of interest are reached with one or more heating/cooling steps of 1000 K during 1 ps. Then at all temperatures and pressures we let the fluids equilibrate for at least 1 ps. We record production runs of 15–20 ps length after the total equilibration and we use the final state to compress or expand the cell in order to reach respectively higher or lower densities.

To increase the speed of calculations and be able to reach low densities down to 0.5 g cm^{-3}, we use pseudopotentials which require a lower plane wave energy cutoff, set to 370 eV. In this region, the production runs last about 4 ps, which is enough to estimate the global pressure and temperature. For the simulations above 3.5 g cm^{-3}, we use hard pseudopotentials in order to reduce the overlap of electronic spheres, in particular for Na-Na pairs. The energy cutoff for this set of pseudopotentials is 950 eV.

2.2 Post Processing

The post-processing was realized using the UMD package (Caracas et al., 2020). The reported values of the thermodynamic potentials, *i.e.* pressure and internal energy, are arithmetic time averages over the entire simulation, the spread in values is given by the standard deviation and the statistical error on the mean is computed using the blocking method (Flyvbjerg & Petersen, 1989).

The radial distribution function ($g(r)$) is the primary tool to analyze the structure of the fluids. It gives the average number of atoms of type B in a spherical shell of radius r and thickness dr centered around each atom of type A, relative to the number of

atoms at the same distance in an ideal gas at the same density. Mathematically $g_{AB}(r)$ is defined as

$$g_{AB}(r) = \frac{n_B(r)}{n_B^{ideal}(r)} \quad (1)$$

$$n_B^{ideal}(r) = \frac{4\pi}{3}\rho_B\left((r+\ \mathrm{d}r)^3 - r^3\right) \quad (2)$$

$$n_B(r) = \frac{1}{N_A \tau_{run}} \sum_{\tau=1}^{\tau_{run}} \sum_{A=1}^{N_A} \sum_{B=1}^{N_B} \Pi_{(r,r+\ \mathrm{d}r)}(r_{AB}) \quad (3)$$

with $\rho_B = \frac{N_B}{V_{cell}}$ being the atomic density of type B atoms in the simulation cell of volume V_{cell}, N_A and N_B the number of atoms of type A and B in the cell, τ_{run} the total number of time steps and $\Pi_{(r,r+\ \mathrm{d}r)}(r_{AB})$ the gate function which is equal to 1 if $r \leq r_{AB} < r+\ \mathrm{d}r$ (r_{AB} being the distance between the center of atoms A and B) and 0 else.

We use $\mathrm{d}r = 0.05\,\text{Å}$ as the discretization step of the computed $g(r)$. The first peak of the $g(r)$ offers a good approximation to the average bond length, representing the highest probability bond length. The first minimum of the $g(r)$ function yield the radius of the first coordination sphere. It is this radius that we use as threshold to define if two atoms are bonded or not: if their interatomic distance r_{AB} is smaller than this radius, they are considered to form a chemical bond. Note that the chemical bonds do not have a temporal minimum limit, but only a maximal spatial extent. As such the minimum lifetime of a bond is the timestep of the simulation.

The integral over *g(r)* up to its first minimum yields the average coordination number. The coordinating polyhedra are defined by the atoms that are found inside the first coordination sphere. Actually, the average coordination number corresponds to the sum of the order of the coordinating polyhedra weighed by their relative concentrations. In a more general way, the chemical species can be defined as the largest chains of connected atoms. At high pressure, as the fluid is compact this actually corresponds to an infinite polymer.

The self-diffusion coefficient, D, is obtained from the Einstein relation:

$$D_A = \lim_{t\to\infty} \frac{1}{6t}\left\langle \frac{1}{N_A}\sum_{i=1}^{N_A} |\overrightarrow{r_{A,i}}(t+t_0) - \overrightarrow{r_{A,i}}(t_0)|^2 \right\rangle, \quad (4)$$

where the term between brackets is the mean square displacement (MSD) for a time window with width t. The first part of the MSD, typical of a few hundred femtoseconds, corresponds to the ballistic part of the transport and the second part to the diffusive part.

Finally, we characterize the shocked state of the feldspars, in terms of pressure (P), density (ρ) and internal energy (E), according to the Hugoniot equation:

$$E - E_0 + \frac{1}{2}(P+P_0)(\frac{1}{\rho} - \frac{1}{\rho_0}) = 0 \quad (5)$$

To obtain the Hugoniot we perform simulations at several temperatures and find the volume for which the pressure and internal energy values satisfy the Hugoniot equation.

2.3 Finding the Critical Point

Figure 1 shows a model for the pressure variation as a function of density for various isotherms. The local maximum and minimum of the isotherms define, respectively, the vapor and the liquid spinodal points. When these points are linked over all isotherms they construct the vapor and liquid spinodal lines. They both meet at the critical point.

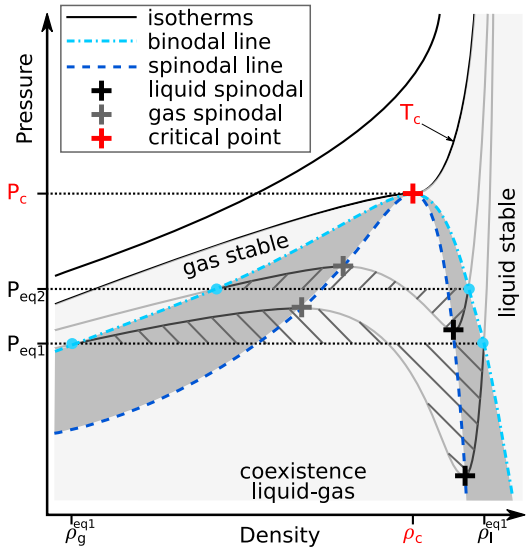

Figure 1. The analysis of the variation of the pressure as a function of density along different isotherms gives the stability domains for liquid, gas, and supercritical fluid. For a given isotherm, the extrema of the pressure correspond to the liquid and gas spinodal points; joining them yields the spinodal lines. The Maxwell equal-area construction (hatched areas) yields the binodal line. At equilibrium, a liquid with density ρ_l^{eq} is in equilibrium with a gas with density ρ_g^{eq}; they are both at the same equilibrium pressure P_{eq}. Both lines have the critical point as a common maximum. The liquid and the gas are stable in the light gray areas and metastable in the dark gray areas, at respectively higher and lower density. The coexistence of gas and liquid is stable in the region between the two spinodals. The supercritical fluid is stable above the critical isotherm line.

The states between the two spinodal lines are unstable as a single phase, *i.e.* liquid or gas; only the mixture of the two is stable between the spinodals.

The Maxwell construction allows to find the equilibrium pressure and densities of the liquid and gas at a given temperature. Its derivation originates from equating the free energies of the liquid and the gas it can be constructed graphically from the pressure-density relations along isotherms. In Figure 1, the equilibrium isobar is found when the area above it and below the P-ρ curve on the gas side is equal to the area below it and above the P-ρ curve on the liquid side. The intersection of the equilibrium isobar with the P-ρ curve at a given isotherm defines the equilibrium liquid and gas density points, ρ_l^{eq} and ρ_g^{eq} respectively. They correspond to the limit of the stability domains: liquids are stable at densities higher than ρ_l^{eq}, and gases are stable at densities lower than ρ_g^{eq}. The spinodal points mark the limit of the metastability region. Liquids are metastable between the ρ_l^{eq} and the liquid spinodal, gases are metastable at densities between the ρ_g^{eq} and the gas spinodal. When connected at all temperatures, the equilibrium points define the liquid-gas dome, also called the vapor-liquid dome. Its importance comes from the role it plays during cooling and depressurization of a hot dense liquid or during condensation of a gas phase. Gas and liquid separate only when the temperature and density fall inside the dome; outside of it the thermodynamic stable state is monophasic: either as a liquid, a gas, or a supercritical fluid.

At low densities and low temperatures the configurational space of the vapor might not be fully sampled by the MD simulations, which prevents us from correctly describing the vapor structure and thus from using the Maxwell construction to obtain the full liquid-gas dome. Nevertheless, we may explore the higher density region and compute the liquid spinodal points. We may sample the vapor region only in the vicinity of the critical point. Then we can estimate the position of the critical point. This method was successfully used in previous theoretical identification of critical points for SiO_2 (Green et al., 2018) and Al (Faussurier et al., 2009). Binder et al. (2012) showed the presence of finite-size effects in classical MD simulations using hard spheres interacting via Lennard-Jones potentials. However to date, the location of the minimum in the pressure-density curves is the best method for obtaining the spinodal curve (Green et al., 2018; Faussurier et al., 2009). The absence of minima in pressure above the critical temperature enforces the validity of the method.

3 Results

3.1 The Critical Points

We perform the calculations along several isotherms, ranging from 2000 K, corresponding to a hot magma, up to 7000 K, corresponding to the supercritical fluid. At each temperature we start at high density and decrease the density of the melt by expanding the volume of the simulation box. Depending on the temperature, we reach ambient pressure at densities of around $2.2\,\mathrm{g\,cm^{-3}}$ at 2000 K, $1.9\,\mathrm{g\,cm^{-3}}$ at 3000 K, $1.7\,\mathrm{g\,cm^{-3}}$ at 4000 K, $1.5\,\mathrm{g\,cm^{-3}}$ at 4500 K and $1.3\,\mathrm{g\,cm^{-3}}$ at 5000 K for the Na-feldspar, and of around $1.9\,\mathrm{g\,cm^{-3}}$ at 3000 K, $1.6\,\mathrm{g\,cm^{-3}}$ at 4000 K and $1.3\,\mathrm{g\,cm^{-3}}$ at 4500 K for the K-feldspar. As we perform simulations at lower densities we go into extension regime and the pressure drops below zero, where the melts are metastable (*i.e.* the dark grey area in Figure 1).

The general equation of states (EoS) describing the liquid, liquid+vapor, and vapor states is the van der Waals EoS, which is a third order expansion of pressure in terms of density, spanning the entire liquid and gas stability regions. As we do not sample the vapor state we approximate the P-ρ variation around the liquid spinodal with third order pressure-density polynomials. We perform the fits along each isotherm. The minima of these curves show the position of the liquid spinodals as defined in the method-

ology section. The position of the critical point lies in density between the gas and the liquid spinodals and in temperature between the last isotherm that shows minima and maxima and the first isotherm that shows a monotonous decrease of pressure.

The Na-feldspar shows pressure minima along isotherms up to 5500 K. The K-feldspar shows minima for isotherms up to 5000 K. In both cases, the minima are less and less pronounced as the isotherms approach the critical temperature. For these temperatures we extend the simulations to low-enough densities to observe a local maximum, corresponding to the gas spinodal (Figure 2 a and b). There are no local minima for the 6000 K isotherm and above for the Na-melt, and for the 5500 K and above for the K-melt. Along these isotherms the pressure only decreases monotonously. As the liquid and the gas spinodal converge into the critical point, the liquid and the gas spinodals on the last isotherm bracket the density of the critical point. The isotherms with and without local minima and maxima bracket the temperature of the critical point. Hence using our fitted values in the polynomial form, we obtain for the Na-feldspar the critical point in the 0.5-0.8 $\mathrm{g\,cm^{-3}}$ and in 5500–6000 K range. For the K-feldspar the critical point lies in the 0.5-0.9 $\mathrm{g\,cm^{-3}}$ and 5000–5500 K range.

Recently, two studies computed the critical point of SiO_2 (Green et al., 2018) and $MgSiO_3$ (Xiao & Stixrude, 2018) using FPMD. They found a supercritical temperature located between 5000 and 6000 K for SiO_2, and around 6600±150 K for $MgSiO_3$, and a supercritical density respectively around 0.5–1.0 $\mathrm{g\,cm^{-3}}$ and 0.48±0.05 $\mathrm{g\,cm^{-3}}$. The critical point of silica has been estimated before by Melosh (2007) to 5400 K and 0.55 $\mathrm{g\,cm^{-3}}$ based on thermodynamic calculations from ANEOS. The critical temperatures for two feldspar systems that we report here are similar to the critical temperature of SiO_2 but all lower than the critical temperature of $MgSiO_3$. The differences might arise from the degree of polymerization of the silica in the fluid.

Figure 2 shows the variation of pressure as a function of density for the Na- and K-feldspar end-members along all computed isotherms. The two sets of pseudopotentials yield a slightly different position of the liquid spinodal at low temperatures. As we approach the critical point these differences considerably decrease. The statistical errors on the mean are included in the size of the points. Due to the large number of steps in each simulation runs, we obtain small uncertainties for the mean pressure even at very low densities. These values, of the order of 10^{-3}–10^{-2} GPa, are smaller or about the same order of magnitude than those obtained by Green et al. (2018) who used the same method to estimate them. The spread of the pressure values during the simulation is about 1.6 GPa, which is typical for first-principles molecular-dynamics. The supplementary references the numerical results for pressure, temperature, density, and internal energy in the Data Sets S1 to S5.

3.2 Compressibility and Structure of the Fluids

In the one-phase region, for pressures above 0, we fit third-order Birch-Murnaghan equations of states to the pressure-density points along the 3000, 4000, 5000 and 6000 K isotherms. They are shown in Figure 2 (c) and (d). Table 1 shows the results and the comparison to existing data in the literature, both experimental (Lange, 2007; Tenner et al., 2007) and calculated (Bajgain & Mookherjee, 2020). The ρ_0 values extrapolated from our simulations using a second-order polynomial are 2.26 $\mathrm{g\,cm^{-3}}$ at 1373 K for $NaAlSi_3O_8$, *i.e.* about 2.7 % smaller than the experimental values (Lange, 2007).

The isobaric expansivity $\alpha = \frac{1}{\rho}\frac{\partial \rho}{\partial T}\big|_P$ and the isothermal compressibility $\beta = -\frac{1}{\rho}\frac{\partial \rho}{\partial P}\big|_T$ are computed from our pressure-temperature-density points using the same method as described by Spera et al. (2009). The values are available in the Data Sets S1 to S5. At 3000 K and about 2.6 $\mathrm{g\,cm^{-3}}$, we obtain $\alpha = 4 \times 10^{-5}\,\mathrm{K^{-1}}$ for alkali feldspars, while Neilson et al. (2016) obtained about $5 \times 10^{-5}\,\mathrm{K^{-1}}$ with their classical MD simulation of liquid

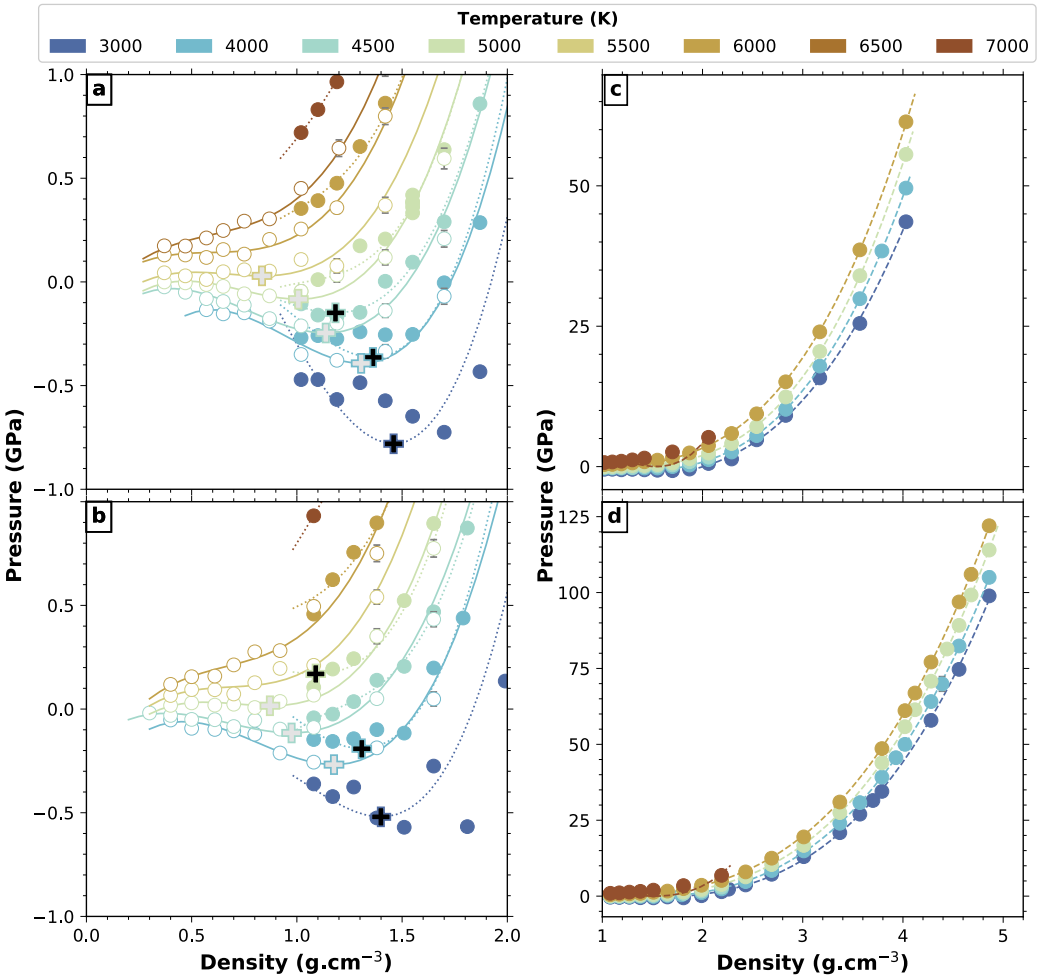

Figure 2. Computed pressure as a function of density around the spinodal part of the phase diagram for the (a) Na- and (b) K-feldspar end-members and their respective view on the complete density range studied here, (c) and (d). Colors indicate temperature.Open symbols indicate values obtained with pseudopotentials which require a lower plane wave energy cutoff than those used to obtain the data set of solid symbols. Solid and dotted lines represent the third order polynomial curve fits corresponding to the respective two sets of data. The open and solid crosses indicate the liquid spinodals corresponding to the minima of the two sets of curves respectively. The dashed curves in (c) and (d) are third-order Birch-Murnaghan equations of state fitted to our data. The statistical errors on the mean are included in the size of the points. For numerical data, the reader can refer to the Data Sets S1 to S5 in supplementary.

Table 1. Parameters of third-order Birch-Murnaghan equation of state fitted to our computed pressure-density values at high temperature and comparison with the available experimental data or theoretical results (FPMD) from the literature.

	Temperature (K)	ρ_0 ($g\,cm^{-3}$)	K_0 (GPa)	K_0'	source
$NaAlSi_3O_8$	298	2.615	56.4	3.9	crystalline albite Tenner et al. (2007)
	1373	2.326	17.5	11	liquid Tenner et al. (2007)
	2500	2.31	12	5.3	FPMD Bajgain and Mookherjee (2020)
	3000	2.01	11	4.9	
	4000	1.82	6.5	5.8	
	5000	1.3	0.8	11	
	6000	0.9	2×10^{-3}	7×10^2	
$KAlSi_3O_8$	295	2.554	57	4	crystalline sanidine Lange (2007)
	1473	2.298	15.8	12	liquid Lange (2007)
	3000	1.8	5	6.5	
	4000	1.69	4.5	6.1	
	5000	1.3	0.9	9	
	6000	0.80	2×10^{-3}	5×10^2	

albite at the same conditions. An intermediate value of $4.7 \times 10^{-5}\,K^{-1}$ was obtained by Stein et al. (1986) for liquid albite.

Figure 3 shows the pair distribution functions for the Na-feldspar at two densities as a function of temperature stemming from our simulations. At $2\,g\,cm^{-3}$ and 3000 K, conditions that are close to a hot magma at ambient pressure, the Si-O, Al-O, Na-O and K-O average bond lengths are 1.64 Å, 1.76 Å, 2.31 Å and 2.79 Å respectively. The T-O bonds (T being Al or Si) vary weakly with both pressure and temperature; over 100 GPa pressure range the relative decrease is about 2 %. However the decrease of the Na-O and K-O average bond lengths over the same pressure range is on the order of 10 and 20 % respectively. In general the bond lengths in the liquid at 3000 K are comparable to the values recorded in the solids at ambient conditions. The radius of the first coordination sphere for the T-O bonds decreases by about 10 % over 100 GPa pressure range, while the radius for the M-O (M being Na or K) follows the trend of the average bond lengths with a decrease of about 20 %.

As tectosilicates, the structure of the solid feldspars is built of a polymerized framework of SiO_4 and AlO_4 tetrahedra with the alkali cations distributed orderly in the pores of this polymer. In the liquid state, the framework and polymerization are still present, but the dominant coordination changes as a function of both pressure or density and temperature.

The average coordination number of Si and of Al by O in the computed fluids is similar for the two feldspar end-members (Figure 4). For Si, it increases from about 3.8 at $2.2\,g\,cm^{-3}$ to more than 5 above $4\,g\,cm^{-3}$; it is only weakly dependent on temperature. At lower densities the dependence is stronger with temperature: at $1\,g\,cm^{-3}$ it decreases from 3.8 at 3000 K to 2.9 at 7000 K. For Al, the coordination increases monotonously from about 3.7 at $1\,g\,cm^{-3}$ to about 6 above $4\,g\,cm^{-3}$ (corresponding to about 50 GPa). The spread of coordination numbers due to temperature is less than 0.5 units between 3000 K and 6000 K at all densities. The coordination number of Al by O is larger than the coordination number of Si by O at all densities and temperatures.

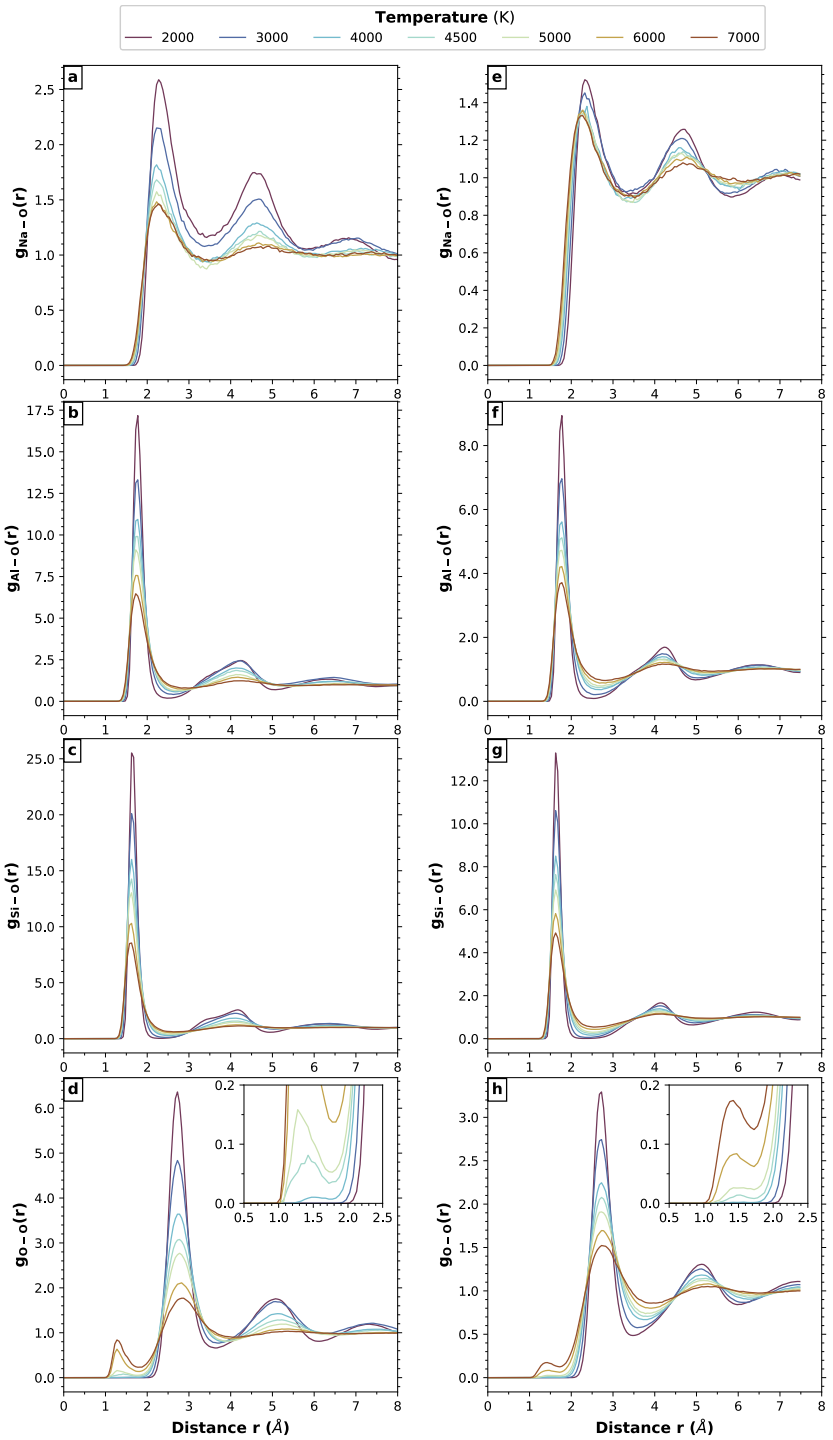

Figure 3. Pair distribution function of X-O (X being Na, Al, Si and O) in $NaAlSi_3O_8$ at $1.02\,g\,cm^{-3}$ (a,b,c,d) and $2.06\,g\,cm^{-3}$ (e,f,g,h). Colors indicate temperatures. The insert shows a zoom on the region 0.5–2.5 Å. The small peak located around 1.4 Å marks the presence of O_2 molecules.

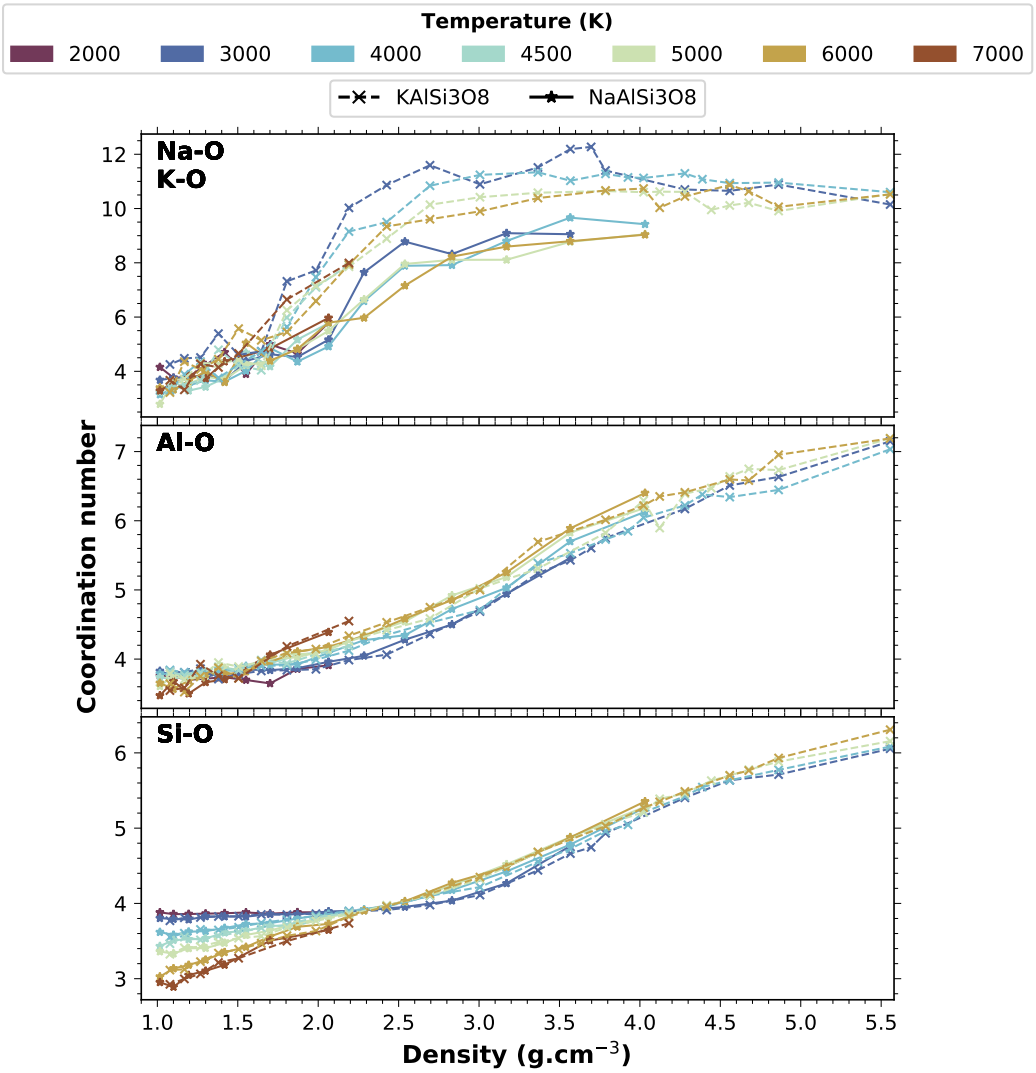

Figure 4. Average coordination number of Na, K, Al and Si by O for the Na- (stars and continuous lines) and K-feldspar (crosses and dashed lines). At ambient conditions the solid or glass feldspars have NaO_{6-9}, KO_9, AlO_4, and SiO_4 coordination polyhedra (Ribbe, 1984; Jackson et al., 1987; Xue & Stebbins, 1993; Muller et al., 1993). Colors indicate temperature.

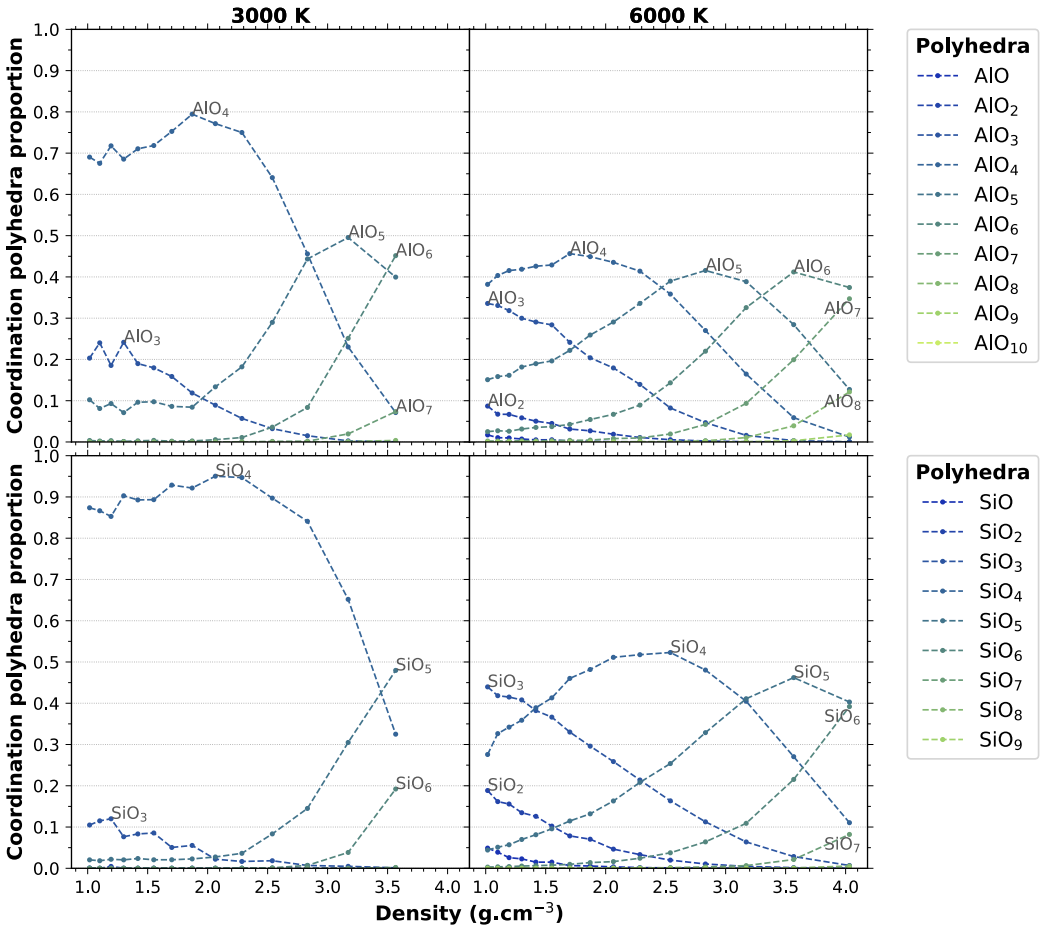

Figure 5. Relative proportion of SiO_x and AlO_x coordination species in $NaAlSi_3O_8$ for 3000 K and 6000 K as a function of density.

In terms of actual species rather than average coordination numbers, the two feldspar systems behave in a similar way to other silicate melts (Karki et al., 2018; Solomatova & Caracas, 2019). Figs. 5 and 6 show the proportion of the SiO_x and AlO_x species in the $NaAlSi_3O_8$ and $KAlSi_3O_8$ systems respectively for two relevant temperatures below (3000 K) and above (6000 K) the critical temperature as a function of density. In general the dominant species contains more O atoms for Al than for Si. At densities below 2.2 g cm^{-3}, the amount of under-coordinated Si and Al, *i.e.* SiO_x and AlO_x species with $x < 4$, increases with decreasing density and increasing temperature. This comes from the decrease of the coordination of cations by oxygen at the interface between the voids and the melt, as the system becomes metastable at lower densities.

At densities above 2.2 g cm^{-3}, under compression, the melt is dominated by SiO_4 tetrahedra up to about 25 GPa at 3000 K and 20 GPa at 6000 K. SiO_5 is present in the melt at low pressures at all temperatures. SiO_6 appears around 10 GPa at 3000 K and 5 GPa at 6000 K; it is the dominant species above 70 GPa at 3000 K and above 50 GPa at 6000 K.

Figure 7 shows the change in the major coordination of Si and Al by O as a function of pressure and temperature and the comparison between the fluids and the solids (crystalline forms). The melts are characterized by a series of structural changes where

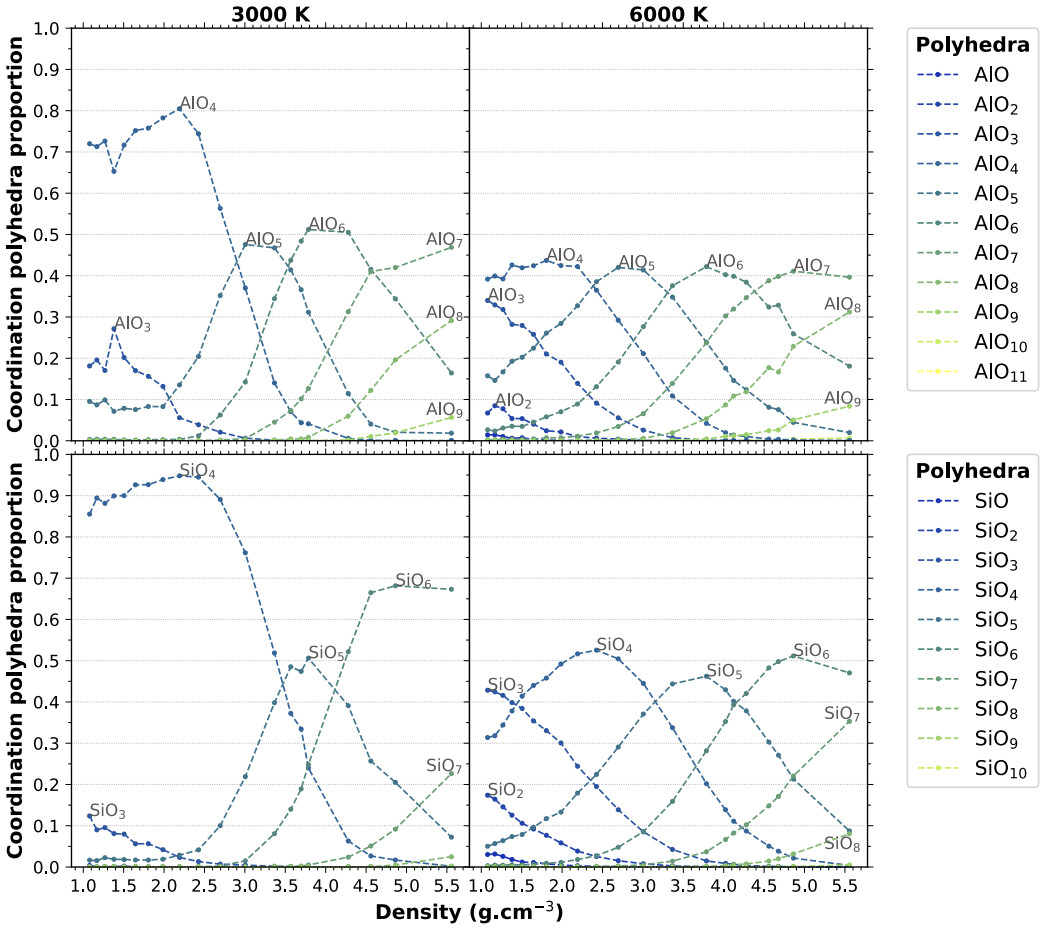

Figure 6. Relative proportion of SiO_x and AlO_x coordination species in $KAlSi_3O_8$ for 3000 K and 6000 K as a function of density.

the dominant coordination goes as $TO_4 \rightarrow TO_5 \rightarrow TO_6 \rightarrow TO_7$ ($\rightarrow TO_8$), T being Si or Al. This transition series follows closely the changes recorded in the solids, but the sequence is generally shifted towards higher pressures. The increasing temperature in the fluid shifts to larger pressure the change in dominant coordination. However the solids do no show five, seven or eight-fold coordination.

The lifetime of the coordination polyhedra underlines the long-lasting nature of the 4-fold coordination species SiO_4 and AlO_4 in the melts below the critical temperature. For example at low densities and 3000 K, the SiO_4 tetrahedra live up to 10 ps, and at 4000 K up to almost 4 ps. Increasing temperature leads to decreasing the maximum lifetime of all coordination polyhedra and extending the tail of lifetimes, as the bonds form and break with higher frequency. The SiO_x species tend to live longer than the AlO_x species at the same density and temperature. Figs. S1 (a) and (b) in supplementary display the lifetime of each type of coordination polyhedron at 3000 K and 6000 K for respectively Na- and K-feldspar melt at about $2.2\,\mathrm{g\,cm^{-3}}$.

Na and K act as interstitial cations in the large Si-Al-O polymer that constitutes the framework of the melt. For this reason their coordination polyhedra by O show a much larger variability than their equivalent Si and Al. Also the lifetime of the NaO_x and KO_x coordination polyhedra (Figure S2 in supplementary) is considerably shorter than the SiO_x and AlO_x.

3.3 Volatilization

The largest chemical species found in the simulations involve forming chains and rings of alternating cations and oxygens, in ... - oxygen - cation - oxygen - cation - oxygen - ... sequences. At high density all 208 atoms are connected in one infinite cluster, like an infinite polymer, which constitutes the liquid.

At low densities and below the critical temperature, long lasting cavities appear in the simulations, where isolated atoms or clusters of atoms may freely float inside. They represent the nucleating gas bubbles. Figure 8 shows a typical snapshot of the simulation cell of $NaAlSi_3O_8$ at 4000 K and $1.02\,\mathrm{g\,cm^{-3}}$ with the electronic density isosurface at $0.01\,\mathrm{e/\AA^3}$ drawn to indicate the different clusters. We see a large interconnected atomic polymer, forming the melt, and one $NaSiO_3$ cluster isolated from the rest of the atoms; this represents one of the first gas components in the nucleating bubbles. The distribution of the size of the atomic clusters is bimodal: the larger polymerized melt that surrounds the cavities and the smaller atomic clusters that populate these cavities (Figure 9). We notice that in all simulations, most of the species above 200 atoms or below 13 atoms live more than 30 fs.

In the melt at 4000 K, a limited number of species appear in the gas bubbles, with average lifetimes between 60 and 300 fs. The gas is dominated by free Na and K cations making up for at least half of the gas. Second in importance are small volatile species, like O_2, SiO, and SiO_2. In both feldspars Al is present in the gas phase only as traces as AlO or more complex species involving K, Na, Si and O. The volatilization of both feldspars is incongruent, mainly due to this lack of Al in the gas phase (see Figure S3 in supplementary). Between $1.4\,\mathrm{g\,cm^{-3}}$ and $1\,\mathrm{g\,cm^{-3}}$ the molar proportion of K and Na in the gas almost double with respect to the total available K and Na in the system, while Al remains almost entirely in the melt.

In the supercritical fluid at 6000 K there are no cavities, so we cannot talk about a gas phase: the species are all in a single fluid phase. The speciation becomes more diverse, with many more clusters being composed of 4 to 13 atoms. These clusters have short lifetimes and high mobility, inducing density fluctuations in the fluid over short time scales, which is characteristic of supercritical fluids. But at larger time and length scales the melt is homogeneous. In parallel there are fewer isolated Na but more isolated O atoms.

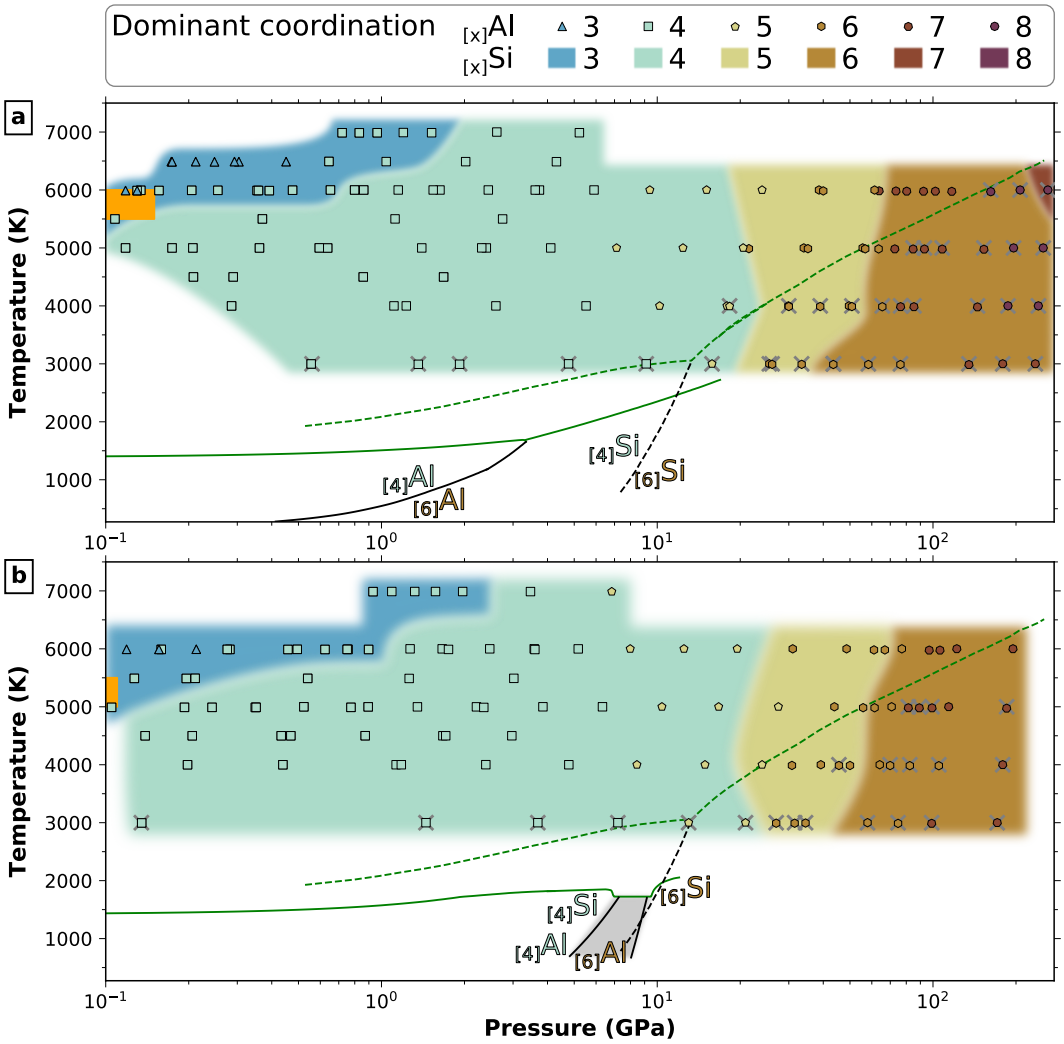

Figure 7. Changes of the major coordination of T by O (T being Al, Si) for (a) $NaAlSi_3O_8$ and (b) $KAlSi_3O_8$ compositions in the temperature-pressure projection plane. Background color indicate the number of O atoms in the SiO_x coordination polyhedra that dominates the structure of our computed melt. The shape and color of symbols indicate the number of O atoms in the AlO_x coordination polyhedra that dominates the structure of our computed melt. Dashed lines are solidus (green) and coesite-stishovite phase transition (black) for silica from Zhang et al. (1996); Tsuchiya and Tsuchiya (2011). Solid lines are solidus (green) and solid-solid phase transitions (black) for alkali feldspars (and jadeite above 2 GPa) from Bell and Roseboom Jr. (1969); Litvin and Gasparik (1993); Newton and Smith (1967); Urakawa et al. (1994); Lindsley (1966); Akaogi et al. (2004). The subsolidus coordination indicated in this diagram (denoted $_{[4]}$T and $_{[6]}$T for coordination number of T by O of 4 and 6 respectively) are for the crystalline phases. They may differ from the glasses coordination. The gray area indicate the region of $K_2Si_4O_9$ wadeite-type mineral, with Si 4 and 6-fold coordinated to O. The orange rectangle indicate the estimated location of the critical point as computed in part 3.1.

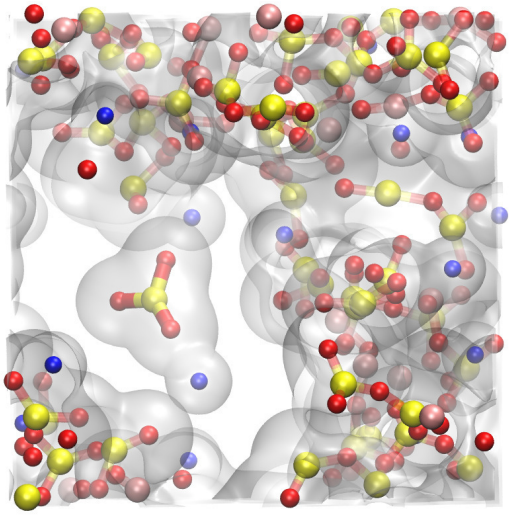

Figure 8. Snapshot of the iso-electronic density surface at 0.01 e/Å^3 in the simulation cell at 4000 K and 1.02 g cm^{-3} created with VMD (Humphrey et al., 1996). We see a clear bubble with a $NaSiO_3$ cluster inside. Colors indicate elements: red - O, yellow - Si, pink - Al, blue - Na.

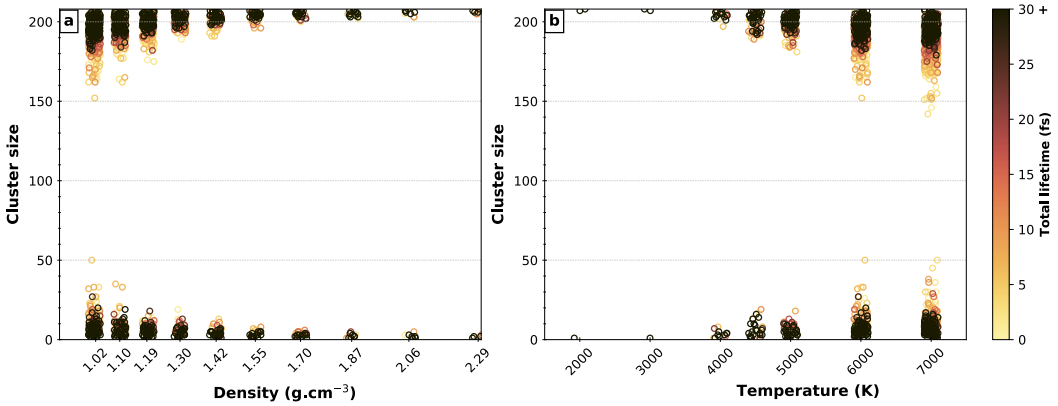

Figure 9. The size of all individual clusters of atoms in $NaAlSi_3O_8$ simulations as a function of (a) density at 6000 K or (b) temperature at 1.02 g cm^{-3} follow a bimodal distribution. The larger clusters polymerize to form the melt and the smaller clusters are separated, forming the gas phase. The analysis of the speciation takes into account the periodic character of the simulations. Each circle represents an individual cluster of the corresponding size (y axis). Color scale indicates the lifetime of each cluster. Clusters in the gas with size larger than 13 atoms have lifetimes shorter than 30 fs, with the large majority even shorter than 10 fs. In all simulations there is a stable liquid part, with big cluster above 200 atoms living more than 30 fs.

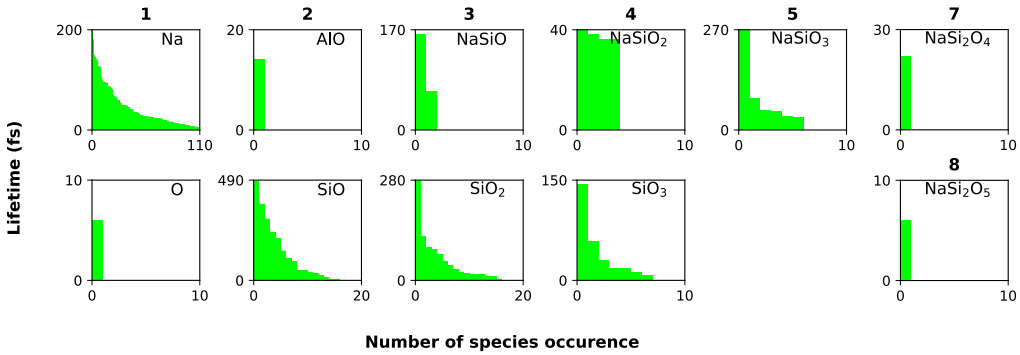

Figure 10. Lifetimes of isolated atomic clusters with less than 13 atoms at $1.02\,\mathrm{g\,cm^{-3}}$ and 4000 K.

The O_2 molecules live up to 550 fs. Figure 10 illustrates the lifetime of the isolated species with less than 13 atoms in the simulation of Na-feldspar end-member at $1.02\,\mathrm{g\,cm^{-3}}$ and 4000 K. Figure 11 shows the relative proportion of species with less than 13 atoms. Visscher and Fegley Jr. (2013) obtained the same major species using the MAGMA code (Fegley & Cameron, 1987; Schaefer & Fegley, 2004), but their species are more abundant, especially O_2 which is present in their estimations at all temperatures.

3.4 O_2 Behavior

A characteristic feature occurring at high temperatures is the presence of free O_2 molecules in the fluid. Figure 3 (d,h) shows the evolution of the pair distribution function of O-O with temperature for two representative densities: $1.0\,\mathrm{g\,cm^{-3}}$, that is below the liquid-gas boundary density and $2.1\,\mathrm{g\,cm^{-3}}$, that is in the fully fluid region. At low temperatures, the pair distribution function of O-O displays one main peak located around 2.7 Å, which represents the position of oxygens sharing the same edge of polyhedra around the Al or Si cations. The peak is found at all densities and temperatures and its position varies from 2.5 Å at high densities to 2.8 Å at low densities. At high temperatures the pair distribution function exhibits a second smaller peak located around 1.4 Å. This represents the O-O bond in a O_2 molecule. This peak can be seen at almost all densities above $3.5\,\mathrm{g\,cm^{-3}}$ only for temperatures higher than or equal to 4500 K, and only at very low densities at 4000 K. Its position varies from approximately 1.5 Å around $3\,\mathrm{g\,cm^{-3}}$ to 1.3 Å at $1.0\,\mathrm{g\,cm^{-3}}$.

We find O_2 molecules in both feldspar compositions studied here. This was also observed in previous simulations on pure SiO_2 (Green et al., 2018) and $MgSiO_3$ (Xiao & Stixrude, 2018). These consistent results suggest that there is potential degassing of O_2 from the silicate melt at high temperatures, independently of the composition of the melt. The process starts between 4000 and 4500 K.

According to Green et al. (2018), O=O pairs in silica survive for less than one vibrational period. For feldspars we observe speciation lifetimes on the order of several hundreds of femtoseconds, which is considerably longer than the vibrational period. It is possible that cations other than Al and Si, like Na and K, reduce the polymerization of the melt at these conditions and then enhance the formation and survival of O_2 groups.

3.5 Transport Properties

The MSD of all atoms at every temperature and density display a ballistic part, which corresponds to the conservation of the velocity of atoms after collisions, which last

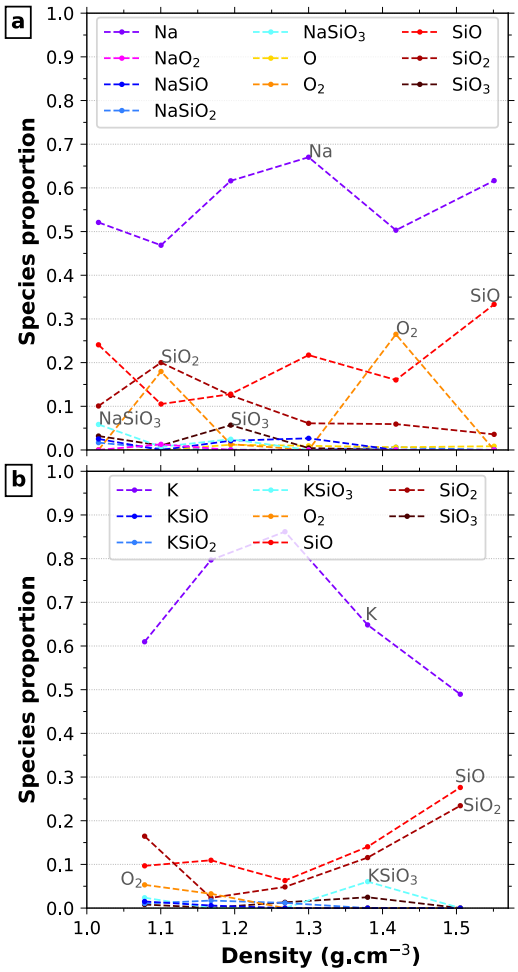

Figure 11. Proportion of all the isolated clusters of length less than 13 atoms as a function of density at 4000 K for (a) Na- and (b) K-feldspar end-members. Species that represent more than 5 % of all the gas species for at least one density point are labeled in the graph. The other species, found in trace amounts are the following (a): AlO, NaO, Si_2O_z ($z \in [\![3,5]\!]$) and some species among $Na_wSi_xO_z$ ($w \in [\![1,3]\!]$, $x \in [\![1,2]\!]$, $z \in [\![1,5]\!]$), (b): O, Si_2O_3, Si_2O_4, K_wAlO_2 ($w \in [\![0,1]\!]$) and some species among $K_wSi_xO_z$ ($w \in [\![1,3]\!]$, $x \in [\![1,3]\!]$, $z \in [\![3,7]\!]$).

on the order of 100 fs, followed by a fully diffusive part, which corresponds to the scattering of the velocity of atoms after collisions (Figures S4 and S5 in supplementary).

Along the 2000 K isotherm we observe a strong decoupling between the diffusion of Na or K and the diffusion of Si, Al, and O, with more than one order of magnitude difference at 1.0 g cm^{-3}. At 3000 K and about 1 GPa, all atoms travel considerably shorter distances on the order of 7–8 and 2 Å for respectively K, Na and Al, Si, O over the same amount of time. At 5000 K and densities around 1 g cm^{-3}, after 8 ps Al travels around 12–14 Å while Si and O travel 16–17 Å, and Na, K travel respectively 25 and 22 Å. At about 2.2 g cm^{-3}, the traveled distances over the same time decrease down to 9 Å for Si, 9–10 Å for Al, 10–11 Å for O, 12 Å for K and 16 Å for Na. There is no abrupt change in the mobility of the atoms during the passage from the hot magma to the supercritical fluid.

Figs. S4 and S5 in supplementary show the MSD for all the temperatures and densities studied here. They are almost linear with respect to time, with some exceptions for Na and K especially at low density. Since free cations move further away than big clusters of atoms, these variations in the curve slopes can be explained by the volatilization of isolated Na and K. Indeed, this is seen in the analysis of the MSD for individual atoms, as the free cations have larger MSD and distinguish themselves from the cations in the melt.

The slope of the MSD yield the self-diffusivity coefficients, which are shown in Figure 12 for Al, Si, O and the cations Na and K as a function of density for temperatures between 3000 K and 7000 K. Na and K are always the most diffusive elements at low densities. Their diffusion coefficients decrease by about one order of magnitude over the 2.0–4.0 g cm^{-3} density range. The self diffusivities of Al, O and Si are similar along each isotherm, resulting from the polymerized character of the melt. Their diffusion coefficient is about half an order of magnitude smaller than for the Na and K cations, which occupy the interstitial space between the silica and alumina polymers. The difference in diffusion coefficients correlates well with the difference in lifetimes of coordination polyhedra of the different species, the NaO_x and KO_x species having shorter lifetimes than the SiO_x and AlO_x. The difference between isotherms is reduced when the temperature increases. At high temperature and low density, the self diffusivity of every element tends toward 1–2 $\times$ 10^{-7} m^2 s^{-1}.

The values for diffusion coefficients that we obtain from our simulations are on the same order of magnitude as the theoretical values published previously on various other silicate melts. For example D_{Si} at 4000 K and 1 GPa that we obtain in hot liquid feldspars is around 6×10^{-9} m^2 s^{-1}, compared to about 1×10^{-8} m^2 s^{-1} in anorthite (de Koker, 2010), 1×10^{-9} m^2 s^{-1} in silica (Karki et al., 2007), and 8×10^{-9} m^2 s^{-1} in pyrolite (Caracas et al., 2019). An Arrhenius fit to the theoretical values of diffusion extrapolated to low temperatures, yields diffusion coefficients similar to experimental values obtained between 1000 and 2000 K in alkali feldspar melts (Freda & Baker, 1998). The agreement between extrapolated values and experimental results is better for Na than for K. Figure 13 shows our theoretical results at low pressure, compared to the available experimental data (Freda & Baker, 1998).

At 2000 K and 3000 K for densities larger than about 1.7 g cm^{-3} diffusion is very sluggish for Al, Si, and O. Indeed, some of the simulations at low temperature are in the regime of undercooled melt, laying below the melting lines. Spera et al. (2009) suggested that in order to be accurate and meaningful, liquid MD simulations must be performed for temperatures above the computer glass transition, estimated around 2800 K for $CaAl_2Si_2O_8$, a value that increases when the pressure increases. Other works (Harvey & Asimow, 2015) suggest that sufficient sampling of the configuration space is achieved when all atoms in a melt change at least one crystallographic site. For a polymerized silicate melt, this corresponds to a displacement of all Si atoms, the least diffusive species, by at least 3 Å according to the pair distribution function of Si-Si, or a mean square displacement of at

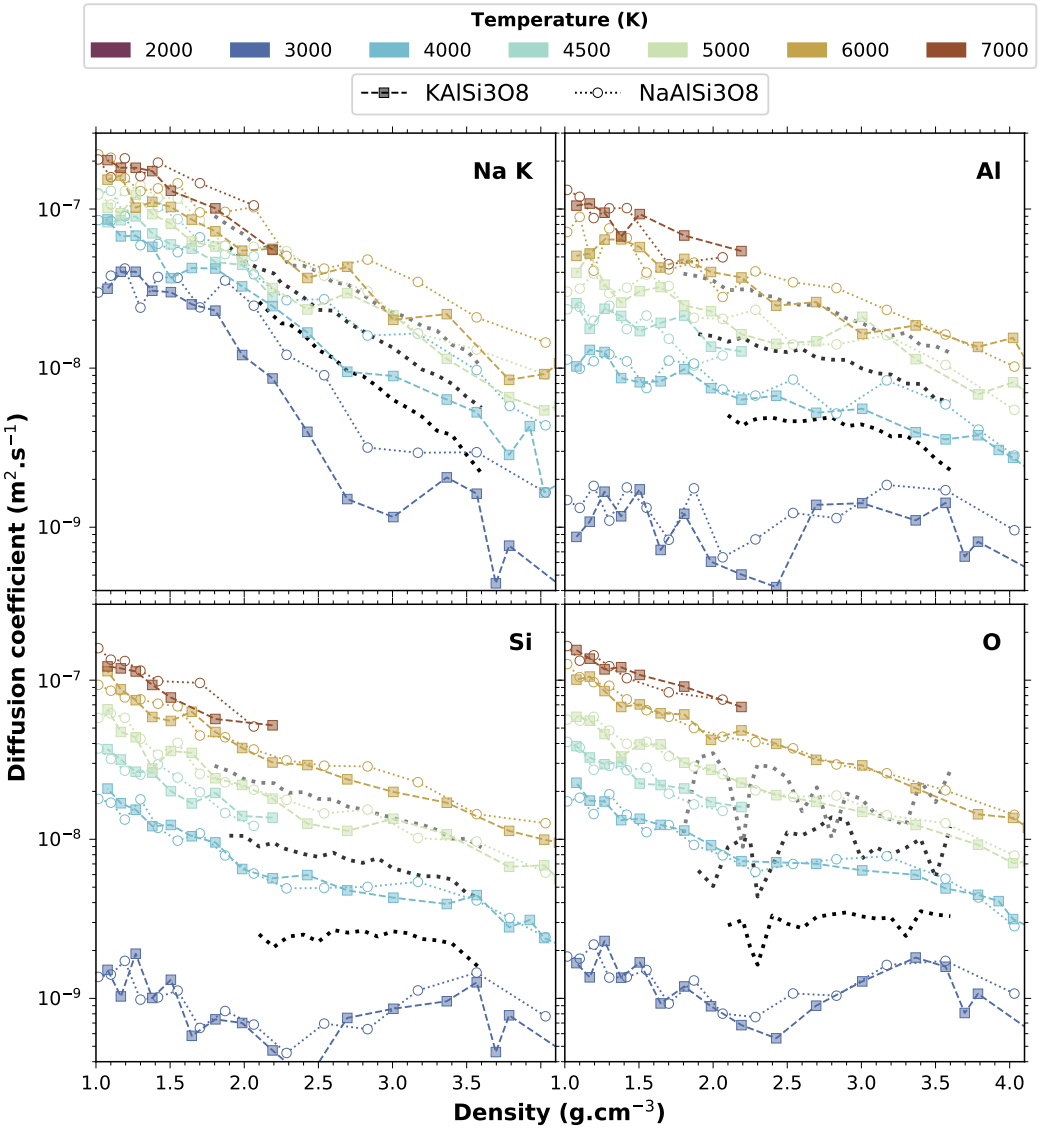

Figure 12. Self-diffusion coefficients for every element as a function of density. The black to light gray lines are theoretical results from Neilson et al. (2016) on $NaAlSi_3O_8$ at approximately 3000, 4000 and 5000 K.

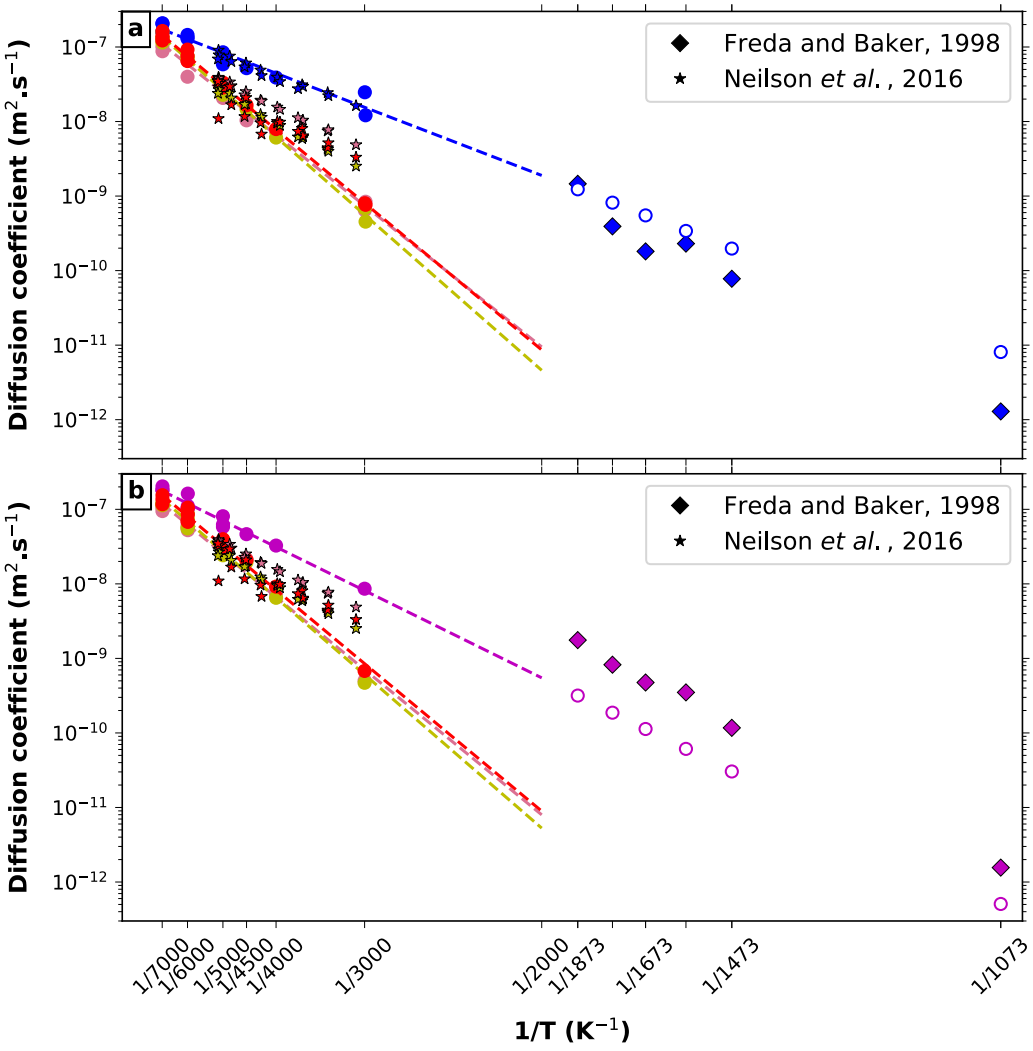

Figure 13. Self diffusion coefficients for (a) Na- and (b) K-feldspar end-members at 1 GPa as a function of the inverse temperature (filled circles), and fit of the Arrhenius law (dashed lines). Colors indicate elements: red - O, yellow - Si, pink - Al, blue - Na, purple - K. The stars indicate results from a classical MD simulation on molten albite (Neilson et al., 2016), and diamonds are experimental results on albite-orthoclase melts (Freda & Baker, 1998). Empty circles are the extrapolated diffusivities at the experimental temperatures using the Arrhenius fit of our data.

least $9\,\text{Å}^2$ within the length of the production run. This value extends beyond the first coordination sphere of Si by Si. This distance can be traveled only by allowing for long simulation times, which is now tractable on the available computational resources. In the large majority our simulations are long enough to show a MSD of Si larger than $9\,\text{Å}^2$.

4 Behavior of a Feldspathic Crust During Impacts

The early part of the Hadean was dominated by impacts as the main phase of the accretion unfolded. Many could have generated partial melting and partial freezing episodes (e.g. Elkins-Tanton, 2012), which in turn could have led to the formation of some primitive crust. The giant impact marked the end of this major part of Earth's history. From the subsequent protolunar disk the Earth condensed and differentiated into the central liquid core enveloped by the magma ocean, *i.e.* the molten state of the entire mantle. The crust eventually separated from cooling of the magma ocean. In a terrestrial-like planet, even if we cannot know precisely what would be the extent of the crust nor the temperature at the surface of the proto-planet, feldspars must have been one of the major components of this crust, because of their buoyancy and their early position in the crystallisation sequence.

In order to model the behavior of the major alkali feldspathic component of the crust during shock as generated by large impacts we build the Hugoniot equations of state, using our computed density-pressure-temperature points. Using the computed Hugoniot equations of state we can infer the shock state after large impacts for the Earth and the Moon crusts using the impedance match method (Forbes, 2012) presented in Figure 14 (a).

We consider three possible initial thermal states, which we denote as cold, warm and hot; for the cold state we further consider three densities at ambient pressure, corresponding to the range found in the continental crust. The Hugoniot equations of state obtained for the different initial states are represented in Figs. 14 (b,c).

For the first scenario, temperatures are considered to be close to the ambient temperature of today. This case is relevant for shock experiments or crustal impacts on cold astronomical bodies, for example depleted of atmosphere. The crust is solid, made of feldspar crystals. As an extreme case, we infer a thickness of up to 50 km (current values are an average of about 30 km for the Earth and about 50 km on the Moon (Taylor & McLennan, 2008)). According to the estimated variations of the pressure as a function of depth inside terrestrial planets (Warren, 1985), the pressure at the bottom of such a crust would be less than 2 GPa. This is translated in densities in the 2.5–2.7 $\text{g}\,\text{cm}^{-3}$ range for the two feldspars. We consider three density points in this range, at 2.5, 2.6, and 2.7 $\text{g}\,\text{cm}^{-3}$ and model the initial state using standard static calculations on ideal triclinic feldspar crystals. We find that the thickness of the crust or the possible presence of a shallow atmosphere have a weak effect on the Hugoniot equations of state (blue curves and areas in Figs. 14 b,c).

For the second scenario, we assume the surface temperature to be above the melting temperature of feldspars, as if a magma ocean has just crystallized. The melting temperature of feldspar varies with the composition. It ranges from 1383 K for Na composition to 1823 K for Ca composition (Bowen, 1913), and is around 1473 K for K end-member (Lange, 2007). We choose to use 1932 K as initial temperature in order to compare our results with those obtained experimentally by Asimow and Ahrens (2010) on anorthite. This scenario is particularly relevant for the crystallization of the Moon. In a dry lunar magma ocean, feldspars float whereas they sink in a terrestrial wet magma ocean (Taylor, 1982). For this case the Hugoniot curve lies at higher temperatures and pressures than in the previous case (orange curves and area in Figs. 14 b,c).

For the third scenario, temperatures are similar to the surface of a hot magma ocean, as covered for example by a thick silicate atmosphere. The density of a liquid feldspar is much lower than its corresponding solid form. This effect combined with the thermal expansion of liquids leads to a density of $2.26\,\mathrm{g\,cm^{-3}}$ at a temperature of 3000 K in the case of the K end-member (Lange, 2007). The calculated Hugoniot line is the highest in both temperature and pressure from all the three cases (red curves and area in Figs. 14 b,c).

Up to 5000 K the two feldspars have similar Hugoniot equations of state. At higher temperatures the pressure along the Hugoniot of the K-feldspar deviates by up to 75 GPa above that of the Na-feldspar and the temperature by about 2000 K above that of the Na-feldspar. For both feldspars, the initial temperature has weak influence on the final temperature and pressure, but decreasing the initial density leads to considerably higher Hugoniot temperatures and lower pressures. We do not specifically calculate the Hugoniot equations of state beyond 20 000 K since the pseudopotentials are missing electronic states that might be occupied at such high temperatures. However we are able to provide an extrapolated estimate based on the computed lower temperatures (see Tables S1 and S2 in supplementary).

For the impedance match method we make the approximation of planar waves generated by the impacts, which propagate in the two bodies after the initial shock. Then equating the pressure in the dynamic impactor and the static target yields the peak shock conditions.

We choose velocities for the impactor of 12.9, 15.2 and $18.1\,\mathrm{km\,s^{-1}}$ for the impact with the Earth and 8.3, 11.5 and $15.2\,\mathrm{km\,s^{-1}}$ for the impact with the Moon. These values correspond respectively to the first, second and third quartile of the Earth and Moon impactor velocities obtained on a basis of 1487 impacts generated for the Earth in the work of Raymond et al. (2013) on planetary impacts during the late veneer (personal communication). We employ the formalism from Raymond et al. (2013) (Eq. 3, 4 and 5) to compute the two-body escape velocities along with the impact velocities on the Moon. We consider all the impactors to have a density of $3.0\,\mathrm{g\,cm^{-3}}$ regardless of their possible composition, as in Raymond et al. (2013), and 0 K temperature.

We obtain the peak shock conditions by intersecting the cold Hugoniot of the impactor with the various Hugoniot equations of the cold, hot, or molten feldspar crust (Figure 14 a). The results are shown in Figure 14 (b,c) for the various possible thermal and dynamical scenarios for both the target and the impactor (for numerical values see Tables S3 and S4 in supplementary).

Our results show that for velocity impacts lower than about $10\,\mathrm{km\,s^{-1}}$ in a cold crust the peak temperatures would remain below 4500 K and pressures below about 100 GPa; at these conditions the crust would enter a pre-melting regime or might even melt. At impact velocities larger than $10\,\mathrm{km\,s^{-1}}$ but still in a cold crust, the peak conditions would exceed 7500 K in temperature and about 200 GPa in pressure. This suggests that the peak conditions of the impacts that produced the large basins on the Moon were energetic enough to have brought the crust into supercritical state. The lava then condensed along the liquid-vapor equilibrium lines, which implies that a large part of the volatile components would have been lost into space.

In the case of early Earth, hot crust or local magma ponds likely existed and impacts into these structures would have had a very different outcome. In this case the temperatures can reach between 10 000 K and up to 30 000 K depending on the impactor velocity. At these conditions the integrity of the crust would be completely erased, as all materials would melt and reach supercritical state. The crust would then be integral part of the protolunar disk, bringing a silica- and alkali-rich contribution. This was the case of the Giant Impact.

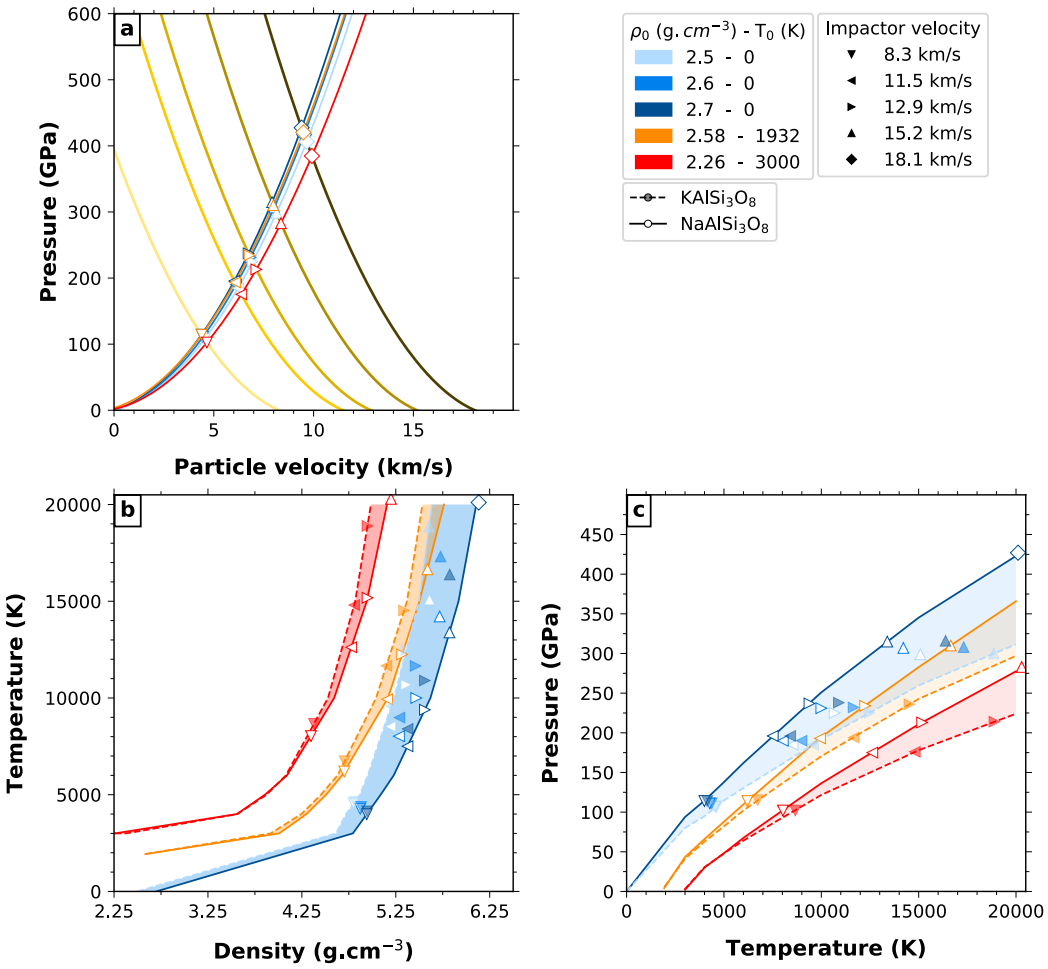

Figure 14. Peak shock conditions are obtained at the intersection between the cold Hugoniot curve of the impactor and the Hugoniot curves of the crust (a). For the crust we consider various initial temperatures and densities, represented by different colors. We consider several possible impactor velocities. The peak conditions are then represented with different symbol shapes in several projections: (b) temperature-density and (c) pressure-temperature. Open and filled symbols for the K and Na-feldspar respectively. Numerical values for the Hugoniot curves and peak shock condition are available in supplementary, Tables S1, S2, S3, S4.

5 Conclusions

We computed the critical point of alkali feldspars, using first-principles molecular dynamics calculations. We find that two critical points lie at similar thermodynamic conditions: 0.5-0.8 g cm^{-3} and 5500–6000 K range for the Na-feldspar, 0.5–0.9 g cm^{-3} and 5000–5500 K range for the K-feldspar.

We determine a number of physical properties of the Na- and K- fluids and find them remarkably similar. The speciation shows increasing coordination to be the favorite mechanism for accommodating compression. At low pressure, the melt is dominated by polymerized silica and alumina tetrahedra; a five-fold coordination component is already present at 0 GPa. As pressure increases, above about 10 GPa, SiO_6 and AlO_6 appear in the melt. Their lifetime is on the order of 30 fs at 3000 K and decreases drastically down to 15 fs at 6000 K. SiO_6 becomes the dominant silica species above 70 GPa at 3000 K and 50 GPa at 6000 K. SiO_7 species appear at around 40 GPa at 6000 K. In general Al shows a larger coordination than Si at any given pressures and temperatures.

Our FPMD simulation suggest that there is potential degassing of O_2 from the silicate melt starting between 4000 and 4500 K independently of the composition of the melt. They also shows that the vaporization at constant temperature is incongruent, the gas being dominated by free Na and K cations and then, second in importance, small volatile species like O_2, SiO, and SiO_2. Vaporization leaves behind a melt that is enriched in Al and Si.

Compared to other available rock-forming minerals, we find that both Na- and K-feldspars have critical temperatures located in the estimated range for silica, and below the critical temperature of $MgSiO_3$. At the moment of a giant impact, materials can attain much higher temperatures, as observed in our Hugoniot equations of state, reaching a complete supercritical phase. Upon cooling of the disk, the $MgSiO_3$ fluid would be the first to hit the liquid-vapor dome if allowed to decompress, and start to separate into two phases, liquid and vapor. The Na-feldspar, closely followed by the K-feldspar, will remain in the supercritical state for a longer time. When these phases hit the liquid-vapor dome they would exhibit a strong chemical incongruent behavior and enrich the gas in alkalis.

Finally, our simulations suggest that impacts on a cold crust could melt the crust and lead to the formation of local magma lakes, like on the Moon. However, large and very large impacts on warm or even molten crust could have pushed the temperature in the first stages of the protolunar disk to extreme values, on the order of 20 000 K–30 000 K. In this case previous giant impact simulations that consider hot or even molten initial states for the proto-Earth might need to be revisited using these new Hugoniot equations of state.

Acknowledgments

The reader can find in supplementary every additional figure or table mentioned in the text. All the data sets referenced in the main text and in the supplementary are available in the Zenodo repository Kobsch and Caracas (2020). The UMD package used for data post-processing is also avalaible in open access (Caracas et al., 2020). The scientific color maps romaO, imola and lajolla (Crameri, 2019) are used in this study to prevent visual distortion of the data and exclusion of readers with color-vision deficiencies (Crameri, 2018). This work was supported by the European Research Council (ERC) under the European Union's Horizon 2020 research and innovation program (grant agreement number 681818 – IMPACT), and by the Research Council of Norway through its Centres of Excellence funding scheme, project number 223272. We acknowledge access to the GENCI supercomputers (Occigen and Ada) through the stl2816 series of eDARI computing grants.

References

Ahrens, T. J., Petersen, C. F., & Rosenberg, J. T. (1969). Shock compression of feldspars. *Journal of Geophysical Research*, *74*(10), 2727–2746.

Akaogi, M., Kamii, N., Kishi, A., & Kojitani, H. (2004). Calorimetric study on high-pressure transitions in $KAlSi_3O_8$. *Physics and Chemistry of Minerals*, *31*(2), 85–91.

Asimow, P. D., & Ahrens, T. J. (2010). Shock compression of liquid silicates to 125 GPa: The anorthite-diopside join. *Journal of Geophysical Research: Solid Earth*, *115*(B10).

Bajgain, S. K., & Mookherjee, M. (2020). Structure and Properties of Albite Melt at High Pressures. *ACS Earth and Space Chemistry*, *4*(1), 1–13.

Bell, P. M., & Roseboom Jr., E. H. (1969). Melting relationships of jadeite and albite to 45 kilobars with comments on melting diagrams of binary systems at high pressures. *Mineralogical Society of America Special Paper*, *2*(Pyroxenes And Amphiboles: Crystal Chemistry And Phase Petrology), 151–162.

Binder, K., Block, B. J., Virnau, P., & Tröster, A. (2012). Beyond the Van Der Waals loop: What can be learned from simulating Lennard-Jones fluids inside the region of phase coexistence. *American Journal of Physics*, *80*(12), 1099–1109.

Blöchl, P. E. (1994). Projector augmented-wave method. *Physical Review B*, *50*, 17953–17979.

Bowen, N. L. (1913). The melting phenomena of the plagioclase feldspars. *American Journal of Science*, *Series 4 Vol. 35*(210), 577–599.

Canup, R. M. (2012). Forming a Moon with an Earth-like Composition via a Giant Impact. *Science*, *338*(6110), 1052–1055.

Canup, R. M., & Esposito, L. W. (1996). Accretion of the Moon from an Impact-Generated Disk. *Icarus*, *119*, 427–446.

Caracas, R., Hirose, K., Nomura, R., & Ballmer, M. D. (2019). Melt–crystal density crossover in a deep magma ocean. *Earth and Planetary Science Letters*, *516*, 202–211.

Caracas, R., Kobsch, A., Solomatova, N. V., Li, Z., Soubiran, F., & Hernandez, J.-A. (2020). *rcaracas/umd_package 1.0.0.* Zenodo. Retrieved from `https://doi.org/10.5281/zenodo.3710978` doi: 10.5281/zenodo.3710978

Crameri, F. (2018). Geodynamic diagnostics, scientific visualisation and StagLab 3.0. *Geoscientific Model Development*, *11*(6), 2541–2562.

Crameri, F. (2019). *Scientific colour maps.* Zenodo. Retrieved from `https://doi.org/10.5281/zenodo.3596401` (The development of the scientific colour maps is supported by the Research Council of Norway through its Centers of Excellence funding scheme, Project Number 223272) doi: 10.5281/zenodo.3596401

Ćuk, M., & Stewart, S. T. (2012). Making the Moon from a Fast-Spinning Earth: A Giant Impact Followed by Resonant Despinning. *Science*, *338*(6110), 1047–1052.

de Koker, N. (2010). Structure, thermodynamics, and diffusion in $CaAl_2Si_2O_8$ liquid from first-principles molecular dynamics. *Geochimica et Cosmochimica Acta*, *74*(19), 5657–5671.

Elkins-Tanton, L. (2012). Magma Oceans in the Inner Solar System. *Annual Review of Earth and Planetary Sciences*, *40*(1), 113–139.

Faussurier, G., Blancard, C., & Silvestrelli, P. L. (2009). Evaluation of aluminum critical point using an ab initio variational approach. *Physical Review B*, *79*, 134202–134202.

Fegley, B., & Cameron, A. G. W. (1987). A vaporization model for iron/silicate fractionation in the Mercury protoplanet. *Earth and Planetary Science Letters*, *82*(3), 207–222.

Flyvbjerg, H., & Petersen, H. G. (1989). Error estimates on averages of correlated data. *The Journal of Chemical Physics*, *91*(1), 461–466.

Forbes, J. W. (2012). *Shock Wave Compression of Condensed Matter: A Primer*. Heidleberg: Springer.

Freda, C., & Baker, D. R. (1998). Na-K interdiffusion in alkali feldspar melts. *Geochimica et Cosmochimica Acta*, *62*(17), 2997–3007.

Gilmore, M., Treiman, A., Helbert, J., & Smrekar, S. (2017). Venus Surface Composition Constrained by Observation and Experiment. *Space Science Reviews*, *212*(3), 1511–1540.

Green, E. C. R., Artacho, E., & Connolly, J. A. D. (2018). Bulk properties and near-critical behaviour of SiO_2 fluid. *Earth and Planetary Science Letters*, *491*, 11–20.

Harvey, J.-P., & Asimow, P. D. (2015). Current limitations of molecular dynamic simulations as probes of thermo-physical behavior of silicate melts. *American Mineralogist*, *100*, 1866–1882.

Hohenberg, P., & Kohn, W. (1964). Inhomogeneous Electron Gas. *Physical Review*, *136*, B864-B871.

Hoover, W. G. (1985). Canonical dynamics: Equilibrium phase-space distributions. *Physical Review A*, *31*(3), 1695–1697.

Humphrey, W., Dalke, A., & Schulten, K. (1996). VMD – Visual Molecular Dynamics. *Journal of Molecular Graphics*, *14*, 33–38.

Jackson, W. E., Brown, G. E., & Ponader, C. W. (1987). X-ray absorption study of the potassium coordination environment in glasses from the $NaAlSi_3O_8$-$KAlSi_3O_8$ binary: Structural implications for the mixed-alkali effect. *Journal of Non-Crystalline Solids*, *93*(2), 311–322.

Karki, B. B., Bhattarai, D., & Stixrude, L. (2007). First-principles simulations of liquid silica: Structural and dynamical behavior at high pressure. *Physical Review B*, *76*(10), 104205.

Karki, B. B., Bohara, B., & Stixrude, L. (2011). First-principles study of diffusion and viscosity of anorthite ($CaAl_2Si_2O_8$) liquid at high pressure. *American Mineralogist*, *96*(5-6), 744–751.

Karki, B. B., Ghosh, D. B., & Bajgain, S. K. (2018). Chapter 16 - Simulation of Silicate Melts Under Pressure. In Y. Kono & C. Sanloup (Eds.), *Magmas Under Pressure* (pp. 419–453). Elsevier.

Kobsch, A., & Caracas, R. (2020). *Thermodynamics data of Alkali Feldspars from FPMD simulations.* Zenodo. Retrieved from `https://doi.org/10.5281/zenodo.3860527` doi: 10.5281/zenodo.3860527

Kohn, W., & Sham, L. J. (1965). Self-Consistent Equations Including Exchange and Correlation Effects. *Physical Review*, *140*, A1133-A1138.

Kraus, R. G., Stewart, S. T., Swift, D. C., Bolme, C. A., Smith, R. F., Hamel, S., ... Collins, G. W. (2012). Shock vaporization of silica and the thermodynamics of planetary impact events. *Journal of Geophysical Research: Planets*, *117*, E09009-E09009.

Kresse, G., & Furthmüller, J. (1996a). Efficiency of ab-initio total energy calculations for metals and semiconductors using a plane-wave basis set. *Computational Materials Science*, *6*(1), 15–50.

Kresse, G., & Furthmüller, J. (1996b). Efficient iterative schemes for ab initio total-energy calculations using a plane-wave basis set. *Physical Review B*, *54*(16), 11169–11186.

Kresse, G., & Hafner, J. (1993). Ab initio molecular dynamics for liquid metals. *Physical Review B*, *47*(1), 558–561.

Kresse, G., & Joubert, D. (1999). From ultrasoft pseudopotentials to the projector augmented-wave method. *Physical Review B*, *59*, 1758–1775.

Lange, R. A. (2007). The density and compressibility of $KAlSi_3O_8$ liquid to 6.5 GPa. *American Mineralogist*, *92*(1), 114–123.

Lindsley, D. H. (1966). Melting relations of $KAlSi_3O_8$: Effect of pressures up to 40 kilobars. *American Mineralogist*, *51*(11-12), 1793–1799.

Litvin, Y. A., & Gasparik, T. (1993). Melting of jadeite to 16.5 GPa and melting relations on the enstatite-jadeite join. *Geochimica et Cosmochimica Acta*, *57*(9), 2033–2040.

Lock, S. J., Stewart, S. T., Petaev, M. I., Leinhardt, Z. M., Mace, M. T., Jacobsen, S. B., & Ćuk, M. (2018). The origin of the Moon within a terrestrial synestia. *Journal of Geophysical Research: Planets*.

Luo, S.-N., Akins, J. A., Ahrens, T. J., & Asimow, P. D. (2004). Shock-compressed $MgSiO_3$ glass, enstatite, olivine, and quartz: Optical emission, temperatures, and melting. *Journal of Geophysical Research: Solid Earth*, *109*(B05205), 1–14.

McQueen, R. G., Marsh, S. P., & Fritz, J. N. (1967). Hugoniot equation of state of twelve rocks. *Journal of Geophysical Research*, *72*(20), 4999–5036.

Melosh, H. J. (2007). A hydrocode equation of state for SiO_2. *Meteoritics & Planetary Science*, *42*(12), 2079–2098.

Mermin, N. D. (1965). Thermal Properties of the Inhomogeneous Electron Gas. *Physical Review*, *137*(5A), A1441-A1443.

Muller, E., Heide, K., & Zanotto, E. D. (1993). Molecular structure and nucleation in silicate glasses. *Journal of Non-Crystalline Solids*, *155*(1), 56–66.

Neilson, R. T., Spera, F. J., & Ghiorso, M. S. (2016). Thermodynamics, self-diffusion, and structure of liquid $NaAlSi_3O_8$ to 30 GPa by classical molecular dynamics simulations. *American Mineralogist*, *101*(9), 2029–2040.

Newton, R. C., & Smith, J. V. (1967). Investigations concerning the Breakdown of Albite at Depth in the Earth. *The Journal of Geology*, *75*(3), 268–286.

Nosé, S. (1984). A unified formulation of the constant temperature molecular dynamics methods. *The Journal of Chemical Physics*, *81*(1), 511–519.

Perdew, J. P., Burke, K., & Ernzerhof, M. (1996). Generalized Gradient Approximation Made Simple. *Physical Review Letters*, *77*(18), 3865–3868.

Raymond, S. N., Schlichting, H. E., Hersant, F., & Selsis, F. (2013). Dynamical and collisional constraints on a stochastic late veneer on the terrestrial planets. *Icarus*, *226*(1), 671–681.

Ribbe, P. H. (1984). Average Structures of Alkali and Plagioclase Feldspars: Systematics and Applications. In W. L. Brown (Ed.), *Feldspars and Feldspathoids: Structures, Properties and Occurrences* (pp. 1–54). Dordrecht: Springer Netherlands.

Root, S., Shulenburger, L., Lemke, R. W., Dolan, D. H., Mattsson, T. R., & Desjarlais, M. P. (2015). Shock Response and Phase Transitions of MgO at Planetary Impact Conditions. *Physical Review Letters*, *115*(19), 198501.

Schaefer, L., & Fegley, B. (2004). A thermodynamic model of high temperature lava vaporization on Io. *Icarus*, *169*(1), 216–241.

Solomatova, N. V., & Caracas, R. (2019). Pressure-induced coordination changes in a pyrolitic silicate melt from ab initio molecular dynamics simulations. *Journal of Geophysical Research: Solid Earth*, *124*(11).

Spera, F. J., Nevins, D., Ghiorso, M., & Cutler, I. (2009). Structure, thermodynamic and transport properties of $CaAl_2Si_2O_8$ liquid. Part I: Molecular dynamics simulations. *Geochimica et Cosmochimica Acta*, *73*(22), 6918–6936.

Stein, D. J., Stebbins, J. F., & Carmichael, I. S. E. (1986). Density of Molten Sodium Aluminosilicates. *Journal of the American Ceramic Society*, *69*(5), 396–399.

Szurgot, M. (2014). Mean Composition of Feldspar in HED Meteorites and in Protoplanet Vesta. In *Poster Abstracts: Vesta at Large* (p. #2052). Houston, Texas.

Taylor, S. R. (1982). *Planetary Science: A Lunar Perspective*. Lunar and Planetary Institute.

Taylor, S. R., & McLennan, S. (2008). A primary crust: The highland crust of the

Moon. In *Planetary Crusts: Their Composition, Origin and Evolution* (pp. 32–60). Cambridge University Press.

Taylor, S. R., & McLennan, S. M. (1995). The geochemical evolution of the continental crust. *Reviews of Geophysics*, *33*(2), 241–265.

Tenner, T. J., Lange, R. A., & Downs, R. T. (2007). The albite fusion curve revisited: New experiments and the high-pressure density and compressibility of high albite and $NaAlSi_3O_8$ liquid. *American Mineralogist*, *92*(10), 1573–1585.

Tsuchiya, T., & Tsuchiya, J. (2011). Prediction of a hexagonal SiO_2 phase affecting stabilities of $MgSiO_3$ and $CaSiO_3$ at multimegabar pressures. *Proceedings of the National Academy of Sciences*, *108*(4), 1252–1255.

Urakawa, S., Kondo, T., Igawa, N., Shimomura, O., & Ohno, H. (1994). Synchrotron radiation study on the high-pressure and high-temperature phase relations of $KAlSi_3O_8$. *Physics and Chemistry of Minerals*, *21*(6), 387–391.

Visscher, C., & Fegley Jr., B. (2013). Chemistry of Impact-generated Silicate Melt-vapor Debris Disks. *The Astrophysical Journal Letters*, *767*(1), L12-L12.

Warell, J., Sprague, A., Kozlowski, R., Rothery, D. A., Lewis, N., Helbert, J., & Cloutis, E. (2010). Constraints on Mercury's surface composition from MESSENGER and ground-based spectroscopy. *Icarus*, *209*(1), 138–163.

Warren, P. H. (1985). The Magma Ocean Concept and Lunar Evolution. *Annual Review of Earth and Planetary Sciences*, *13*(1), 201–240.

Xiao, B., & Stixrude, L. (2018). Critical vaporization of $MgSiO_3$. *Proceedings of the National Academy of Sciences*, *115*(21), 5371–5376.

Xue, X., & Stebbins, J. F. (1993). ^{23}Na NMR chemical shifts and local Na coordination environments in silicate crystals, melts and glasses. *Physics and Chemistry of Minerals*, *20*(5), 297–307.

Zhang, J., Li, B., Utsumi, W., & Liebermann, R. C. (1996). In situ X-ray observations of the coesite-stishovite transition: Reversed phase boundary and kinetics. *Physics and Chemistry of Minerals*, *23*(1), 1–10.